The Long-Term Outcomes of Double White Dwarf Mergers

By

Josiah Schwab

A dissertation submitted in partial satisfaction of the

requirements for the degree of

Doctor of Philosophy

in

Physics

in the

Graduate Division

of the

University of California, Berkeley

Committee in charge:

Professor Eliot Quataert, Chair
Professor Daniel Kasen
Professor Burkhard Militzer

Spring 2016

The Long-Term Outcomes of Double White Dwarf Mergers

Abstract

The Long-Term Outcomes of Double White Dwarf Mergers

by

Josiah Schwab

Doctor of Philosophy in Physics

University of California, Berkeley

Professor Eliot Quataert, Chair

In double white dwarf (WD) systems with sufficiently short initial orbital periods, angular momentum losses from gravitational wave radiation shrink the orbit and can lead to the merger of the WDs. Simulations of the merger show that the less massive WD is tidally disrupted, forming a disk around the more massive WD. Beginning with output from WD merger simulations, I study the subsequent viscous evolution using multi-dimensional hydrodynamical simulations. I find that the remnants evolve towards a spherical end-state, where the rotationally-supported disk has been converted into a hot, thermally-supported envelope. I then map these results into a stellar evolution code and evolve them over thermal and nuclear timescales. This is a necessary procedure to self-consistently study the long-term outcomes of WD mergers. I apply this to the merger of two carbon-oxygen WDs with a total mass in excess of the Chandrasekhar mass. My work follows the evolution of the remnants for longer than previous calculations and finds alternating episodes of fusion and contraction can lead to the formation and subsequent collapse of an iron core. I also characterize the observable properties of the remnant during this evolution. Additionally, I develop a framework to compute weak reaction rates that are essential in the evolution of massive, accreting WDs. I apply these results to understand the evolution of oxygen-neon WDs towards accretion-induced collapse to a neutron star.

In memory of my father.

Contents

List of Figures

List of Tables

Acknowledgments

My twenty-four years of schooling—seven of which are reflected in this thesis—have involved many more people than I can reasonably acknowledge here.

First and foremost, I thank my parents Charles and Renae, my wife Annelise, my brother Jared, and my grandmother Esther, for their unwavering love and support.

Thanks to Tom Cummings, for showing me that the world was far bigger than I had ever imagined. Thanks to Saul Rappaport for his teaching and mentorship while I was at MIT; it has proved a strong foundation upon which to build.

I thank Eliot Quataert for his guidance. He has been an exemplary thesis advisor, generous with both his time and his insight. I also thank Lars Bildsten for his mentorship; he has, in many ways, been like a second advisor to me. I thank everyone involved with MESA, especially Bill Paxton.

I am grateful to my fellow graduate students and postdocs for many things both big and small. I especially thank Jacob Lynn, Nathaniel Roth, and Ken Shen. Thanks to Peter Williams this dissertation was typeset using the ucastrothesis LaTeX template.

Chapter 1

Introduction

1.1   Background

White dwarfs (WDs) are the end product of the stellar evolution of low mass stars ($M \lesssim 8\,\mathrm{M_\odot}$). Significant mass loss occurs over the star's lifetime, resulting in the formation of objects below the maximum mass ($\approx 1.4\,\mathrm{M_\odot}$) that can be supported by electron degeneracy pressure (Chandrasekhar 1931). More massive WDs come from more massive stars and as a result, the composition of a WD is also related to its mass, reflecting the additional stages of fusion that occurred. The lowest mass WDs ($M_{\mathrm{WD}} \lesssim 0.5\,\mathrm{M_\odot}$) are composed primarily of helium (He WDs); intermediate mass WDs ($0.5\,\mathrm{M_\odot} \lesssim M_{\mathrm{WD}} \lesssim 1.1\,\mathrm{M_\odot}$) of carbon and oxygen (CO WDs); the highest mass WDs ($1.1\,\mathrm{M_\odot} \lesssim M_{\mathrm{WD}}$) are of oxygen and neon (ONe WDs). The characteristic radii of these objects is $\sim 10^{-2}\,\mathrm{R_\odot}$. Left undisturbed, a WD will peacefully cool for the age of the universe (e.g. Hansen & Liebert 2003).

However, star formation produces many stars in binary systems (e.g., Duchêne & Kraus 2013). When the two stars are close enough that they are able to transfer mass during their evolution, processes such as the formation and ejection of a common envelope can shrink the orbit, producing close binary systems consisting of two WDs (e.g., Iben & Livio 1993). When the WD binary has a sufficiently short orbital period ($\lesssim 10\,\mathrm{hr}$), the angular momentum losses from gravitational wave radiation will shrink the orbit on a timescale shorter than the age of the universe, causing the WDs to interact. The gravitational waves radiated by these compact binaries are important sources for space-based interferometers capable of detecting mHz gravitational waves (e.g., Evans et al. 1987; Nelemans et al. 2001; Ruiter et al. 2010). The expectation that close WD binaries should exist (e.g., Paczyński 1967; Webbink 1979) developed well in advance of the first secure detection of a detached double WD with a period less than a day (Marsh 1995).

Ongoing observational efforts have since discovered many more close double degenerate systems. The SPY survey (Napiwotzki et al. 2001b) has discovered some of the most massive known double WD binaries (Napiwotzki et al. 2001a, 2002; Karl et al. 2003; Nelemans et al. 2005; Geier et al. 2010, 2011). Spectra from the Sloan Digital Sky Survey (SDSS: York et al. 2000) enabled the SWARMS survey (Badenes et al. 2009) and its discovery of a system

that will merge within 100 Myr (Mullally et al. 2009). Taken together, the SDSS spectra also provided constrains on the merger rate of binary WDs in the Milky Way disk (Badenes & Maoz 2012; Maoz et al. 2012). Searching for extremely low mass WDs—which cannot have formed via single star evolution in the age of the universe—has also proved to be an extremely fruitful avenue. The ELM survey (Brown et al. 2010; Kilic et al. 2011a; Brown et al. 2012; Kilic et al. 2012; Brown et al. 2013; Gianninas et al. 2015; Brown et al. 2016) has led to the detection of 76 new double degenerate binaries containing a low mass WD. This includes 4 with merger timescales less than 25 Myr (Brown et al. 2011; Kilic et al. 2011b,c, 2014).

Understanding the orbital evolution of double WDs continues to be an active area of research. The rate at which gravitational waves remove angular momentum from the system is known, but the effects of other processes that influence the orbital evolution are not as well understood. Tidal forces are thought to synchronize the spin and orbital periods of the WDs by the time that the WDs are close enough to begin transferring mass (Fuller & Lai 2012a; Burkart et al. 2013). During mass transfer, the orbital evolution depends on whether material is accreted via direct impact or through a disk; it is also sensitive to the prescriptions used to model the transfer of angular momentum between the WD spins and the orbit (Marsh et al. 2004; Gokhale et al. 2007; Sepinsky & Kalogera 2014; Kremer et al. 2015). The transferred mass can lead to nova explosions on the surface of the accretor and Shen (2015) has suggested that dynamical friction with the novae ejecta may cause all WD binaries to merge.

For those double WD systems that do merge, the final outcome is primarily controlled by the masses of the two WDs (which can alternatively be parameterized as the mass ratio and the total mass). Work by Iben & Tutukov (1984a) and Webbink (1984) roughly mapped out the outcomes as follows:

- The merger of two He WDs is thought to be a channel for producing single sub-dwarf B and O stars. These are blue, core He fusing stars that cannot be produced from the stellar evolution of a single star (Heber 2009).

- The merger of a He WD and a CO WD likely produces the R Coronae Borealis stars (Clayton 2012). These are cool, giant stars powered by shell He fusion; dust formation episodes in their atmospheres make them highly variable. They are also observed to have peculiar chemical compositions—extremely overabundant in ^{18}O (Clayton et al. 2007).

- The merger of two CO WDs with a total mass in excess of the Chandrasekhar mass was suggested as the progenitor of a Type Ia supernovae; however, see Nomoto & Iben (1985), Saio & Nomoto (1985), and Chapter 3 for arguments that these mergers lead to the formation of a neutron star.

This is an incomplete accounting. For two recent schematic views of the cornucopia of outcomes see Figure 1 in Dan et al. (2014) or Figure 3 in Shen (2015).

Beginning with the first results of Benz et al. (1990), numerical hydrodynamics calculations have been deployed to study the merging process, from the onset of dynamically unstable mass transfer through the disruption of one or both of the WDs. Over the past decade, work in this area has continued with the addition of new input physics, more accurate initial conditions, higher resolution and more sophisticated numerical techniques (e.g., Lorén-Aguilar et al. 2009; Dan et al. 2011; Raskin et al. 2012; Pakmor et al. 2012a; Sato et al. 2015; Katz et al. 2016). Several studies have found that some mergers can lead to a detonation (e.g., Guillochon et al. 2010; Pakmor et al. 2010; Dan et al. 2012; Moll et al. 2014), and substantial effort has been and continues to be invested in quantifying the properties of these explosions and comparing them to observed thermonuclear supernovae

However, the focus of this thesis is on double WD systems in which the merger *does not* lead to its catastrophic destruction. Instead, I focus on "long-term" outcomes, which occur as the structure of the WD merger remnant cools and adjusts to its new state created during the energetic merger. In what follows, I describe the arc of my research, deferring a detailed discussion of prior work to the individual chapters.

1.2   Overview of Research and Chapter Context

Viewed broadly, my work makes two key contributions. First, in Chapters 2 and 3, I develop the formalism necessary to take output from WD merger simulations, study the viscous evolution using multi-dimensional hydrodynamical simulations, and then map the results into a stellar evolution code. This is a necessary procedure to self-consistently study the long-term outcomes of WD mergers. Second, I develop a framework to compute weak reaction rates that are essential in the evolution of massive, accreting WDs. In Chapters 4 and 5, I apply these results to understand the evolution of ONe WDs towards accretion-induced collapse (AIC) to a neutron star.

1.2.1   Chapters 2 & 3 and Related Work

Simulations of the merger of two WDs (e.g., Dan et al. 2011) show that the less massive WD is tidally disrupted, forming a disk around the more massive WD. For some systems, the merger process is sufficiently violent to ignite runaway nuclear burning that leads to the destruction of the remaining WD. But in the many cases where this does not occur, the remnant disk, unstable to the magneto-rotational instability, evolves viscously on a timescale of hours (Shen et al. 2012). In Chapter 2, based on Schwab et al. (2012), I modify the ZEUS-MP2 hydrodynamics code—adding an appropriate equation of state and an α-viscosity—and perform the first multidimensional hydrodynamics simulations of the evolution of the viscous disks formed by WD mergers. This work finds a key new result: the remnants evolve towards a spherical end-state, where the rotationally-supported disk has been converted into a hot, thermally-supported envelope. This is contrary to decades of work which modeled the long-term evolution as the accretion of the low mass WD onto the massive WD. My results show

that this formulation of the problem is incorrect and that the post-merger evolution is instead a stellar evolution problem driven by the internal redistribution of heat and momentum and not by the external accretion of mass.

My numerical simulations also show that in some cases, viscous heating could potentially trigger a nuclear runaway in the remnant. This detonation might then trigger a thermonuclear supernova explosion. If this were to occur while there was still a significant amount of mass in the disk, the disk would have a substantial viewing-angle dependent effect on the observed properties of the supernova explosion. Raskin et al. (2014) generated light curves and spectra for explosions in which such a disk was present, in part using models I created.

The results of Schwab et al. (2012) are important input into calculations that follow the structure of the WD merger remnant as it cools and adjusts to the new state created during the energetic merger. A major thread of my ongoing work is exploring the variety of outcomes that can occur depending on the masses and compositions of the merging WDs.

Chapter 3 studies the merger of two massive CO WDs. I find that this event likely leads to the formation of a neutron star instead of a thermonuclear supernova, a result in in agreement with Nomoto & Iben (1985) and Saio & Nomoto (1985). Before the core can be compressed enough to cause an explosion, the initially off-center carbon fusion migrates inward to the core, converting the object to an oxygen-neon composition. My work, which follows the evolution of the remnants for longer than previous calculations, suggests alternating episodes of fusion and contraction can lead to the formation and subsequent collapse of an iron core. The presence of an iron core is a new and unexpected result, not part of standard AIC scenarios. This work also describes the observable properties of the remnant during this evolution, which previous approaches have been unable to address.

The burning fronts formed in these calculations take the form of convectively-bounded deflagration. Denissenkov et al. (2013) has suggested that convection can induce efficient mixing across these interfaces leading to disruption of the flame. In Lecoanet et al. (2016) I contributed to a set of 3D hydrodynamic simulations that quantified the mixing at these boundaries and found that mixing was unable to substantially affect the flame propagation.

1.2.2 Chapters 4 & 5 and Related Work

The thermal and compositional evolution of the central part of massive ONe WDs that are undergoing compression is largely driven by weak reactions. Such objects can arise in several contexts: the late stages of evolution for super asymptotic giant branch (SAGB) stars (e.g. Miyaji & Nomoto 1987), where the compression is caused by the deposition of material from exterior shell-burning; in a binary system with a massive ONe white dwarf (e.g. Nomoto & Kondo 1991), where the compression is caused by accretion from a non-degenerate companion; or as the remnant of a WD-WD merger, where the compression is caused by the cooling of the outer layers (e.g. Saio & Nomoto 1985). In these electron-degenerate conditions, the rates of electron-capture and beta-decay reactions are sufficiently sensitive to density and temperature that existing tabulations of weak rates are no longer suitable (e.g., Toki et al. 2013). I developed a capability for the MESA stellar evolution code

(Modules for Experiments in Stellar Astrophysics; Paxton et al. 2011, 2013) that calculates weak reaction rates on-the-fly from input nuclear data (Paxton et al. 2015). I have applied this feature in two studies of accreting ONe WDs.

In Chapter 4, based on Schwab et al. (2015), I focus on WDs composed of ^{16}O, ^{20}Ne, and ^{24}Mg. I confirm previous work (e.g. Miyaji & Nomoto 1987) that demonstrated the role that the A = 20 and 24 isotopes play in reducing the electron fraction and heating the core. I demonstrate the presence of a thermal runaway in the core triggered by the temperature and density sensitivity of the ^{20}Ne electron-capture reactions. Both analytics and numerics show that this thermal runaway does not trigger core convection, but rather launches an oxygen deflagration wave from the center of the star. The ability of MESA to perform extremely small spatial zoning allowed the models to reach length-scales that, for the first time, directly connect full-star simulations to studies of oxygen deflagrations performed using micro-zoned hydrodynamics codes (Timmes & Woosley 1992). I perform a parameter study that quantifies the influence of the ^{24}Mg mass fraction, the central temperature, the compression rate, and uncertainties in the electron-capture reaction rates on the ONe WD evolution. This establishes a lower limit on the central density at which the oxygen deflagration wave initiates. Based on previous work and order-of-magnitude calculations, objects which ignite oxygen at or above these densities will collapse and form a neutron star.

Chapter 5 focuses on the effects of the presence of the carbon-burning products ^{23}Na and ^{25}Mg. I demonstrated that these isotopes lead to substantial cooling of the WD via A = 23 and 25 Urca pairs. I derived an analytic formula for the peak Urca-process cooling rate and obtained a simple expression for the temperature to which the Urca process cools the WD, a result of significant utility for future work. For example, in Martínez-Rodríguez et al. (2016) I applied this understanding of weak reactions in dense plasmas to the evolution of accreting CO WDs—likely progenitors of Type Ia supernovae—before and during the simmering phase present in single degenerate progenitor models.

The calculations in Chapters 4 & 5 are important steps in producing more realistic progenitor models for studies of the signature of accretion-induced collapse (AIC). They provide key input physics and establish an analytic framework in which to understand more realistic models. In Brooks et al. (2016a), I applied the understanding of the balance between compressional heating and neutrino cooling that sets the core temperature of accreting WDs. This is important for determining whether an accreting WD will experience core or shell ignition. In Brooks et al. (2016b), I am applying this understanding to the evolution of binary systems consisting of a helium star and an ONe WD. This will be the first calculation of the evolution towards AIC in which both stars and their orbit are self-consistently modeled.

Chapter 2

The viscous evolution of white dwarf merger remnants

Abstract

The merger of two white dwarfs (WDs) creates a differentially rotating remnant which is unstable to magnetohydrodynamic instabilities. These instabilities can lead to viscous evolution on a time-scale short compared to the thermal evolution of the remnant. We present multi-dimensional hydrodynamic simulations of the evolution of WD merger remnants under the action of an α-viscosity. We initialize our calculations using the output of eight WD merger simulations from Dan et al. (2011), which span a range of mass ratios and total masses. We generically find that the merger remnants evolve towards spherical states on time-scales of hours, even though a significant fraction of the mass is initially rotationally supported. The viscous evolution unbinds only a very small amount of mass ($\lesssim 10^{-5} M_{\odot}$). Viscous heating causes some of the systems we study with He WD secondaries to reach conditions of nearly dynamical burning. It is thus possible that the post-merger viscous phase triggers detonation of the He envelope in some WD mergers, potentially producing a Type Ia supernova via a double detonation scenario. Our calculations provide the proper initial conditions for studying the long-term thermal evolution of WD merger remnants. This is important for understanding WD mergers as progenitors of Type Ia supernovae, neutron stars, R Coronae Borealis stars and other phenomena.

2.1   Introduction

Systems consisting of two white dwarfs (WDs) are natural outcomes of binary stellar evolution. These binaries are not static; absent any other torques the loss of angular mo-

mentum via gravitational wave (GW) emission will drive the binary together. Programs such as the SWARMS survey (Mullally et al. 2009) and the ELM survey (Brown et al. 2010) have dramatically increased the number of known WD binaries, including some systems that will merge within a Hubble time (Kilic et al. 2012). The Galactic population of WD binaries is expected to be a source of unresolved GW foregrounds at mHz frequencies, though only a handful of presently known systems would be individually detectable by a space-based GW interferometer mission (Nelemans 2009).

Details of the inspiral, in particular whether tidal torques cause the binary to be synchronized and the location of the tidal heating, are active areas of inquiry that can have a significant impact on the dynamics of the binary and the thermal state of the WDs (Fuller & Lai 2012b). As the orbital separation shrinks, the less massive (and hence larger) WD will eventually overflow its Roche lobe and begin transferring mass to the companion. The stability of this mass transfer depends on e.g., whether the material forms a disc or flows directly onto the companion, which in turn depends on the mass ratio (q) and total mass (M_{tot}) of the binary (e.g. Marsh et al. 2004).

Those systems that do undergo unstable mass transfer and subsequently merge have been of substantial theoretical interest. In particular, such systems have received attention as the possible progenitors of Type Ia supernovae (Iben & Tutukov 1984a; Webbink 1984). Considerable work exists exploring this "double degenerate" scenario and recent observational results have begun to favor it (e.g. Bloom et al. 2012; Schaefer & Pagnotta 2012). Another possibility is that double white dwarf binaries with total masses exceeding the Chandrasekhar mass undergo accretion induced collapse to form a neutron star (e.g. Saio & Nomoto 1985). Less massive double degenerate systems are likely to have non-explosive outcomes and have been invoked to explain objects like the R Coronae Borealis stars and extreme helium stars (Webbink 1984; Saio & Jeffery 2000; Clayton et al. 2007).

An accurate simulation of the merger process requires a 3D code without prescribed geometry and with good numerical conservation properties. For these reasons, the pioneering study of Benz et al. (1990) used smoothed particle hydrodynamics (SPH). More recent studies (e.g. Dan et al. 2011; Raskin et al. 2012; Pakmor et al. 2012b) have improved on these first results by contributing additional physics, more accurate initial conditions, higher resolution and more sophisticated numerical techniques. These simulations follow the evolution of the binary through the tidal disruption of one of the components. In some cases the merger is sufficiently violent that an explosion may result (Pakmor et al. 2010; Dan et al. 2012). When the merger itself does not trigger an explosion, some material from the disrupted lower mass WD forms a shock-heated layer at the surface of the primary WD while the rest of the material forms a thick disc at larger radii.

The evolution of such systems has frequently been treated in the literature as a long-lived ($\sim 10^5$ yr) phase of accretion from a disc at the Eddington limit (e.g. Nomoto & Iben 1985). This picture was improved by Yoon et al. (2007), who considered accretion at a similar rate but onto a hot envelope, and by van Kerkwijk et al. (2010a), who made simple α-disc estimates of the accretion time-scale and found it to be far more rapid ($\sim$ hours) than the time-scale for accretion at the Eddington limit.

Recently, Shen et al. (2012) provided a new model of the different evolutionary phases of WD merger remnants. They argued that the evolution is much more "star-like" than the accretion disc oriented models that have dominated the literature. More concretely, Shen et al. (2012) showed that the rapid dynamical evolution of the merger ($\sim 10^2$ s) gives way to a longer lived viscous phase driven by magnetohydrodynamic instabilities ($\sim 10^4 - 10^8$ s) before the onset of a long ($\sim 10^4$ yr) thermal phase. In contrast with previous work, this implies that the long term evolution of a white dwarf merger remnant is not determined by accretion, but rather by the internal redistribution of heat/momentum and the external cooling rate of the viscously heated, nearly shear-free remnant.

In Shen et al. (2012), the viscous evolution was calculated in 1D using a γ-law equation of state. The goal of this work is to refine the understanding of the outcome of the viscous evolution of WD merger remnants using higher dimensional numerical simulations. In addition, we consider a wider variety of WD+WD systems than Shen et al. (2012), who focused on roughly Chandrasekhar mass CO+CO mergers.

In §2 we outline the numerical methods we use, including how we construct our initial conditions from simulations by Dan et al. (2011). In §3 we present the results of each of our calculations. §4 provides a discussion of the end states of the calculations. In §5 we state our conclusions and propose avenues for future work. In an Appendix, we show various test calculations that confirm the results we focus on in the main text.

2.2   Numerical Methods

We perform our calculations using the ZEUS-MP2 (Hayes et al. 2006) code, a massively parallel implementation of the algorithms used in the ZEUS family of codes. These codes solve the fluid equations using finite differences on a staggered mesh. The internals of ZEUS are well-documented in the literature (for example, Stone & Norman 1992). While there have been other, more modern developments in astrophysical fluid codes, we chose to use ZEUS-MP2 because of its supported features (e.g. spherical coordinates, non-ideal equations of state) and because its structure allows for the relatively easy addition of new features.

Our calculations are done in spherical coordinates, anticipating the evolution of the remnant to a quasi-spherical end state. In order to minimize the computational demands, we primarily perform 2.5D simulations, in which vector quantities can have a ϕ component, but its value does not vary along the ϕ direction. In general, we also assume reflection symmetry about $\theta = \pi/2$. In the Appendix, we briefly report additional calculations which confirmed the validity of these simplifications.

Our typical computational domain is characterized by the grid spacing in the r and θ directions and by the radius of the inner boundary. Unless otherwise specified, we adopt a logarithmic radial grid with $N_r = 64$ points per decade. The angular grid is uniform from $[0, \pi/2]$ with $N_\theta = 48$ angular zones. These values give a grid in which individual cells are roughly equal in radial and θ extent. We choose an inner radius such that only 0.1 per cent of the mass lies interior to that radius and then place the outer boundary at $10^4 \ r_{\text{inner}}$.

We perform higher resolution simulations to confirm that our simulations are converged (see §2.A.1).

We make several modifications to ZEUS-MP2 (based off of v2.12) in order to perform our calculations; we describe these modifications in the rest of this section.

2.2.1 Equation of State

The existing equation of state (EoS) options in ZEUS-MP2 are a gamma-law EoS and an isothermal EoS. Neither of these choices are suitable for simulating a WD merger, which has material over a range of thermodynamic conditions, including both cold, electron-degeneracy-pressure dominated material and hot, radiation-pressure dominated material. We modify the code by the addition of the "Helmholtz" EoS (Timmes & Swesty 2000), which is the EoS of fully-ionized material consisting of an ideal gas of ions, blackbody radiation, and a non-interacting Fermi gas of electron and positrons. Importantly, this is the same EoS used in the SPH simulations of the WD merger, which simplifies the remapping procedure reported in Section 2.2.4; it is also the EoS used in MESA for material under similar conditions, which will prove important in later calculations (see Section 3.A and 4.B.1 for details).

The "Helmholtz" equation of state is so-named because it is constructed in a Helmholtz free energy basis, meaning that temperature (T) and density (ρ) are the natural thermodynamic variables. ZEUS-MP2 evolves the internal energy (E) and density. Therefore, in order to obtain the pressure (P) and any other thermodynamic quantities of interest, we must solve for T given ρ, E, and the composition. We implement a routine that finds the value of T corresponding to a value of E (given ρ and the composition), using a simple Newton-Raphson iteration scheme. With the addition of the EoS routines, one small algorithmic change is made: as suggested in Stone & Norman (1992), a predictor-corrector method is used to improve energy conservation during the calculation of the compressional heating term.

2.2.2 Shear Viscosity

In order to approximate the effects of magnetic stresses, we add shear stress terms to the hydrodynamic equations. That is, we are solving the equations

$$D_t\rho + \rho\partial_j v_j = 0 \tag{2.1}$$

$$\rho D_t v_i = -\partial_i P - \rho\partial_i\Phi + \partial_j T_{ij} \tag{2.2}$$

$$\rho D_t(e/\rho) = -P\partial_i v_i + T_{ij}T_{ij}/(\rho\nu) \tag{2.3}$$

where $D_t = \partial_t + v_i\partial_i$ is the convective derivative and we observe the usual Einstein summation conventions. The pressure is denoted by P, and the mass and internal energy densities are represented by ρ and e respectively. The velocity vector is v_i. The anomalous stress tensor T_{ij} is defined as

$$T_{ij} = \rho\nu\left(\partial_i v_j + \partial_j v_i\right) \tag{2.4}$$

where ν is the dynamic viscosity.

A very similar modification of the ZEUS-2D code was made by Stone et al. (1999). We benefited from inspecting the source code that was used to perform the calculations reported in that work. We also used the results reported in Stone et al. (1999) as a reference against which to test our own implementation.

The viscous terms are evaluated using an operator split method and are updated during the source step (Stone & Norman 1992). To ensure numerical stability, the time step Δt must be chosen to be less than $\Delta t_{\text{visc}} \sim \min((\Delta r)^2/\nu)$, where the minimum is evaluated over the computational domain.

As a dimensionally motivated form for the dynamic viscosity coefficient, we adopt

$$\nu(r, \theta) = \alpha \frac{c_s^2(r, \theta)}{\Omega_k(r)} \tag{2.5}$$

where c_s is the local sound speed and Ω_k is the Keplerian angular velocity calculated using the mass enclosed at a given spherical radius. Portions of the merger remnant (see Fig. 2.1) are unstable to the magneto-rotational instability (MRI; Balbus & Hawley 1991) and the Tayler-Spruit dynamo (Tayler 1973; Spruit 2002). These processes may generate viscous stresses corresponding to α in the range $10^{-4} - 10^{-1}$; for order of magnitude estimates, see Shen et al. (2012). We adopt a fiducial value of $\alpha = 3 \times 10^{-2}$, though we confirm that the results of our calculations are not sensitive to this choice (see §2.A.2).

As one moves to small r, (the origin being at the centre of the surviving WD; see §2.2.4), c_s and Ω_k approach constant values. We are using a logarithmic grid, so $\Delta r \propto r$ and therefore $\Delta t_{\text{visc}} \propto r^2$. The timestep constraint imposed by the Courant-Friedrichs-Lewy (CFL) condition depends linearly on Δr, so $\Delta t_{\text{CFL}} \propto r$. At sufficiently small radii, the viscous timestep becomes much less than the timestep required by the CFL condition. In practice, this occurs at a radius that is in our computational domain. In order to evolve the remnant over many viscous times, we apply the following *ad hoc* prescription. Within some radius r_ν we suppress the viscosity by a factor of $1/r$ such that the ratio of $t_{\text{visc}}/t_{\text{CFL}}$ remains constant. In order to make the cutoff smooth, the exact prescription is

$$\nu'(r, \theta) = \nu(r, \theta) \left(\frac{1}{1 + (r/r_\nu)^\beta} \right)^{1/\beta} \tag{2.6}$$

where $\beta = 4$ and r_ν is approximately the half-mass radius of the inner WD. As shown in the Appendix, we have verified that our results are insensitive to the details of this prescription. Physically, we would not expect the viscosity prescription in Equation 2.5 to hold as $r \to 0$ because this region within the WD is in approximate solid body rotation and is not MHD unstable.

Local numerical simulations of the MRI in accretion discs indicate that the azimuthal components of the stress-tensor, $T_{r\phi}$ and $T_{\theta\phi}$, are roughly a factor of 10 larger than the other components (e.g. Hawley et al. 1995; Stone et al. 1996). Our default assumption then is to evolve with only these components in the stress tensor being non-zero. In §2.A.3, we test

the effect of including all components and find some quantitative, though not qualitative, differences between the two choices.

2.2.3 Nuclear Burning

In several of the model systems the temperatures reached are sufficiently high that the energy release from fusion is not negligible on the viscous time-scale. However, the conditions are not such that the local burning time-scale ever falls below Δt_{CFL}. Therefore, in order to minimize the computational load associated with calculating the burning, we implement an extremely simple 5 isotope nuclear network which is explicitly integrated at the hydrodynamic timestep. This captures the bulk of the energy release.

The 5 species we track are He, C, O, Ne, Mg (these are the 5 isotopes present in the initial compositions). These isotopes are connected by 4 processes, the triple-α process and α capture on each of C, O, and Ne. The rates of these processes were taken from the JINA REACLIB database (Cyburt et al. 2010). We neglect additional physics such as screening corrections because the burning primarily occurs at densities where such effects are unimportant. We refer to our own burning implementation as HeCONe.

As a test of both our own implementation and the assumptions that motivate it, we also coupled the 13 isotope α-chain network aprox13 to the code (Timmes & Swesty 2000). The results were virtually identical, confirming the validity of our approach. See §2.A.6 for quantitative comparisons of the results of these tests.

ZEUS-MP2 provides the ability to advect scalar quantities; we use this feature to track the mass fractions of the isotopes in our network. The algorithms do not guarantee the sum of the mass fractions remains equal to one after the advection step. Methods to restore this constraint in fluid codes have been reported in the literature (for example, Plewa & Müller 1999). However, for the sake of simplicity, immediately before evaluating the energy release from nuclear burning, we enforce the constraint $\sum X_i = 1$ by appropriately adjusting the mass fraction of the most abundant isotope.

2.2.4 Construction of Initial Conditions

Our starting point is the results of SPH simulations of double white dwarfs performed by Dan et al. (2011). The simulations were notable for their use of a more accurate initialization of the binary system at the onset of mass transfer than had been used in previous work. We calculate the viscous evolution of the merger remnants formed in each of their eight production runs, the parameters of which are summarized in Table 2.1. Throughout the rest of this paper, when we refer to "initial conditions," this refers to the matter configurations at the end of these SPH simulations.

In order to map between the output of the SPH calculations and the staggered mesh of ZEUS-MP2 we adopt the following procedure. In SPH, the value of a quantity f at a

ID	M_2	M_1	M_{tot}	q	t_{end}	C_2	C_1
P1	0.2	0.8	1.0	0.25	95.0	He	CO
P2	0.3	1.1	1.4	0.27	62.0	He	CO
P3	0.5	1.2	1.7	0.42	35.0	He	ONeMg
P4	0.3	0.6	0.9	0.50	50.0	He	CO
P5	0.6	0.9	1.5	0.67	35.7	CO	CO
P6	0.2	0.3	0.5	0.67	30.0	He	He
P7	0.3	0.4	0.7	0.75	18.0	He	He
P8	0.9	1.2	2.1	0.75	30.0	CO	CO

Table 2.1: A summary of the systems simulated by Dan et al. (2011). ID is their run number. M_2 is the mass (in $M_\odot$) of the secondary, the less massive of the two WD; M_1 is the mass of the more massive primary. M_{tot} is the total mass of the system and $q = M_2/M_1$ is the mass ratio. t_{end} is the duration of the SPH simulation in terms of the initial orbital period. C_1 and C_2 are the compositions of the primary and the secondary WDs. See Table 1 in Dan et al. (2011) for more details.

position $\vec{x}$ is given by

$$f(\vec{x}) = \sum_{i=1}^{n} \frac{m_i}{\rho_i} f_i W(|\vec{x} - \vec{x_i}|, h_i) \tag{2.7}$$

where W is the kernel function. The quantity of interest associated with the i-th SPH particle is denoted f_i. The SPH particle has mass, density, position and smoothing length m_i, ρ_i, $\vec{x_i}$ and h_i respectively (e.g. Monaghan 1992). The sum runs over the total number of SPH particles, n.

Schematically, we construct our grid-based initial conditions by evaluating the five quantities that ZEUS-MP2 evolves (mass density ρ, internal energy density e and velocity $\vec{v}$) at each grid point. In our standard 2D simulations, we construct initial conditions that are explicitly invariant in the ϕ direction and are reflection-symmetric about $\theta = \pi/2$. Given these conditions, the total linear momentum of the remnant is guaranteed to be zero. Therefore, we choose the origin of our simulation coordinate system to be at the point of peak density, corresponding to the centre of the more massive (surviving) WD.

Explicitly, in order to calculate the value of a density (e or ρ) at a grid point with coordinates (r_i, θ_j) we evaluate

$$\rho_{ij} = \frac{1}{2N_\phi} \sum_{k=1}^{N_\phi} [\rho_{\text{SPH}}(r_i, \theta_j, \phi_k) + \rho_{\text{SPH}}(r_i, \pi - \theta_j, \phi_k)] \tag{2.8}$$

where N_ϕ is the number (typically $N_\phi = 32$) of equally-spaced points used to cover the interval $\phi \in [0, 2\pi)$. Now and throughout this section, the subscript SPH indicates a quantity extracted from the SPH simulation by the evaluation of Eq. 2.7.

Constructing the initial velocity vector requires slightly more complicated ϕ averaging. From the SPH data, we first construct the full velocity vector (with the components rep-

resented in Cartesian coordinates) at each of the grid locations where a component of the velocity will be defined. The staggered mesh employed by ZEUS-MP2 means that each velocity component is defined at a different spatial point (for details see Stone & Norman 1992). We take this into account, though we do not manifestly indicate it in the formulae below for the sake of compactness.

It is not simultaneously possible to conserve the kinetic energy of the fluid and its linear and angular momentum when performing the ϕ-averaging. (This is simply a statement of the fact that in a non-uniform field, $\langle v^2 \rangle \neq \langle v \rangle^2$.) Given that we are interested in investigating the angular momentum evolution of the remnant, we choose to conserve momentum. In practice, the difference is relatively small; for the fiducial remnant, this averaging procedure changes the total kinetic energy by 1 per cent.

Therefore, to obtain the value of a component of the velocity $\vec{v}$, defined at a point (r_i, θ_j) we calculate

$$v_{ij} = \frac{1}{2N_\phi}\frac{1}{\rho_{ij}}\sum_{k=1}^{N_\phi} [\vec{p}_{\mathrm{SPH}}(r_i, \theta_j, \phi_k) \cdot \hat{e}_{ij}(\phi_k) \\ + \vec{p}_{\mathrm{SPH}}(r_i, \pi - \theta_j, \phi_k) \cdot \hat{e}_{ij}(\phi_k)] \tag{2.9}$$

where $\vec{p}$ is the momentum vector and $\hat{e}_{ij}$ is the unit vector of the velocity component of interest at the point.

2.3 Results

We expect that systems with similar mass ratios (q) and total masses (M_{tot}) will undergo similar evolution. Since the composition of a WD maps to a relatively well-defined mass range, we organize our discussion by the composition of the merging WDs. First, we discuss our fiducial $0.6+0.9$ M$_\odot$ CO+CO system. The outcomes of He+He, He+CO and He+ONeMg mergers are discussed on a more limited basis, emphasizing only the notable differences between these systems and our fiducial one. See Table 2.2 for a summary of the properties of our primary simulations. As shown in Table 2.1, Dan et al. (2011) label their simulations with a short identifier of the form Pn, where P represents production and n in an integer. For our own short IDs (shown in Table 2.2), we simply prepend Z (representing "ZEUS") to the ID of the Dan et al. (2011) simulation that was used as the initial conditions.

In order to easily visualize our multi-D simulations, we will plot spherically averaged quantities against spherical radius. To calculate densities we perform a volume average, e.g.

$$\rho(r) = \frac{1}{2}\int_0^\pi d\theta \sin(\theta)\rho(r, \theta) \tag{2.10}$$

so that the appropriate quantity (e.g. mass) is conserved. To calculate other thermodynamic quantities such as temperature, we first calculate the spherically averaged mass and energy densities and then apply the equation of state. To calculate angular velocities, we restrict

ID	$M_2 + M_1$	r_{inner} [cm]	Network	t_{end} [s]
ZP1	0.2 + 0.8	3.6×10^7	HeCONe	3.0×10^4
ZP2	0.3 + 1.1	2.2×10^7	HeCONe	3.0×10^4
ZP3	0.5 + 1.2	1.9×10^7	HeCONe	1.5×10^4
ZP4	0.3 + 0.6	4.4×10^7	HeCONe	4.0×10^4
ZP5*	0.6 + 0.9	2.9×10^7	None	3.0×10^4
ZP6	0.2 + 0.3	6.6×10^7	HeCONe	4.0×10^4
ZP7	0.3 + 0.4	5.7×10^7	HeCONe	4.0×10^4
ZP8†	0.9 + 1.2	1.9×10^7	aprox13	1.0×10^4

Table 2.2: Details of the viscous evolution calculations discussed in this paper. As an ID, we simply prepend Z (representing "ZEUS") to the ID of the Dan et al. (2011) simulation that was used as the initial conditions. $M_2 + M_1$ is the mass of the secondary + primary in $M_\odot$. We will sometimes refer to systems by this sum. r_{inner} is the location of the inner boundary of our computational domain. Network indicates which nuclear network was used in the calculation. t_{end} is the end time of the simulation. All of the simulation parameters which were held fixed across all runs are discussed in the text. * fiducial model discussed in the most detail in the main text (in §2.3.1) † this simulation had a lower resolution, $N_r, N_\theta = 48,32$.

the average to a 45° wedge centred on the equator. As our simulations evolve toward a spherical end state, these 1D averages become an increasingly complete summary of the 2D structure of the remnant.

2.3.1 CO+CO systems

Our fiducial system (ZP5) is a super-Chandrasekhar CO+CO merger with $M_{\mathrm{tot}} = 1.5 M_\odot$ and $q = 2/3$. We simulate this system for 3×10^4s, which is $\sim 5 \times 10^7$ timesteps of the hydrodynamics code. The simulation conserves mass to 1 part in 10^4, energy to 0.5 per cent and angular momentum to one part in 10^3. The evolution of an identical system was discussed in Shen et al. (2012), who performed a simple 1D calculation of the viscous evolution. Our multidimensional calculations confirm the schematic picture presented therein.

At the end of the SPH simulation, the primary white dwarf is relatively undisturbed and is surrounded by the remnants of the disrupted secondary. More than half of the disrupted material has primarily rotational support; the remainder was shock-heated in the merger and has thermal support. (A small amount $\sim 10^{-3} M_\odot$ is unbound in a tidal tail.) The merger remnant is in quasi-hydrostatic equilibrium, which we confirm by evolving these initial conditions without the action of viscous torques for many dynamical times, observing little change.

The black lines in Fig. 2.1 show the initial rotation profile. The primary WD is rotating rigidly; exterior to that is the disrupted secondary which is in Keplerian rotation. This hot, fully ionized material is unstable to magnetohydrodynamic instabilities such as the MRI. The turbulence generated by the saturation of the MRI leads to an enhanced viscosity and

concomitant transport of angular momentum to larger radii (Balbus & Hawley 1991; Balbus 2003). As described in §2.2.2 we model this using an α-viscosity.

The viscosity also liberates energy present in the ϕ-velocity shear. Fig. 2.2 shows the evolution of the temperature and specific entropy profiles during the viscous evolution. Fig. 2.3 shows the final $\rho - T$ distribution and the evolution of the temperature peak in the $\rho - T$ plane during the viscous evolution. The viscous heating causes the peak temperature in the remnant to increase over the duration of the viscous phase by a factor of ~ 2, to $\sim 8 \times 10^8$ K. The temperature peak is at a density of $\sim 5 \times 10^5 \mathrm{g\,cm^{-3}}$ and at those conditions the energy released from carbon burning exceeds neutrino losses and the burning becomes self-sustaining.

The carbon burning in our fiducial model is an unimportant energy source on the viscous time-scale, so the viscous evolution is not directly affected. However, the fact that carbon burning begins during the viscous evolution means that a convective carbon burning shell will develop in $\sim 10^6$ s. One consequence of this is that we expect the material exterior to the temperature peak at the end of the viscous evolution to quickly form a convective envelope. Future work will investigate the structure of this envelope, which is important for understanding the thermal evolution of the remnant and characterizing its observational properties.

One of the most striking results of our multi-D simulation is that the merger remnant evolves towards a final quasi-spherical steady state. (Given that there is rotation, the final state will actually be oblate, though in practice, the rotational velocities we find imply that it is quite spherical.) To quantify this, we define a simple "aspect ratio" as follows: draw an isodensity contour and take the ratio of the distance from the origin at the equator to that at the pole. As a rule of thumb, we find that the aspect ratio associated with a given radius approaches unity after about 10 viscous times have passed at that radius. The bottom panel of Fig. 2.4 shows this convergence clearly. The primary WD ends up with a thermally supported, nearly spherical envelope. The top panel of Fig. 2.4 shows the mass enclosed as a function of radius which illustrates how the outer thermally supported envelope expands to larger radii during the viscous evolution.

Our multi-dimensional simulations also allow us to capture processes like convection. We find that the viscous heating causes the remnant to evolve towards a convectively unstable state. Recently, García-Berro et al. (2012) discussed how convectively generated magnetic fields in merger remnants could potentially explain the origin of high-field WDs. They noted that the conditions at the end of their own SPH simulations were unstable by the Schwarzschild criterion. However, given that this system has substantial rotational support and that we are evolving it in axisymmetry, a more appropriate test is the Høiland criterion. Our initial conditions are not unstable by the Høiland criterion and do not to evolve towards an unstable state without the action of the viscous stresses.[1]

Fig. 2.5 shows the 2D evolution of the fiducial system. In addition to the entropy and temperature, we plot two energy densities which are helpful in interpreting the evolution.

---

[1]The physical initial conditions are of course unstable in MHD, as it is the MRI that is giving rise to the effective viscosity.
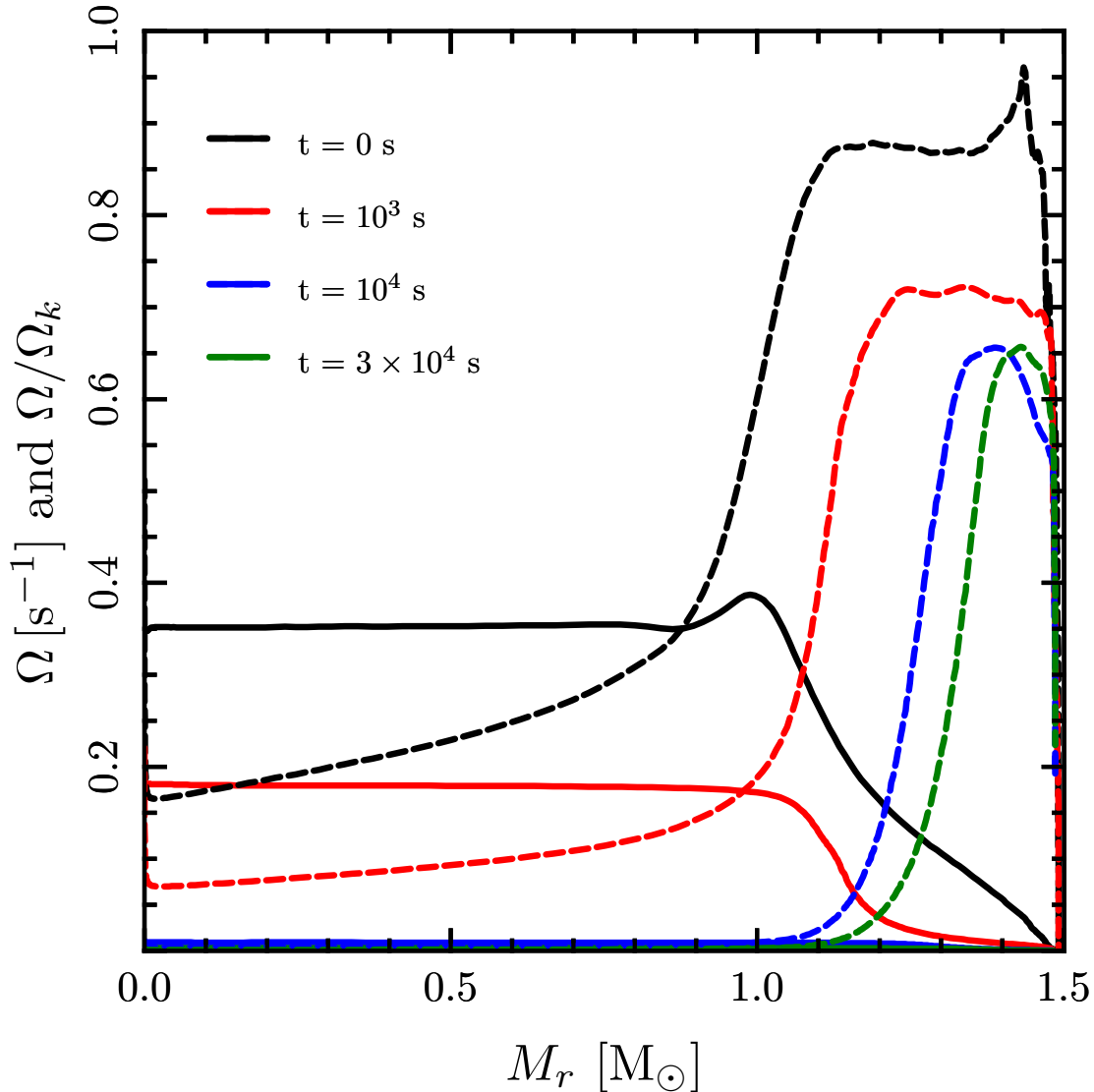
Figure 2.1: The evolution of the rotation profile of the fiducial $0.6+0.9$ $M_\odot$ CO+CO remnant. The solid lines are the angular velocity Ω and the dashed lines are its ratio to the Keplerian angular velocity, Ω/Ω_k. (The angular velocity is calculated using the material in a $45°$ wedge centred on the equator.) In the initial profiles (black), most of the material from the disrupted secondary ($M_r > 0.9$) is rotationally-supported with an angular velocity profile unstable to the MRI. The action of viscosity drives more of the remnant to solid body rotation and the accompanying heating leads to more of the remnant being thermally supported. We set $\alpha = 0.03$ for all the results in the main text. The Appendix shows that our results are nearly independent of α.
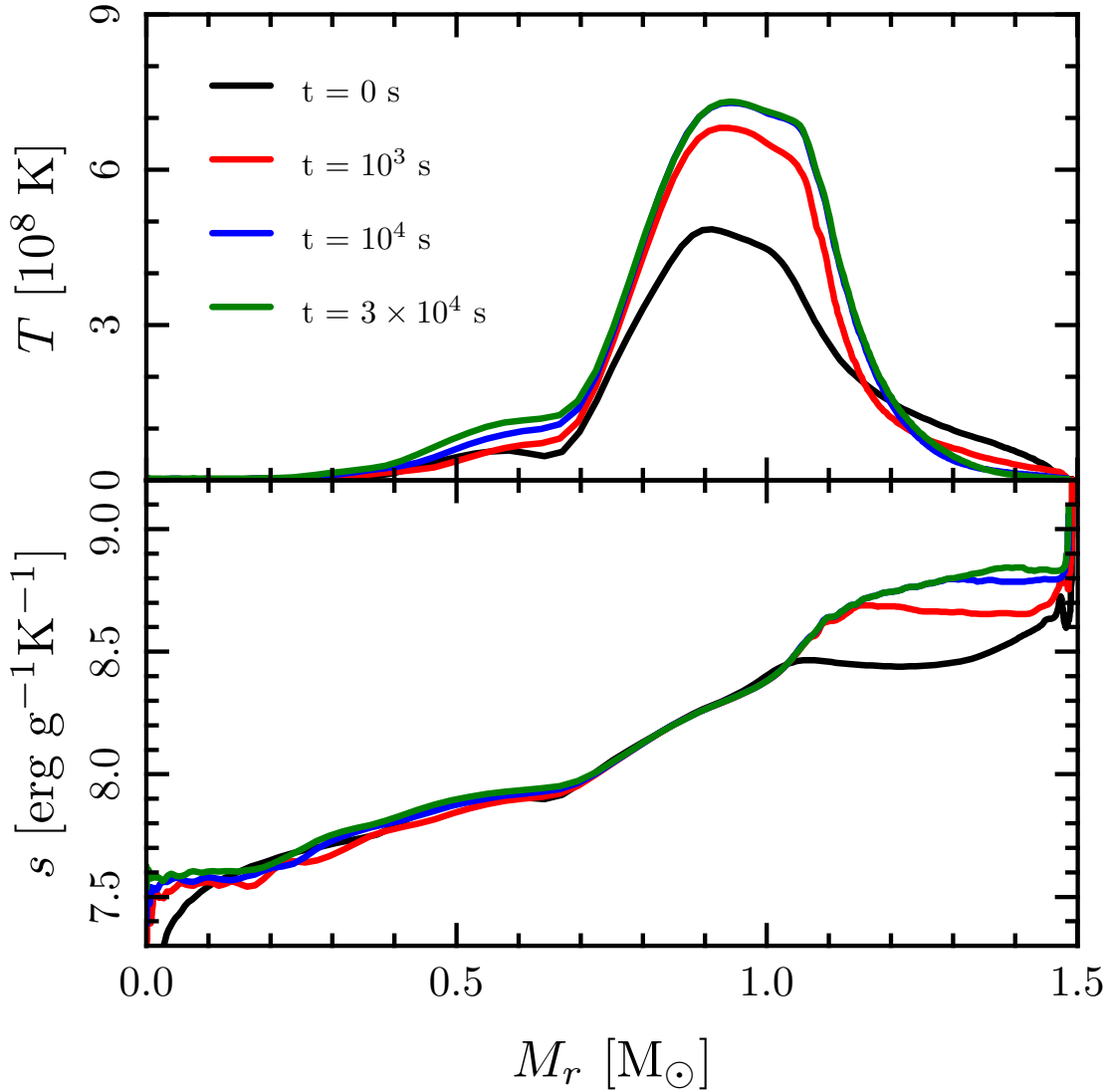
Figure 2.2: The evolution of the temperature (top) and specific entropy (bottom) profiles of the fiducial 0.6+0.9 M$_\odot$ CO+CO remnant. Viscous heating increases the peak temperature by roughly a factor of two. Convection and viscous heating both contribute to the entropy evolution of the material from the disrupted secondary. As discussed in the text, these curves are 1D spherical averages of our 2D simulations.
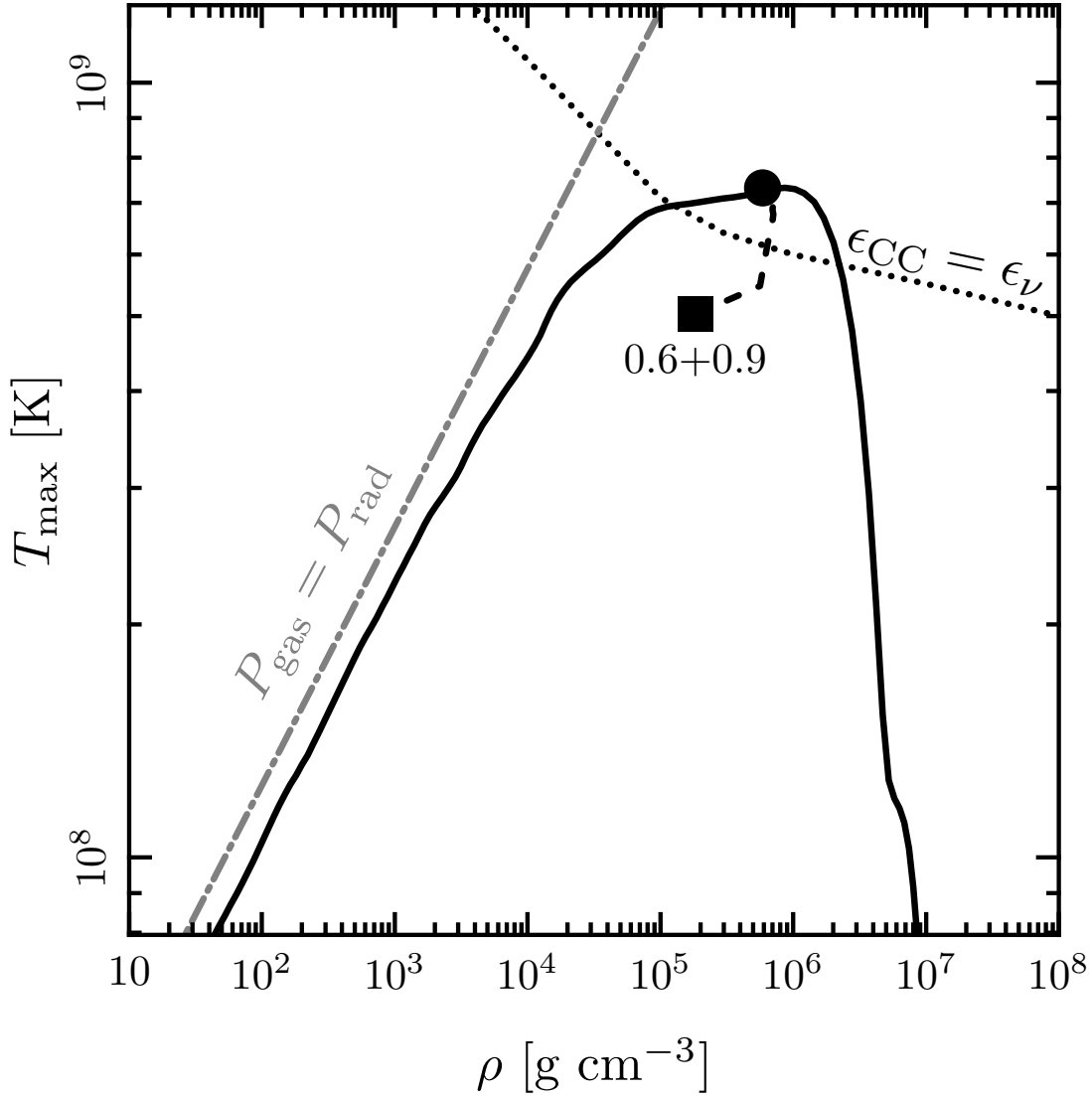
Figure 2.3: The evolution of the temperature peak in the $\rho - T$ plane. The dotted line indicates the break-even point where the energy release from carbon burning is equal to neutrino losses. The filled square (circle) is the peak temperature and corresponding density at the start (end) of the simulation, and the dashed line that connects them traces its evolution. The solid line is the full 1D $\rho - T$ profile of the quasi-spherical end state. The grey dash-dot line indicates where gas and radiation pressure are equal.
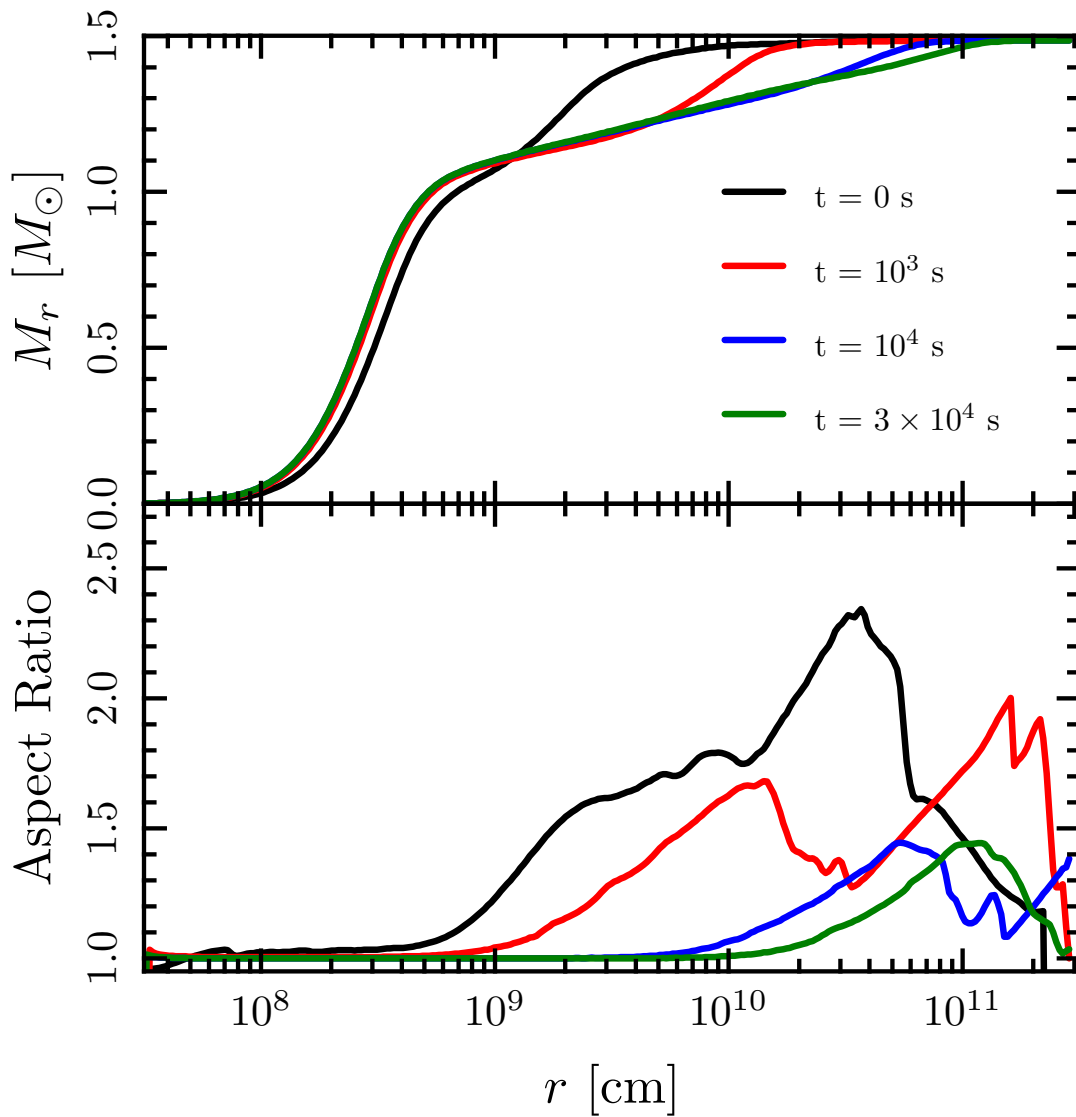
Figure 2.4: The evolution of the mass enclosed (top) as a function of spherical radius and the aspect ratio (bottom; see text for definition) for the fiducial 0.6+0.9 M$_\odot$ CO+CO remnant. The convergence of the aspect ratio to a constant value ≈ 1 provides an indication that the end state has approximately been reached.

One is the free energy available in the ϕ-velocity shear

$$\mathrm{KE}_{\phi-\mathrm{shear}} = \frac{1}{4}\rho \left(R\frac{d\Omega}{d\log R}\right)^2 \quad , \tag{2.11}$$

which shows the energy available for viscous heating. The other is the kinetic energy density in non-azimuthal motions

$$\mathrm{KE}_{r,\theta} = \frac{1}{2}\rho \left(v_r^2 + v_\theta^2 \right) \quad , \tag{2.12}$$

which is related to the kinetic energy associated with convective motions. Fig. 2.5 also plots isodensity contours, which emphasize the approach of the remnant to a spherical state.

Given previous work on viscous, geometrically thick accretion flows, one might expect that material would outflow along the poles during the viscous evolution. When the viscous time is much less than the cooling time and the mass inflow is assumed to be conservative (that is, mass does not leave the system), the transport of energy and the release of gravitational potential energy are such that material has a positive Bernoulli parameter (Be) (Narayan & Yi 1994; Blandford & Begelman 1999). Therefore, solutions in which the mass flow is not conservative may be more physical. Non-radiative accretion flows are also predicted to be convectively unstable. Models based on these ideas (e.g Blandford & Begelman 2004) developed solutions with prominent outflows. Hydrodynamic numerical simulations such as those by Stone et al. (1999) exhibited the slow outflow of marginally bound material in the polar direction. MHD simulations such as those by Stone & Pringle (2001) found somewhat more prominent outflows than in the hydrodynamic simulations.

We do not observe outflows in our simulations. Fig. 2.6 shows the fraction of mass on our grid with positive Be $\equiv f_{\mathrm{Be}>0}$. Initially $f_{\mathrm{Be}>0} \sim 3 \times 10^{-3}$, corresponding to the unbound material in the tidal tail. This material flows out of the outflow boundary and afterwards there is little unbound mass ($f_{\mathrm{Be}>0} \sim 10^{-5}$). In order to isolate the effects of viscosity on the unbound material, we ran a simulation without the viscosity and calculated $f_{\mathrm{Be}>0}$ (dotted blue line). The orange line in Fig. 2.6 shows the integrated difference in the mass that flowed through the outer boundary with Be > 0 in simulations with and without viscosity. This difference is very small $< 10^{-5}\mathrm{M}_\odot$. We do not claim that this specific value is robust, but the conclusion that the viscous evolution of WD merger remnants unbinds a only a very small amount of mass appears to be.

The initial conditions of our simulations are rather different than the initial conditions of most radiatively inefficient accretion simulations. Such simulations typically allow the material to move through several orders of magnitude in radius before reaching an inflow boundary representing a black hole. By contrast, the radial dynamic range between the surface of the primary WD and the bulk of the material in the initial rotationally-supported disc is small, a factor of ~ 5. The presence of a "hard surface" (the primary WD) means that as material accretes, the radius where material is pressure-supported moves outward, further suppressing the dynamic range between the effective inner boundary and the disc.

In order to understand the results of our WD merger remnant simulations in the context of accretion tori simulations, we generate accretion tori like those in Stone et al. (1999)
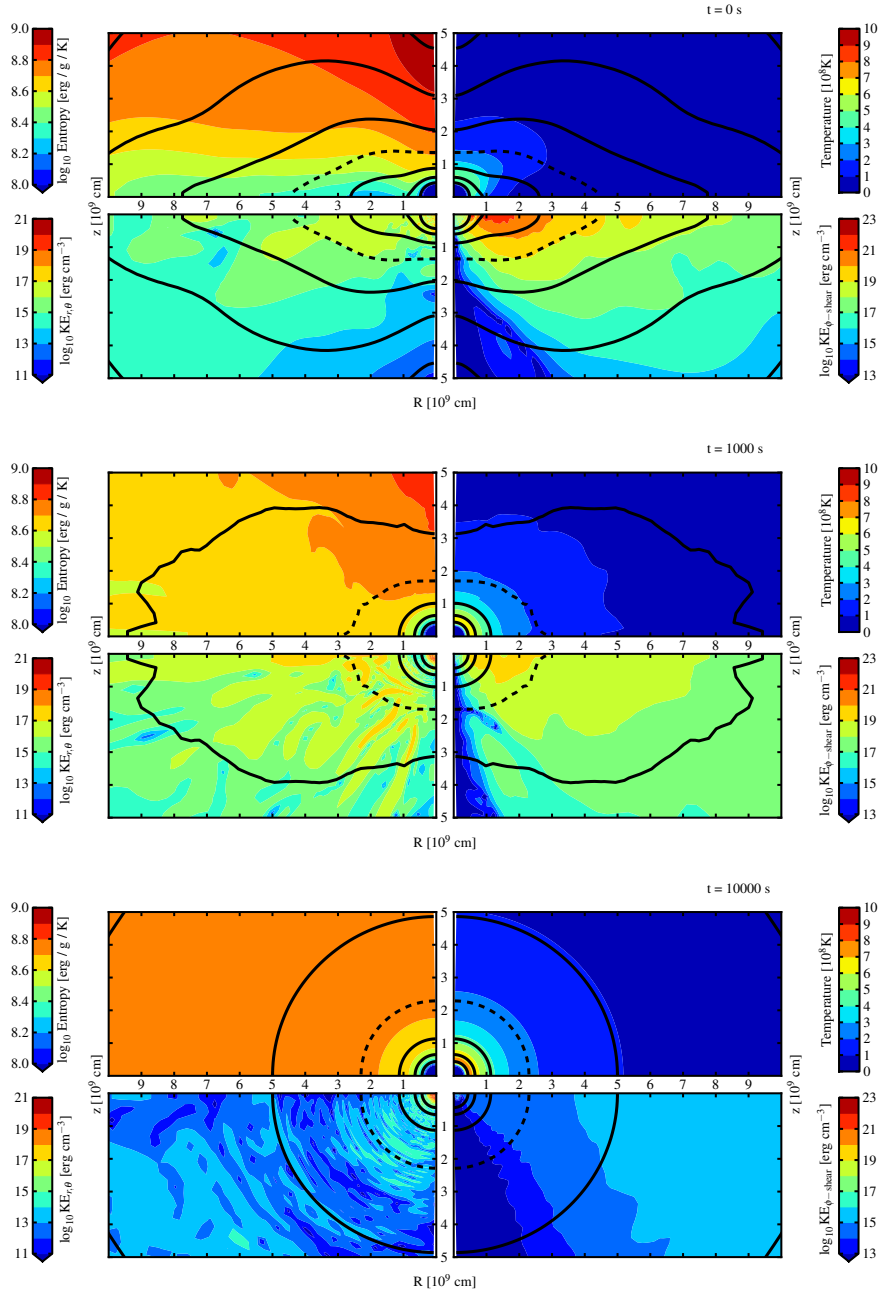
Figure 2.5: A visual overview of the 2D evolution of the fiducial 0.6+0.9 M$_\odot$ CO+CO merger remnant. Within each panel, the top two subpanels are thermodynamic quantities (s, T) and the bottom two subpanels are kinetic energy densities (non-azimuthal, ϕ-shear). The black contours are density, spaced one per decade. The dashed contour is $\rho = 10^3$ g cm^{-3}. The main panels are snapshots of the simulation at the indicated times. *Top Panel*: The initial conditions, note the large "free" energy apparent in the shearing, Keplerian disc. *Middle Panel*: The action of viscosity has dissipated some of the shear and heated the material. The remnant has become convectively unstable as can be seen in the striation of the non-azimuthal KE. *Bottom Panel*: The remnant has settled down into a quasi-spherical steady state.
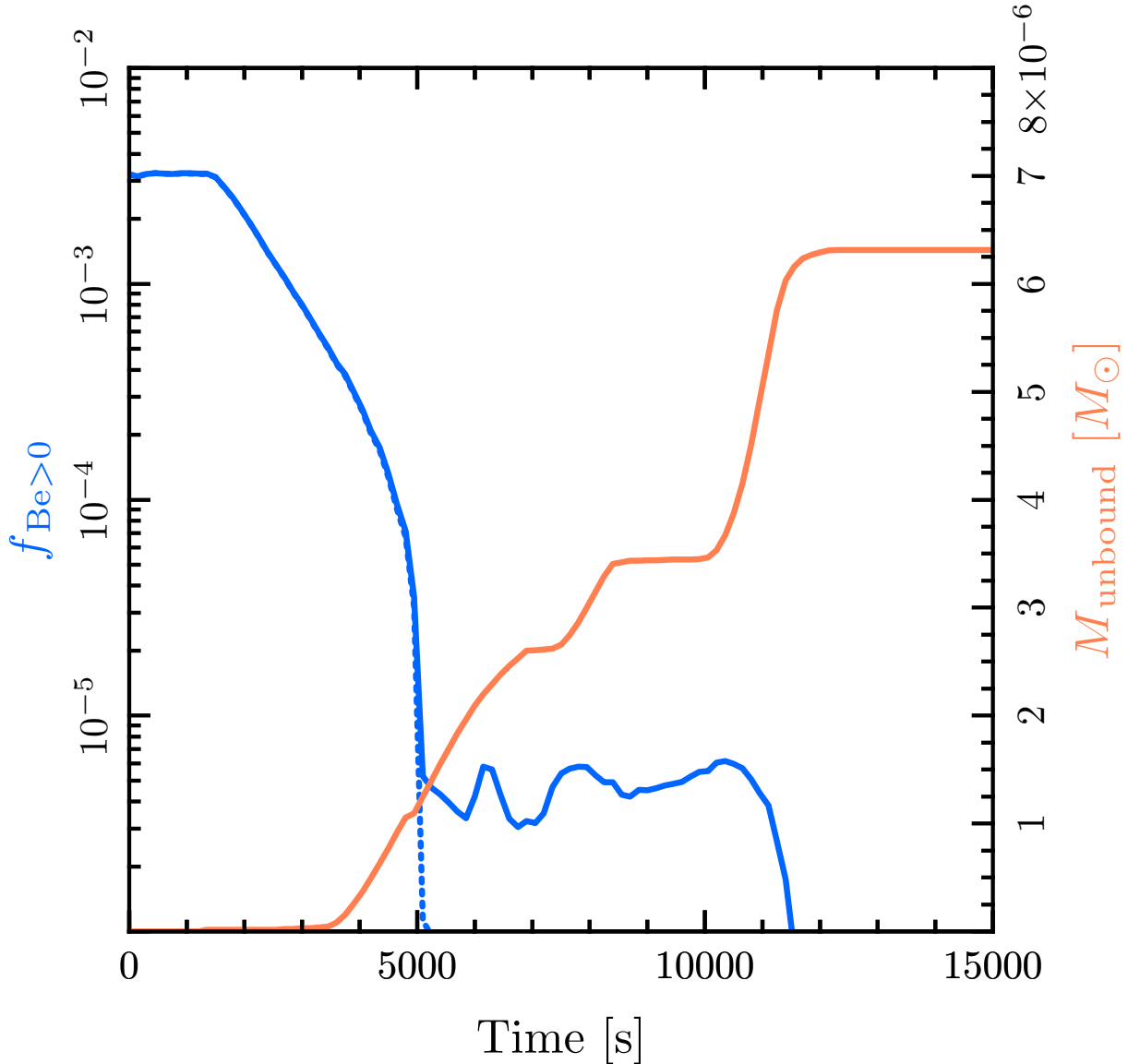
Figure 2.6: Viscously unbound material. The left (blue) scale indicates the fraction of mass with positive Bernoulli constant at a given time in the evolution of the fiducial 0.6+0.9 $M_\odot$ CO+CO merger remnant. The dominant contribution is the tidal tail; the large decrease in $f_{\mathrm{Be}>0}$ over the first 5000 s is this material flowing out of the simulation domain. The solid (dotted) line is the mass fraction with Be > 0 in a simulation with (without) viscosity. The right (orange) scale is the integrated amount of mass that has flowed out of the simulation domain with positive Be due to the influence of viscosity. This is the integrated difference between the two blue curves. Little additional material ($\leq 10^{-5} M_\odot$) is unbound by the viscous evolution .

and adjusted the inner boundary condition (reflecting vs. inflow) and the dynamic range between the initial torus and the inner boundary. We run the simulations for several orbits and calculate the resulting amount of unbound material $f_{\mathrm{Be}>0}$. At a radial dynamic range between the initial torus and the inner boundary of 100 and with an inflow boundary, we find $f_{\mathrm{Be}>0} \sim 4 \times 10^{-2}$, much larger than in our WD merger remnant calculations (see Fig. 2.6). Decreasing the dynamic range to 10 results in $f_{\mathrm{Be}>0} \sim 4 \times 10^{-3}$. At this dynamic range, changing the inner boundary condition to reflecting causes $f_{\mathrm{Be}>0}$ to peak $\sim 10^{-4}$ and then fall as the simulation continues. These results support our conclusion that only a very small amount of mass is unbound during the viscous evolution of WD merger remnants ($f_{\mathrm{Be}>0} \lesssim 10^{-5}$) .

In addition to our fiducial $0.6+0.9$ $M_{\odot}$ CO+CO system, we also simulate a very super-Chandra $0.9+1.2$ $M_{\odot}$ system (ZP8). This system quickly starts C+C burning, although the burning does not become dynamical (see Section 2.4.2). While the energy release from the burning on the viscous time is locally non-negligible, the mass outflow is not affected by the presence of nuclear energy generation. As shown in the Appendix, the energy release is not significant enough to affect the global behavior of the remnant.

2.3.2 He+He systems

The evolution of He+He merger remnants is broadly similar to our fiducial CO+CO case. The larger size and lower mass of the He WDs mean that the temperatures reached at the end of the SPH calculations are not as high. However, these temperatures are still high enough that we elect to track the energy release from He burning in our simulations. We do this using the simple nuclear network described in Section 2.2.3.

Fig. 2.7 shows the evolution of the temperature and rotation rate for a $0.2+0.3$ $M_{\odot}$ system (ZP6). This has the same mass ratio $q = 2/3$ as the fiducial system, but with a total mass 3 times lower. The initial temperature and rotation profiles look qualitatively similar to our fiducial system. Appropriately scaling these values by the total mass, they are even quantitatively similar. However, the final state appears somewhat different, most conspicuously because of the narrow temperature peak that forms at an enclosed mass of $\sim 0.38 M_{\odot}$.

This qualitative difference in evolution is most clear in Fig. 2.8, which shows the evolution of the temperature maximum and the corresponding density. The temperature maximum evolves to lower density during the viscous phase, unlike in CO+CO mergers where it evolves to higher density (see Fig. 2.3). This effect is unrelated to the presence of fusion, as the time-scale for burning is still relatively long. This difference in evolution is also not a qualitative difference in the merger outcome or the viscous evolution, but rather is due to the different contribution of gas and radiation pressure in the merger remnants. The grey dash dot line in Figs. 2.3 and 2.8 shows where $P_{\mathrm{gas}} = P_{\mathrm{rad}}$. The He+He case remains gas pressure dominated, so the location of the peak temperature corresponds to the location of the viscous heating. Lower densities, which are at larger radii and have corresponding longer viscous time-scales, are heated at later times. In the CO+CO case, radiation pressure has a

larger relative contribution initially and once material has been heated such that radiation pressure begins to become important, additional heating is no longer as effective in raising the temperature. Therefore, larger relative increases in T occur at higher densities where gas pressure continues to dominate, and thus the peak T moves to higher densities.

2.3.3   He+CO systems

In the He+CO systems, the primary is more massive and hence more compact than in the He+He mergers. This leads to higher temperatures during the merger. The lower temperatures required for He burning (versus C burning) mean that the effects of nuclear burning are more pronounced in these systems. Fig. 2.9 shows the evolution of the temperature peak in these simulations.

The 0.3+0.6 $M_\odot$ He+CO system (ZP4) is the only one of the systems we simulate in which the final state deviates significantly from approximate spherical symmetry. The remnant itself is spherical, but at the interface between the material from the He and CO WDs the composition varies between the equator and pole. This explains why the final peak temperature does not lie on the final spherically-averaged $\rho - T$ profile shown in Fig. 2.9. This system has the highest mass ratio of any mixed composition system we simulated and at higher mass ratios the secondary more strongly affects the primary. However, because the efficiency of mixing likely depends on dimensionality and angular momentum transport (α-viscosity vs MHD), we do not expect our work to provide a robust prediction of the details of such mixing.

2.3.4   He+ONeMg

One system in our study is composed of a $0.5 M_\odot$ He WD and a $1.2 M_\odot$ ONeMg WD. Its evolution is very similar to the systems previously discussed. Notably, the high primary WD mass means that the He (from the secondary) reaches quite high temperatures. The burning time in this system is thus quite short, less than the viscous time, though not less than the dynamical time (see §2.4.2).

2.4   Discussion

2.4.1   Fitting Formulas

The end states of our simulations will be useful as a starting point for future work concerning the thermal evolution of WD merger remnants. To aid such work, we provide fitting formulae that allow one to easily construct a physical state that is in rough quantitative agreement with our results.

The 1D profiles we extract at the end of our calculations have the following schematic form. At the centre is a core of cold, degenerate material. This is surrounded by a hot
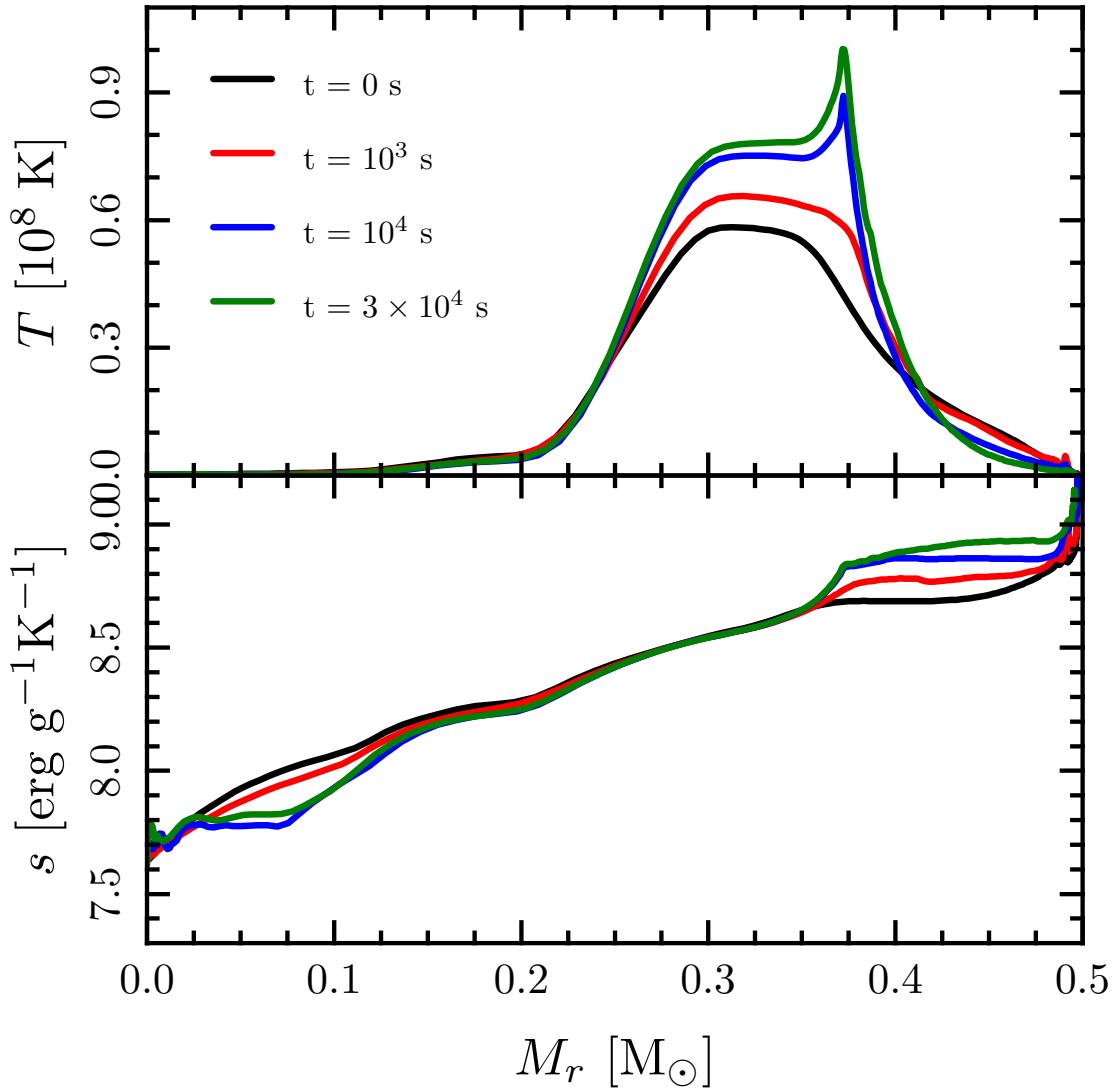
Figure 2.7: A 1D summary of the 0.2+0.3 $M_\odot$ He+He remnant evolution. The temperature (top panel) and rotation (bottom panel) profile at beginning, intermediate and final times. The temperature evolution appears qualitatively different than our fiducial model; as explained in the text, this is due to this lower mass remnant remaining gas pressure dominated. The rotation evolution is qualitatively the same as the fiducial model.
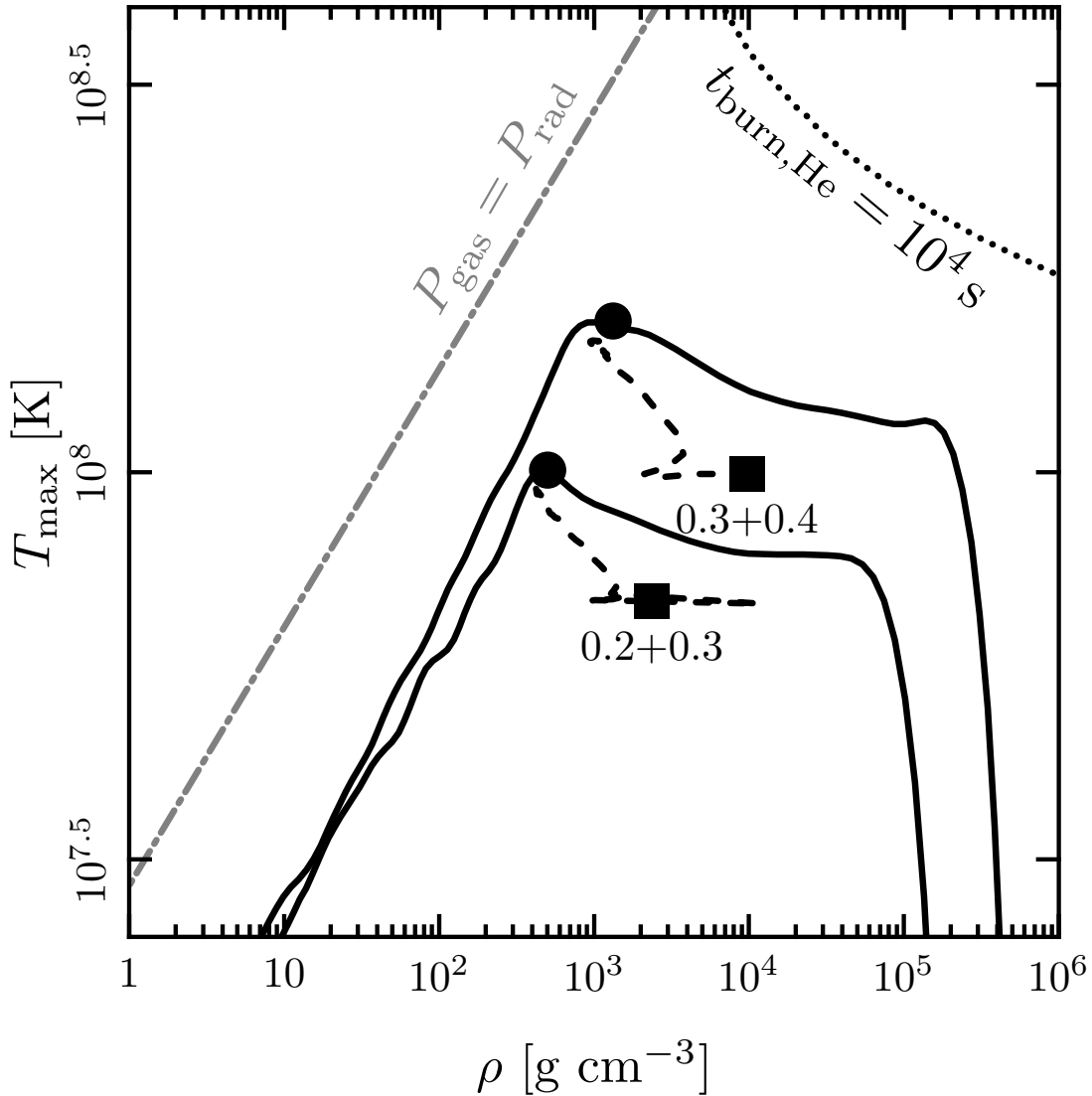
Figure 2.8: The evolution of the temperature peak for the He+He merger remnants. The dotted line labeled $t_{\mathrm{burn,He}} = 10^4$ s indicates the region where the time-scale for energy release by He fusion is equal to the time-scale of the simulation. The filled square (circle) is the peak temperature and corresponding density at the start (end) of the simulation, and the dashed line that connects them traces its evolution. The solid line is the full 1D $\rho - T$ profile of the quasi-spherical end state. The grey dash-dot line indicates where gas and radiation pressure are equal.
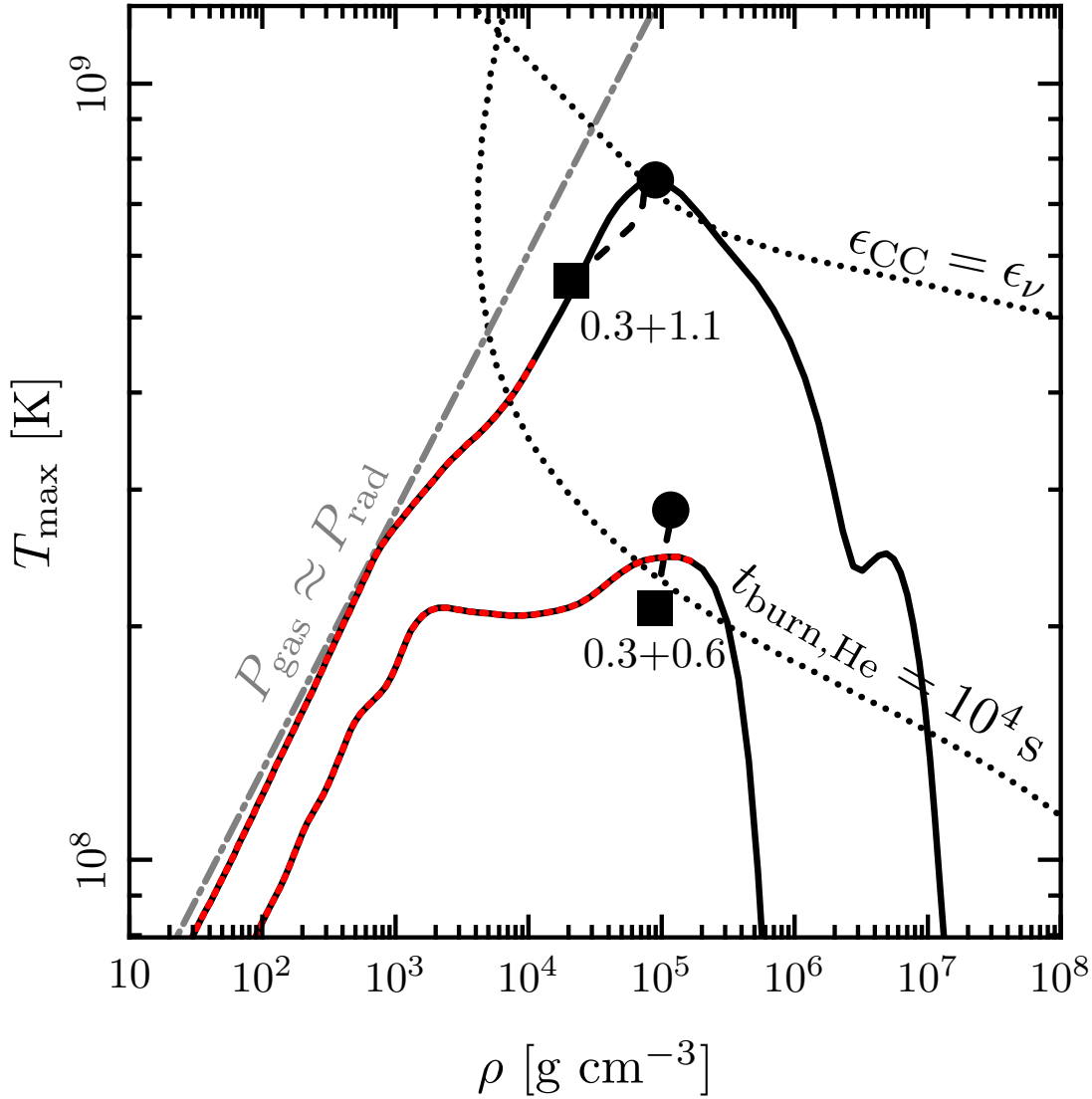
Figure 2.9: The evolution of the temperature peak for the He+CO remnants. The dotted line labeled $\epsilon_{CC} = \epsilon_\nu$ indicates the break-even point where the energy release from carbon burning is equal to neutrino losses. The dotted line labeled $t_{burn,He} = 10^4$ s indicates the region where the time-scale for energy release by He fusion is equal to the time-scale of the simulation. The filled square (circle) is the peak temperature and corresponding density at the start (end) of the simulation, and the dashed line that connects them traces its evolution. The solid line is the full 1D $\rho - T$ profile of the quasi-spherical end state. The red dotted section shows where the helium mass fraction exceeds 50 per cent. The grey dash-dot line indicates where gas and radiation pressure are equal. The peak temperature in the 0.3+0.6 $\rho - T$ profile does not correspond to the final peak temperature indicated by the solid circle. At the spherical radius of the temperature peak, the chemical composition varies from pole to equator and hence the averaged temperature at that point is not equal to the 2D peak.

envelope, the outer portion of which was convective and so has an entropy that is roughly spatially constant.

This picture allows a simple, *post hoc* model of the end state of our simulations. We write down a piecewise equation of state in which there is a central mass (M_c) described by a zero-temperature equation of state. This is surrounded by an isothermal region corresponding to the temperature peak which has mass M_{tp}. The rest of the external material has a polytropic equation of state. Empirically the polytropic index of $n = 3$ provides a good fit to all of our simulations. For systems at high temperatures, such as our $0.3+1.1$ M$_\odot$ He+CO merger, this is unsurprising as the material in the convective region is nearly radiation dominated, implying an adiabatic index near $\gamma = 4/3$. For systems such as low total mass He+He mergers (ZP6 & ZP7), the matter is gas pressure dominated, which would imply an adiabatic index of 5/3. However these systems have larger residual entropy gradients, such that the relationship $P \propto \rho^{4/3}$ roughly holds. Since we can provide satisfactory fits without introducing an additional parameter, we choose $n = 3$ for all our fits.

Quantitatively

$$
P(\rho) = \begin{cases} P_{ZT}(\rho) & \text{if } M_r < M_c \\ K_1 \rho & \text{if } M_c < M_r < M_c + M_{tp} \\ K_2 \rho^{1+1/n} & \text{if } M_c + M_{tp} < M_r \end{cases} \tag{2.13}
$$

where P_{ZT} is the pressure of a zero temperature Fermi gas with $\mu_e = 2$ (e.g Shapiro & Teukolsky 1983). K_1 and K_2 are set by the condition that ρ, P are continuous at the transitions between regimes.

In combination with the equations of hydrostatic equilibrium and mass conservation in 1D spherical coordinates

$$
\frac{dM_r}{dr} = 4\pi r^2 \rho \tag{2.14}
$$

$$
\frac{dP}{dr} = -\frac{GM_r \rho}{r^2} \tag{2.15}
$$

and a central boundary condition $\rho(r_{inner}) = \rho_c$, this is sufficient to fully specify a 1D model. We set ρ_c to be the value of the central density at the end of our simulations.

For each of our simulations we fit for the two masses M_c and M_{tp}. Table 2.3 reports the results of these fits. Fig. 2.10 shows the results of the fit to our fiducial model. The fit reproduces the observed quantities to within ~ 30 per cent. The fit is worst in the region described by the isothermal equation of state, which is unsurprising since this is the least physically motivated part of our effective equation of state.

Our fitting procedure does not use or provide any spatial information about the chemical composition. As a rough approximation, one can simply retain the initial Lagrangian composition of the system with the secondary outside of the primary. In the mergers where the chemical compositions of the WDs were initially identical, this is a good approximation because nuclear reactions do not significantly alter the composition (for the set of mergers
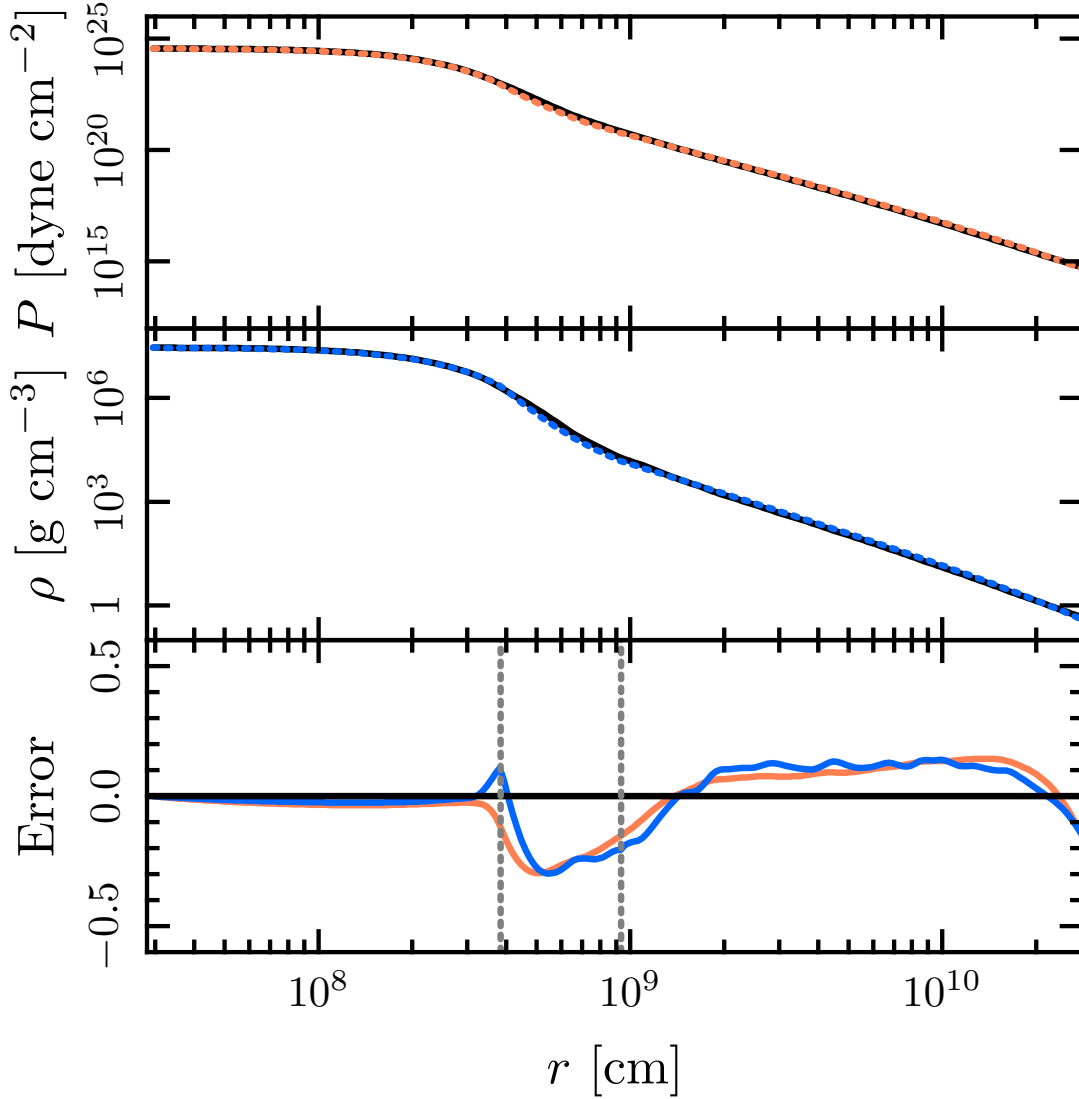
Figure 2.10: The simple two-parameter fit to the fiducial 0.6+0.9 M$_\odot$ CO+CO merger remnant (see Equations 2.13-2.15 and surrounding discussion). The upper two panels show the pressure and density profiles from the simulation as solid lines. The fits are shown as dashed lines. The bottom panel shows the relative error between the fit and the simulation. The vertical grey lines show the position of the transitions in the piecewise equation of state.

ID	ρ_c [g cm^{-3}]	M_{c}	M_{tp}
ZP1†	8.8×10^6	0.71	0.10
ZP2†	4.7×10^7	0.98	0.12
ZP3†	9.5×10^7	1.05	0.16
ZP4†	3.8×10^6	0.53	0.13
ZP5	2.8×10^7	0.84	0.20
ZP6	6.4×10^5	0.28	0.08
ZP7	1.5×10^6	0.38	0.12
ZP8	3.3×10^8	1.11	0.24

Table 2.3: The parameters from our fits (see Equations 2.13-2.15 and surrounding discussion). ID is the run ID. ρ_c is the central density extracted from the end of our simulations. M_{c} is the amount of mass (in M$_\odot$) in the zero-temperature degenerate core. M_{tp} is the amount of mass (in M$_\odot$) in the isothermal region, loosely corresponding to the temperature peak. †marks those systems which have a mixed chemical composition.

we considered). For mergers where the WDs had different compositions (which are marked in Table 2.3), the assumption that the composition is conserved in a Lagrangian sense is substantially more crude because of mixing and the effects of nuclear burning. In those cases, these simple fits would be inappropriate for work in which inaccuracies in the chemical composition could have a large effect.

2.4.2 Burning Time

Recently there has been considerable interest in the possibility of central carbon detonations triggered by the detonation of a helium layer on the surface of a CO WD. During a WD merger, conditions for detonations may be reached in instabilities in the accretion stream (Guillochon et al. 2010) or at surface contact (e.g. Dan et al. 2012). The systems we consider did not reach detonation conditions during the SPH simulations (though those could not resolve accretion stream instabilities).

During the phase of evolution that we simulate, viscous heating does increase the temperature and either initiate or increase the rate of burning. Fig. 2.11 shows the minimum burning times and corresponding temperatures for the eight systems we simulate. We calculate the minimum nuclear burning time as $t_{\mathrm{burn}} = c_P T / \epsilon_{\mathrm{nuc}}$, where c_P is the specific heat at constant pressure, T is the temperature and ϵ_{nuc} is the specific energy generation rate from nuclear reactions.

The minimum burning time is not necessarily located at the location of peak temperature, as differences in the chemical composition (for example, the presence of helium) may make the rate of energy release greater at a different location. In general, the viscous heating causes a monotonic increase in the temperature. Therefore, initially the burning time drops. Then, in cases where the burning time is less than the viscous time, changes in the composition (such as the depletion of helium) begin to shift the minimum burning time to slightly lower

temperatures where more material remains to burn.

In the case of the 0.5+1.2 M$_\odot$ merger, the burning time, which is $\sim 40 t_{\rm dyn}$ at the beginning of the simulation, decreases to as low as $\sim 2 t_{\rm dyn}$, where the dynamical time is calculated as $t_{\rm dyn} = P/(\rho g c_s)$. The ratio $t_{\rm burn}/t_{\rm dyn} \lesssim 1$ provides a rough criterion for possible detonation. Detailed conditions for detonations are still a topic of current research and almost certainly require resolving smaller length scales than our current simulations can do (for example, see discussion in §3.2 of Woosley & Kasen 2011).

Using the value of $t_{\rm burn}/t_{\rm dyn}$ as a guide, viscous heating does not cause any of the remnants that we simulated to experience dynamical burning. However, with the low value of $t_{\rm burn}/t_{\rm dyn}$ for the 0.5+1.2 M$_\odot$ system and the temperature sensitivity of nuclear reactions, we expect that systems only slightly more massive would experience dynamical burning. Furthermore, if there are stochastic fluctuations, it is even possible that this particular system could experience dynamical burning.

Dan et al. (2012) surveyed the parameter space of primary/secondary WD mass and mapped out regions where they found conditions during contact that could lead to detonation. In general, these conditions happen at a "hot spot". If the system does not detonate, the subsequent evolution toward an axisymmetric state causes the peak temperature to fall. Heating during the viscous evolution reverses this trend and creates a hot shell, which, as discussed previously, may reach conditions of dynamical burning. Some simple estimates based on figure 8 of Dan et al. (2012) suggest that the region of parameter space where systems would not reach conditions of dynamical burning at contact but would reach such conditions later on during the viscous evolution is relatively small. Future work will quantitatively address this question by simulating a wider range of merger remnants. However, if contact detonations (or other earlier detonation mechanisms such as accretion stream instabilities) do not prove to be robust, viscous heating could potentially ensure that a wide range of WD mergers trigger a surface detonation.

2.5   Conclusions

The merger remnants of binary white dwarfs are differentially rotating and unstable to MHD instabilities like the MRI. As outlined by Shen et al. (2012), MHD stresses give rise to a viscous phase of evolution which occurs on a time-scale much less than the thermal time. To investigate the outcome of this viscous evolution, we perform multi-dimensional hydrodynamic calculations of the evolution of WD binary remnants under the action of an α-viscosity. The initial conditions for these calculations are the SPH simulations by Dan et al. (2011). We find that these remnants evolve towards spherical states on time-scales of hours. This confirms the arguments in Shen et al. (2012) that the post-merger evolution of WD merger remnants is via viscous redistribution of angular momentum that leads to nearly solid body rotation. The transport of angular momentum outwards removes rotational support from the majority of the mass leading to a nearly spherical remnant. *The dynamics during this phase is not consistent with accretion at the Eddington limit,* as in previous models of
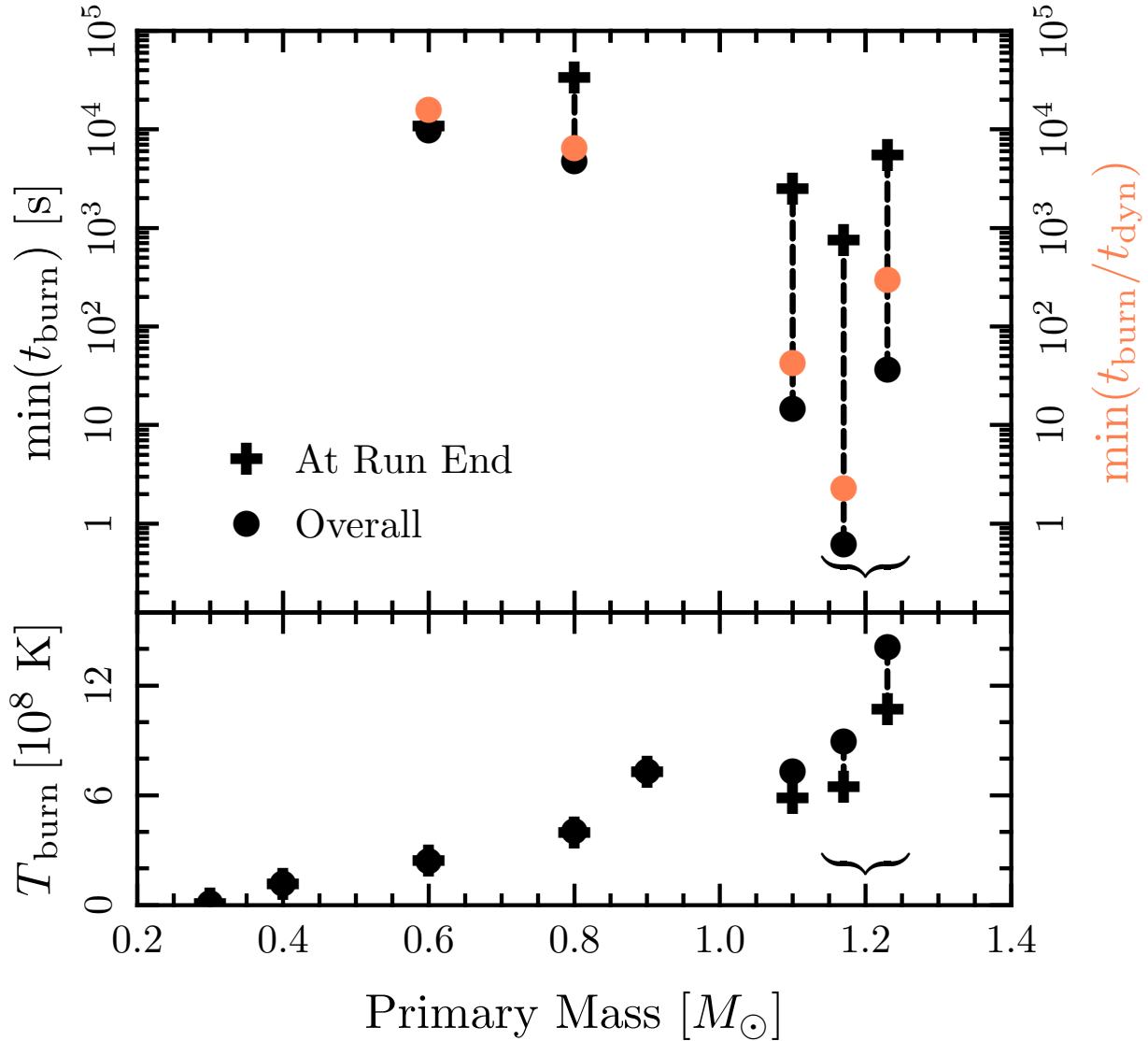
Figure 2.11: The shortest burning time (top panel) and corresponding temperature (bottom panel) for each of our simulated systems. The x-axis is the mass of the primary WD. Two systems have the same primary mass of 1.2 $M_\odot$ and are slightly offset on the x-axis for visual clarity (ZP3 to the left and ZP8 to the right). In the top panel, the circle represents the shortest burning time reached overall, that is at any point during the simulation; the cross represents the burning time at the end of the simulation. They are connected by a dashed line to guide the eye and indicate that intermediate values are achieved. The same symbols in the bottom panel show the temperatures at the corresponding locations. Because of varying chemical composition, the temperature associated with the shortest burning time is not necessarily the global peak temperature. The right axis of the top panel and the orange circles show the ratio $t_{\text{burn}}/t_{\text{dyn}}$ (as defined in the text) at conditions corresponding to the black circles. In no case does the burning time ever reach the dynamical time, though in ZP3 it is within a factor of two.

WD merger remnants (e.g. Nomoto & Iben 1985; Saio & Nomoto 1998, 2004; Piersanti et al. 2003b,a). Instead, the viscous evolution of WD merger remnants is much more analogous to that of a differentially rotating star.

Viscous heating associated with the approach to solid body rotation unbinds only a very small amount of mass ($\lesssim 10^{-5}M_\odot$ in our fiducial calculation). This is in contrast to some of the intuition developed in the context of radiatively inefficient accretion flows, which predict outflows. To understand this, we perform simple accretion tori calculations which indicate that the relatively small radius difference between the disc and the surface of the WD can explain why only a small amount of mass becomes unbound (see §2.3.1).

Viscous heating causes one of the systems we simulate to reach conditions of nearly dynamical He burning, so it is possible that the post-merger viscous evolution triggers a detonation in some cases. Recently Dan et al. (2012) presented a suite of more than 200 WD merger simulations which more thoroughly populate the q-$M_{\rm tot}$ plane. They found that many of these systems reached the conditions for detonation during the merger (see for example their figures 6 & 8). In our calculations, $\min(t_{\rm burn}/t_{\rm dyn})$ decreases by a factor of ~ 10 during the viscous phase (see §4.2). We speculate that systems that have $t_{\rm burn}/t_{\rm dyn} \lesssim 10$ at the merger may reach conditions for detonation during the subsequent viscous phase. However, we estimate that the number of systems which would satisfy this condition but have not reached $\min(t_{\rm burn}/t_{\rm dyn}) < 1$ during the dynamical phases of the merger is likely to be small. If other earlier detonation mechanisms do not prove to be robust, viscous heating could potentially trigger a surface detonation after the merger, causing either a .Ia supernovae (Bildsten et al. 2007) or a Type Ia supernova via a double detonation scenario.

Our purely hydrodynamic simulations cannot address the effects of magnetic fields. MHD simulations resolving the action of the MRI would allow a more realistic treatment of the viscous stresses than an α-viscosity[2], though the quantitative insensitivity of our results to the value of α leads us to think that our conclusions are robust. Converting our fiducial value of α to a magnetic field strength gives $|B| \sim \sqrt{4\pi\alpha\rho c_S^2} \sim 10^{10}$G. The implications of this estimate for the subsequent evolution of the merger remnant depend on the structure of the field. The generation of a large-scale field could lead to the formation of a strongly magnetized WD, which would be rapidly rotating and would quickly spin down via a magnetized wind. The presence of a strong magnetic field would also affect the conduction of heat in the interior of the WD. Alternatively, it is possible that the strong field is relatively small scale and so efficiently redistributes angular momentum in the interior of the remnant but does not significantly affect its global properties.

The end states of our calculations provide a starting point for investigations of the long-term thermal evolution of WD merger remnants. In our fiducial case, we expect that the luminosity from the nuclear burning will drive convection, establishing an extended convec-

---

[2]It is worth noting that MHD simulations which capture the evolution of the entire remnant promise to be quite challenging. The instabilities in regions where $d\Omega/dr > 0$ are likely to be short wavelength non-axisymmetric modes that have a different time-scale and spatial scale than the MRI modes that operate where $d\Omega/dr < 0$. Correctly capturing the physics both inside and outside the rotation peak will be extremely difficult.

tive envelope with its base at slightly larger radii than the temperature peak. The object will likely grow to have a radius comparable to that of a giant star and correspondingly a relatively cool effective temperature like the models presented in Shen et al. (2012). There are clear opportunities for future work in the self-consistent thermal evolution of these objects and their consequences for Type Ia supernovae, neutron stars, R Coronae Borealis stars and other phenomena.

Acknowledgments

2.A Verification Tests

We perform a number of tests to confirm that our results are insensitive to the details of our approximations and numerical methods. A summary of these test runs is shown in Table 2.4. Each run has an ID, which begins ZTn, where ZT represents "ZEUS testing" and n is an integer, indicating that SPH simulation Pn of Dan et al. (2011) was used to generate the initial conditions. The results of these tests are discussed in the following sections.

2.A.1 Resolution

We confirm that our solutions are numerically converged by performing runs at different resolutions. We perform runs with 2/3 and 4/3 the linear resolution of the fiducial calculation. Fig. 2.12 shows 1D profiles from each of these runs after 10^4 s. There is only a small variation between the fiducial run (ZP5) and the high resolution run (ZT5-HR). The lower resolution run (ZT5-LR) also agrees quite well; the visible variation is in the interior

ID	Parameter	Value
ZT5-LR	N_r, N_θ	48,32
ZT5-HR	N_r, N_θ	96,64
ZT5-alpha-m	α	10^{-2}
ZT5-alpha-p	α	10^{-1}
ZT5-hydro	α-viscosity	Off
ZT5-visc-full	α-viscosity	All components
ZT2-burn-ap13[†]	Network	aprox13
ZT2-burn-heco[†]	Network	HeCONe
ZT2-burn-off[†]	Network	No Burning
ZT5-IC1	$t_{\mathrm{end,SPH}}$	35 P_0
ZT5-IC2	$t_{\mathrm{end,SPH}}$	35.6 P_0
ZT5c-rnu-m	r_ν	2.5×10^8 cm
ZT5c-rnu-p	r_ν	5.0×10^8 cm

Table 2.4: Details of the test runs discussed in this appendix. ID is the run ID: ZT represents "ZEUS testing" and the number indicates which initial conditions are being simulated. The string following the first dash briefly describes the parameter being changed. Parameter is a description of the aspect of the run that was varied. Value is its value. [†]this simulation had a lower resolution, $N_r, N_\theta = 48,32$

of the surviving WD, not the viscously evolving exterior. These results demonstrate that our simulations are converged in the quantities of interest.

2.A.2 Independence of α

We expect our simulations to be insensitive to the exact value of α so long as the hierarchy of time-scales in the problem remains unchanged. Specifically, α must not be so small that energy transport by radiation (or energy release from nuclear reactions) becomes important and not so large that the viscous time becomes less than the orbital time. Fig. 2.13 shows that we observe only weak variation in our results with α in the range $0.01 - 0.1$. The simulations are compared after a constant number of viscous times, such that $\alpha t_{\mathrm{end}} = 3 \times 10^2$ s.

2.A.3 Viscosity Tensor

Motivated by numerical simulations of the MRI we choose a prescription in which only the azimuthal components of the viscous shear tensor were retained. We relax this assumption and explore the effects of retaining all components of the tensor. This choice has virtually no effect on the evolution of the material near the temperature peak, as the large initial ϕ velocity shear means that the non-azimuthal components of the tensor are small in comparison anyways. In the outer regions where azimuthal shear is not always so dominant, this choice can have an effect. In the fiducial case the evolution of the outer $\sim 0.2 M_\odot$ of material
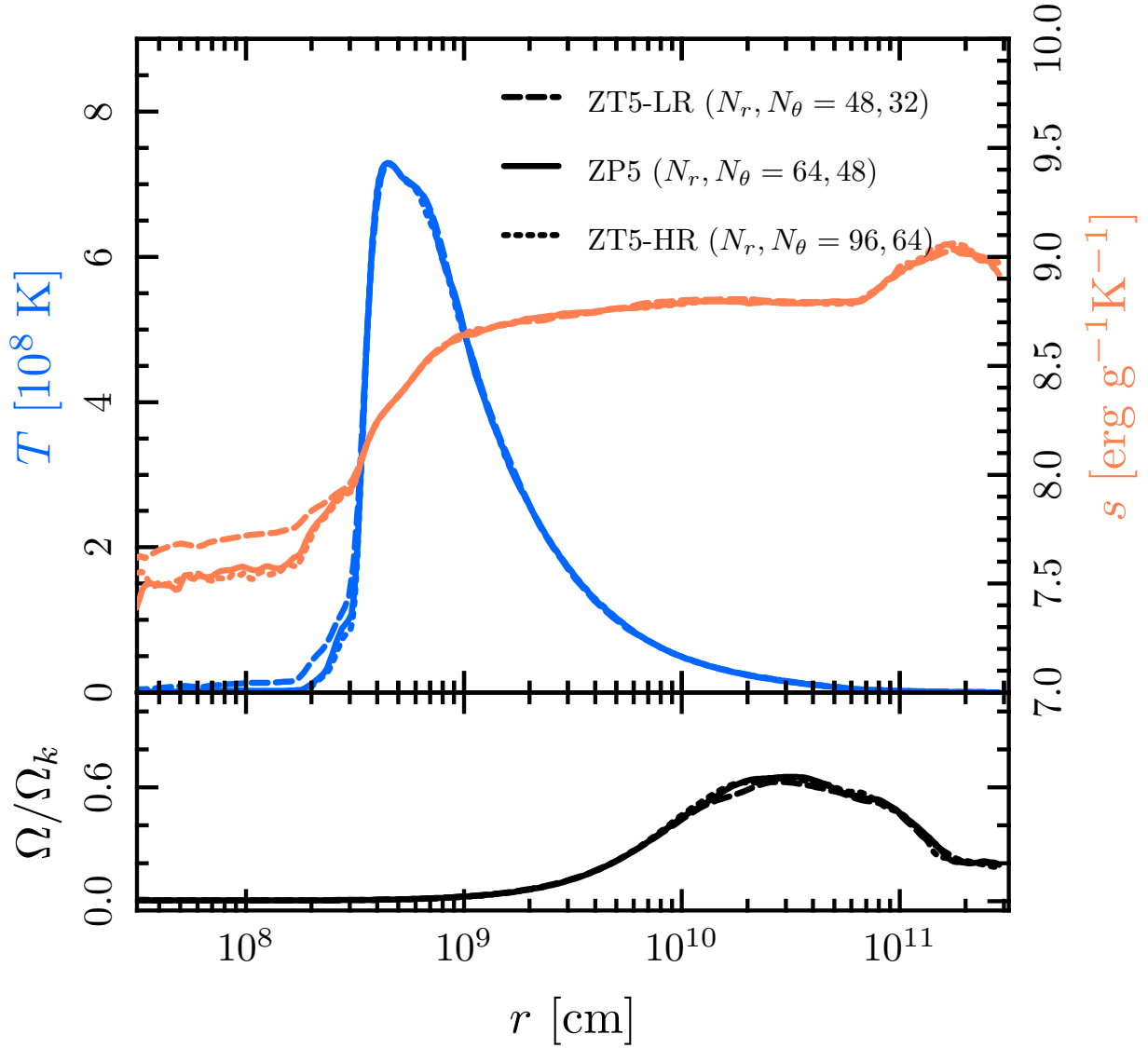
Figure 2.12: The convergence of our simulations of the fiducial remnant with numerical resolution. The top panel shows 1D temperature and entropy profiles and the bottom panel shows the ratio of the angular velocity to the Keplerian angular velocity. The overlap of the fiducial run (ZP5) and the high resolution run (ZT5-HR) indicate our simulations are converged in these quantities.
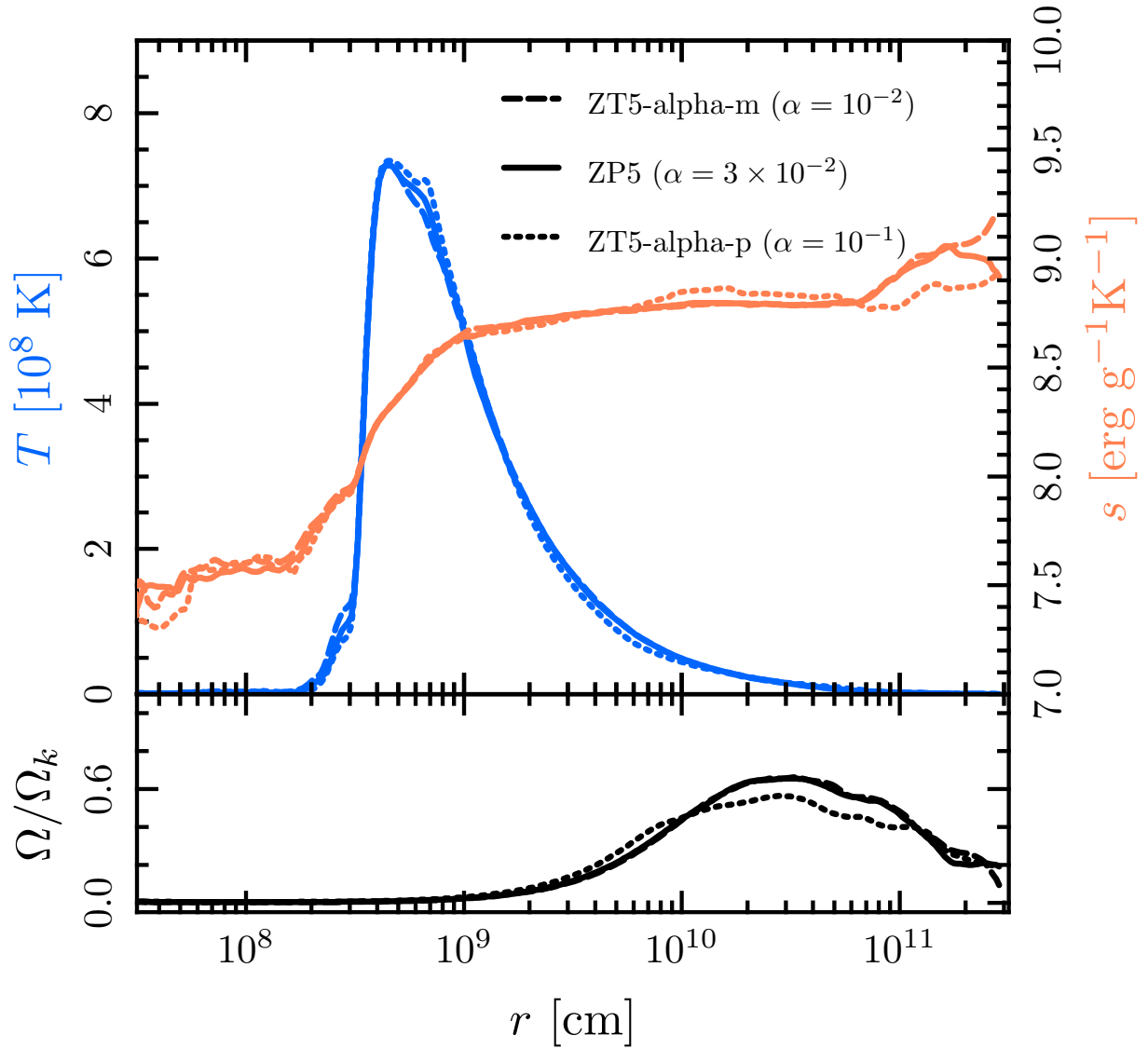
Figure 2.13: The variation of our simulations of the fiducial remnant with different values of α. The top panel shows 1D temperature and entropy profiles and the bottom panel shows the ratio of the angular velocity to the Keplerian angular velocity. The profiles are shown after the same number of viscous times, at $\alpha t_{\mathrm{end}} = 3 \times 10^2$ s. While there are small variations between runs, we see no significant change in our results for values of α spanning an order of magnitude.

shows some minor differences. However, none of our conclusions are based on the detailed structure of the outer material, so this does not alter any of our conclusions.

2.A.4 Initial Conditions

In order to confirm that our results are independent of small details of the initial conditions, we initialize our simulations with output from the same SPH calculation taken at three different times. By default, we start from the end of the SPH calculation, which for the fiducial model was after 35.7 initial orbital periods had elapsed. (The secondary was tidally disrupted after 29 orbits.) The results we obtain with initial conditions from output taken 0.1 and 0.7 initial orbital periods before the end of the calculation are virtually identical. The outcome of our calculation is insensitive to the duration of the SPH simulation, so long as the remnant has had sufficient time to evolve towards axisymmetry.

2.A.5 Viscosity Cutoff

As expected, we confirm that out results are insensitive to the location of the cutoff radius defined in Equation 2.6 and the surrounding discussion.

2.A.6 Nuclear Network

As discussed in Section 2.2.3 we implement a simple 5 isotope (He,C,O,Ne,Mg) nuclear network. We confirm that this simple nuclear network reproduces the results of the more sophisticated aprox13 network. Because of the high computational cost of the full network, we perform these test calculations at a lower resolution. We perform these tests on the $0.3 + 1.1$ He+CO system (ZP2) as it has the shortest burning time of any of the He+CO mergers we consider. Fig. 2.14 shows that the two networks give identical results. We also show the effect of omitting the nuclear burning, which does change the values of the thermodynamic quantities near the temperature peak, but does not alter the overall structure of the remnant.

2.A.7 3D

Moving to 3D makes the viscous evolution substantially more computationally demanding because of the strong timestep constraint imposed by our explicit evolution of the viscous terms, $\Delta t_{\mathrm{visc}} \sim \min((\Delta r)^2/\nu)$. A zone near the pole ($\theta \approx \pi/(4N_\theta)$) has size $\Delta r = 2\pi r\theta/N_\phi$, where N_ϕ is the number of ϕ zones. The means that at the same r, θ resolution, a 3D calculation will require evolving approximately N_ϕ as many zones at timestep smaller by a factor of N_ϕ^2. This issue can be helped somewhat by subcycling, that is advancing the viscous terms at Δt_{visc} but integrating the rest of the hydrodynamics at Δt_{CFL}.

In light of these issues, the simulation we perform is a simple one in which we initialize the same azimuthally symmetric initial conditions used in 2D on a lower resolution 3D grid
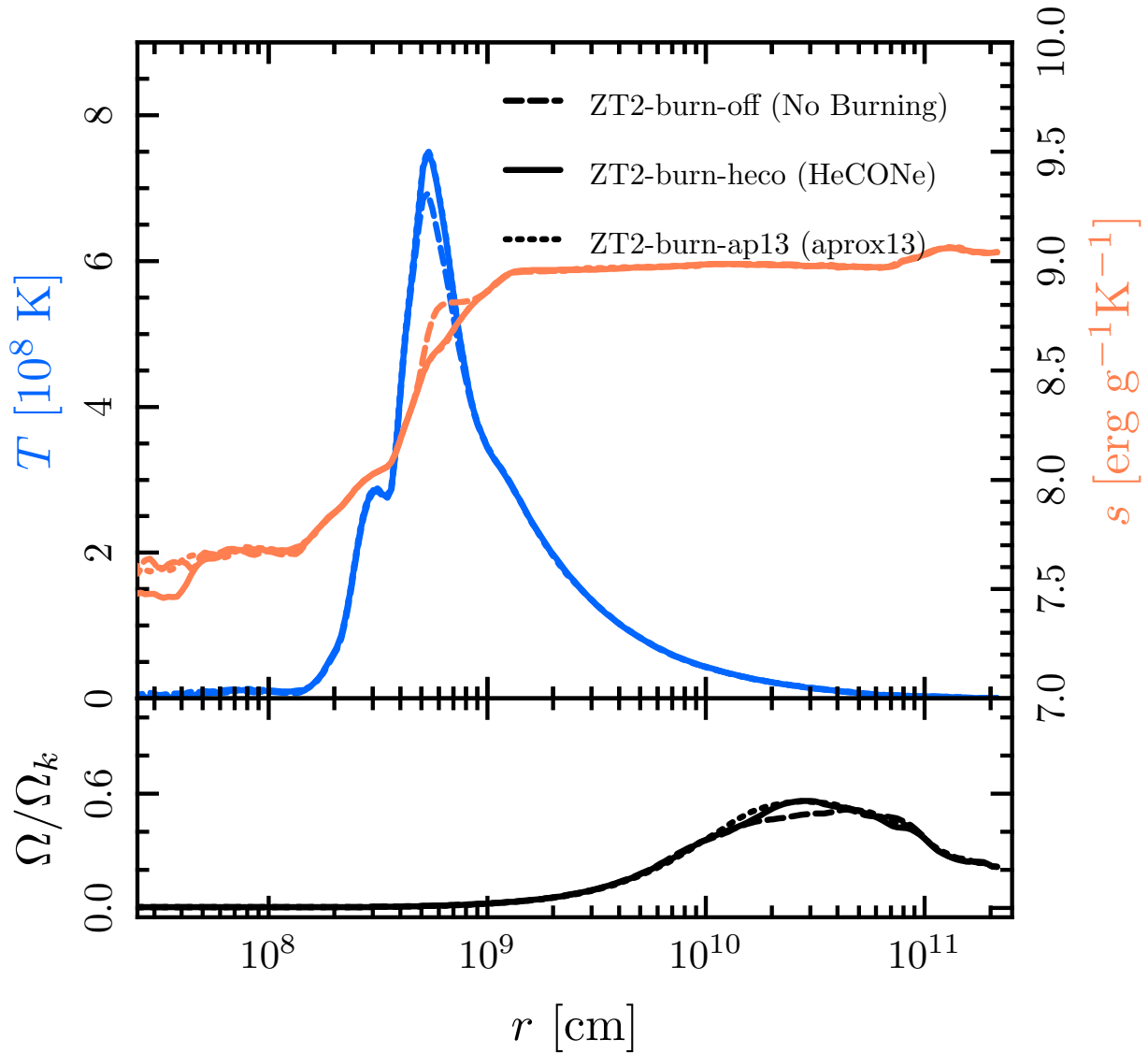
Figure 2.14: The variation of our simulations of the $0.3 + 1.1\mathrm{M}_\odot$ remnant with different nuclear networks. The top panel shows 1D temperature and entropy profiles and the bottom panel shows the ratio of the angular velocity to the Keplerian angular velocity. The results of our simple network (HeCONe) and the aprox13 network are almost indistinguishable. We show the results of omitting the network entirely to illustrate the small impact of nuclear burning on the remnant structure over the viscous time-scales of interest.

$(N_r = 48, N_\theta = 32, N_\phi = 32)$. We evolve the system for a substantially shorter time, only 1×10^2 s. Over that limited time, we observe no qualitative differences which would affect our conclusions.

Chapter 3

The Evolution of Super-Chandrasekhar Mass White Dwarf Merger Remnants

Abstract

We present stellar evolution calculations of the remnant of the merger of two carbon-oxygen white dwarfs (CO WDs). We focus on cases that have a total mass in excess of the Chandrasekhar mass. After the merger, the remnant manifests as an $L \sim 3 \times 10^4 \, \mathrm{L_\odot}$ source for $\sim 10^4 \, \mathrm{yr}$. A dusty wind may develop, leading these sources to be self-obscured and to appear similar to extreme AGB stars. Roughly ~ 10 such objects should exist in the Milky Way and M31 at any time. As found in previous work, off-center carbon fusion is ignited within the merger remnant and propagates inward via a carbon flame, converting the WD to an oxygen-neon (ONe) composition. By following the evolution for longer than previous calculations, we demonstrate that after carbon-burning reaches the center, neutrino-cooled Kelvin-Helmholtz contraction leads to off-center neon ignition in remnants with masses $\geq 1.35 \, \mathrm{M_\odot}$. The resulting Ne flame converts the core to a silicon WD. Thus, super-Chandrasekhar WD merger remnants do not undergo electron-capture induced collapse as traditionally assumed. Instead, if the remnant mass remains above the Chandrasekhar mass, we expect that it will form a low-mass iron core and collapse to form a neutron star. Remnants that lose sufficient mass will end up as massive, isolated ONe or Si WDs.

3.1 Introduction

In double WD systems with sufficiently short initial orbital periods, angular momentum losses from gravitational wave radiation shrink the orbit and can lead to a merger of the WDs. The outcome of such a merger is strongly dependent on the mass of the individual WDs and their mass ratio. For recent summaries of the many possible outcomes, see fig. 1 in Dan et al. (2014) or fig. 3 in Shen (2015).

Iben & Tutukov (1984b) and Webbink (1984) proposed that mergers of two carbon-oxygen (CO) WDs whose total mass was in excess of the Chandrasekhar mass would lead to the central ignition of carbon fusion and hence to a Type Ia supernova. It was quickly pointed out by Saio & Nomoto (1985) and by Nomoto & Iben (1985) that the rapid mass transfer in such an event would lead to the off-center ignition of carbon, triggering the quiescent conversion of the remnant to an oxygen-neon (ONe) composition. Standard models conclude that subsequently, electron-capture reactions cause the ONe core to collapse and form a neutron star (Miyaji et al. 1980; Schwab et al. 2015).

Saio & Nomoto (1985) and Nomoto & Iben (1985) approximated the effects of the WD merger as the accretion of material on to the more massive WD. They studied constant accretion rates $\dot{M} \lesssim 10^{-5} \, M_\odot \, \mathrm{yr}^{-1}$, motivated by the assumption that the material is accreting from a disc at a rate bounded by the Eddington limit. Since this early work, smoothed-particle hydrodynamics (SPH) simulations (e.g., Benz et al. 1990; Dan et al. 2011) of double WD systems have been used to investigate the dynamics of the merger. Schematically, the primary (more massive) WD remains relatively undisturbed and the secondary (less massive) WD is tidally disrupted. Some material from the disrupted WD is shock-heated, forming a thermally-supported layer at the surface of the primary WD; the rest of the material is rotationally-supported, forming a thick disc at larger radii.[1]

Motivated by these results, Shen et al. (2012) and Schwab et al. (2012) studied the post-merger evolution of these systems in more detail. They showed that the transport of angular momentum occurs on a time-scale ($\sim 10^4 \, \mathrm{s}$) far shorter than the time-scale on which the remnant cools ($\sim 10^4 \, \mathrm{yr}$). One of the key conclusions of Shen et al. (2012) and Schwab et al. (2012) was thus that the viscous evolution should be taken into account before exploring the long-term thermal evolution of the merger remnant.

In this work, we follow the long-term evolution of the merger of two CO WDs. The initial conditions for these calculations are generated self-consistently, beginning from SPH simulations of the dynamical merger of the two WDs (Dan et al. 2011; Raskin et al. 2014) and explicitly modeling the subsequent phase of viscous evolution as in Schwab et al. (2012). We then use the MESA stellar evolution code (Paxton et al. 2011, 2013, 2015) to follow the evolution of these merger remnants over thermal and nuclear time-scales.

In Section 3.2 we discuss our initial models along with the key options and input physics that enable our MESA calculations. In Section 3.3 we discuss the ignition and propagation of a carbon flame. In Section 3.4 we discuss the ignition of a neon flame and then in Section 3.5 outline how subsequent evolution may lead to the formation of a neutron star. In Section 3.6 we discuss the observational properties of the remnant. In Section 3.7 we conclude, presenting a schematic overview of our results and suggesting avenues for future work. Fig. 3.12 summarizes the possible end states of super-Chandrasekhar WD mergers.

---

[1]Exceptions to this picture include WD collisions (e.g., Raskin et al. 2009) or cases where the mass ratio is nearly unity (e.g., van Kerkwijk et al. 2010b).

ID	SPH Ref.	M_2	M_1	Viscous Ref.	M_{tot}
M15	Dan11	0.60	0.90	Schwab12	1.486
M16	Raskin14	0.64	0.96	Raskin14	1.586

Table 3.1: A summary of the two merger systems studied in this work. The ID reflects the total mass of the system. "SPH ref." indicates the primary reference containing the details of the SPH calculation of the merger (Dan11: Dan et al. 2011, Raskin14: Raskin et al. 2014). M_2 is the mass (in $M_\odot$) of the secondary, the less massive of the two WDs; M_1 is the mass of the more massive primary. "Viscous ref." refers to the primary reference containing the details of the subsequent viscous evolution (Schwab12: Schwab et al. 2012, Raskin14: Raskin et al. 2014). M_{tot} is the total mass of the system (in $M_\odot$) at the end of the viscous phase simulation, and hence the initial mass of the MESA model.

3.2 Setup of MESA Calculations

3.2.1 Initial Models

As discussed in the introduction, SPH simulations of WD mergers show that at the end of the dynamical phase of the merger, the primary white dwarf remains mostly undisturbed. It is now surrounded by the tidally disrupted secondary, which includes a significant amount of material in a rotationally-supported disc. In Schwab et al. (2012), we took the output of SPH merger calculations, mapped them into a grid-based hydrodynamics code, and followed the evolution of these remnants under the action of an α-viscosity. We found that the viscous stresses transformed the disc material into a spherical, thermally-supported envelope on a time-scale of hours.

In this work, we focus on two super-Chandrasekhar WD merger remnants, one with a total mass of approximately $1.5\,M_\odot$ (model M15) and another with total mass of approximately $1.6\,M_\odot$ (model M16). Both remnants are the result of a merger with mass ratio $q = 2/3$ and have a composition of 50 per cent carbon and 50 per cent oxygen by mass. Table 3.1 contains a summary of these models, including references to the papers in which the simulations of the dynamical and viscous phases were first reported.

The initial conditions for the thermal evolution calculations in this work are the end states of our viscous evolution calculations. In Appendix 3.A, we discuss the details of how we transfer the output of our hydrodynamic simulations into MESA. In Fig. 3.2, we show the density-temperature profiles of our initial MESA models. We define the burning time as $t_{\text{burn}} = c_{\text{p}}T/\epsilon_{\text{nuc}}$, where c_{p} is the specific heat at constant pressure, T is the temperature and ϵ_{nuc} is the specific energy generation rate from nuclear reactions. At the temperature peaks of both models, $t_{\text{burn}} \gtrsim 10^4\,$s, the approximate duration of the viscous evolution. This demonstrates that substantial nuclear energy was not liberated during the viscous phase.
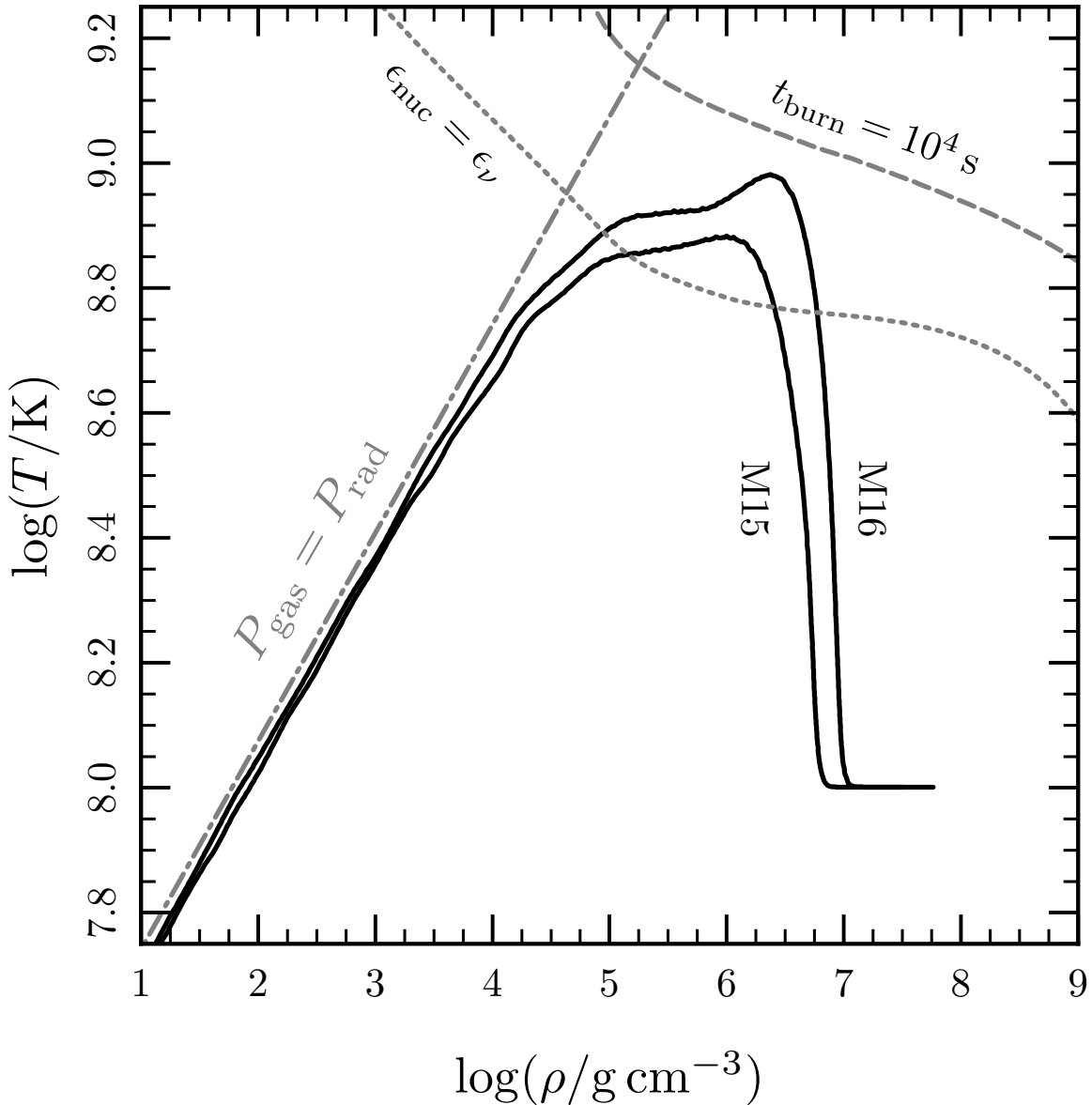
Figure 3.1: The initial density-temperature profiles of our MESA models M15 and M16, taken from the end state of simulations of the viscous phase of WD merger remnants (see Appendix 3.A). The dotted line shows where the energy release from nuclear burning is equal to the neutrino losses. The dashed line shows where the burning time-scale $t_{\text{burn}} = 10^4$ s. The dash-dot line indicates where gas and radiation pressure are equal. Both models reached carbon ignition conditions during the viscous evolution, but the duration of the viscous phase was not long enough to allow significant nuclear burning to occur. Since the structure of the $1.6\,\text{M}_\odot$ model is so similar to that of the $1.5\,\text{M}_\odot$ model, its evolution and outcomes are similar (aside from the possible effects of mass loss; see Section 3.4).
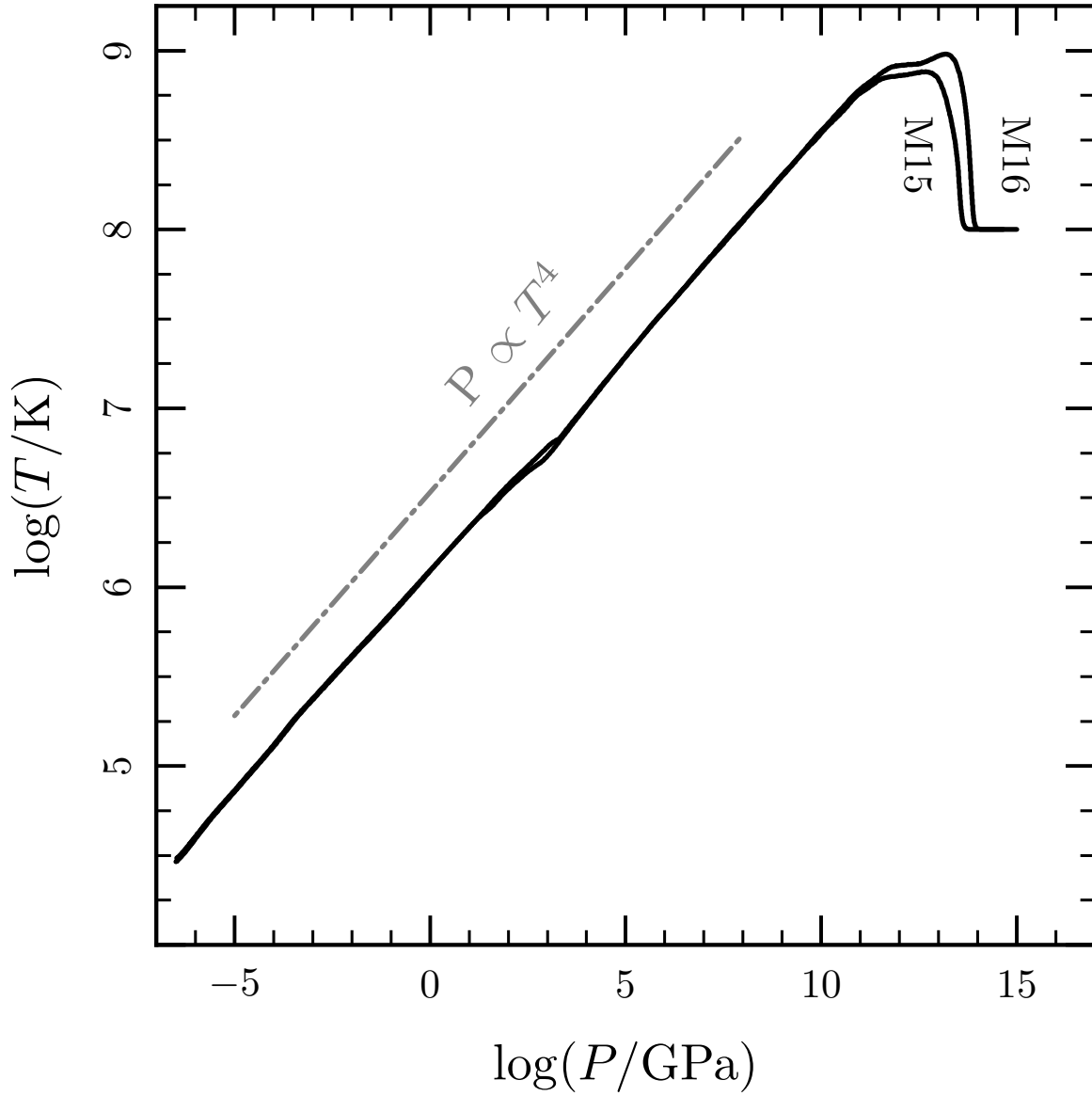
Figure 3.2: The initial pressure-temperature profiles of our MESA models M15 and M16, taken from the end state of simulations of the viscous phase of WD merger remnants (see Appendix 3.A). The dash-dot line indicates the slope corresponding to the pressure-temperature relationship for blackbody radiation.

3.2.2 MESA Version and Important Options

The calculations performed in this paper use MESA version r6596 (released 2014-06-08). As required by the MESA manifesto, the inlists necessary to reproduce our calculations will be posted on http://mesastar.org.

We use `approx21.net`, a 21-isotope α-chain nuclear network. In order to avoid spurious flashes, it is important to resolve the burning fronts in the convectively-bounded deflagrations that develop in our models (e.g., Saio & Nomoto 1998). We use the options selected by Farmer et al. (2015) in their study of carbon flames in super-AGB stars. In particular, we use the controls

```
mesh_dlog_burn_c_dlogP_extra = 0.10
mesh_dlog_cc_dlogP_extra = 0.10
mesh_dlog_co_dlogP_extra = 0.10
```

which add additional spatial resolution in regions where carbon burning is occurring. This ensures that that flame is well-resolved. We use analogous controls to ensure that the neon-burning flames in our models are also well-resolved.

3.2.3 Input Physics

The initial composition of the model is pure carbon and oxygen. We use the OPAL radiative opacities for carbon and oxygen-rich mixtures (Iglesias & Rogers 1993, 1996). These are referred to as OPAL "Type 2" tables in MESA. We select a base metallicity using the control $\texttt{Zbase} = 0.02$. The lower temperature boundary of these tabulations is $\log(T/\mathrm{K}) = 3.75$.

As we show in Section 3.6, when the outer layers of the remnant expand, they reach temperatures below this threshold. MESA does not provide low-temperature opacities that include separate carbon and oxygen enhancements. As a result, MESA is usually forced to fall back to opacity tabulations which assume a different composition. Thus, when blending between the OPAL tables and any of the included low-temperature tables, there are dramatic and unphysical changes in opacity at the location of the blend.

In order to ensure that the composition assumed by the opacities approximately matches the composition of the model, we generate a new opacity table. These calculations and their results are briefly described in Appendix 3.B. We consider only a single composition: $X_\mathrm{C} = 0.49, X_\mathrm{O} = 0.49, Z = 0.02$, where the relative metal abundances are drawn from Grevesse & Sauval (1998). We do not consider the effects of molecular opacities in these calculations, putting a rough lower limit on their validity of $\log(T/\mathrm{K}) \gtrsim 3.5$. Using these tables, our models obey $\log(T_\mathrm{eff}/\mathrm{K}) > 3.6$ and so do not violate this assumption. We will discuss the role of molecule and dust formation in these objects in Section 3.6.

3.3   Carbon Flame

In each of the initial models shown in Fig. 3.2, the rate of energy release from nuclear reactions exceeds the rate of energy loss from neutrino cooling at the initial temperature peak. As described in Schwab et al. (2012), this is because heating by viscous dissipation leads to off-center ignition of self-sustaining carbon fusion within hours of the merger.[2] When we begin our MESA calculation, there is thus immediately off-center carbon burning in the remnant. The energy release in this carbon-burning shell quickly leads to the formation of a convection zone. Heat from the burning region is conducted into the degenerate interior, giving rise to a deflagration wave that begins propagate towards the center of the remnant. We refer to this deflagration as the "carbon flame". Fig. 3.3 shows the evolution of this flame in our MESA calculations of model M15. After an initial transient phase with a duration of $\lesssim 100$ years ($t = 0$ to point 1), the deflagration forms and propagates to the center over ≈ 20 kyr (point 1 to point 4). Because the structure of the $1.6\,M_\odot$ model is so similar to that of the $1.5\,M_\odot$ model (see Fig. 3.2) its evolution and outcomes are similar; for simplicity, we will primarily discuss model M15.

It is important to note that the carbon flame, while off-center, is still deep in the interior. The convective zone outside the burning region satisfies a "balanced power" condition, where the total luminosity of thermal neutrino emission from the zone is approximately equal to the rate of energy release from fusion at its base (Timmes et al. 1994). This neutrino-cooled convective zone has a radial extent of order the pressure scale height, and its upper boundary is sufficiently deep that the time-scale for radiative diffusion to transport the energy to the surface is longer than the evolutionary time-scale of the remnant. Thus, while key to the final fate of the remnant, the energy release of the carbon flame is not coupled to the surface, and does not power the luminosity of the remnant. Instead, the behavior of the surface layers— which we discuss in more detail in Section 3.6—is driven by the thermal energy generated during the merger.

A snapshot of the carbon flame structure is shown in Fig. 3.4. At this time, the flame is at a density $\rho \approx 4 \times 10^5\,\mathrm{g\,cm^{-3}}$ and temperature $T \approx 7 \times 10^8\,\mathrm{K}$, with a carbon mass fraction $X_\mathrm{C} \approx 0.5$. At these conditions, the flame width is $\approx 2 \times 10^7\,\mathrm{cm}$ and the flame speed is $\approx 4 \times 10^{-4}\,\mathrm{cm\,s^{-1}}$. While this exact density, temperature, and composition are not present in Timmes et al. (1994), the flame speed and thickness we observe are consistent with their tabulated results.

Denissenkov et al. (2013) suggested that efficient mixing at the convective boundary can quench inwardly propagating carbon flames in super-AGB stars. If a similar phenomenon were to occur here, the death of the carbon flame would lead to qualitatively different

---

[2]This is in contrast to calculations that model the merger as Eddington-limited accretion, in which carbon ignition does not occur for $\gtrsim 10^4$ yr, until sufficient material has accreted to adiabatically compress the base of the shell to higher temperatures. In a lower mass merger, say $M_\mathrm{tot} \approx 1.4\,M_\odot$, we find that carbon fusion does not ignite during the viscous evolution. In this case, there is a similar time delay, as carbon ignition must wait for the cooling envelope to compress material at its base. An example of such evolution is shown in Shen et al. (2012).
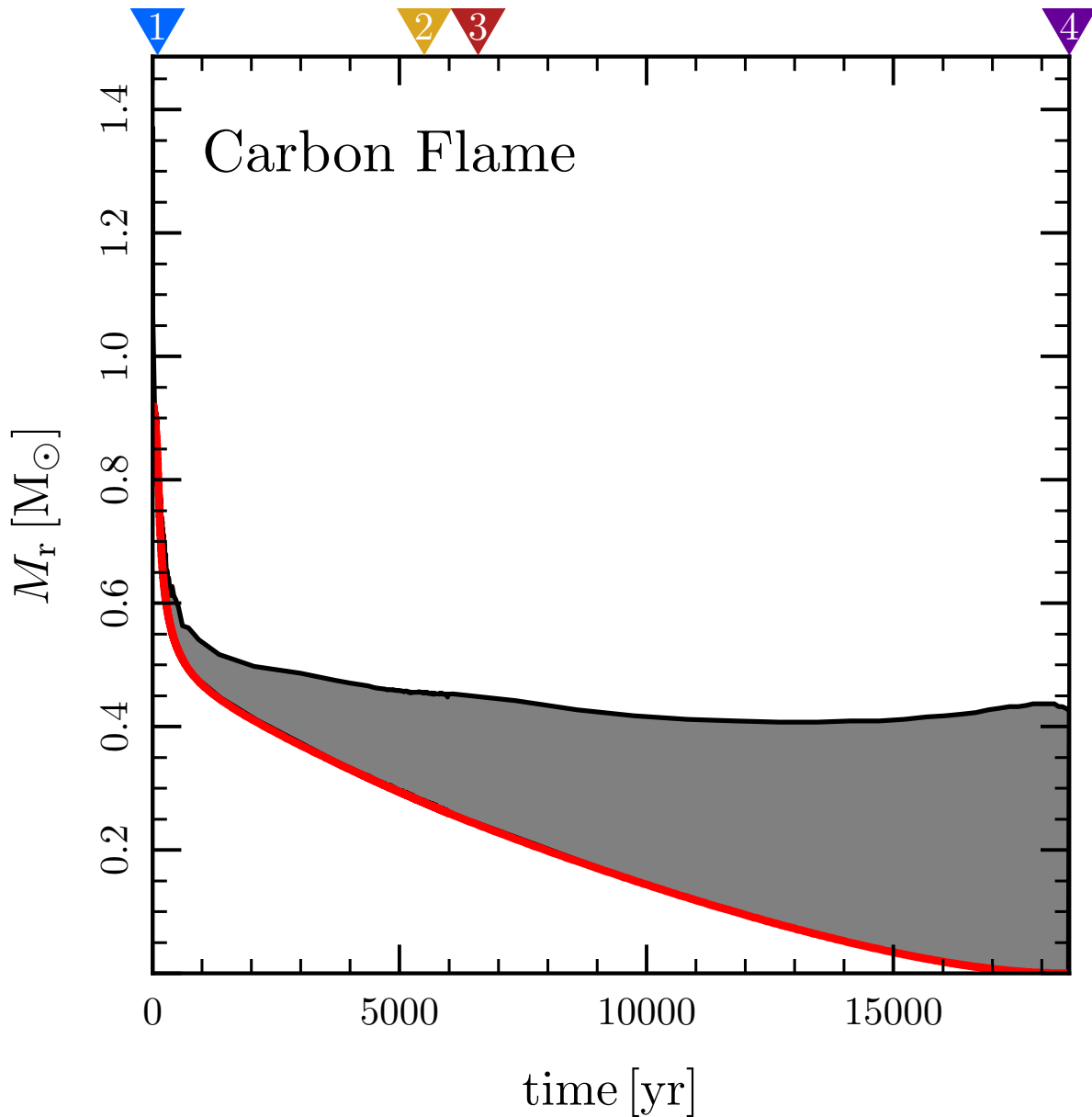
Figure 3.3: The propagation of the carbon flame in model M15 with no convective boundary mixing. The x-axis shows time, as measured from the beginning of the MESA calculation; effectively this is the time since merger. The y-axis shows the Lagrangian mass coordinate. The extent of the convective region associated with the flame is shaded. The location of maximum nuclear energy release, a proxy for the location of the flame, is indicated by the thick red line at the bottom of this region. After approximately 20 kyr, the flame reaches the center. The numbered triangles at the top of the plot indicate times in the evolution that will be referenced in Figs. 3.5 and 3.11.
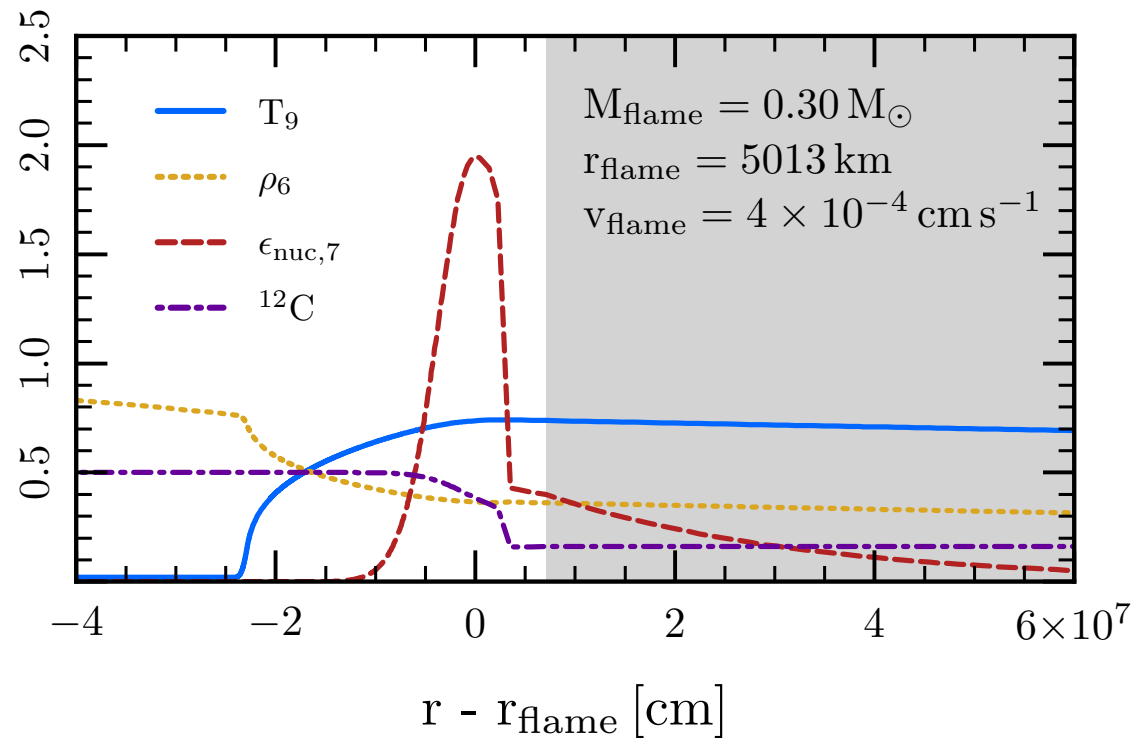
Figure 3.4: Structure of a carbon-burning flame. The shaded grey region marks the convection zone. The temperature ($T/10^9\,$K), density ($\rho/10^6\,$g$\,$cm^{-3}), energy generation rate ($\epsilon_{\mathrm{nuc}}/10^7\,erg\,s^{-1}\,$g^{-1}), and ^{12}C mass fraction are shown as function of radius. The thickness of the flame is $\sim 10^7\,$cm. This profile from our MESA calculation is from a time slightly before point 2, as marked in Fig. 3.3.

results, as it would create a "hybrid" WD with a CO core and an ONe mantle. We include this possibility in the flow chart presented in Section 3.7. However, Lecoanet et al. (2016) find that convective plumes fail to induce sufficient mixing to lead to flame disruption and conclude that these "hybrid" WDs are not a typical product of stellar evolution.

3.4   Kelvin-Helmholtz Contraction and Neon Ignition

When the carbon flame reaches the center, it lifts the degeneracy of the material. This is illustrated in Fig. 3.5, where the dash-dot line (labeled point 4) shows the temperature-density profile of the model at the time of central carbon exhaustion. The newly non-degenerate core will now Kelvin-Helmholtz (KH) contract. The core is sufficiently hot and dense that it cools through thermal neutrino losses. As a result, it will develop an off-center temperature peak. We note that the evolution of the central density and temperature is similar to that observed in intermediate mass stars, as these objects also develop degenerate cores with similar masses (e.g., Jones et al. 2013, 2014).

As discussed by Nomoto (1984), there is a critical core mass for off-center neon ignition. Nomoto demonstrated this by means of a simple calculation in which stellar models of pure neon were constructed and allowed to KH contract. Neon ignition occurred only in models with a mass above $1.37 M_\odot$. We repeated this calculation and find a slightly lower critical mass of $1.35 M_\odot$ for pure ^{20}Ne models (see Appendix 3.C). We use the results of these pure neon models to guide our interpretation of the central evolution of the WD merger remnants.

Fig. 3.6 shows a Kippenhahn diagram of model M15 from the time the carbon flame reaches the center until neon ignition. Initially carbon is being burned in the core, but over the first $\approx 1 \, \mathrm{kyr}$, the central convection zone shrinks and vanishes as the carbon in the center is exhausted. As the star KH contracts, a series of off-center carbon flashes occur. Additionally, an off-center temperature peak develops. Its mass coordinate is indicated by the black dotted line.

Fig. 3.7 shows the evolution of the temperature and density at both the center (solid black line) and the off-center temperature peak (dashed black line) in model M15 during the KH contraction phase. The "wiggles" in the evolution of the center are manifestations of changes to the stellar structure due to the off-center carbon flashes shown in Fig. 3.6. The grey lines show the analogous temperature and density evolution of a $1.385 M_\odot$ pure neon model. The qualitative agreement between the two models is good.

The agreement between our full remnant models and our simple pure neon calculations demonstrates that the off-center neon ignition is a simple consequence of the mass of the remnant. Once ignited, the neon burning will propagate to the center in a manner similar to the carbon burning, converting the object to silicon-group elements. (See Section 3.5 for more discussion of this process and the subsequent evolution.) Because the critical mass for neon ignition ($1.35 M_\odot$) is less than the critical mass needed to trigger the collapse of an ONe core ($1.38 M_\odot$; Schwab et al. 2015), we conclude that is is difficult to produce an ONe core with a sufficient mass to undergo AIC in a WD merger.
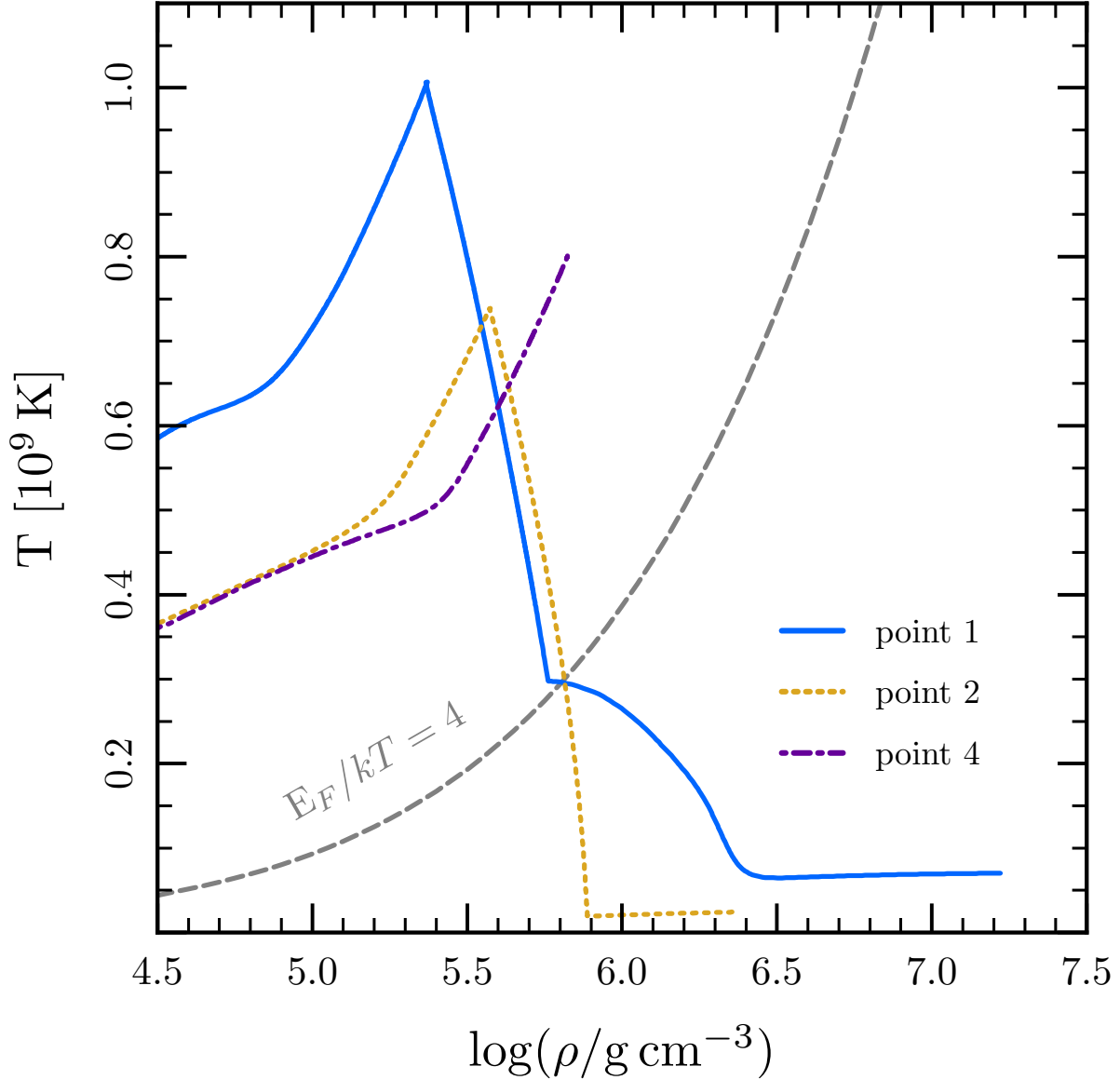
Figure 3.5: The evolution of the core of model M15 in temperature-density space as the carbon flame propagates inward. Each line corresponds to one of the times indicated in Fig. 3.3; point 3 is omitted because it appears extremely similar to point 2. The location of the flame corresponds to the location of maximum temperature in each line. The dashed grey line marks the degeneracy condition (above/left is non-degenerate; below/right is degenerate). Early in the evolution (point 1) the center has $\log(\rho/\mathrm{g\,cm^{-3}}) > 7$. As the flame lifts the degeneracy, the central density decreases (point 2). Once the flame reaches the center (point 4), is lifts the degeneracy throughout the star.

Off-center neon ignition does not appear to have been observed in previous studies of CO WD merger remnants. The salient difference between this work and previous work appears to be that we evolved the remnants for longer. Saio & Nomoto (1985) halted their calculation when the carbon flame was at a mass coordinate of $M_r = 0.005\,\mathrm{M_\odot}$ because it had become too computationally costly to continue. Later work by the same authors (Saio & Nomoto 1998) allowed the flame to reach the center, but did not continue the evolution beyond this point. Other work on the long-term evolution of CO WD merger remnants has focused on avoiding off-center ignition (e.g., Yoon et al. 2007).

As an illustration of the effects of mass loss on the core, we run a version of model M15 with a mass loss rates drawn from Bloecker (1995). That is, we use the MESA options

```
AGB_wind_scheme = 'Blocker'
Blocker_wind_eta = 0.1d0
```

The Bloecker (1995) mass loss rates were motivated by atmosphere calculations of Mira-like stars and thus they are not directly applicable to this problem. However, we simply want to remove some mass when the object is cool and luminous, and so this a suitable heuristic.

Fig. 3.8 shows the same quantities as Fig. 3.7, but for a model in which the remnant shed approximately $0.2\,\mathrm{M_\odot}$ of material during the phase while the carbon flame was propagating to the center. As the object contracts, an off-center temperature peak develops, but it fails to reach temperatures where neon burning exceeds thermal neutrino losses. Instead, the core becomes supported by electron degeneracy pressure, halting the KH contraction. As a result, the peak temperature reaches a maximum and then begins to decrease. The remnant will retain its ONe composition and cool to become a massive WD.

3.5 Neon Flame and Subsequent Evolution

The phase beginning with off-center neon ignition is relatively unexplored. We are unable to self-consistently evolve the remnants all the way to their final fate, but the likely outcome is formation of a neutron star via an iron core collapse. Analogous phases of evolution in single intermediate mass stars (Jones et al. 2014; Woosley & Heger 2015) and in ultra-stripped binary systems (i.e., ones that form helium cores 2.5-3.5 $\mathrm{M_\odot}$; Tauris et al. 2013, 2015) continue to be active areas of research. Future results in these areas can be applied to the evolution of super-Chandrasekhar mass WD merger remnants.

3.5.1 Neon Flame

In model M15, off-center neon ignition occurs at a mass coordinate $M_r \approx 0.6\,\mathrm{M_\odot}$. This quickly forms a convectively-bounded neon-burning deflagration front which begins to propagate inwards towards the center of the star. Fig. 3.9 shows the location of the flame and its accompanying convection zone during this phase. In our MESA calculations, we assume that there is no additional mixing at the convective boundary.
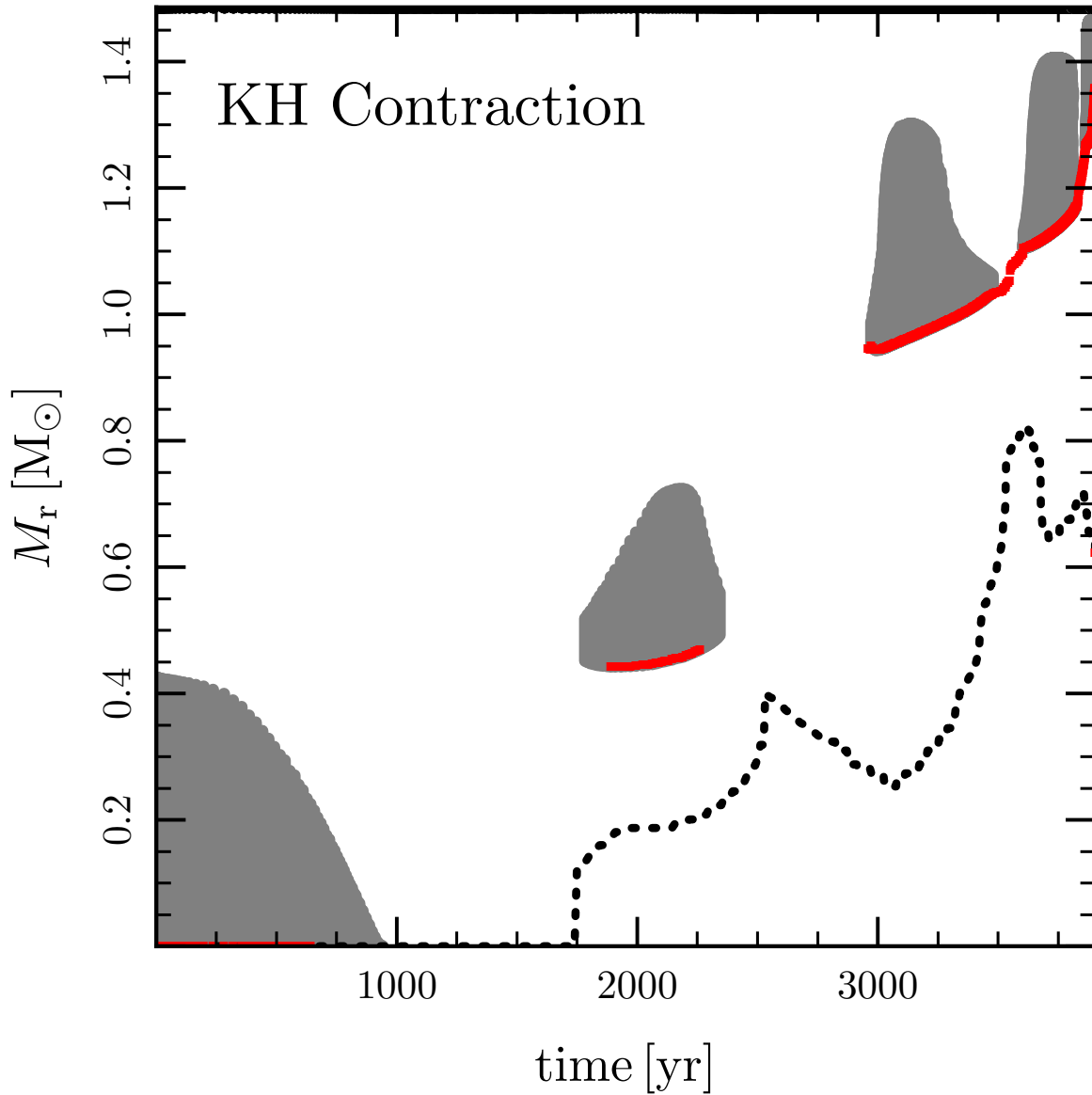
Figure 3.6: A Kippenhahn diagram of model M15 from the time the carbon flame reaches the center until off-center neon ignition. The x-axis shows time, as measured from the time when the carbon flame reached the center. The y-axis shows the Lagrangian mass coordinate. Convective regions are shaded grey and the locations of carbon burning (with $\epsilon_{\mathrm{nuc}} > 10^7\,\mathrm{ergs\,s^{-1}\,g^{-1}}$) are marked in red. The dotted black line indicates the location of the local maximum in the temperature profile that is closest to the center.
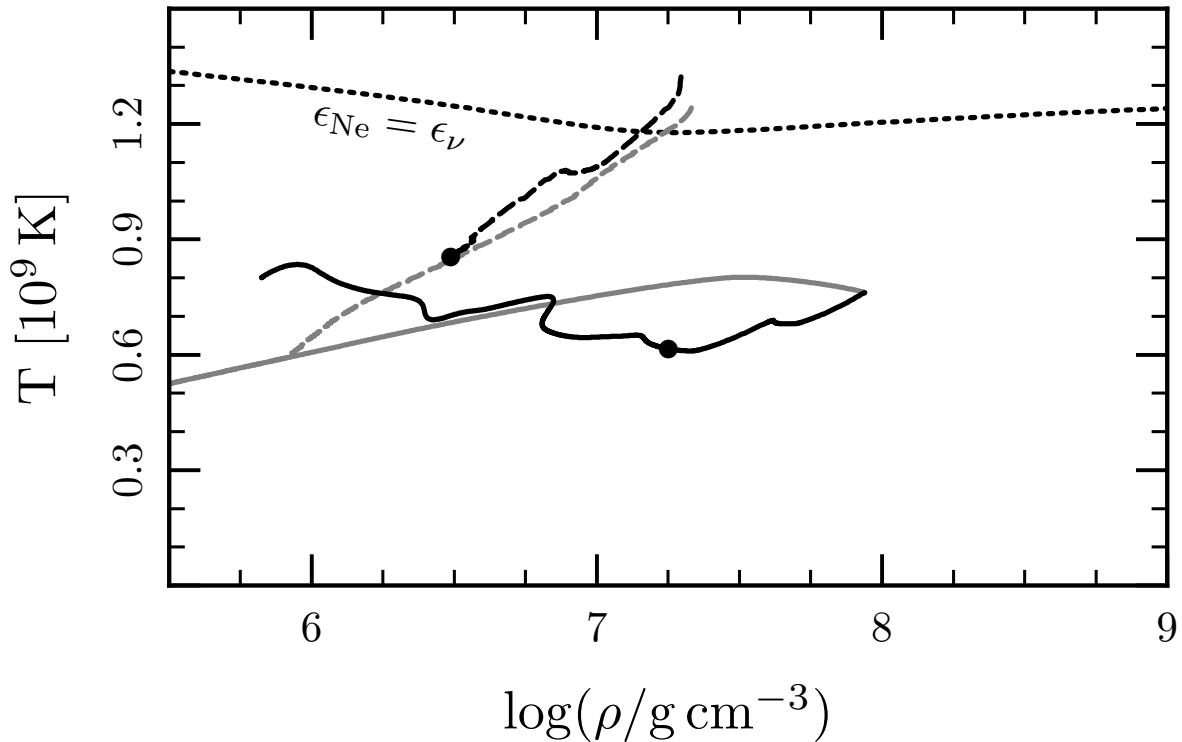
Figure 3.7: The evolution of temperature and density at the center of model M15 (solid black line) and at the temperature peak (dashed black line) during the KH contraction shown in Fig. 3.6. The total mass of the remnant is $\approx 1.5\,M_\odot$. For visual clarity, the line for the temperature peak is shown only after the central density reaches $\log(\rho/\mathrm{g\,cm^{-3}}) \approx 7.25$, which is marked by the black circle. The grey lines show the evolution of a contracting $1.385\,M_\odot$ pure neon model; the solid grey line shows conditions at the center and the dashed grey line shows conditions at the temperature peak, which due to neutrino cooling, develops off-center. The black dotted line shows approximately where the energy release from neon burning is equal to the energy loss rate from thermal neutrinos. Off-center neon ignition occurs in this model.
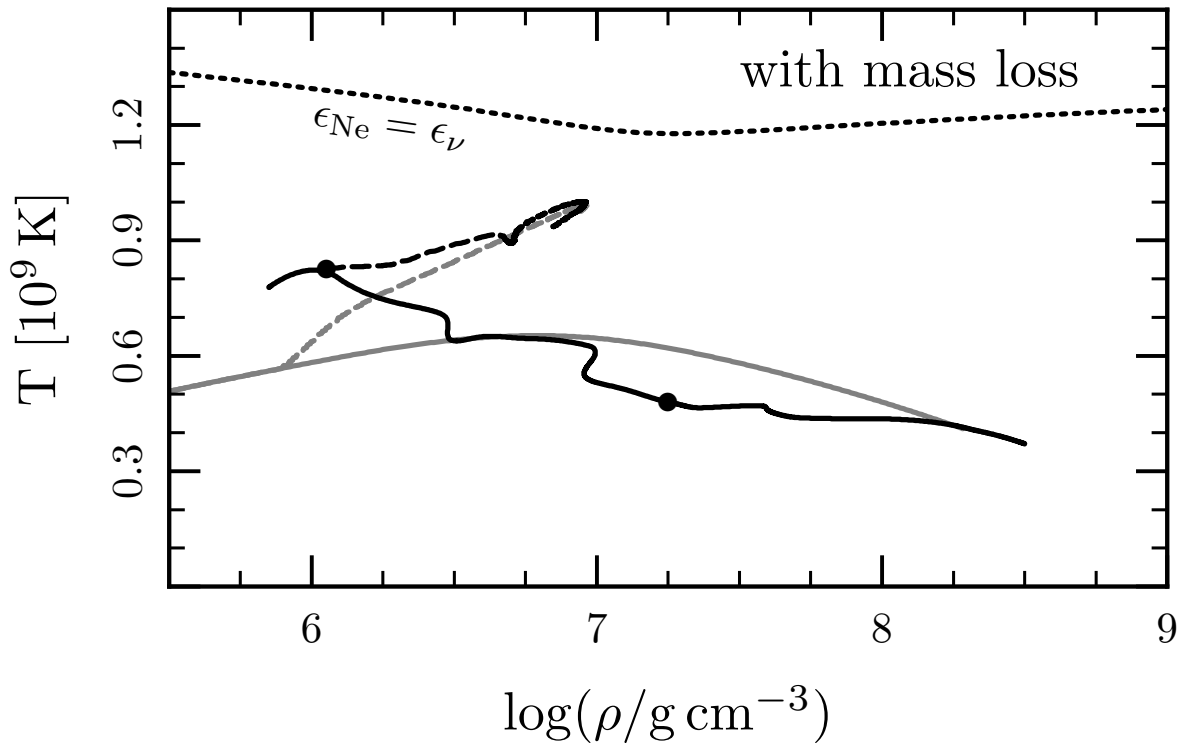
Figure 3.8: Same as Fig. 3.7, but for the version of model M15 with mass loss during the cool giant phase (see Section 3.4). The remnant shed $\approx 0.2\,\mathrm{M_\odot}$ and now has a total mass of $\approx 1.3\,\mathrm{M_\odot}$. The grey lines show the evolution of a contracting $1.30\,\mathrm{M_\odot}$ pure neon model. Neon ignition does not occur and the core instead becomes supported by electron degeneracy pressure. The remnant will cool to form an ONe WD.

As can be shown from the analytic estimates given in Timmes et al. (1994) and as discussed in Woosley & Heger (2015), oxygen-neon-burning flames are much faster (though still extremely subsonic) and thinner than carbon-burning flames. Fig. 3.10 shows the structure of the neon-burning flame in our MESA model; note that the flame thickness is $\sim 10^3$ cm and the flame velocity is $\sim 0.1 \, \mathrm{cm \, s^{-1}}$.

In our MESA calculation we are directly resolving the flame, which is extremely computationally inefficient.[3] Future work will benefit from a sub-grid model such as that used in Woosley & Heger (2015), where the flame is not resolved in the full-star simulation, but tabulated velocities from resolved, micro-zoned flame calculations are used to propagate a model for the flame.

3.5.2 Silicon Burning and Core Collapse

As neon-burning migrates to the center, it leaves behind silicon-group ashes. The degeneracy of these ashes is also lifted and it seems likely that the cycle of KH contraction and subsequent off-center ignition will continue. In Appendix 3.C we find a critical mass for Si ignition of $\approx 1.43 \, \mathrm{M_\odot}$. This suggests that in a narrow range of WD mergers (remnants with masses $1.35 \, \mathrm{M_\odot} \lesssim M \lesssim 1.43 \, \mathrm{M_\odot}$, accounting for mass loss), the final merger remnant could be a WD with a Si-group composition.

Recently, Woosley & Heger (2015) discussed the presence of Si-flashes in the evolution of $9 - 11 \, \mathrm{M_\odot}$ stars. They found Si-deflagrations beginning in models with CO core masses of $\approx 1.4 \, \mathrm{M_\odot}$, with increasingly intense Si-burning flashes as the mass increased. We do not explore this phase in our MESA models. It is difficult to map our remnants on to any particular model in the Woosley & Heger (2015) results, but it does appear that we are in the regime where this unstable Si-burning may play a role. Future work will clarify its importance.

For now, we assume that Si-burning in remnants with $M \geq 1.43 \, \mathrm{M_\odot}$ (accounting for mass loss) quiescently leads to the formation of an Fe-core and that subsequently this low mass Fe core will collapse to form a neutron star. Thus, while we have revised the evolutionary story for super-Chandrasekhar WD mergers, we think they are still likely to produce a population of single, low-mass neutron stars.

3.6 Observational Properties of the Merger Remnant

In this section we describe the observational properties of super-Chandra WD merger remnants, focusing on the time between the merger and the final collapse to form a neutron star. As described in Sections 3.3 and 3.5.1, the energy released by fusion during the carbon and neon flames does not reach the surface. It is instead lost primarily to neutrino cooling deep in the stellar interior, at sufficiently high optical depths that the existence of the flame

---

[3]The calculation shown in Fig. 3.9 required approximately 3×10^7 timesteps and two wall-clock months on a pair of Intel Xeon E5-2670 v2 processors.
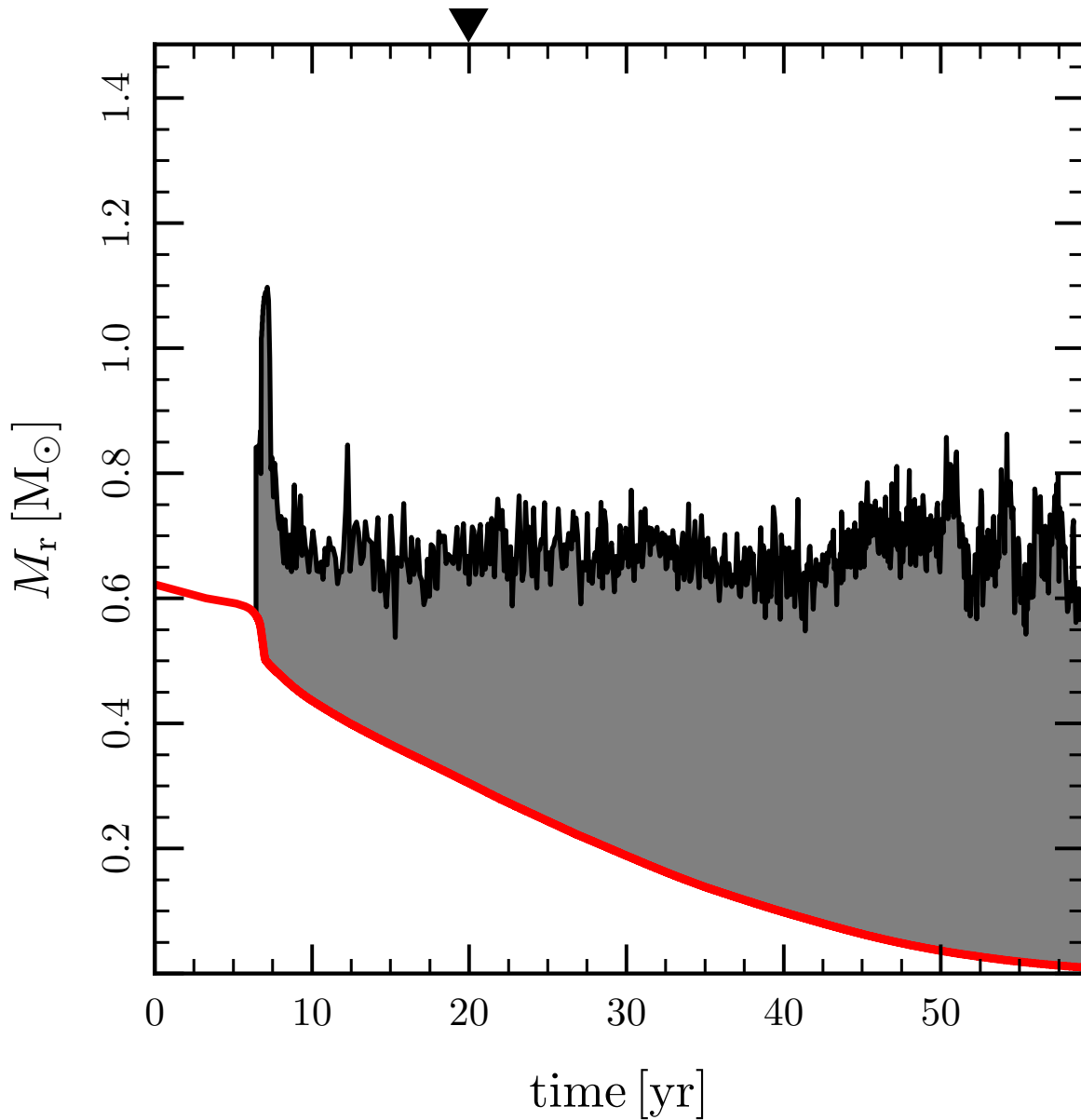
Figure 3.9: The propagation of the neon flame in model M15 with no convective boundary mixing. The x-axis shows time, as measured from the beginning of neon burning. Note that the neon flame propigates to the center ~ 100 times more quickly than the carbon flame shown in Fig. 3.3. The y-axis shows the Lagrangian mass coordinate. The extent of the convective region associated with the flame is shaded. The outer extent of the convection zone varies significantly from timestep-to-timestep, so for visual clarity, this has been smoothed. The location of maximum nuclear energy release, a proxy for the location of the flame, is indicated by the red thick line at the bottom of this region. The triangle at the top of the plot marks the point at which the flame structure is shown in Fig. 3.10.
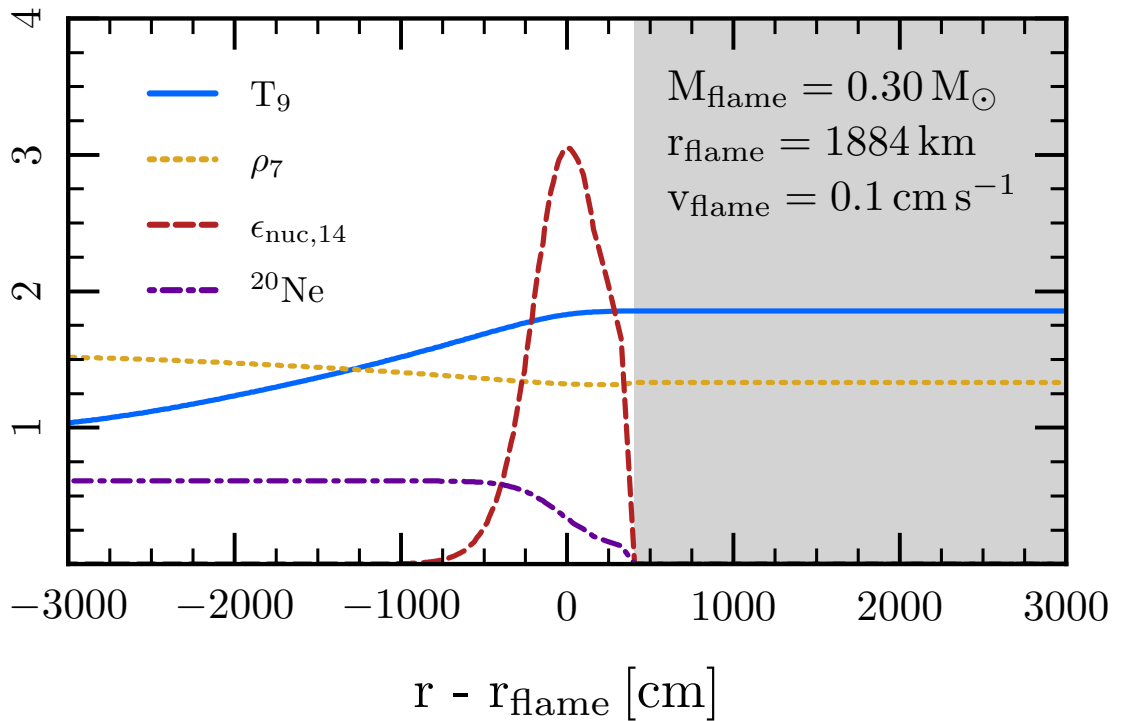
Figure 3.10: Structure of a neon-burning flame. The shaded grey region marks the convection zone. The temperature ($T/10^9$ K), density ($\rho/10^7$ g cm^{-3}), energy generation rate ($\epsilon_{nuc}/10^{14}$ erg s^{-1} g^{-1}), and ^{20}Ne mass fraction are shown as function of radius. This illustrates that the thickness of the flame is $\sim 10^3$ cm which makes directly resolving the propagation of the neon-burning flame computationally costly. This profile from our MESA calculation is from the time marked by the black triangle in Fig. 3.9.

does not modify the observational properties of the WD merger remnant. The latter are instead governed by the heat released during the merger.

The outer envelope of the remnant responds to the energy deposited during the merger and begins to radiate away this energy. Fig. 3.11 shows the location of model M15 in the HR diagram during our MESA calculation, over the phase in which the carbon flame is propagating to the center. The remnant radiates at the Eddington luminosity for a solar mass object with an effective temperature $\approx 4000 - 5000\,\mathrm{K}$ for $\approx 5\,\mathrm{kyr}$, and then evolves to the blue, spending $\approx 10\,\mathrm{kyr}$ with $T_{\mathrm{eff}} \gtrsim 10^5\,\mathrm{K}$.

The track shown in Fig. 3.11 for the remnant resembles that of a star evolving from the AGB to the planetary nebula stage (e.g., Kwok 1993). In some ways, the merger has formed an object similar to the core of an intermediate mass star. However, the lack of hydrogen- and helium-burning shells means that thermal pulses will be absent. Near the end of the AGB phase, stars are seen to exhibit extreme ($\dot{M} \gtrsim 10^4\,\mathrm{M_\odot\,yr^{-1}}$) mass loss rates (e.g., van Loon et al. 1999). The track shown in Fig. 3.11 does not include the effects of mass loss. The inclusion of mass loss has two primary effects: (1) it alters the observational properties of the remnant, likely obscuring it in an dusty wind and (2) it reduces the mass of the remnant, potentially influencing the final outcome. In particular, with $\dot{M} \approx 10^{-4}\,\mathrm{M_\odot\,yr^{-1}}$, over the duration of the cool giant phase, the remnant would shed $\Delta M \approx 0.1\,\mathrm{M_\odot}$, sufficient to change a model with total mass $\approx 1.5\,\mathrm{M_\odot}$ from super-to-sub Chandrasekhar (see Section 3.4). However, we note that our model M16 displays similar evolution as M15, but with its higher total mass $\approx 1.6\,\mathrm{M_\odot}$, it can shed $\Delta M \approx 0.1\,\mathrm{M_\odot}$ and remain super-Chandrasekhar.

In Fig. 3.11 the lowest effective temperature ($T_{\mathrm{eff}} \approx 4000 - 5000\,\mathrm{K}$) reflects the steep decline in the opacities at these temperatures—see Section 3.2.3 and Appendix 3.B. The R Coronae Borealis stars are giants with similar effective temperatures ($4000 - 7000\,\mathrm{K}$) with He-dominated, C-enhanced atmospheres (e.g., Clayton 1996). These objects exhibit high-amplitude dimming events ($\approx 10\,\mathrm{mag}$ in the optical) which are understood to be the result of dust formation events outside the photosphere. It is possible that the super-Chandrasekhar WD merger remnants would exhibit similar variability.

Given their cool photospheres between points 1 and 2 in Fig. 3.11 and their almost pure carbon and oxygen composition, it seems likely that these remnants would form copious amounts of dust. The mass loss rate is then set by the dust formation rate near the stellar photosphere. Reprocessing by this dust makes obscured objects bright infrared (IR) sources, though because the remnants are hydrogen-free, such an object should not exhibit any OH-maser emission, as seen in the OH/IR stars (Wilson & Barrett 1968). The properties of the dust also depends on the C/O ratio and as such, the remnants could manifest either as C-rich or O-rich objects. We expect that the surface C/O ratio will be set largely by the C/O ratio of the disrupted WD. This quantity is likely not universal—depending on the mass of the disrupted WD, for example—and from a modeling perspective, this depends on still-uncertain input physics such as the $^{12}\mathrm{C}(\alpha, \gamma)^{16}\mathrm{O}$ reaction rate (e.g., Fields et al. 2016).

If these objects are obscured by a dusty wind, then they may appear in the same luminosity-color cuts used to identify extreme AGB stars (see e.g., Thompson et al. 2009; approximately 9 of their sources are coincident with the luminosities of our objects). In the
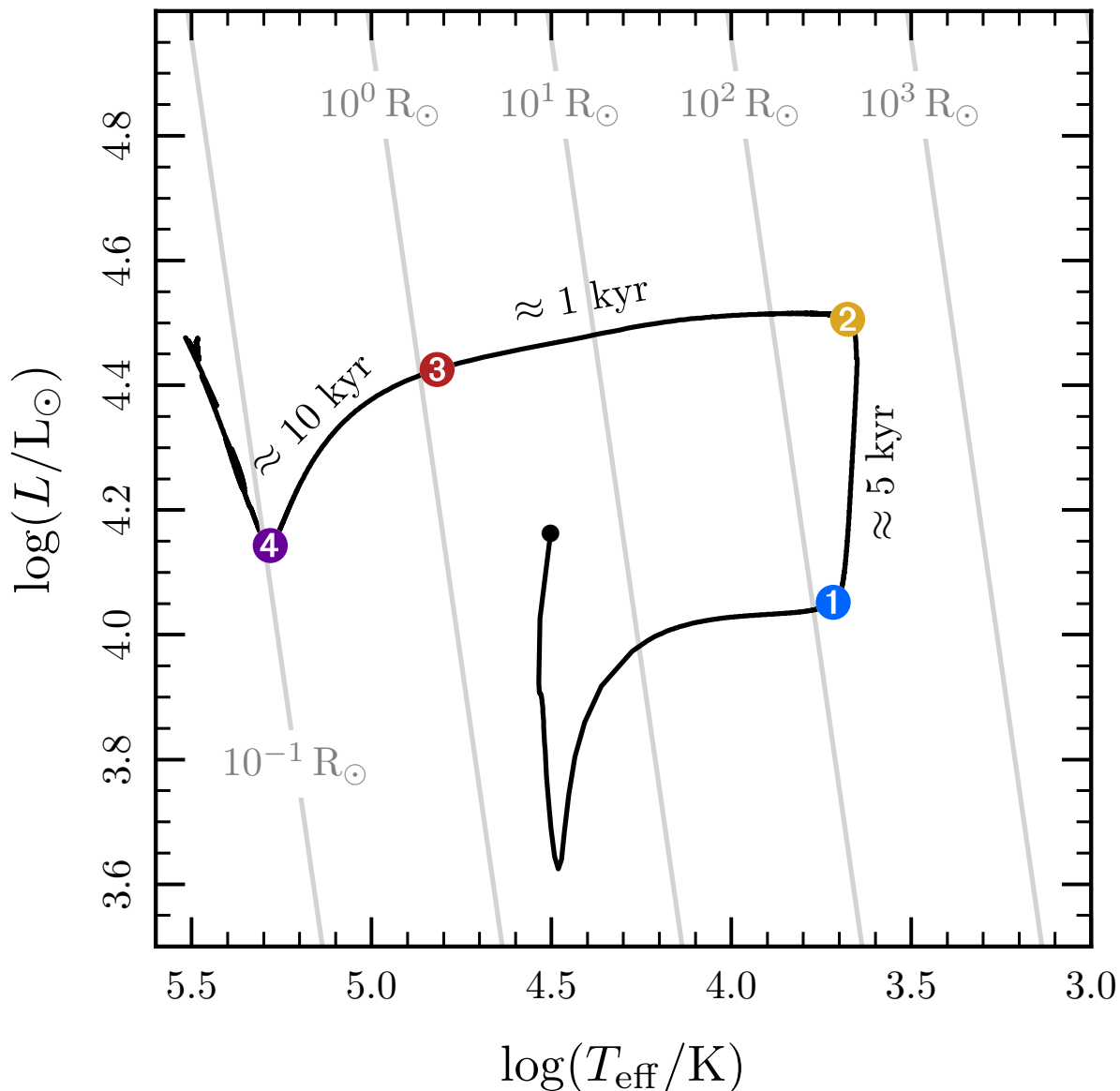
Figure 3.11: Evolution of model M15 in the HR diagram. Grey lines of constant radius are shown in the background. The numbered circles each correspond to one of the times indicated in Fig. 3.3. The approximate elapsed time between adjacent circles is indicated. The KH contraction phase (Section 3.4) occurs after point 4, with the Ne flame phase (Section 3.5.1) corresponding to the end of the track. The total duration of evolution is ≈ 25 kyr. As we discuss in Section 3.6, the presence of a dusty wind around these objects may modify their appearance.

wind, $\tau(r) \approx \dot{M}\kappa/(4\pi rv)$, where τ is the optical depth, κ is the opacity, and v is the wind velocity. Since $\tau(r_{\mathrm{ph}}) \approx 1$,

$$r_{\mathrm{ph}} \sim \frac{\dot{M}\kappa}{4\pi v} \sim 1.5 \times 10^{15}\,\mathrm{cm} \left(\frac{\dot{M}}{10^{-4}\,\mathrm{M_\odot\,yr^{-1}}}\right) \left(\frac{\kappa}{10\,\mathrm{cm^2\,g^{-1}}}\right) \left(\frac{v}{30\,\mathrm{km\,s^{-1}}}\right)^{-1} \quad . \tag{3.1}$$

Given the luminosity of our sources, this radius would imply an effective temperature

$$T_{\mathrm{eff}} = 500\,\mathrm{K} \left(\frac{L}{10^{4.5}\mathrm{L_\odot}}\right)^{1/4} \left(\frac{r_{\mathrm{ph}}}{100\,\mathrm{AU}}\right)^{-1/2} \tag{3.2}$$

which is consistent with extreme AGB stars.

We can make a rough estimate of the number of merger remnants in this cool giant or self-obscured phase at a given time. The specific rate of super-Chandrasekhar double WD mergers estimated by Badenes & Maoz (2012) is $1.0^{+1.6}_{-0.6} \times 10^{-14}\,\mathrm{yr^{-1}\,M_\odot^{-1}}$. This implies that the number of sources active in a galaxy is

$$N_{\mathrm{active}} \approx 1 \times \left(\frac{\mathrm{merger\ rate}}{10^{-14}\,\mathrm{yr^{-1}\,M_\odot^{-1}}}\right) \left(\frac{\mathrm{stellar\ mass}}{10^{10}\,\mathrm{M_\odot}}\right) \left(\frac{\mathrm{lifetime}}{10^4\,\mathrm{yr}}\right) \tag{3.3}$$

meaning that roughly one of these remnants will be currently active in M33 and 20 in M31.[4] However, we have no reason to expect sub- and super-Chandrasekhar models to be observationally distinguishable during this phase.[5] Thus, the number of objects in this phase may be a factor of few higher, since sub-Chandrasekhar total mass mergers include lower mass CO WDs closer to the peak of the individual WD mass distribution (Kepler et al. 2007).

Around point 2, in Fig. 3.11, we expect the extreme mass loss to end and the dusty envelope to detach from the photosphere. The evolution from point 2 to point 3, taking $\approx 1\,\mathrm{kyr}$, is similar to a proto-planetary nebula phase (e.g., Kwok 1993). This transitions into a planetary nebula phase as the temperature of the central object rises to $T_{\mathrm{eff}} \gtrsim 10^5\,\mathrm{K}$, making it a bright extreme ultraviolet / soft X-ray source. This emission will begin to ionize material shed during the earlier phase, forming a planetary nebula with composition dominated by C and O.

Depending on the amount of dust formed, the remnant could continue to remain obscured through these later phases. The dust surface density is roughly

$$\Sigma_{\mathrm{d}} \sim 10^{-5}\,\mathrm{g\,cm^{-2}} \left(\frac{f_{\mathrm{dust}}}{1.0}\right) \left(\frac{M_{\mathrm{wind}}}{0.1\,\mathrm{M_\odot}}\right) \left(\frac{v}{30\,\mathrm{km\,s^{-1}}}\right)^{-2} \left(\frac{\Delta t}{10^4\,\mathrm{yr}}\right)^{-2} \tag{3.4}$$

where M_{wind} is the total amount of material ejected in the wind and f_{dust} is the fraction of this material that forms dust. Approximating the cross-section for EUV photons ($\lambda \approx 10-$

---

[4]The stellar mass of M33 is $\mathrm{M_\star} \approx 3 - 6 \times 10^9\,\mathrm{M_\odot}$ (Corbelli 2003); the stellar mass of M31 is $\mathrm{M_\star} \approx 10 - 15 \times 10^{10}\,\mathrm{M_\odot}$ (Tamm et al. 2012).

[5]A lower total mass merger will not yet have ignited carbon, but recall that the luminous giant phase is powered by thermal energy release during the merger, not carbon burning.

100 nm) as geometric, the dust opacity for a grain size a is $\kappa_{\mathrm{dust}} \approx 10^5 \, \mathrm{cm}^2 \, \mathrm{g}^{-1} \, (a/10^{-5} \, \mathrm{cm})^{-1}$, which is roughly appropriate when $a > \lambda$. Given Eq. (3.4), the dust optical depth could be ~ 1 even $10^4 \, \mathrm{yr}$ after merger. However, the hard radiation from the central object may also destroy some of the dust; the efficiency of this process will depend on both the composition and grain size (e.g., Waxman & Draine 2000). Whether or not they remain completely obscured, it seems likely that these objects would continue to display significant infrared excesses.

During the Ne flame and later phases of evolution (see Sections 3.4 and 3.5), the remnant remains in the vicinity of point 4 (in Fig. 3.11). This evolution is relatively rapid ($\approx 5 \, \mathrm{kyr}$) and so the object does not yet begin to move down the WD cooling track if the mass remains above the Chandrasekhar mass. However, if the object has shed enough mass that it is below the mass that will lead to neon ignition, then it will begin to cool. Continuing the analogy to existing systems, these objects may then resemble helium-free versions of GW Vir. Such objects would likely also exhibit g-mode pulsations, as these are driven by ionization of carbon and oxygen (Quirion et al. 2007). As the objects continue to cool, merger remnants that remain below the Chandrasekhar mass may later appear as carbon (DQ) WDs (Dufour et al. 2007, 2008).

3.7 Conclusions

We have presented stellar evolution calculations that follow the evolution of the remnant of the merger of two CO WDs. We focused on systems with a total mass in excess of the Chandrasekhar mass; our fiducial system is the merger of an $0.6 \, \mathrm{M}_\odot$ WD and a $0.9 \, \mathrm{M}_\odot$ WD (model M15 in Table 3.1), but we find similar results for a system with a total mass of $1.6 \, \mathrm{M}_\odot$ (model M16). Our calculations use the results of SPH simulations of the merger (Dan et al. 2011; Raskin et al. 2014) to set the initial properties of the remnant. Its post-merger viscous evolution was then followed as in Schwab et al. (2012) and the results of these simulations form the initial conditions for our MESA calculations. Thus, our results do not apply to the case in which a merger may lead to the detonation of the primary WD, as may occur for particularly massive CO+CO WD mergers (Pakmor et al. 2012c). The flowchart shown in Fig. 3.12 summarizes the potential final fates of these systems, indicating relevant uncertainties in our models.

Our study has focused on two major questions. First, what is the post-merger observational appearance of super-Chandrasekhar WD merger remnants? Second, what is the fate of such objects? The viscous evolution converts the thick, rotationally-supported disc into a spherical, thermally-supported envelope. Our calculations self-consistently include this material, as opposed to approximating its effects by imposing an Eddington-limited accretion rate at the outer boundary. We can thus better address the emission from WD merger remnants. We find a post-merger phase, powered by thermal energy deposited during the merger, in which the remnant manifests as an Eddington-luminosity ($L \sim 3 \times 10^4 \, \mathrm{L}_\odot$) source for $\sim 10^4 \, \mathrm{yr}$. This is consistent, in luminosity and lifetime, with the signature suggested by
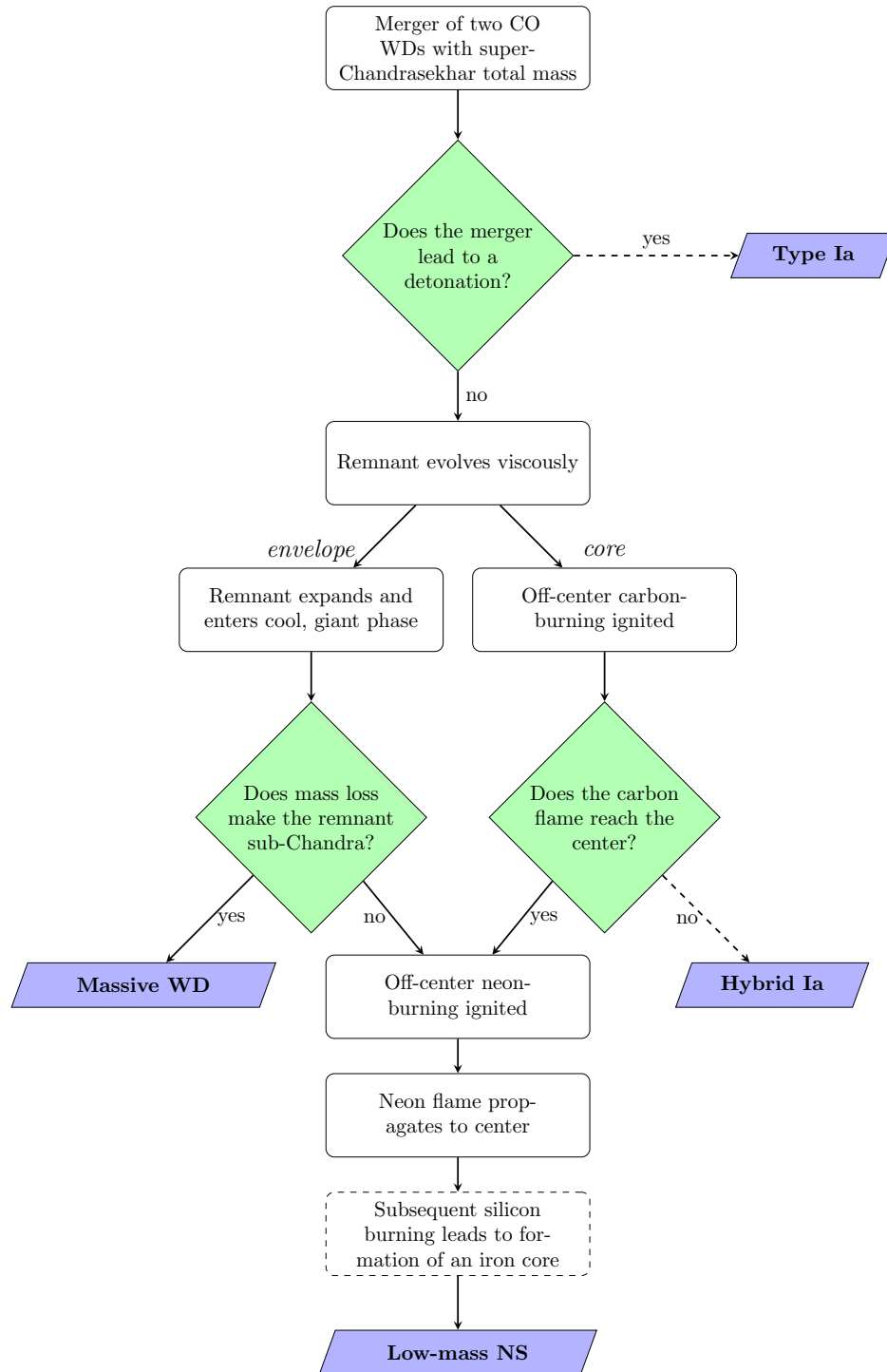
Figure 3.12: A summary of the final fates of super-Chandrasekhar WD merger remnants. Dashed lines indicate phases not explored in this work. Detonations of CO WDs during merger likely requires total masses $\geq 2.0\,\mathrm{M_\odot}$ (Dan et al. 2014; Sato et al. 2015), so this is a rare channel. Hybrid Ias are unlikely according to Lecoanet et al. (2016). Thus, most super-Chandrasekhar mergers will produce a single massive WD or a low mass NS, with the relative rates depending on the uncertain role of mass loss.

Shen et al. (2012) who also constructed related stellar evolution models. We improve upon these models by drawing our initial conditions from multi-dimensional viscous simulations and by incorporating more realistic opacities.

The effective temperature in our models during the giant phase is $\approx 4000 - 5000$ K. However, the mass loss properties of these carbon and oxygen dominated envelopes are uncertain. It seems likely that a dusty wind could develop, leading these sources to be self-obscured and to appear similar to extreme AGB stars. The mass loss during the post-merger phase can also influence the later stages of evolution, leaving an initially super-Chandrasekhar remnant with a sub-Chandrasekhar mass (see Figs. 3.8 and 3.12). Based on the observed WD merger rates, we estimate that tens (few) of remnants are presently in this giant phase in the nearby galaxies M31 (M33). As the giant phase ends, the central source evolves, likely producing proto-planetary nebula and planetary nebula phases in which the surrounding nebula would lack hydrogen or helium. These sources might remain dust-obscured throughout, depending on the amount of dust produced and its properties.

In the massive mergers we consider, off-center carbon fusion is robustly ignited within the remnant. Most of the fusion energy released is lost to neutrinos, and that which is not, fails to reach the surface in the evolutionary time-scale. Thus, the surface emission is powered solely by the thermal energy release during the merger. As found previously (Saio & Nomoto 1985; Nomoto & Iben 1985; Saio & Nomoto 1998), the carbon-burning quiescently propagates inward, converting the WD to an oxygen-neon composition. However, we follow the evolution of these remnants for longer than previous calculations and demonstrate that when carbon-burning reaches the center it lifts the degeneracy of the remnant.

As the non-degenerate oxygen-neon core undergoes a phase of neutrino-cooled KH contraction, the remnant can ignite off-center neon burning. There is a critical mass for a "hot" (i.e., non-degenerate) ONe core, $M_{\rm Ne,hot} \approx 1.35 \, {\rm M_\odot}$, above which off-center neon ignition will occur (Nomoto 1984; see also Appendix 3.C); this is set by the rate of neon fusion and the rate of thermal neutrino losses. There is also a critical mass for electron-capture-initiated central ignition in a "cold" (i.e., degenerate) ONe core, $M_{\rm Ne,cold} \approx 1.38 \, {\rm M_\odot}$; this is set by the electron Fermi energy needed to favor electron captures on ^{20}Ne (Schwab et al. 2015). The off-center carbon burning ignited in the merger remnant leads to the production of a "hot" ONe core. Because $M_{\rm Ne,hot} < M_{\rm Ne,cold}$, we therefore conclude that lower mass merger remnants ($M < M_{\rm Ne,hot}$) will form massive ONe WDs which will then quiescently cool, while higher mass objects ($M > M_{\rm Ne,hot}$) will be processed to compositions beyond neon. Thus, contrary to standard models, it is difficult to produce an *oxygen-neon* core with a sufficient mass to undergo accretion-induced collapse in a WD merger. We emphasize that our conclusions apply to WD mergers and do not affect standard single degenerate AIC scenarios. In the single degenerate case, an ONe core below $M_{\rm Ne,hot}$ forms in an intermediate mass star and cools. Subsequently, it accretes material and grows to a mass in excess of $M_{\rm Ne,cold}$ at which point it collapses.

One of the major uncertainties in our calculation is the extent of mass loss during the $\sim 10^4$ yr post-merger thermal evolution. In addition to our fiducial model, we also evolved a remnant with a total mass $\approx 1.6 \, {\rm M_\odot}$. Both models had similar initial profiles (Fig. 3.2) and

underwent a qualitatively similar course of evolution. We suspect that yet higher masses would behave similarly, up to the point where carbon detonations are likely to occur during the merger. The results of both Dan et al. (2014) and Sato et al. (2015) suggest that the threshold for carbon detonations is around a total mass $\gtrsim 2\,M_\odot$ for CO+CO WD mergers. Since this threshold is significantly super-Chandrasekhar, this suggests that even in the presence of significant mass loss ($\approx 0.2\,M_\odot$) both the massive WD and the low mass NS fates in Fig. 3.12 are realized. However, the exact mapping of merger masses to outcome is uncertain.

If the remnant mass remains super-Chandrasekhar and experiences off-center neon ignition, we expect that it will ultimately collapse to form a neutron star. The neon flame propagates to the center converting the remnant to silicon-group elements (Figs. 3.9 and 3.10). Computational limitations prevent us from continuing our calculations beyond the point at which the neon flame reaches the center. However, we then argue, based on the work of Jones et al. (2013, 2014) and Woosley & Heger (2015) that Si-burning leads to the formation of an iron core, which will then collapse. Future work in this area will be important in understanding the role of violent Si-burning and examining the structure of the remnant at the time of core infall. The low mass core, with steep density gradients near its edge, means that this progenitor will likely produce a neutrino-driven explosion a short time after core bounce, as is seen in core-collapse calculations involving ONe cores (Kitaura et al. 2006; Janka et al. 2008). A shorter time between core bounce and explosion suggests that there is less time for instabilities to grow, leading to less asymmetry and lower neutron star kicks (e.g., Wongwathanarat et al. 2013).

Our calculations assume that the bounding convection zone does not induce significant mixing in either the carbon flame or the neon flame. The results of Lecoanet et al. (2016), which we invoked to justify this assumption in the case of the carbon flame do not strictly apply to the neon flame. The neon flame self-crossing time (which is equivalent to the burning time-scale) is much shorter, $\sim 10^4\,$s, on the order of the convective turnover time in the zone behind the flame. This invalidates the assumption that the flame is effectively stationary over a convective turnover time that was made in the calculations of Lecoanet et al. (2016). Naïvely, however, it seems likely that fewer convective turnover times make it even less likely that convection will disrupt the flame, as convective perturbations will not be able to accumulate because the flame moves away.

Because the duration of the giant phase is shorter than the time for the carbon flame to reach the center, our results indicate that at the time of neutron star formation the remnant is likely in a compact configuration (Fig. 3.11), implying minimal signatures due to interaction or shock breakout. At late times after the SN explosion ($\sim 10\,$yr), the ejecta from the explosion (with $v \sim 10^4\,\mathrm{km\,s^{-1}}$) will catch up to the wind generated during the giant phase (with $v \sim 10\,\mathrm{km\,s^{-1}}$); however the low densities at this time makes it unlikely that this interaction will be radiatively efficient.

Future work should continue to explore the variety of final outcomes shown in Fig. 3.12 and work to clarify further differences between neutron stars formed via single-degenerate accretion-induced collapse and those formed in WD mergers.

Acknowledgments

3.A   Importing Models into MESA

Mapping results from one simulation code into another can be a difficult process. Differences in the input microphysics, the equations being solved, and the numerical solution techniques mean that output of one code is rarely immediately suitable for input into another code. Each approach is problem-specific: one must identify the important parts of the solution and design a mapping that preserves them. Our goal is to use the output of a 2D Eulerian code (ZEUS-MP2, which solves the viscous fluid equations) as input to a 1D Lagrangian code (MESA, which solves the stellar structure equations).

At the end of our hydrodynamic simulations of the viscous phase of evolution, most of the merger remnant is slowly rotating and in hydrostatic equilibrium and thus quite spherical (e.g., fig. 5 in Schwab et al. 2012). We make the choice to study the non-rotating case and thus do not initialize or evolve a rotational velocity variable. Under the assumption of spherical hydrostatic equilibrium, the complete structure of an object can be specified by its specific entropy, $s(M_r)$, and composition, $X_i(M_r)$, as a function of Lagrangian mass, M_r. Therefore, the first step is to spherically average our multi-D simulations and calculate these quantities.

We perform volume averages[6],

$$\rho(r) = \frac{1}{2} \int_0^\pi d\theta \sin(\theta) \rho(r, \theta) \tag{3.5}$$

$$e(r) = \frac{1}{2} \int_0^\pi d\theta \sin(\theta) e(r, \theta) \tag{3.6}$$

$$\rho(r) X_i(r) = \frac{1}{2} \int_0^\pi d\theta \sin(\theta) \rho(r, \theta) X_i(r, \theta) \tag{3.7}$$

so that the appropriate quantities (e.g. mass, energy) are conserved. Assuming full ionization, it is simple to calculate $\bar{A}$ (the average mass per ion) and $\bar{Z}$ (the average charge per ion) from the mass fractions X_i. Given ρ, e, $\bar{A}$, and $\bar{Z}$, we use the Helmholtz (Timmes & Swesty 2000) equation of state, which is used by both our ZEUS-MP2 simulations and MESA (for $\rho \gtrsim 3 \times 10^2\,\mathrm{g\,cm^{-3}}$), to calculate the specific entropy $s(r)$. The Lagrangian mass is

$$M_r = \int_0^r dr' 4\pi r'^2 \rho(r') \tag{3.8}$$

and we record a 1D approximation to our 2D simulation consisting of the values of M_r, $s(r)$, and $X_i(r)$ for each radial grid point in the computational domain.

We want to create a MESA model which matches this profile. Instead of trying to create a MESA model file and then reading it in, we begin with a model unlike what we want, but slowly reshape it into our desired profile. The steps in this procedure were arrived at by trial-and-error. There is nothing inherently correct about many of the particulars of this approach; we demonstrate at the end that this stellar engineering gives us the desired result.

First, we create a pre-main sequence model with the mass of the remnant. We evolve this model, with nuclear reactions turned off, until the central density is equal to $10^3\,\mathrm{g\,cm^{-3}}$. Then we resume the evolution, using the built-in capability of MESA to relax our model to a specified composition. With the composition relaxation complete, we evolve this model, with nuclear reactions and mixing turned off, until the central density reaches $10^5\,\mathrm{g\,cm^{-3}}$.

Again, we resume the evolution, this time making use of a custom routine in `run_star_extras.f` which relaxes the model to the desired thermodynamic profile. We take advantage of the `other_energy` routine, which allows us to add an additional term to the energy equation, and set

$$Q_{\mathrm{extra,k}} = -\frac{c_{v,k} T_k}{t_o} \alpha_k \tag{3.9}$$

where c_v is the specific heat at constant volume and T is the temperature. The subscripts k indicate that these quantities are evaluated on a per-cell basis. The values of α_k were chosen to drive the model towards the desired profile. We chose a heating/cooling time-scale, t_0, which is short compared to the thermal time of the star and is comparable to the total duration of our viscous evolution calculations, typically $t_0 = 10^3\,\mathrm{s}$.

---

[6]We write these averages as integrals, but because we are operating on the output of a grid-based code, these integral quantities represent the appropriate discretized sums.

To determine α_k, we read in the spherically-averaged entropy profile from ZEUS and use built-in MESA interpolation routines to sample it such that we have a target entropy function, $\tilde{s}(q)$, where $q = M_r/M_{\text{tot}}$. In the inner part of the model, which corresponds to the cold, undisturbed primary WD, we will ignore the entropy profile and instead relax the profile to an isothermal one. This approach requires three additional parameters: the isothermal temperature, $\tilde{T}$, the region which should be isothermal, $\tilde{q}$, and the width of a region in which we blend between these, Δ. At each point in the MESA model, we evaluate

$$\delta_1 = 1 - \tilde{s}(q_k)/s_k \tag{3.10}$$

$$\delta_2 = 1 - \tilde{T}/T_k \tag{3.11}$$

$$\delta_k = f_k\delta_1 + (1 - f_k)\delta_2 \tag{3.12}$$

where

$$f_k = \frac{1}{2}\left[\tanh\left(\frac{q_k - \tilde{q}}{\Delta}\right) + 1\right] \tag{3.13}$$

From these quantities, we locally calculate

$$\alpha_k = \delta_k \tanh(|\delta_k|) \tag{3.14}$$

and in order to check whether the profile matches, calculate a global quantity

$$\epsilon = \sum_{k=1}^{n_z} |\delta_k| dq_k \tag{3.15}$$

We consider our relaxation complete when $\epsilon < 3 \times 10^{-4}$. Empirically, this approach works quickly and robustly.

Fig. 3.13 compares the 1D-averaged ZEUS-MP2 profiles and the initial MESA profiles for our model M15. The density, entropy, and temperature are in good agreement for $0.5 \lesssim q \lesssim 0.9$. This is the critical region, because it is where carbon ignition will occur and where the thermal energy that will power the giant phase is located. In the deep interior ($q \lesssim 0.5$), our assumed isothermality means the temperature and entropy of the material has been altered, but because the material is degenerate, this has little effect on the structure (i.e., the density agrees well). In the outer regions ($q \gtrsim 0.9$), differences are introduced by the fact that the material was not spherical, but is now assumed to be.

3.B Opacities

As discussed in Section 3.2.3, we generate and use a set of low temperature opacities for material with a carbon-oxygen composition. The code calculates Rosseland mean opacities considering the bound-bound, bound-free, free-free, and electron-scattering contributions. It assumes local thermodynamic equilibrium and all photoionization cross-sections are assumed to be hydrogenic. The input atomic data is that compiled as part of CMFGEN (Hillier 2011).
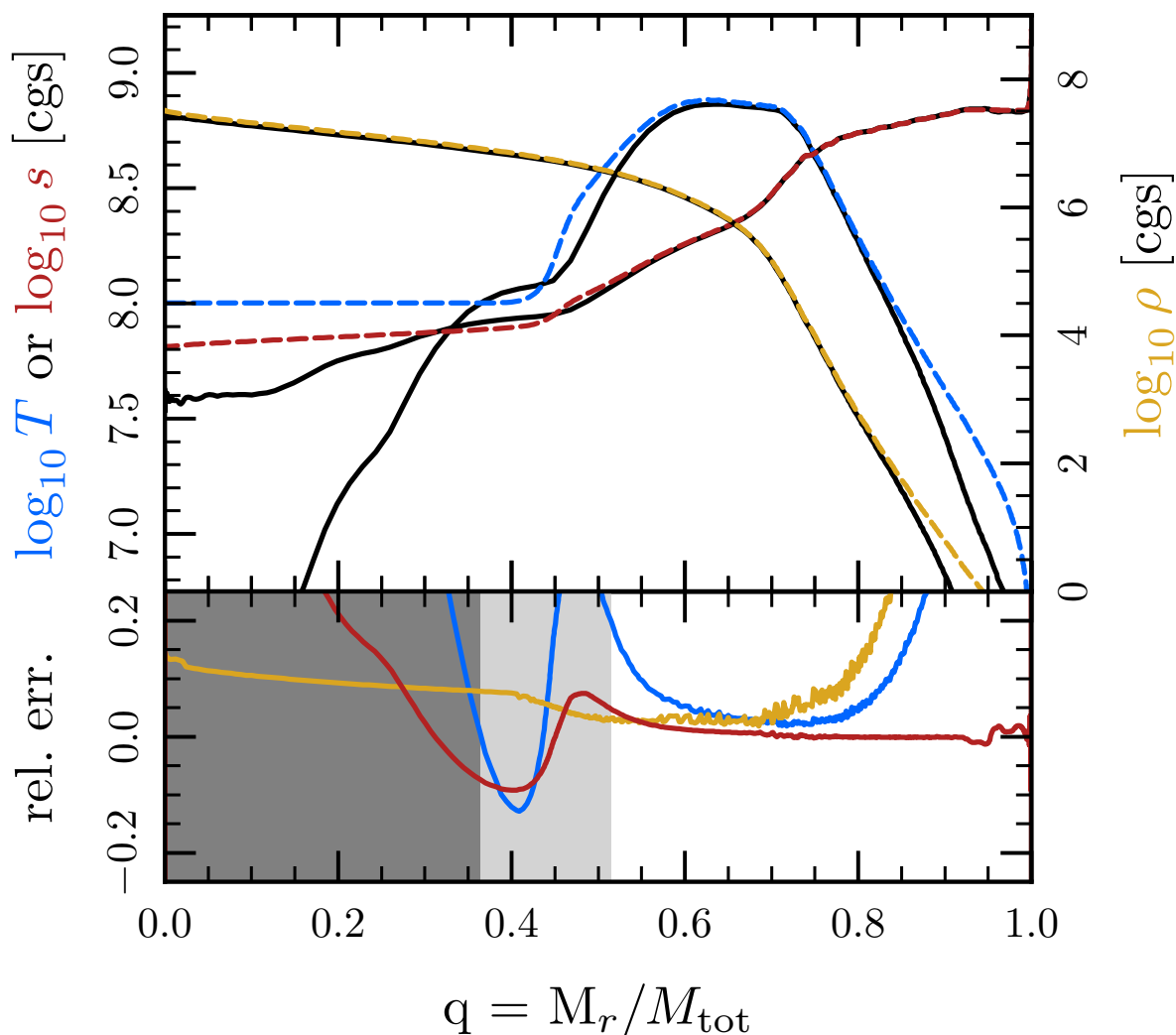
Figure 3.13: A comparison of the 1D-averaged ZEUS-MP2 model and the initial MESA model for our model M15. The top panel overplots the 1D-averaged ZEUS-MP2 models (black solid lines) and the initial MESA model (colored dashed lines). Shown are the temperature (blue; in K), specific entropy (red; in ergs s^{-1} g^{-1}), and density (yellow; in g cm^{-3}). The bottom panel shows the relative error in the three thermodynamic quantities. The dark shaded region indicates where the model was relaxed to an isothermal profile and the unshaded region shows where model was relaxed to a given entropy profile. The lighter shaded region shows the region which blends between the two.

We calculated and used a table for a single composition: $X_C = 0.49, X_O = 0.49, Z = 0.02$, where the relative metal abundances are drawn from Grevesse & Sauval (1998).

Fig. 3.14 shows examples of these opacities near conditions where they are applied in our models. We also show the higher temperature opacities that we use (OPAL Type 2) and the low temperature opacity that MESA would use if we did not override this choice via the `other_kap` routines. In our calculation, we blend the OPAL and Kasen opacities between $\log(T/K) = 4.1$ and 4.2. Fig. 3.15 shows the regions of temperature-density space covered by each of the opacity tables used in our MESA calculation. Additionally, the temperature-density profiles of model M15 at the same 4 times indicated in Fig. 3.11 are shown.

The OPAL Type 2 tables are compiled as functions of X, Y, and Z (H, He, and metals) as well as dXC and dXO (carbon and oxygen enhancements). At this time, low-temperature tables that incorporate the effects of C and O enhancement are not included in MESA. Therefore, when transitioning to low temperature opacities, MESA is also transitioning into a region in which the opacities are tabulated only as a function of X, Y, and Z. Thus, the compositions assumed in the calculation of the low and high temperature opacities are necessarily different. The carbon and oxygen composition of our WD model nominally corresponds to $Z = 1$, but since the assumed abundance distribution within Z is based on solar abundances, a choice of $Z = 1$ effectively assumes the material is dominated by N and Fe. One of the ways MESA can handle this is to assume a user-specified value of Z (`Zbase`), use the value of X, and put the rest of the abundance in Y. The line for the low temperature FA05 opacities in Fig. 3.14 makes this choice, assuming $Z = 0.02$ and thus $X = 0, Y = 0.98$. In addition to being physically inconsistent, these choices are numerically unsatisfactory because they result in large change in opacity over a small temperature range. Our use of the Kasen opacities avoids both of these issues.

The opacities used in the MESA calculations do not include the effects of molecules. If we were to include these effects, the opacity at $\log(T/K) \lesssim 3.5$ would be extremely sensitive to the C/O ratio of the material (e.g., Ferguson & Dotter 2008). This quantity was not, however, self-consistently determined in our initial WD models, which have equal mass fractions of ^{12}C and ^{16}O.

3.C Critical Masses

For a contracting stellar model of a given composition, there is a critical mass above which the temperature will become sufficiently high to ignite nuclear fusion. This is familiar for typical hydrogen-rich compositions, where this critical mass marks the boundary between a brown dwarf and a low mass star. Nomoto et al. (1984) calculated this critical mass for pure neon stars and used this simple model to gain insight into the evolution of contracting ONe cores. For pure neon models, the higher density and temperatures mean the KH contraction is driven by neutrino cooling from the interior as opposed to photon cooling from the surface. The density dependence of the neutrino cooling rates lead to the formation of an off-center
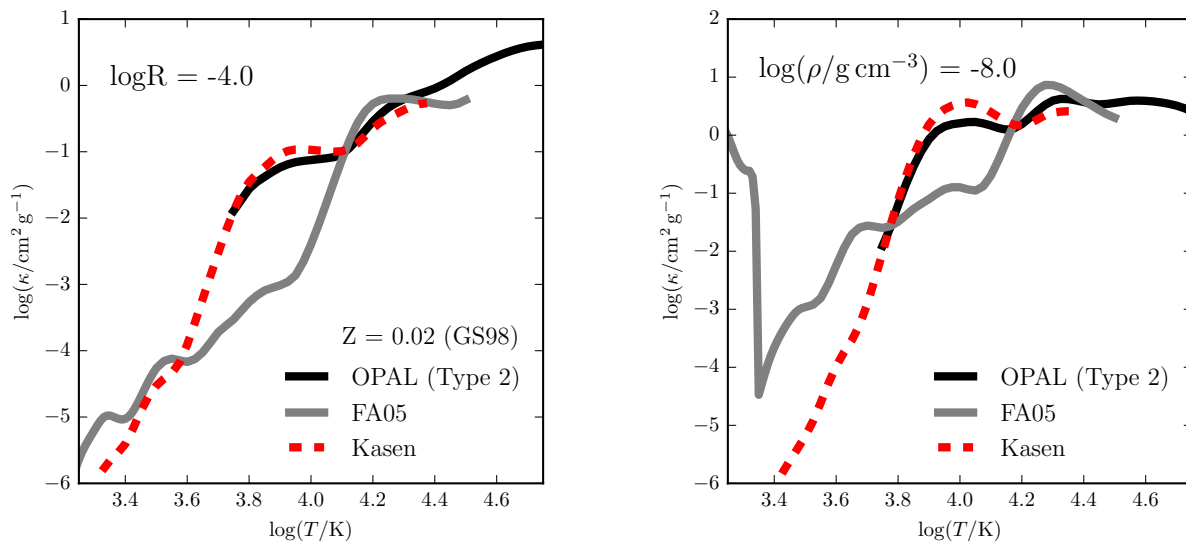
Figure 3.14: The solid black line (labeled OPAL Type 2) is the carbon- and oxygen-enhanced radiative opacities from Iglesias & Rogers (1996). The solid grey line (labeled FA05) is the low-temperature opacities from Ferguson et al. (2005). The difference between the OPAL and FA05 curves reflects a difference in assumed composition (see text for discussion). The calculations presented in this paper use low temperature opacities calculated with a code developed by one of us (Kasen; red dashed line). In all cases, the relative metal abundances are drawn from Grevesse & Sauval (1998). We blend the OPAL and Kasen opacities between $\log(T/\mathrm{K}) = 4.1$ and 4.2 (see Fig. 3.15). The left panel shows the opacity as a function of temperature at fixed R; the right panel shows it at fixed ρ.
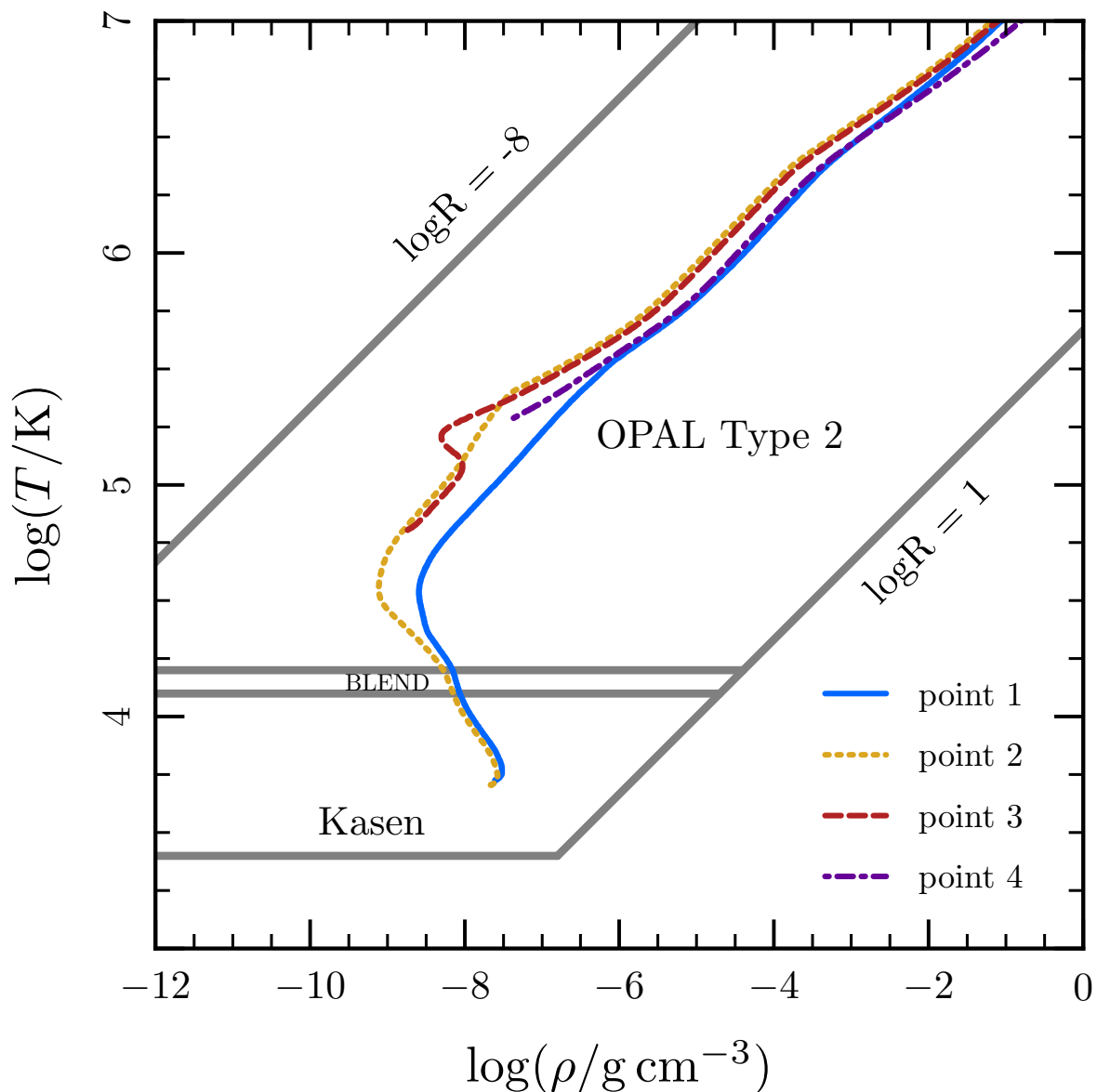
Figure 3.15: Coverage of temperature-density space by the opacity tables used in our MESA calculation. Solid grey lines show the boundaries of the two types of opacity tables: Opal Type 2 (Iglesias & Rogers 1996) and Kasen (Appendix 3.B). "Blend" indicates a smooth blend between these two values. Recall $\log R = \log \rho - 3 \log T + 18$ (cgs). The other lines show the temperature-density profiles of our model at the set of points also marked in Figs. 3.3, 3.5, and 3.11. We observe density inversions at both the Fe opacity bump ($\log(T/\mathrm{K}) \approx 5.3$) and in bumps associated with carbon and oxygen.

temperature peak, and when ignition does occur, it occurs off center.

In the spirit of Nomoto et al. (1984), we run a series of MESA models with masses in the range $1.30\,\mathrm{M_\odot}$ to $1.44\,\mathrm{M_\odot}$, using a stride of $0.005\,\mathrm{M_\odot}$, and with neon, oxygen-neon, oxygen, and silicon compositions. We create a pre-main sequence model with the desired mass and then relax the model to the desired composition. With nuclear reactions off, we evolve the model until $\log(\rho_c/\mathrm{g\,cm^{-3}}) = 4$. At this point, we load the model using the `approx21` nuclear network. We then evolve each model until either (1) the rate of energy release from nuclear reactions exceeds the rate of energy loss from neutrinos anywhere in the star, in which case we classify the model as having ignited or (2) the peak temperature reaches a maximum value and subsequently declines, in which case we know the model will never ignite.

In Fig. 3.16, we show the evolution of three of our pure neon models. We find the lowest mass model that ignites has $M = 1.35\,\mathrm{M_\odot}$. This is slightly lower than the value of $1.37\,\mathrm{M_\odot}$ reported by Nomoto et al. (1984). We speculate that this minor difference is due to differences in the input microphysics. Curves analogous to these, but for different masses, are shown as the grey lines in Figs. 3.7 and 3.8. The qualitative agreement between our remnant models and these simple homogeneous models demonstrates that the off-center neon ignition found in our WD remnants is a simple consequence of their mass.

The central conditions in each model at the time of ignition are shown in Fig. 3.17. We show 4 different compositions: pure $^{20}\mathrm{Ne}$, 50/50 $^{20}\mathrm{Ne}$-$^{16}\mathrm{O}$, pure $^{16}\mathrm{O}$, and pure $^{28}\mathrm{Si}$. The large, annotated dots indicate the lowest mass models in which off-center ignition was observed; these are the critical ignition masses quoted in the text.
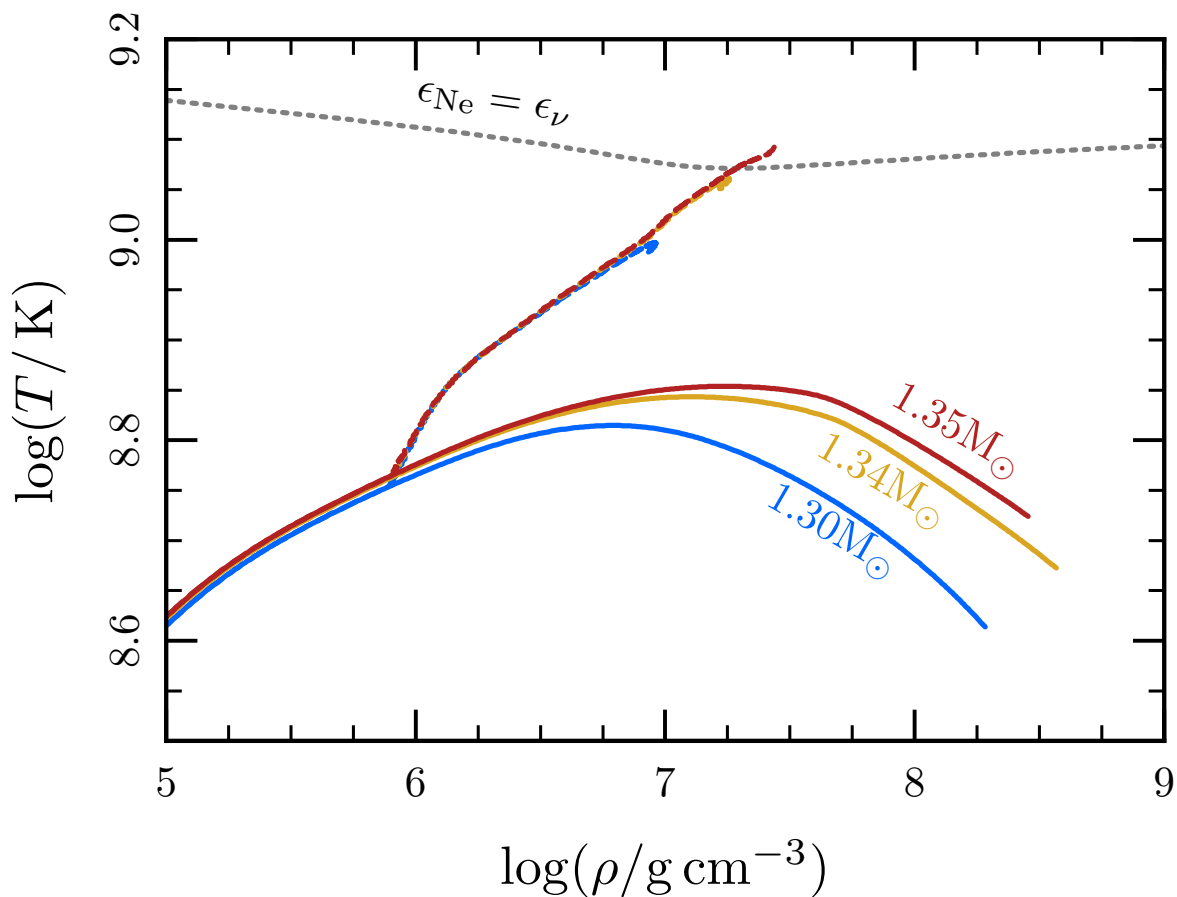
Figure 3.16: The evolution of temperature and density at the center (solid lines) and at the temperature peak (dashed lines) during the KH contraction of pure neon models. The dotted line shows approximately where the rate of energy release from neon burning is equal to the energy loss rate from thermal neutrinos. The assumed energy release rate for neon-burning was that given in Woosley et al. (2002). This figure is a reproduction of the results presented in fig. 1 of Nomoto et al. (1984) using MESA. We find a slightly lower critical mass for neon ignition of 1.35 $M_\odot$.
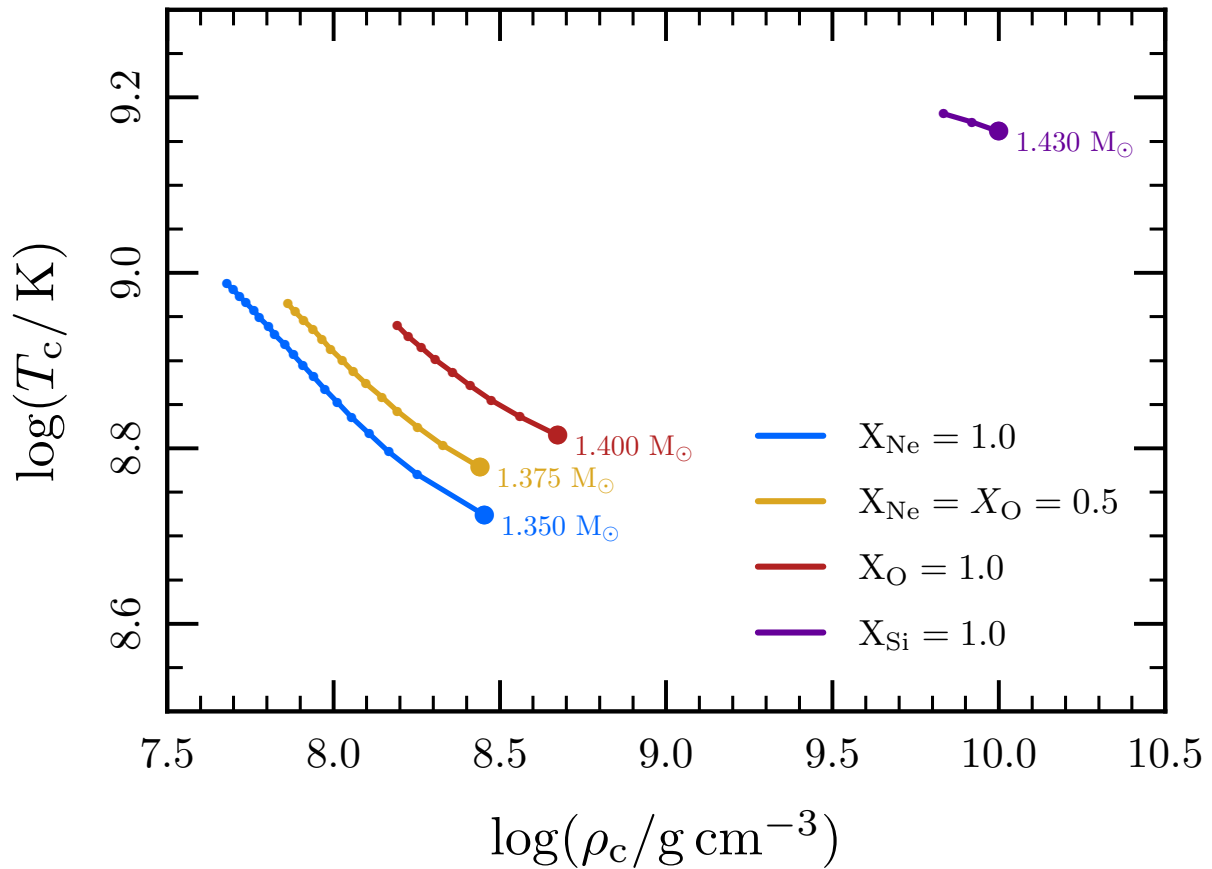
Figure 3.17: The central density and temperature of a given model at the time of off-center ignition, for different assumed compositions. Each model is indicated with a dot; the lowest mass model that ignited is indicated with a large dot and labeled by its mass. The dots are connected by lines to guide the eye.

Chapter 4

Thermal Runaway During the Evolution of ONeMg Cores towards Accretion-Induced Collapse

An earlier version of this chapter was previously published as Schwab, J. and Quataert, E. and Bildsten, L., MNRAS, 453, 1910.

Abstract

We study the evolution of degenerate electron cores primarily composed of the carbon burning products ^{16}O, ^{20}Ne, and ^{24}Mg (hereafter ONeMg cores) that are undergoing compression. Electron capture reactions on $A = 20$ and $A = 24$ isotopes reduce the electron fraction and heat the core. We develop and use a new capability of the Modules for Experiments in Stellar Astrophysics (MESA) stellar evolution code that provides a highly accurate implementation of these key reactions. These new accurate rates and the ability of MESA to perform extremely small spatial zoning demonstrates a thermal runaway in the core triggered by the temperature and density sensitivity of the ^{20}Ne electron capture reactions. Both analytics and numerics show that this thermal runaway does not trigger core convection, but rather leads to a centrally concentrated ($r <$ km) thermal runaway that will subsequently launch an oxygen deflagration wave from the center of the star. We use MESA to perform a parameter study that quantifies the influence of the ^{24}Mg mass fraction, the central temperature, the compression rate, and uncertainties in the electron capture reaction rates on the ONeMg core evolution. This allows us to establish a lower limit on the central density at which the oxygen deflagration wave initiates of $\rho_c \gtrsim 8.5 \times 10^9 \, \mathrm{g \, cm^{-3}}$. Based on previous work and order-of-magnitude calculations, we expect objects which ignite oxygen at or above these densities to collapse and form a neutron star. Calculations such as these are an important step in producing more realistic progenitor models for studies of the signature of accretion-induced collapse.

4.1   Introduction

In this paper, we study the evolution of degenerate electron cores primarily composed of the carbon burning products ^{16}O, ^{20}Ne, and ^{24}Mg which are undergoing compression. Such objects can arise in several contexts: the late stages of evolution for super asymptotic giant branch (SAGB) stars (e.g. Miyaji & Nomoto 1987; Ritossa et al. 1999; Takahashi et al. 2013; Jones et al. 2013), where the compression is caused by the deposition of material from exterior shell-burning; in a binary system with a massive ONeMg white dwarf (WD) (e.g. Nomoto & Kondo 1991), where the compression is caused by accretion from a non-degenerate companion; or as the remnant of a WD-WD merger, where the compression is caused by the cooling of the outer layers (e.g. Saio & Nomoto 1985).

As the core is compressed, the electron Fermi energy rises, eventually triggering exothermic electron capture reactions. Typically, exothermic captures on ^{20}Ne release enough energy to cause thermonuclear ignition of ^{16}O and formation of a deflagration. The final fate of the core (either explosion or collapse) is determined by a competition between the energy release from the outgoing oxygen deflagration and the energy losses and decline in the electron fraction due to electron captures on the post-deflagration material, which has burned to nuclear statistical equilibrium (NSE). The evolution of these cores has been a subject of considerable previous study (e.g. Miyaji et al. 1980; Nomoto 1984; Isern et al. 1991; Canal et al. 1992; Gutierrez et al. 1996; Gutiérrez et al. 2005; Jones et al. 2014).

However, we revisit this topic (i) to test the effect of using the state-of-the-art Modules for Experiments in Stellar Astrophysics (MESA) stellar evolution code (Paxton et al. 2011, 2013, 2015), (ii) to demonstrate the effects of using the latest nuclear reaction rates (Martínez-Pinedo et al. 2014), (iii) to perform a more detailed parameter study of the effects of a number of quantities, including the accretion rate $\dot{M}$, magnesium mass fraction X_{Mg}, and initial core temperature, T_c, and (iv) to provide analytic estimates of the evolution up-to and including the onset of the oxygen deflagration.

In the present paper, we follow the common treatment in the literature and parameterize the evolution of ONeMg WDs as they approach the Chandrasekhar mass via compression of the outer layers. In future work we will assess whether the revised evolutionary model of WD merger remnants proposed by Shen et al. (2012) and Schwab et al. (2012) modifies the likelihood of AIC in super-Chandrasekhar WD mergers. In § 4.2 we describe the treatment of weak reactions in the MESA code. In § 4.3 we provide analytic estimates relevant to the evolution of the core. In § 4.4 we discuss the inputs to our MESA calculations and in § 4.5 present the results of these numerical simulations. § 4.6 discusses the final fate of these cores. In § 4.7 we draw our conclusions and describe some important avenues for future work.

4.2   Weak Reactions in MESA

Weak reactions, specifically electron-capture and beta-decay, are central to the evolution of accreting degenerate ONeMg cores. The reduction in electron fraction (and corresponding

reduction in pressure) due to electron captures accelerates the contraction of the cores and the entropy generation from these electron captures can directly ignite thermonuclear reactions.

This study makes use of MESA, a state-of-the-art open source code for stellar evolution calculations (Paxton et al. 2011, 2013). In particular we use the capability to calculate weak reaction rates directly from nuclear level and transition data, which is documented in the upcoming MESA Instrument Paper III (Paxton et al. 2015). This section summarizes the input data to this capability. The precise expressions which are evaluated as part of MESA's on-the-fly weak reaction treatment are given in Appendix 4.A.

We restrict ourselves to considering only a small set of $A = 24$ isotopes (^{24}Mg, ^{24}Na, ^{24}Ne) and $A = 20$ isotopes (^{20}Ne, ^{20}F, ^{20}O). Over the range of thermodynamic conditions encountered during the evolution of ONeMg cores, roughly $9 \lesssim \log_{10} \rho \lesssim 10$ and $8 \lesssim \log_{10} T \lesssim 9$ (in cgs units), Takahara et al. (1989) identified the transitions that dominate the rate of each reaction. We consider only this limited set of transitions; they are listed in Table 4.1. We have taken the comparative half-lives of these reactions from the up-to-date information compiled in Martínez-Pinedo et al. (2014).

In order to more easily visualize the data in Table 4.1, we present energy level diagrams for the $A = 24$ (Fig. 4.1) and $A = 20$ (Fig. 4.2) nuclei. These figures are modeled after those found in Takahara et al. (1989). The level structure of these nuclei is drawn from recent compilations of nuclear data (Tilley et al. 1998; Firestone 2007b). We show all of the low-lying states that we consider, labeled with their J^π (spin$^{\text{parity}}$) values. The arrows indicate the limited set of transitions that we consider, which are only those which are "allowed" (Gamow-Teller: $J_i = J_j, J_j \pm 1$, $\pi_i \pi_j = 1$; excluding $J_i = J_f = 0$).

4.3 Analytic Estimates

Miyaji et al. (1980) provide a thorough discussion of the different phases of the evolution of an ONeMg core undergoing compression. In order to gain some insight into the relevant physics, we first discuss a simple model of the evolution up until the onset of thermonuclear oxygen burning. In discussing the analytic estimates below, we reference some of the numerical results from our fiducial MESA model for comparison. This model is a cold ONeMg WD ($X_{\rm O} = 0.5$, $X_{\rm Ne} = 0.45$, $X_{\rm Mg} = 0.05$) accreting at $\dot{M} = 10^{-6}\,M_\odot\,{\rm yr}^{-1}$.

4.3.1 Overview of evolution

We have a dense, degenerate core near the Chandrasekhar mass with a spatially-uniform composition of the carbon-burning products ^{16}O, ^{20}Ne and ^{24}Mg, with mass fractions $X_{\rm O}$, $X_{\rm Ne}$, $X_{\rm Mg}$, respectively. Fiducially, we choose $X_{\rm O} = 0.5$, $X_{\rm Ne} = 0.45$, $X_{\rm Mg} = 0.05$. This is similar to the central abundances observed in recent calculations of the evolution of intermediate mass stars that develop these cores (see e.g., figure 10 of Takahashi et al. 2013). Other recent models of super-AGB evolution (Farmer et al. 2015) show typical central magnesium fractions $X_{\rm Mg} \approx 0.03$ in the cases where the carbon deflagration wave reaches the center (R.
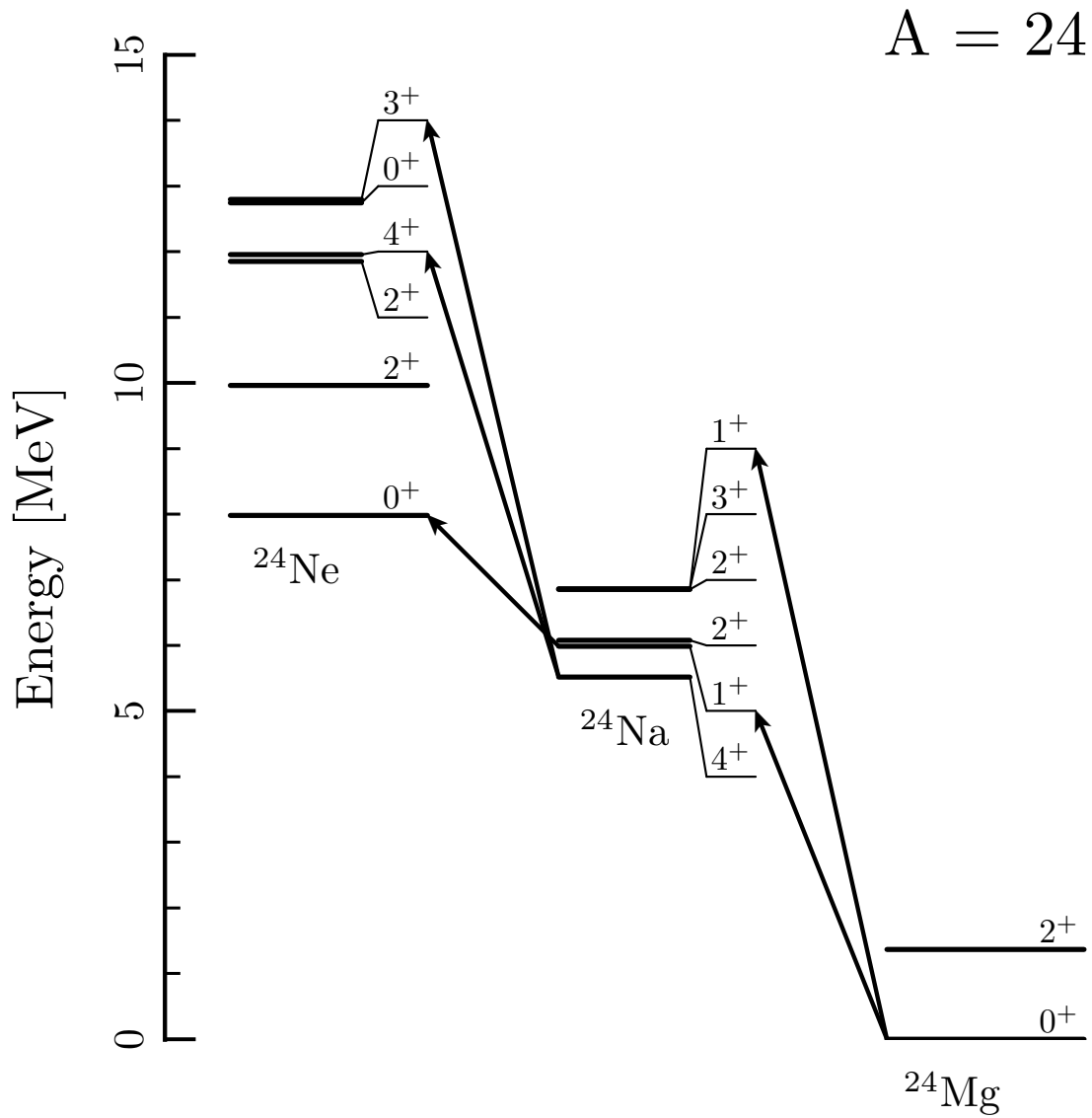
Figure 4.1: Energy level diagram for the $A = 24$ nuclei that we consider. The J^π values are sometimes given an arbitrary offset (indicated via thin lines) in order to enhance legibility. The transitions we consider are indicated with arrows.
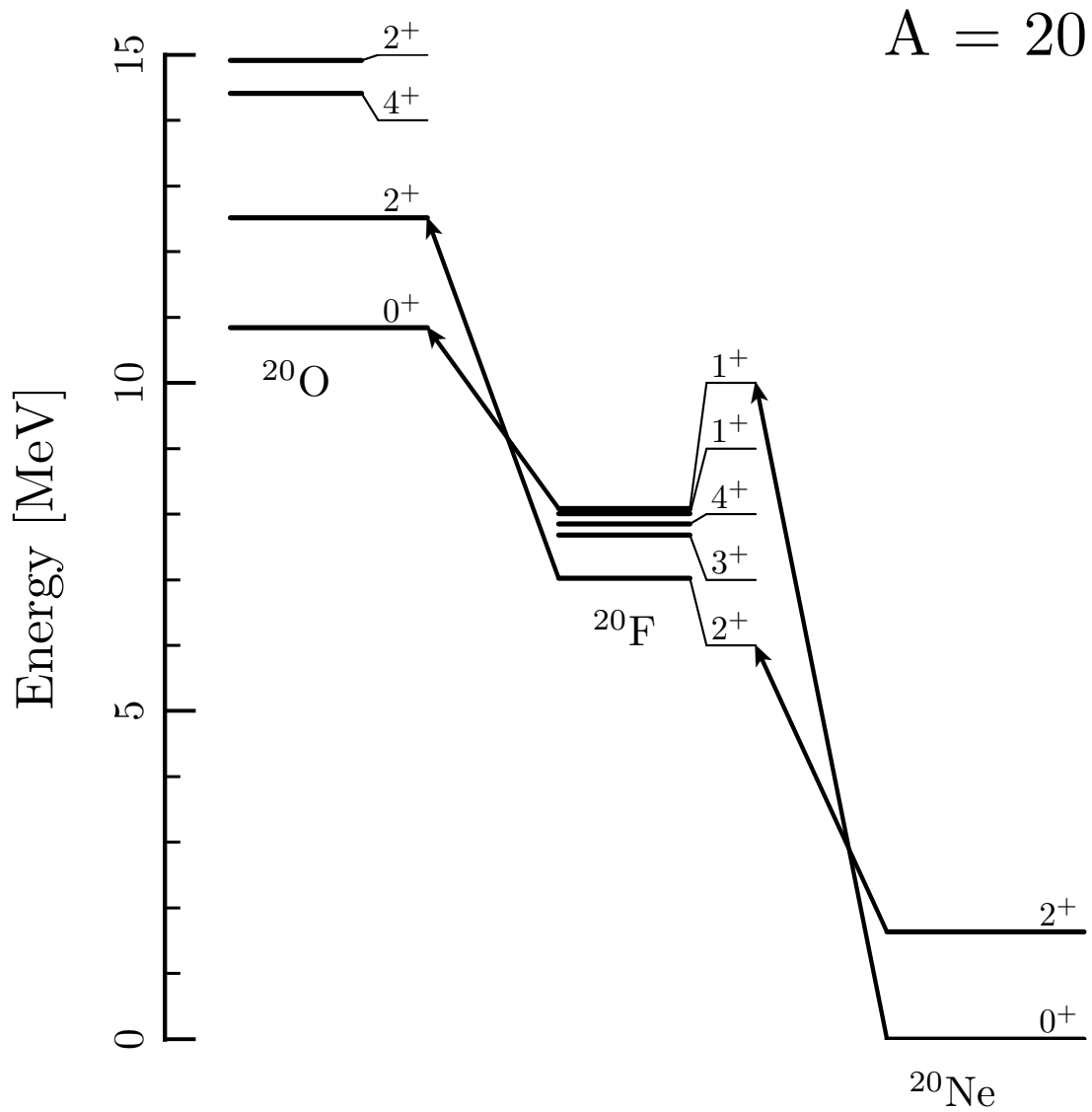
Figure 4.2: Energy level diagram for the $A = 20$ nuclei that we consider. The J^π values are sometimes given an arbitrary offset (indicated via thin lines) in order to enhance legibility. The transitions we consider are indicated with arrows.

Initial	Final	Q_g	E_i	J_i^π	E_f	J_f^π	$\log_{10}(ft)$
^{24}Mg	^{24}Na	5.515	0.000	0^+	0.472	1^+	4.815
			0.000	0^+	1.347	1^+	3.838
^{24}Na	^{24}Ne	2.467	0.000	4^+	3.972	4^+	6.209
			0.000	4^+	4.866	3^+	4.423
			0.472	1^+	0.000	0^+	4.829
^{20}Ne	^{20}F	7.025	1.634	2^+	0.000	2^+	4.970
			0.000	0^+	1.057	1^+	4.380
			0.000	0^+	0.000	2^+	*9.801*
^{20}F	^{20}O	3.815	0.000	2^+	1.674	2^+	5.429
			1.057	1^+	0.000	0^+	4.211

Table 4.1: The transitions used in the rate calculations. They are written as electron capture transitions, but the same transitions were used for beta-decay (swapping initial and final states). Q_g is the energy difference between the ground states of the isotopes. E_i and E_f are respectively the excitation energies of the initial and final states, relative to the ground state. J_i^π and J_f^π are the spins and parities of the initial and final states. Allowed transitions do not have parity changes. (ft) is the comparative half-life in seconds, taken from Martínez-Pinedo et al. (2014) by dividing the constant 6144 s by their tabulated values of the transition matrix elements. The italicized (ft) value indicates an experimental upper limit; the effects of this transition will be discussed in § 4.5.3. All energies are in MeV. For level diagrams which illustrate the transitions, see Figs. 4.1 and 4.2.

Farmer, private communication).

The degenerate core is "accreting" at a rate $\dot{M}$; such accretion might be set by carbon shell burning in an evolved star, accretion from a companion in a binary system, or cooling (and the concomitant reduction in pressure support) of the outer layers of a WD merger remnant. The key impact is that the core is being compressed on a timescale

$$t_\mathrm{compress} = \left(\frac{d \ln \rho_c}{dt} \right)^{-1} = \left(\frac{d \ln \rho_c}{d \ln M} \right)^{-1} \frac{M}{\dot{M}} \quad . \tag{4.1}$$

For an object supported by degeneracy pressure and in hydrostatic equilibrium, the central density rises rapidly as one approaches the Chandrasekhar mass. Therefore, the compression timescale is significantly shorter than the timescale for the growth of the core. For an ideal, zero-temperature white dwarf, in the range $9 \lesssim \log_{10} \rho_c \lesssim 10$,

$$\frac{d \ln \rho_c}{d \ln M} \approx 28 \left(\frac{\rho_c}{10^9 \ \mathrm{g \ cm^{-3}}} \right)^{0.55} \quad , \tag{4.2}$$

which we obtained by calculating a sequence of models and fitting a power-law to the results. This implies

$$t_\mathrm{compress} \approx 5 \times 10^4 \ \mathrm{yr} \left(\frac{\rho_c}{10^9 \ \mathrm{g \ cm^{-3}}} \right)^{-0.55} \left(\frac{\dot{M}}{10^{-6} \ \mathrm{M_\odot \ yr^{-1}}} \right)^{-1} \quad . \tag{4.3}$$

The dynamical time of the white dwarf is extremely short

$$t_{\rm dyn} \approx \frac{1}{\sqrt{G\rho}} \approx 10^{-1}{\rm s} \left(\frac{\rho}{10^9 \, {\rm g \, cm}^{-3}} \right)^{-1/2} \tag{4.4}$$

and so hydrostatic equilibrium will always be preserved (until collapse ensues, which we do not study in detail in this paper).

The temperature of the core will be influenced by details of its previous evolution, such as the accretion history and by the abundances of isotopes which participate in Urca process cooling. However, if the compression timescale (and hence overall evolutionary timescale) is sufficiently slow, heating from compression and cooling from thermal neutrinos will reach a quasi-equilibrium (Paczyński 1971). Define the cooling time

$$t_{\rm cool} = \frac{c_P T}{\epsilon_\nu}, \tag{4.5}$$

where c_P is the specific heat at constant pressure and ϵ_ν is the specific neutrino cooling rate. Then the relation $t_{\rm cool} = t_{\rm compress}$ implicitly defines a temperature for a given density and will characterize the thermal state of the core aside from periods when e-captures rapidly release energy. In Fig. 4.3, we show this relation as a blue, dashed line and demonstrate that our MESA models (the black solid line) described in § 4.4 and § 4.5 exhibit this relationship.

4.3.2   Effects of electron captures

At low temperature, the electron chemical potential is approximately the Fermi energy E_F (the first correction enters at order $(kT/E_F)^2$), and so we use the terms Fermi energy and electron chemical potential interchangeably. As the core is compressed, the electron chemical potential increases. At zero temperature, the electron captures would occur when the Fermi energy reached the energy difference between the initial and final nuclear states, and electrons of sufficient energy first became available. We refer to the density corresponding to this value of the electron chemical potential as the threshold density; the terms sub-threshold and super-threshold reference this density. At non-zero temperature, even when the electron chemical potential is below this threshold, there are some electrons in the high energy tail of the Fermi-Dirac distribution which are available to capture. As a result, the electron capture rate has an exponential dependence on the density and temperature in the sub-threshold case.

A simple form for the sub-threshold capture rate can be obtained by expanding equation (4.40) in the limit that $\mu_e + Q \ll -kT$ (where μ_e is the electron chemical potential and $Q = Q_g + E_i - E_f$ is the energy difference between the parent and daughter nuclear state) and assuming that the rate is dominated by a single transition that begins in the ground state,

$$\lambda_{\rm ec} \approx \frac{2\ln 2}{(ft)} \left(\frac{kT}{m_e c^2} \right)^5 \left(\frac{Q}{kT} \right)^2 \exp \left(\frac{\mu_e + Q}{kT} \right) . \tag{4.6}$$
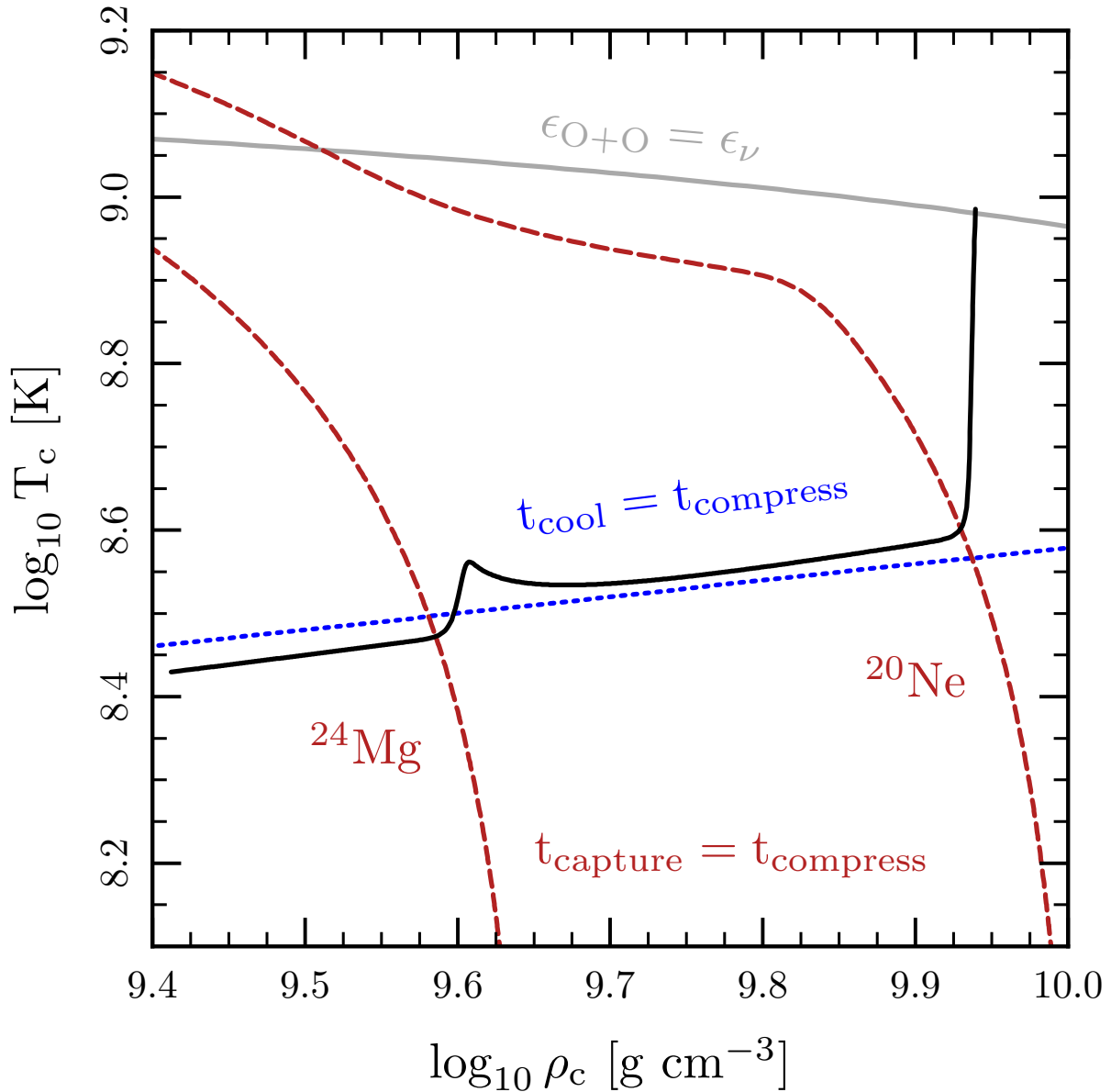
Figure 4.3: The black solid line shows the central density and temperature of the core as it is compressed with a surface accretion rate of $\dot{M} = 10^{-6}\,\mathrm{M_\odot yr^{-1}}$ for approximately 20000 years of evolution. The red dashed lines indicate when the capture timescales for ^{24}Mg and ^{20}Ne become equal to the fiducial compression time of 10^4 yr. The blue dotted line shows where the neutrino cooling time and compression time are equal. This balance between compressional heating and neutrino cooling determines the thermal state of the contracting WD core (aside from brief periods when electron captures heat the core). The grey solid line shows where the energy generation from thermonuclear oxygen burning exceeds the thermal neutrino losses and we stop the calculation.

Define the capture timescale to be the inverse of the electron capture rate $t_{\text{capture}} = \lambda_{\text{ec}}^{-1}$. The onset of significant electron captures will occur when the capture time and the compression time become approximately equal. Setting $t_{\text{compress}} = t_{\text{capture}}$ gives an implicit relationship between ρ and T, which is a function of $\dot{M}$.

At zero temperature, the electron captures would occur at a density $\rho_{\text{ec},0}$ such that $\mu_e(\rho_{\text{ec},0}) + Q \approx 0$. Solving equation (4.6) for μ_e and rewriting the solution in terms of ρ, we find that $t_{\text{compress}} = t_{\text{capture}}$ when

$$\rho_{\text{ec}} \approx \rho_{ec,0} \left[1 + \frac{3kT}{Q} \ln \left(2 \ln 2 \frac{t_{\text{compress}}}{(ft)} \left(\frac{kT}{m_e c^2} \right)^5 \left(\frac{Q}{kT} \right)^2 \right) \right] \quad , \tag{4.7}$$

where we have neglected the much weaker density dependence of t_{compress} itself.

Equation (4.7) will be valid up until a temperature at which the transition rate from an excited state, suppressed by $\exp(-E_i/kT)$, becomes the dominant contribution to the rate. As a rule of thumb, for the transitions we consider, this will happen when $T \approx E_i/(25k)$.

Fig. 4.4 shows numerical solutions for the location in density-temperature space at which $t_{\text{capture}} = 10^4 \, \text{yr}$ (which is approximately the compression timescale associated with an $\dot{M} = 10^{-6} \, \text{M}_\odot \, \text{yr}^{-1}$) for ^{24}Mg, ^{24}Na, ^{20}Ne, and ^{20}F. The approximations for the critical density based on equation (4.7) are overlaid as dashed black lines and are in excellent agreement. The line for ^{20}F is always at lower density than that of ^{20}Ne, meaning once the first capture in the $^{20}\text{Ne} \to {}^{20}\text{F} \to {}^{20}\text{O}$ chain occurs, the second will immediately follow. This is not true for ^{24}Na relative to its parent ^{24}Mg, meaning the captures in the $^{24}\text{Mg} \to {}^{24}\text{Na} \to {}^{24}\text{Ne}$ chain will happen at separate densities when $\log_{10} T \lesssim 8.4$.

The electron captures also influence the temperature evolution of the core. When a capture occurs, the chemical potential of the captured electron, minus the change in nuclear rest mass and the energy in the emitted neutrinos, is thermalized, heating the plasma.[1] This heating is substantial, because the first capture is often into an excited state (meaning the chemical potential is higher when the rate of this transition becomes significant) and the second is typically super-threshold. Does this heating drive convection? If so, this convection will efficiently transport the entropy out of the core while mixing in fresh fuel for electron captures.

The electron captures generate entropy, creating a negative radial entropy gradient in the core. The captures also reduce the electron fraction in the core, creating a positive radial gradient in Y_e. The entropy gradient is destabilizing, but the Y_e gradient is stabilizing. Simulations which invoked the Schwarzschild criterion for convection (e.g. Miyaji et al. 1980), which does not consider composition gradients, found that the captures do trigger convection. Simulations which invoke the Ledoux criterion, which does consider composition gradients, found that the captures do not trigger convection (e.g. Miyaji & Nomoto 1987). Hence the different choices lead to qualitatively different evolution.

---

[1] A more precise definition of the heating rate is given in Appendix 4.A, specifically equations (4.54) and (4.55).
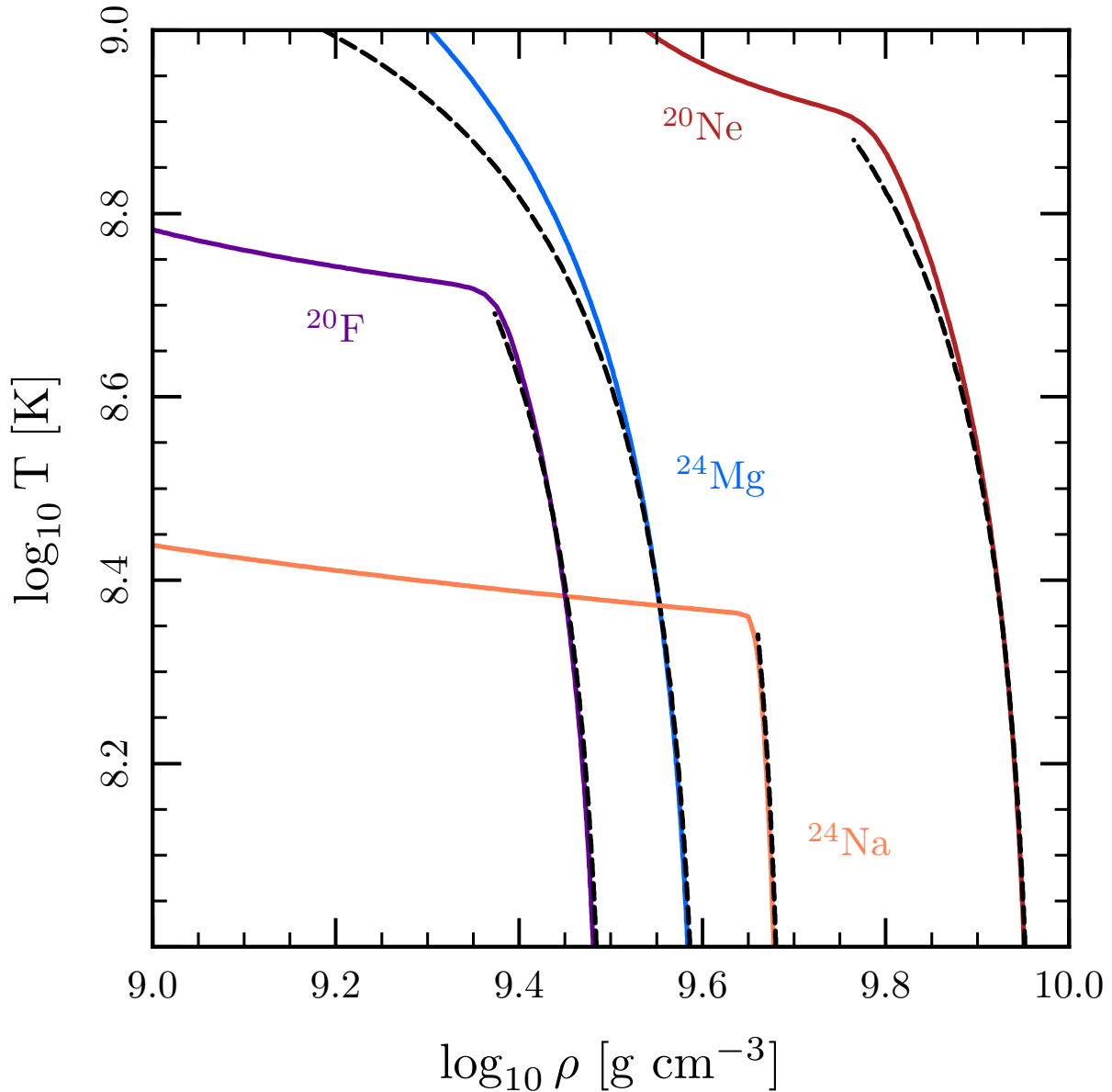
Figure 4.4: The solid lines show where the electron capture timescale is equal to 10^4 yr (which is approximately the compression timescale of the WD core for $\dot{M} = 10^{-6}\,\mathrm{M_\odot\,yr^{-1}}$). At ρ and T greater than those delineated by the solid lines, the capture time is less than the compression time. Each line is labeled by the name of the isotope undergoing electron capture. The black dashed lines show the analytic approximation given in equation (4.7). For ease of comparison with the analytic results, the Coulomb corrections discussed in Appendix 4.B are not present in these calculations.

The following calculation demonstrates why the electron captures are unable to trigger convection when accounting for stabilizing composition gradients. The Ledoux criterion for convective instability is

$$\nabla_{\mathrm{ad}} - \nabla_T + B < 0 \tag{4.8}$$

where

$$B = -\frac{1}{\chi_T} \left(\frac{\partial \ln P}{\partial \ln Y_e} \right)_{\rho,T} \frac{d \ln Y_e}{d \ln P} \; . \tag{4.9}$$

The captures occur over a narrow range in Fermi energy, and hence density. Therefore the gradients in T and Y_e across the region where the captures occur will be large. This allows us to drop the ∇_{ad} term. Replacing the gradients with finite differences, we then check the inequality

$$\Delta \left(\ln T \right) > -\frac{1}{\chi_T} \left(\frac{\partial \ln P}{\partial \ln Y_e} \right)_{\rho,T} \Delta \left(\ln Y_e \right) . \tag{4.10}$$

For a cold plasma with degenerate electrons and ideal ions, $(\partial \ln P / \partial \ln Y_e)_{\rho,T} \approx 4/3$ and $\chi_T \approx 4kT/(\bar{Z}E_{\mathrm{F}})$. If a mass fraction ΔX_c has undergone electron captures, the associated change in temperature is

$$\Delta T \approx \frac{\bar{A}}{A_c} \left(\frac{E_c}{c_P} \right) \Delta X_c \; , \tag{4.11}$$

where A_c is the nuclear mass number of the species that is capturing and E_c is the average energy deposited by a capture. At the typical densities and temperatures in our calculation, the ions are a Coulomb liquid and so $c_P \approx 3k$. The change in Y_e due to the captures is

$$\Delta Y_e \approx \frac{\Delta Z}{A_c} \Delta X_c \; . \tag{4.12}$$

Both the $A = 24$ and $A = 20$ chains that we consider are two electron captures long, so we set $\Delta Z = -2$.

Substituting these estimates into equation (4.10) and simplifying, the condition for convective instability becomes

$$\frac{E_c}{E_F} > 2 \; . \tag{4.13}$$

This inequality demonstrates that in order to trigger convective instability, the two captured electrons—which each have a characteristic energy of E_F—would have to deposit nearly all their energy as thermal energy. This is unrealistic, since substantial amounts of energy go into the rest mass of the daughter nucleus and to neutrinos. From our calculation of the heating rates, it is clear this inequality is far from being violated: the $A = 24$ captures occur at $E_F \approx 6.5\,\mathrm{MeV}$ and release $E_c \approx 0.5\,\mathrm{MeV}$; the $A = 20$ captures occur at $E_F \approx 8.5\,\mathrm{MeV}$ and and release $E_c \approx 3\,\mathrm{MeV}$. Electron captures do not directly trigger convection.

A region which is Schwarzschild-unstable but Ledoux-stable is semiconvective. The semi-convective diffusion coefficient used in MESA (Paxton et al. 2013, following Langer et al.

1983) is

$$D_{\rm sc} = \alpha_{\rm sc} \left(\frac{K}{6 c_P \rho} \right) \left(\frac{\nabla_T - \nabla_{\rm ad}}{B + \nabla_{\rm ad} - \nabla_T} \right), \tag{4.14}$$

where K is the radiative conductivity. The values of $\alpha_{\rm sc}$, the semiconvective efficiency adopted in the literature span the range $10^{-3} \lesssim \alpha_{\rm sc} \lesssim 1$ (Paxton et al. 2013, citing Langer 1991; Yoon et al. 2006).

Regions where the electron captures have not yet occurred and regions where they have completed do not have a Y_e gradient. Therefore the width of the semiconvective zone $H_{\rm sc}$ will be roughly the length over which the density changes by an amount that shifts E_F by kT. We expect

$$H_{\rm sc} \sim 4 \left(\frac{kT}{E_F} \right) H_P \tag{4.15}$$

where H_P is the pressure scale height. Defining $f = H_{\rm sc}/H_P$, we find $f \approx 0.03$ in our MESA models, consistent with the above estimate. We define the timescale for semiconvection to modify the composition and thermal structure in our models as

$$t_{\rm sc} = \frac{H_{\rm sc}^2}{D_{\rm sc}} \sim 3 \times 10^4 \, {\rm yr} \left(\frac{1}{\alpha_{\rm sc}} \right) \left(\frac{f}{0.03} \right)^2 \quad . \tag{4.16}$$

For $\alpha_{\rm sc} \lesssim 1$, $t_{\rm sc}$ in equation (4.16) is equal to or longer than time that elapses between ^{24}Mg captures and oxygen ignitions in our fiducial model. Moreover, $t_{\rm sc}$ is an upper limit: because of the thinness of the region with a Y_e-gradient, an individual parcel spends less time in a semiconvective region. Therefore, we do not consider semiconvection in our models.

For realistic ^{24}Mg fractions, e-captures on ^{24}Mg do not release enough energy to initiate thermonuclear fusion. As a result, the core continues to compress and we eventually reach the density where the captures begin on the $A = 20$ nuclei. Once the capture on ^{20}Ne occurs, the capture on ^{20}F occurs immediately. Like the $A = 24$ captures, the bulk of the energy deposition comes from this super-threshold capture, but in this case the energy per capture is substantially greater, $E_c \approx 3 \, {\rm MeV}$. The characteristic temperature for oxygen ignition is approximately $10^9 \, {\rm K}$ and so from equation (4.11), we estimate that oxygen will ignite after an amount $\Delta X_{\rm Ne} \approx 0.1$ has undergone capture. We halt our main MESA calculations when the energy generation rate from oxygen burning exceeds the cooling from neutrinos, implying that a nuclear runaway is assured.

We have focused primarily on the evolution of the center of the core, but the density of the rest of the core increases during compression. Electron captures on the $A = 24$ elements have been occurring off-center as parcels of the star reach conditions favorable for these captures. This is illustrated in Fig. 4.5, where one can see the depletion of ^{24}Mg in the inner $0.3 M_\odot$ of the star.
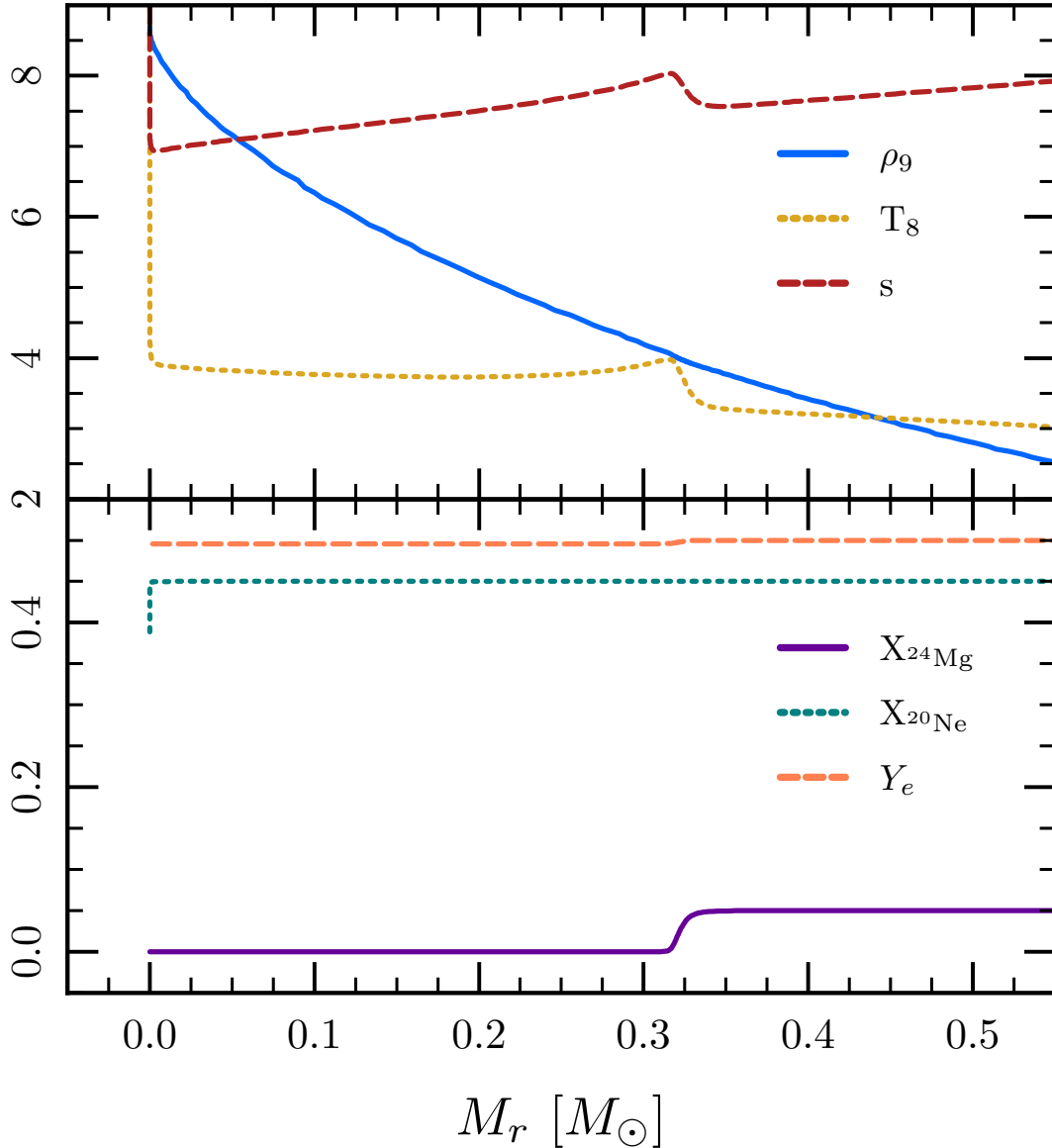
Figure 4.5: The structure of the model from Fig. 4.3 at the end of the MESA calculation (when the energy generation rate from oxygen burning exceeded the neutrino cooling). The top panel shows the density (ρ_9, ρ in units of $10^9 \, \mathrm{g \, cm^{-3}}$), the temperature ($T_8$, T in units of $10^8 \, \mathrm{K}$), and the entropy per baryon s (in units of k), as a function of enclosed mass. The bottom panel shows the mass fractions of $^{24}\mathrm{Mg}$ and $^{20}\mathrm{Ne}$ as well as the electron fraction Y_e. The small region in which there is a Y_e gradient due to the $A = 24$ captures has been moving outward in a Lagrangian sense. By the time the center reaches the density for $^{20}\mathrm{Ne}$ captures, the inner $0.3 M_\odot$ has already been depleted of $^{24}\mathrm{Mg}$ due to e-captures. The subsequent evolution is discussed in § 4.6.

4.3.3 Thermal runaway from ^{20}Ne Captures and Oxygen Deflagration Initiation

In Fig. 4.6 we show the evolution of the center of our MESA models as the $A = 20$ captures begin.[2] The profiles are labeled by the central heating time of the model, $t_{\text{heat,c}} = c_p T / \epsilon_{\text{nuc}}$. At these temperatures, the energy generation rate is dominated by the $A = 20$ captures, which are undergoing a thermal runaway in the thermally conducting core. From equation (4.11), the change in Y_e associated with increasing the temperature from its value before the $A = 20$ captures, $T \approx 4 \times 10^8$ K, to the temperature for oxygen ignition, $T \approx 10^9$ K, is $\Delta Y_e \approx 0.006$, in good agreement with the change observed in the lower panel of Fig. 4.6. Changes in T and Y_e will no longer be so tightly coupled once energy release from oxygen fusion exceeds that from electron captures, pushing the core towards convective instability. However, in order to reach convective instability, equation (4.10) requires

$$\Delta T > \frac{\bar{A} E_F}{3k} \Delta Y_e \approx 3.5 \times 10^9 \, \text{K} \left(\frac{\Delta Y_e}{0.006} \right) \, , \tag{4.17}$$

a temperature so large that the central heating timescale from oxygen fusion would be $t_{\text{heat,c}} \approx 10^{-5}$ s. We show here that a thermal runway is triggered long before such a condition is reached.

The $A = 20$ electron captures occur in an environment where the electron Fermi energy is below the energy threshold. In this sub-threshold case, those electrons that capture are on the thermal tail of the distribution, making the rate very sensitive to both density and temperature.[3] We now show that this naturally leads to a local thermal runaway in the core whose size is limited by thermal conduction. This runaway provides the "hot-spot" needed to initiate the oxygen deflagration from the center of the star.

The strong density sensitivity of the $A = 20$ captures implies that the runaway will begin at the exact center of the isothermal core. However, the pressure declines away from the core, leading to a temperature gradient on the scale over which the electron capture rate (and hence the heating rate) varies by order unity. In this sub-threshold case, $d \ln \lambda / d \ln P = E_F / (4kT)$, so the change in pressure needed to have the rate be less at the outer edge than the center is

$$\Delta P \approx 4 P_c \left(\frac{kT}{E_F} \right) \approx \left(\frac{\rho_c Y_e}{m_p} \right) kT_c \, . \tag{4.18}$$

Hydrostatic equilibrium provides such a pressure change over a length scale

$$l_T = \left(\frac{3 \Delta P}{2 \pi G \rho_c^2} \right)^{1/2} \approx 4 \times 10^6 \, \text{cm} \, , \tag{4.19}$$

---

[2]The MESA run shown in this plot used a finer central spatial and temporal resolution than our fiducial case in order to better resolve the onset of these steep central gradients.

[3]Because the bulk of the heating comes from the super-threshold electron capture on ^{20}F that immediately follows the ^{20}Ne capture, the capture rate on ^{20}Ne is a good proxy for the temperature and density dependence of the heating rate.
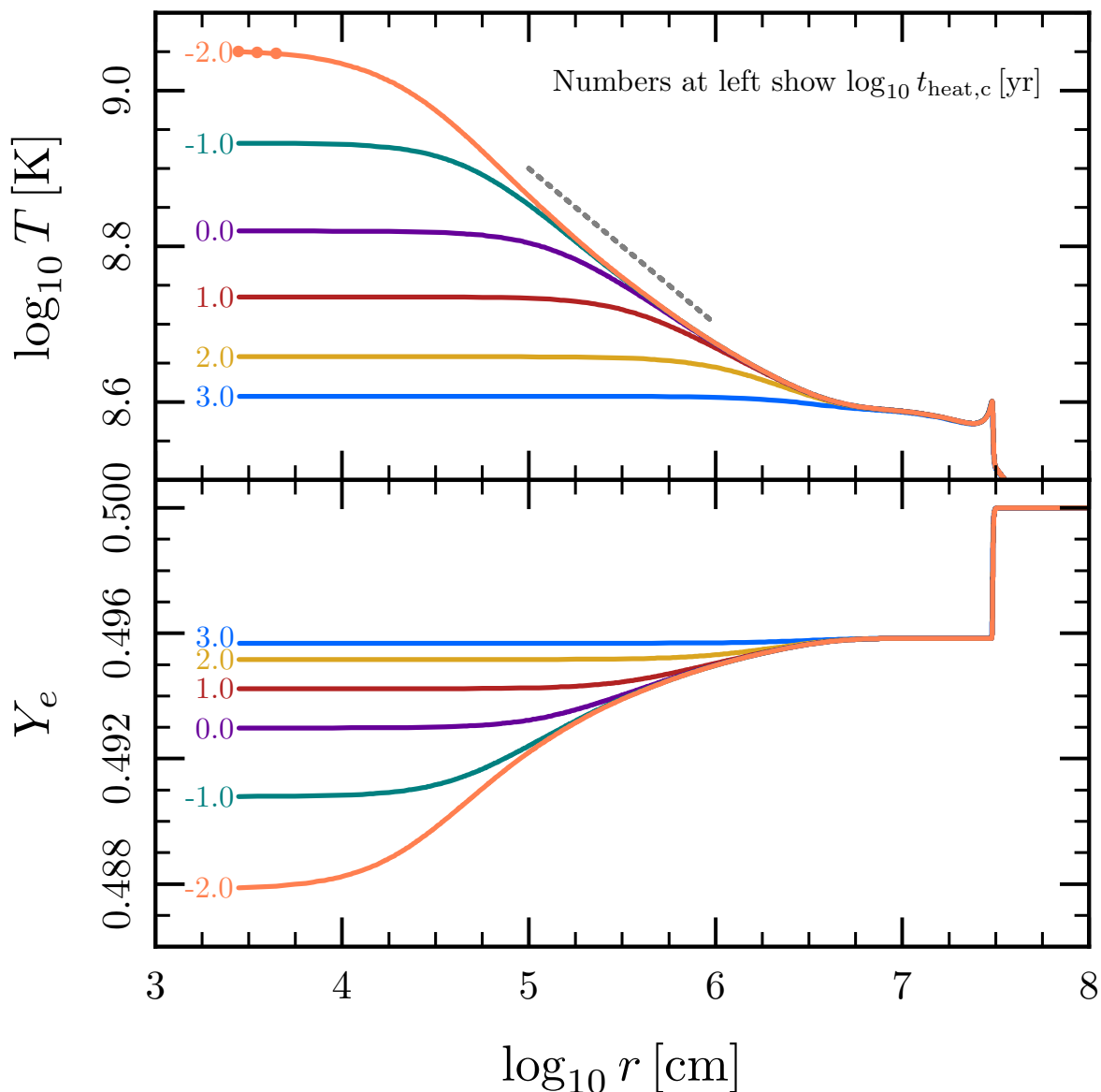
Figure 4.6: The temperature (T) and electron fraction (Y_e) profiles in the MESA model shown in Fig. 4.5, as it is approaching the onset of O fusion. At these temperatures, the energy release is dominated by the $A = 20$ captures, so T and Y_e are closely tied. The lines are labeled by the heating timescale at the center of the model. The dotted grey line in the top panel shows the slope of the temperature profile expected for a thermal runaway with diffusion. The mass resolution in this calculation is significantly higher than that in other figures in order to resolve the small region (regulated by thermal diffusion) within which thermal runaway sets in. The dots on the orange (hottest) temperature curve indicate the locations of the innermost three MESA zones; the mass in the central zone is roughly $4 \times 10^{-13} M_\odot$.

where we have used $T_c \approx 4 \times 10^8$ K and $\rho_c \approx 9 \times 10^9$ g cm^{-3}, corresponding to the onset of $A = 20$ captures in our fiducial model. This estimate is consistent with the length scale observed at the onset of the runaway in Fig. 4.6.

The subsequent evolution of the runaway is driven by the temperature sensitivity of the sub-threshold electron capture rate. This rate is well-approximated by equation (4.6), yielding a logarithmic derivative of the rate with respect to temperature of

$$\frac{d \ln \lambda}{d \ln T} = 3 - \frac{\mu_e + Q}{kT} \ . \tag{4.20}$$

Physically, the second term is the how far the transition is below its threshold energy (in units of kT). As in the $A = 24$ case, electron captures become important when $\lambda_{\text{ec}}^{-1} \approx t_{\text{compress}}$; from equation (4.6) this occurs at $(\mu_e + Q)/(kT) \approx -14$. The thermal runaway is sufficiently rapid that $\mu_e + Q$ remains approximately fixed. This implies that the captures will be extremely temperature sensitive, scaling as $\lambda \propto T^n$, where

$$n \equiv \frac{d \ln \lambda}{d \ln T} \approx 3 + 14 \left(\frac{T}{4 \times 10^8 \text{ K}} \right)^{-1} \ . \tag{4.21}$$

In the following estimates, we will take $n \approx 12$, and since $n \gg 1$, we will treat $n \approx n \pm 1$.

Hence, as captures begin, their density dependence leads to a temperature gradient on the length scale given by equation (4.19). Because convection is not initiated, the heating remains local, and this temperature gradient will grow with time in a thermal runaway. Once it is sufficient to cause an order unity variation of the capture rate across a given length r, the gradient will become non-linear. The hotter part will begin to evolve more rapidly and the evolution of the cooler part will freeze-out. This will occur when $dT/dr \approx (T/n)/r$ and so on its own, thermal runaway leads to a characteristic profile where $d \ln T/d \ln r \approx 1/n$. However, thermal conduction limits the volume that can runaway to a fixed temperature, keeping regions where $t_{\text{th}} \lesssim t_{\text{heat}}$ approximately isothermal. The thermal diffusivity from electron conduction is $D_{\text{th}} \approx 30 \text{ cm}^2 \text{ s}^{-1}(T/10^9 \text{ K})$, meaning that the timescale for conduction to modify the thermal structure over a lengthscale r is

$$t_{\text{th}} = \frac{r^2}{D_{\text{th}}} \approx 10^3 \text{ yr} \left(\frac{r}{10^6 \text{ cm}} \right)^2 \left(\frac{T}{10^9 \text{ K}} \right)^{-1} \ . \tag{4.22}$$

Therefore, the size of the isothermal region at the center of the model scales like $r \propto T_c^{1-n/2}$. Thus, as the runaway progresses, it will create a temperature profile with $d \ln T/d \ln r \approx -1/5$. The dotted grey line in the top panel of Fig. 4.6 shows this slope, which agrees well with the temperature evolution in the MESA calculations. The semiconvective instability grows on the thermal diffusion time. During the thermal runaway, by definition, $t_{\text{heat}} \lesssim t_{\text{th}}$. Hence, the evolution of the core during this phase will be sufficiently fast that semiconvection will not modify the temperature or composition.

This thermal runaway leads to a small volume at the core reaching very high tempertures, eventually to values large enough for heating from oxygen fusion to play a role. This occurs

when $T \approx 1.1 \times 10^9\,\mathrm{K}$, where the heating time is $t_{\mathrm{heat}} \approx 10^{-2}\,\mathrm{yr}$. From equation (4.22), the hottest (isothermal, so $t_{\mathrm{th}} \approx t_{\mathrm{heat}}$) part of the core will have a size $r \approx 3 \times 10^3\,\mathrm{cm}$, which encompasses about 3×10^{-13} of the total mass. The finest central zoning that we were able to achieve in our MESA calculations (as shown in Fig. 4.6) was a mass resolution of approximately $4 \times 10^{-13} M_\odot$. Therefore, just as oxygen burning begins to dominate the energy release, the small size of this region prevents us from continuing to follow its evolution in our full star MESA simulations.

The conditions created in the core of the star as energy generation by oxygen fusion begins to dominate over $A = 20$ captures lead naturally to the development of an oxygen deflagration wave. In particular, we have shown that oxygen fusion begins in a region at the core of the star whose size is determined by $t_{\mathrm{th}} \lesssim t_{\mathrm{heat}}$. With t_{heat} identified as the heating time associated with oxygen fusion, this is precisely the condition for the onset of an oxygen deflagration wave; Timmes & Woosley (1992) defined the deflagration "trigger mass" to be the mass contained within the region satisfying this constraint. Therefore, we are confident that the hot central region present at the end of our MESA calculations, being unstable to thermal runaway, will continue to grow in temperature and shrink in size, eventually reaching the laminar deflagration solutions of Timmes & Woosley (1992).[4] The outgoing deflagration wave will sweep across this thermally unstable core in less than one second.

It is important to stress that the onset of the oxygen deflagration in the AIC context is substantially different than the "simmering phase" in single degenerate Type Ia supernovae progenitors. There, after pycnonuclear carbon ignition occurs, the entropy release from carbon burning drives the formation of a central convection zone. The growth and heating of this convective zone lead to a significant decrease in the central density between the time of carbon ignition and the development of a deflagration.

In our models, by contrast, no central mixing occurs because of the stabilizing effect of the composition gradient associated with $A = 20$ captures. Therefore the central density at which oxygen ignition occurs, and at which we halt our MESA calculations, is a good estimate of the central density at which the oxygen deflagration develops. We discuss the propagation of this deflagration and its influence on the final outcome in § 4.6.

4.4 Details of MESA Calculations

All of the calculations performed in this paper are based on revision 6596 (released 2014-06-07), with some modifications to support our weak rate calculations. The incorporation of these changes into the mainline MESA code will be discussed in the upcoming MESA Instrument Paper III (Paxton et al. 2015). As required by the MESA manifesto, the inlists and source code modifications necessary to reproduce our calculations will be posted on http://mesastar.org.

---

[4]At the density in our MESA calculations, the laminar deflagration width is $\delta \approx 3 \times 10^{-5}\,\mathrm{cm}$, far below our ability to resolve in our full star simulations.

4.4.1   Generation of Initial Models

In order to perform the parameter study discussed § 4.5, it is necessary to have a set of models of ONeMg cores with a range of different temperatures and compositions to use as initial conditions. We generate an idealized set of models via the following *ad hoc* steps. During each step, all nuclear reactions are turned off, ensuring that the model will continually contract until halted by degeneracy pressure.

We begin with a $1.325 M_\odot$ pre-main sequence model of normal (roughly solar) composition. We evolve this model until it reaches a central density of $\log_{10} \rho = 3$ (cgs). We then relax the (homogeneous) composition to the desired ^{16}O, ^{20}Ne, and ^{24}Mg mass fractions and allow the model to evolve until the central density reaches $\log_{10} \rho = 7$. Then we set the model to accrete at a constant $\dot{M}$ and evolve until the central density reaches $\log_{10} \rho = 9.4$, which is still below the threshold for the onset of the electron capture reactions of interest. In order to achieve different core temperatures, we vary $\dot{M}$; models with higher (lower) accretion rates have less (more) time for neutrino cooling to carry away energy and are correspondingly hotter (colder). By this means, we arrive a set of models with varied compositions and central temperatures to use as initial models.

4.4.2   Important MESA Options

While our full inlists will be made publicly available, we highlight some of the most important MESA options used in the calculations. This section assumes the reader is familiar with specific MESA options. Please consult the instrument papers (Paxton et al. 2011, 2013) and the MESA website[5] for a full explanation of the meaning of these options.

Since MESA is an implicit code, it is important that we choose timesteps that will resolve the processes of interest. The evolution of the ONeMg cores is driven by the increase in central density (and hence Fermi energy) caused by the ongoing compression. Therefore, our default runs include a timestep criterion based specifically on changes in central density

```
delta_lgRho_cntr_hard_limit = 3e-3
delta_lgRho_cntr_limit = 1e-3
```

in addition to the primary spatial and temporal convergence settings of

```
varcontrol_target = 1e-3
mesh_delta_coeff = 1.0 .
```

Evidence demonstrating that this set of MESA options yields a converged result is shown in Appendix 4.C.

These calculations use a nuclear network based on the `co_burn.net` network included with MESA with the addition of the isotopes ^{20}O, ^{20}F, ^{24}Ne, and ^{24}Na and the weak reactions linking the $A = 20$ isotopes to ^{20}Ne and the $A = 24$ isotopes to ^{24}Mg. The special treatment of these weak reactions (as discussed in Appendix 4.A) is activated with the options

---

[5]http://mesa.sourceforge.net

```
    use_special_weak_rates = .true.
    ion_coulomb_corrections = 'PCR2009'
    electron_coulomb_corrections = 'Itoh2002'
```

where the last two lines select the Coulomb corrections discussed in Appendix 4.B.

4.5 Parameter Studies

In this section, we use a suite of MESA calculations to study how a variety of parameters affect the evolution of these cores. The key question we will answer is whether reasonable variation in these parameters will affect the final outcome.

The first parameter (§ 4.5.1), the initial ^{24}Mg mass fraction (X_{Mg}), is an intrinsic property of the ONeMg core, set during the process that produced the core. Variation in this value may reflect variation in the formation process (e.g., the initial mass of the star that produced it) as well as limits of our knowledge (e.g., uncertainties in quantities such as the ^{12}C$(\alpha, \gamma)^{16}$O reaction rate). The second parameter (§ 4.5.2), the accretion rate $\dot{M}$, is set by the current state of the system (e.g., the properties of a binary companion, the details of shell-burning). The third parameter (§ 4.5.3), the strength of the second forbidden transition between the ground states of ^{20}Ne and ^{20}F, reflects a limit in our current knowledge.

4.5.1 Effect of a ^{24}Mg mass fraction

Gutiérrez et al. (2005) performed a parameter study of the effects of the ^{24}Mg mass fraction. We follow their approach of varying the central ^{24}Mg fraction, while holding the ^{16}O/^{20}Ne ratio fixed.[6] We explore a wide range of ^{24}Mg mass fractions, from 0.01 up to 0.20. This latter value is well above the expected ^{24}Mg fraction given current reaction rates. Our results are shown in Fig. 4.7.

The temperature increase due to the $A = 24$ electron captures scales roughly linearly with X_{Mg}, as expected from equation (4.11). For $X_{\mathrm{Mg}} \lesssim 0.07$, neutrino cooling erases the effect of the heating and the trajectories converge back towards the $t_{\mathrm{cool}} = t_{\mathrm{compress}}$ relation described in § 4.3. Correspondingly, the density at which the captures on ^{20}Ne occur—and thus the density at which oxygen ignites—is independent of X_{Mg}. For $X_{\mathrm{Mg}} \gtrsim 0.07$, an increase in X_{Mg} leads to the onset of ^{20}Ne captures (and oxygen ignition) at a higher density. At even higher values (not shown), the heating from the $A = 24$ captures is sufficient to directly ignite oxygen burning as noted by Miyaji & Nomoto (1987) and Gutiérrez et al. (2005).

In the limited set of models presented in Gutiérrez et al. (2005) this bifurcation in the core evolution around $X_{\mathrm{Mg}} \approx 0.07$ is not evident. However, it has a clear physical explanation. In Appendix 4.D we discuss a simple model of a zero-temperature white dwarf with a low-Y_e

---

[6]In accordance with our fiducial model, we set this ratio be at 10/9. The choice of this ratio does slightly influence the density at which captures occur through the dependence of the Coulomb corrections on $\bar{Z}$. However, as a small shift on top of a small shift, we do not explore variations in this ratio.

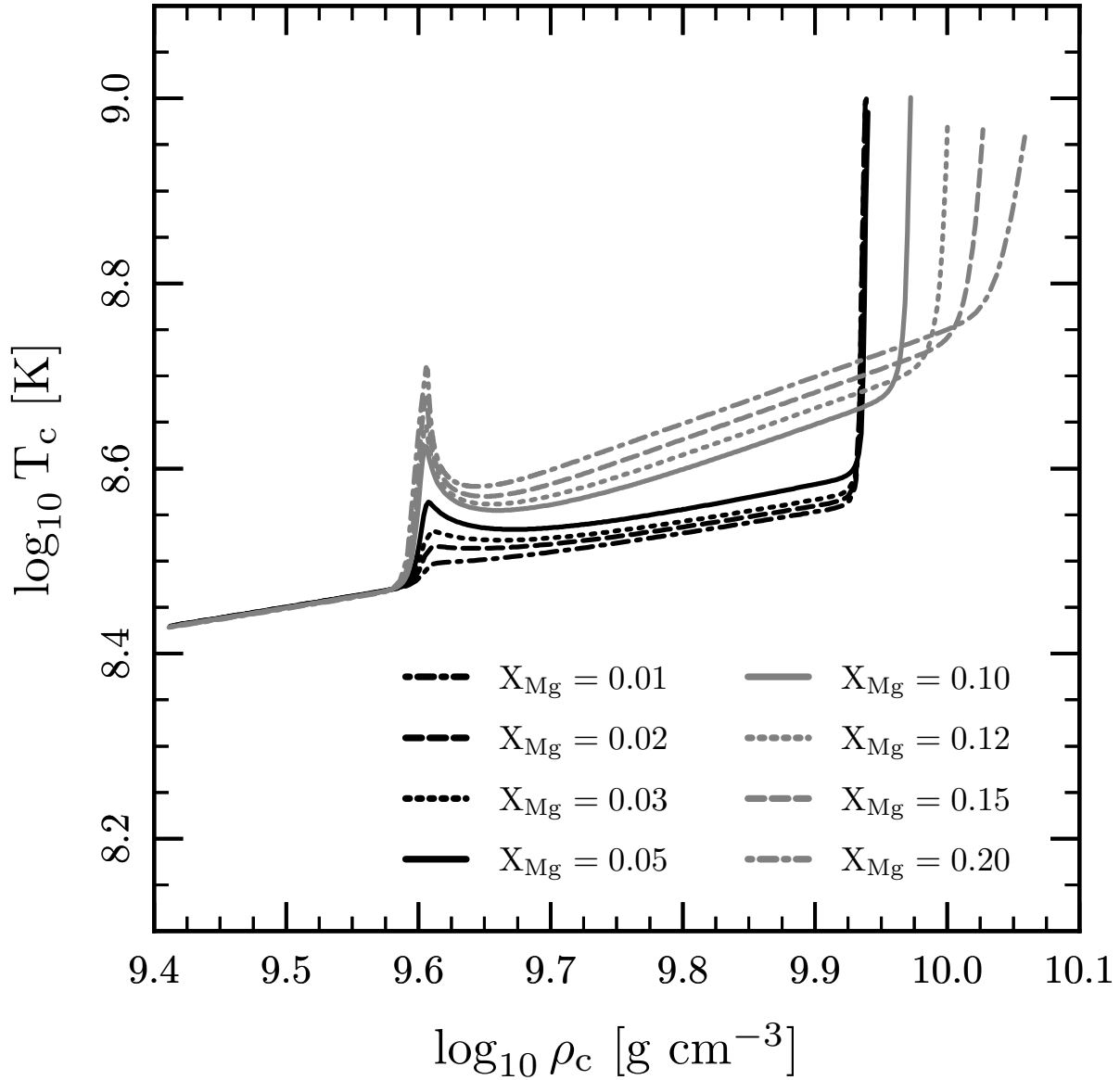*Figure 4.7*: The evolution of the central density and temperature for different magnesium mass fractions. At lower X_{Mg} values, the density at which oxygen ignition occurs (the end of the track) is independent of X_{Mg}; at higher X_{Mg} values, the density at which oxygen ignition occurs increases with increasing X_{Mg}. The text and Figs. 4.8 and 4.9 explain the origin of this trend.

core that explains these results; here, we demonstrate the consistency of these calculations with our MESA models, eliding the details.

Fig. 4.8 shows the compression time in two models, one on each side of this threshold value of X_{Mg}. The core evolution for both models follows the dashed black line defined by equation (4.3) up until the onset of the $A = 24$ electron captures at $\log_{10} \rho_c \approx 9.6$. Above this density, the $X_{\mathrm{Mg}} = 0.05$ model (blue line) follows the dotted line, which is the track expected for the fiducial value of $\dot{M}$ and the value of $d \ln M / d \ln \rho_c$ in equation (4.1) calculated from a zero-temperature white dwarf model in which Y_e decreases for $\log_{10} \rho > 9.6$. See Fig. 4.17 and surrounding discussion for the details of this zero-temperature model.

In the $X_{\mathrm{Mg}} = 0.15$ model (yellow line in Fig. 4.8), once the ^{24}Mg captures occur at $\log_{10} \rho_c \approx 9.6$, the compression timescale begins to fall dramatically. By the time ^{20}Ne capture densities are reached ($\log_{10} \rho \approx 10$), the compression timescale is orders of magnitude smaller than in the lower X_{Mg} models, though it remains significantly longer than the dynamical time. Recall that significant electron captures only occur when the capture time satisfies the relation $t_{\mathrm{compress}} = t_{\mathrm{capture}}$; this means that for shorter compression timescales, the core must reach higher densities, and hence higher capture rates, before the effects of the captures become apparent. As X_{Mg} increases, models experience a larger drop in Y_e, and compress more quickly. This explains the trend of increasing oxygen ignition density with increasing X_{Mg} seen in Fig. 4.7.

To physically understand the different evolution of the $X_{\mathrm{Mg}} \gtrsim 0.07$ models, we consider an idealized model of the effect of Mg captures on the structure and stability of the ONeMg core. We assume that the $A = 24$ electron captures occur instantaneously above a density of $\rho_n = 9.6$. Using the approach described in Appendix 4.D, we can then determine the central density of the zero temperature model with the maximum mass. The result of this calculation is shown as the dashed line in Fig. 4.9. Any model with $X_{\mathrm{Mg}} \gtrsim 0.07$ will cross the stability line before the onset of ^{20}Ne captures. Moreover, for a larger change in Y_e (associated with a larger X_{Mg} in the current example), the onset of instability occurs at lower central density. These results explain the qualitatively different behavior of the high X_{Mg} models in Fig. 4.7.

Above the dashed line in Fig. 4.9, the zero temperature models are dynamically unstable and would contract on the dynamical timescale. But the characteristic electron capture timescales are longer than the dynamical time, and so the assumption that the captures are effectively instantaneous (used in the idealized models in Appendix D) does not hold in the real MESA models. As the contraction timescale gets shorter, only material at densities where the capture timescale is shorter than the contraction timescale can have had significant captures. Therefore the density above which the captures have completed, ρ_n, shifts to higher values. There is no longer time for the total mass to change and so the timescale for the evolution of the central density is no longer set by the accretion rate. Instead, the core compresses on the significantly shorter neutronization timescale,

$$t_n = \left(\frac{d \ln Y_e}{dt} \right)^{-1} = \frac{Y_e A_{\mathrm{Mg}}}{X_{\mathrm{Mg}} \lambda_{\mathrm{ec}}} \approx 80 \left(\frac{X_{\mathrm{Mg}}}{0.15} \right)^{-1} t_{\mathrm{capture}}. \qquad (4.23)$$
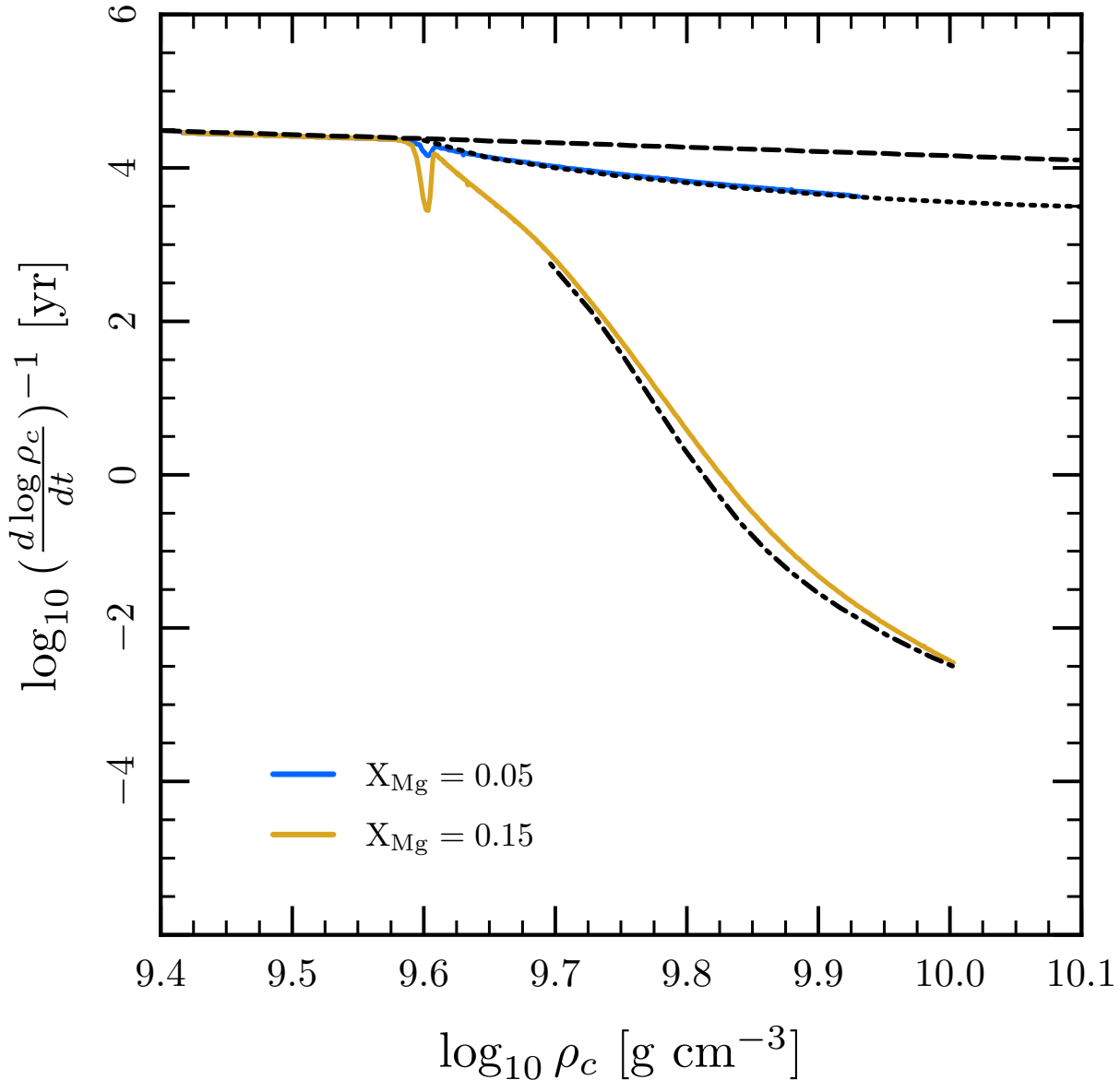
Figure 4.8: The compression time of selected MESA models. The model with $X_{\mathrm{Mg}} = 0.05$ is compressed at a rate controlled by the accretion rate. The dashed line shows the compression rate given in equation (4.3) and the dotted line shows the compression rate expected for a zero temperature white dwarf in which Y_e suddenly falls at $\log_{10}\rho = 9.6$, due to the electron captures on ^{24}Mg and ^{24}Na. The agreement demonstrates that the central density is controlled by the total mass. The model with $X_{\mathrm{Mg}} = 0.15$ experiences a much more dramatic decrease in the compression time because of the larger decrease in Y_e (see Fig. 4.9). The black dash dotted line shows the neutronization timescale expected from the calculations in Appendix 4.D, where the central density is evolving at fixed mass. Note that in both cases the compression timescale still remains orders of magnitude longer than the dynamical time.

Given a fixed M, the models in Appendix 4.D give a relationship between ρ_c and ρ_n. Calculating t_n by evaluating t_{capture} at the ρ_n corresponding to each ρ_c gives the dash dotted line in Fig. 4.8, which agrees well with the result of the MESA calculation. See Fig. 4.18 and surrounding discussion for the details of these zero-temperature models.

4.5.2 Effect of central temperature and accretion rate

As illustrated in Fig. 4.4, the density at which electron captures begin is temperature dependent. Our fiducial model begins at a central density $\log_{10} \rho_c \approx 9.4$ and $\log_{10} T_c \approx 8.4$. This central temperature is a free parameter, but as discussed in § 4.3, a new central temperature will be established by the balance between neutrino cooling and compressional heating. Therefore, the central temperature when captures occur (in particular the $A = 20$ captures, and quickly thereafter oxygen ignition) is weakly dependent on the initial temperature. This fact makes it difficult to separately illustrate the effects of the temperature and accretion rate.

In Fig. 4.10 we show the evolution of our fiducial model with 4 different accretion rates. The onset of captures is less temperature sensitive than one would infer from Fig. 4.4. This is because at a higher $\dot{M}$, while the quasi-equilibrium core temperature is higher (increasing the electron capture rates), the compression time is also shorter, and so the density at which $t_{\text{compress}} \approx t_{\text{capture}}$ ends up having a weaker dependence on the accretion rate. At the lowest accretion rate shown in Fig. 4.10 ($\dot{M} = 10^{-8} M_\odot \, \text{yr}^{-1}$), the evolution appears qualitatively different. Looking at Fig. 4.4, this is because the central temperature remains sufficiently low that electron captures on ^{24}Na do not occur immediately after electron captures on ^{24}Mg, but are delayed until higher densities ($\log_{10} \rho_c \approx 9.7$).

Fig. 4.11 demonstrates the independence of the oxygen ignition density on the initial central temperature. These models begin right before the $A = 24$ captures, at $\log_{10} \rho_c \approx 9.55$, so that the core temperature does not change substantially before the onset of the captures. By the time the $A = 20$ captures occur, the temperature differences have been erased by neutrino cooling and compressional heating, as the core evolves towards the $t_{\text{compress}} = t_{\text{cool}}$ thermal state discussed in § 4.3. As a result, there is little effect on the density at which oxygen ignition occurs.

4.5.3 Effect of a ^{20}Ne forbidden transition

Martínez-Pinedo et al. (2014) discuss the non-unique second forbidden transition from the 0^+ ground state of ^{20}Ne to the 2^+ ground state of ^{20}F. The matrix element for this transition only has an experimental upper limit. They show that this transition can potentially dominate the rate for temperatures less than 9×10^8 K.[7]

---

[7]The results of both Martínez-Pinedo et al. (2014) and of this work are obtained by treating the phase space factor of this second forbidden transition as that of an allowed transition. As discussed by Martínez-Pinedo et al. (2014), the true shape factor could contain additional powers of the energy, which would further increase the rate, and can potentially offset the possibility that the matrix element is below the
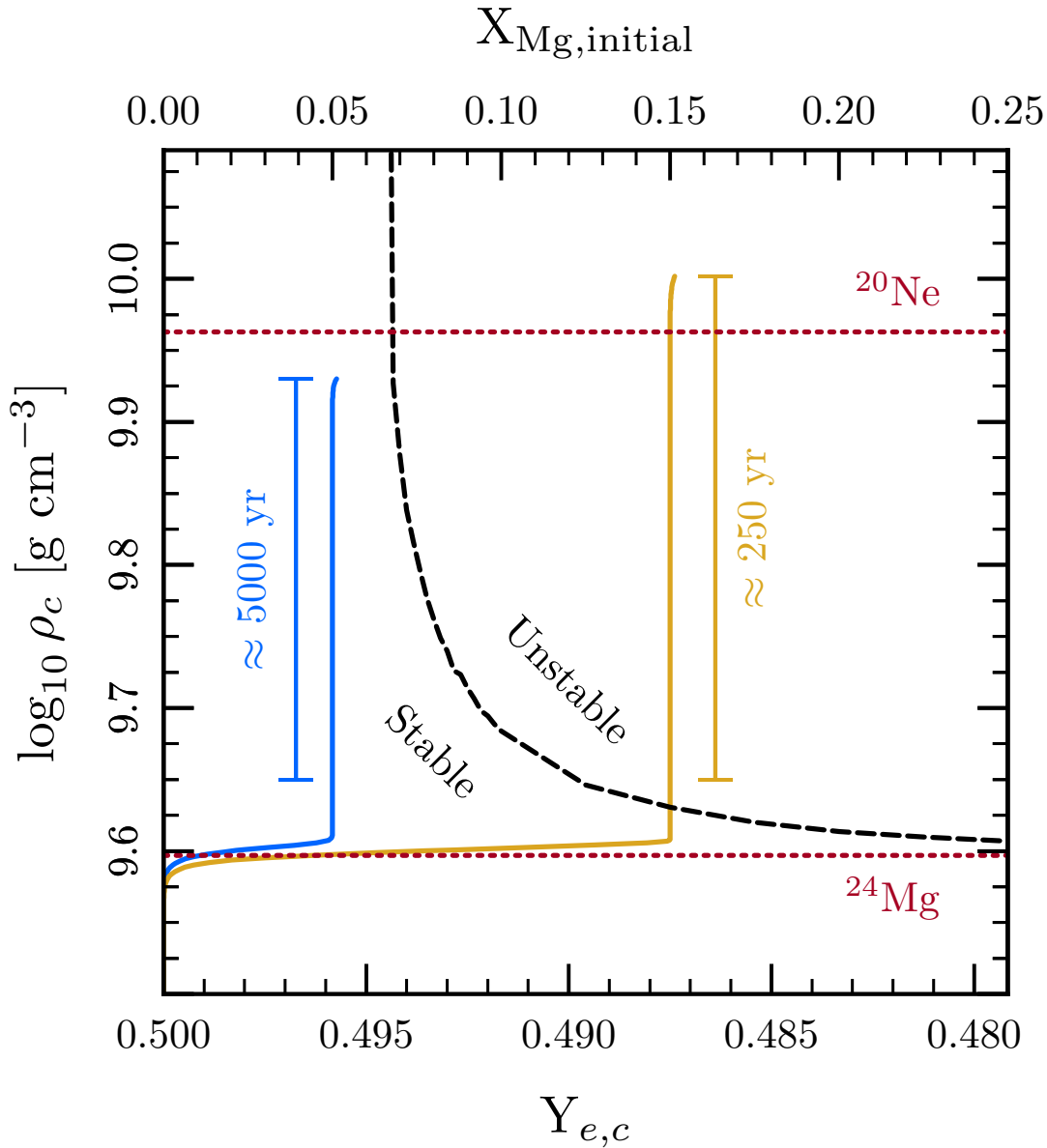
Figure 4.9: The evolution of the central electron fraction and central density for two values of X_{Mg} (blue and yellow solid lines). The time elapsed during the evolution from $\log_{10} \rho = 9.65$ to the onset of ^{20}Ne captures is indicated next to each track. The dashed line shows the stability curve for a zero temperature white dwarf which neutronizes to the value of $Y_{e,c}$ shown on the x-axis at a density of $\log_{10} \rho = 9.6$. The dotted red lines show the threshold electron capture densities for ^{20}Ne and ^{24}Mg. For $X_{\mathrm{Mg}} \gtrsim 0.07$, the onset of $A = 24$ electron captures reduces Y_e such that subsequent compression drives the equivalent zero temperature models into a dynamically unstable region of parameter space. Past this point, the contraction accelerates significantly (as shown in Fig. 4.8). In these cases, ^{24}Mg captures alone have assured collapse.
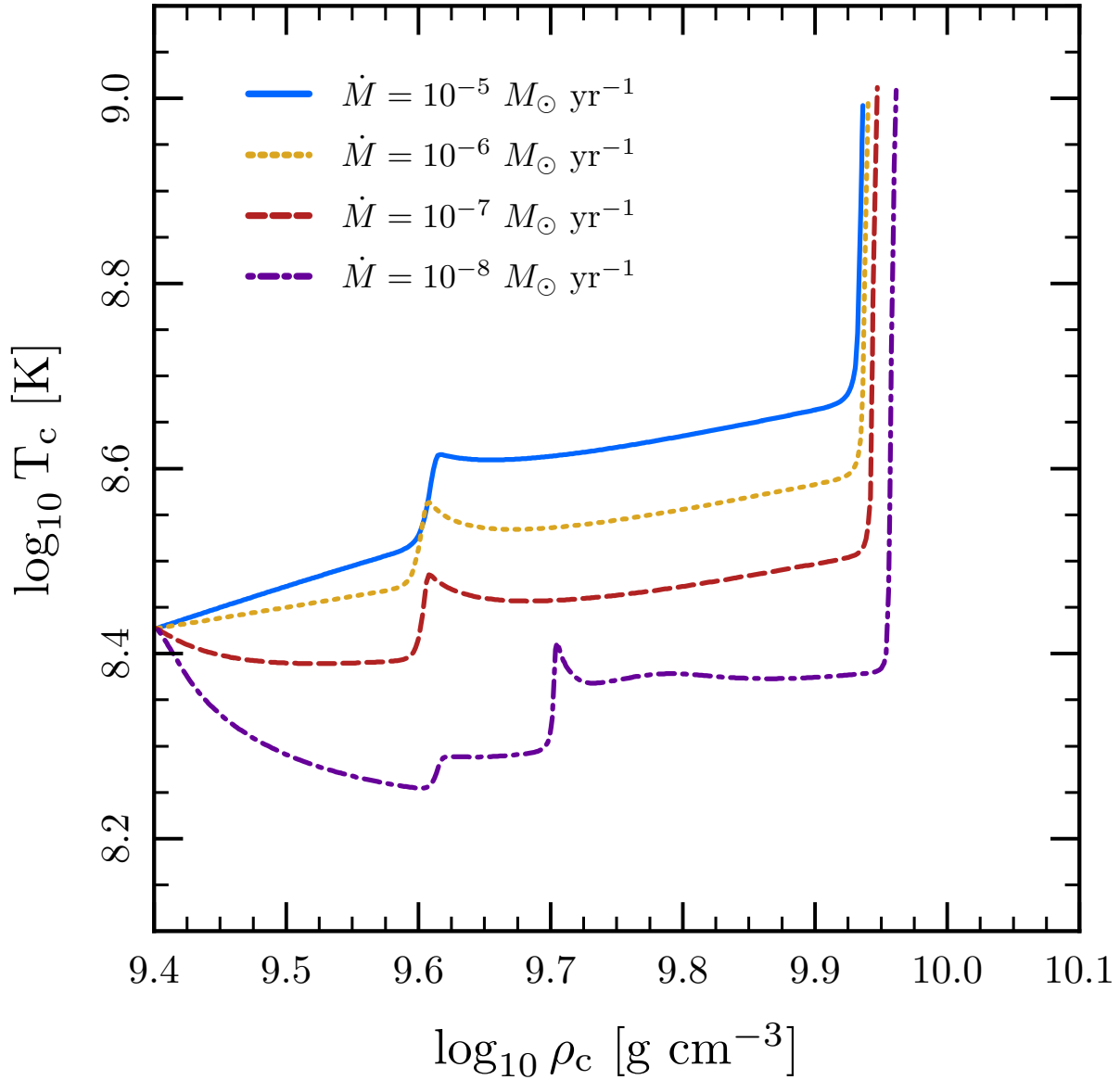
Figure 4.10: The fiducial model evolved with different values of $\dot{M}$. The central density at which the $A = 20$ captures occur depends weakly on the accretion rate. At $\dot{M} = 10^{-8} M_\odot \, \mathrm{yr}^{-1}$ the central temperature remains low enough that the ^{24}Mg and ^{24}Na captures occur at two separate critical densities. The dependence of the oxygen ignition density on $\dot{M}$ is weak.
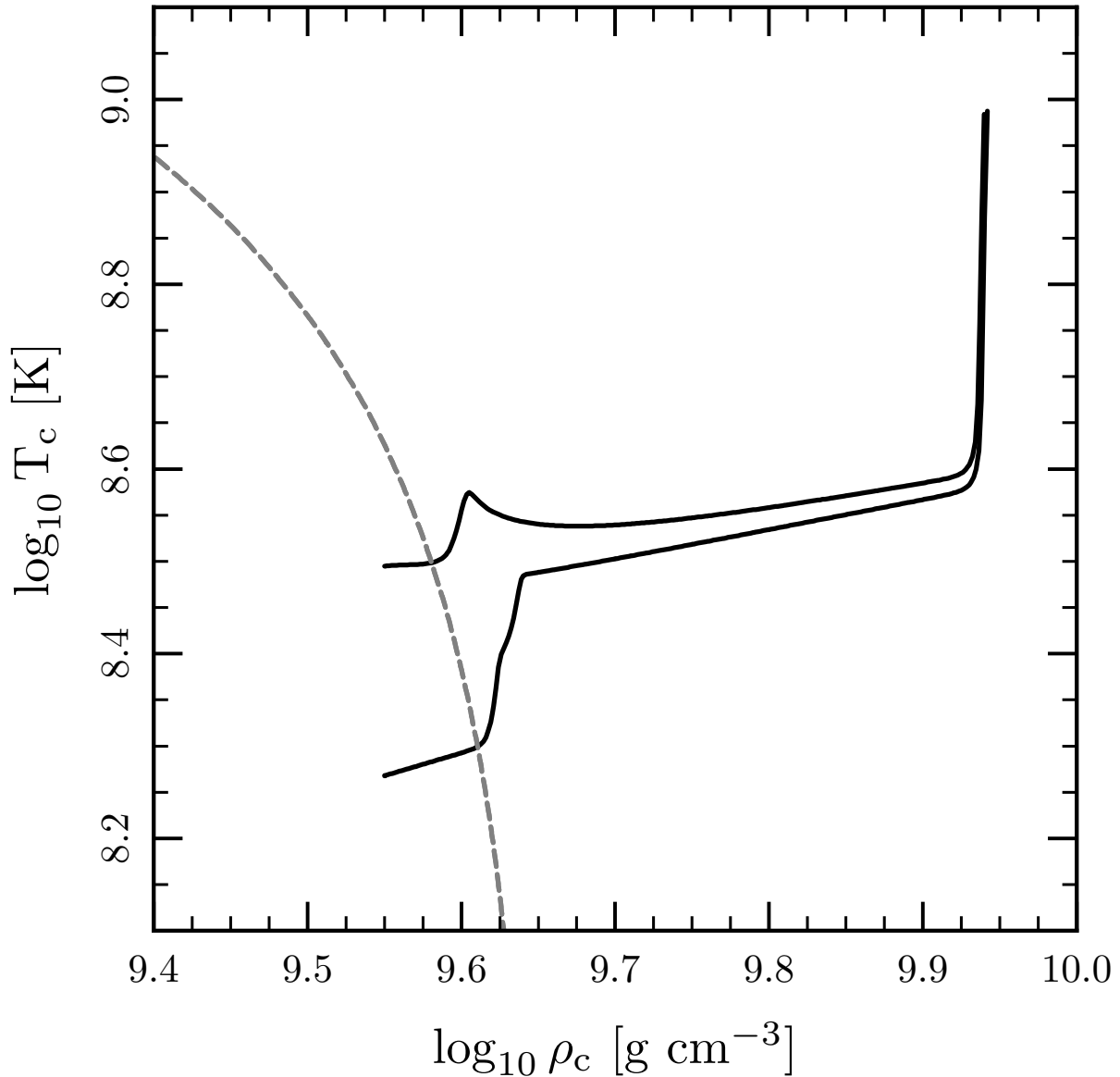
Figure 4.11: An illustration that the oxygen ignition density is independent of the initial central temperature. The models begin with $\log_{10} \rho_c \approx 9.55$, before the $A = 24$ e-captures. The grey dashed lines show when $t_{\text{capture}} = t_{\text{compress}}$ for ^{24}Mg and the models show the expected temperature dependence for the $A = 24$ captures. However, by the time the $A = 20$ captures occur, the temperature differences have been erased by neutrino cooling and compressional heating, and thus there is little effect on the density at which oxygen ignition occurs.
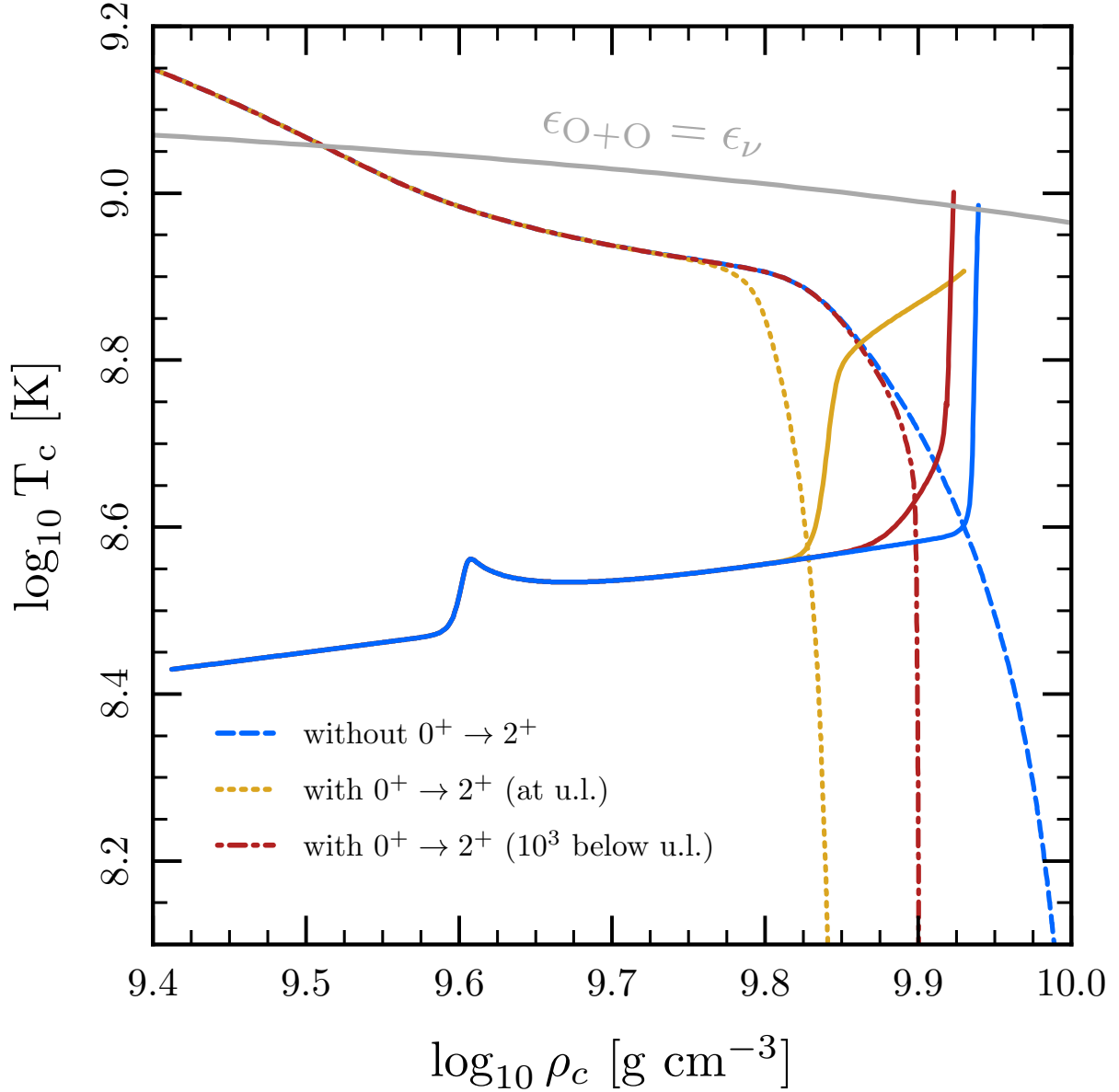
Figure 4.12: The effect of the second forbidden transition from the 0^+ ground state of ^{20}Ne to the 2^+ ground state of ^{20}F. The dotted, dashed, and dash-dotted lines show where the timescale for ^{20}Ne captures is equal to the fiducial compression timescale (10^4 yr) for different values of the matrix element (see plot legend). The solid lines of matching color show the evolution of the fiducial MESA model using these rates. While the onset of ^{20}Ne captures shifts significantly if the $0^+ \rightarrow 2^+$ transition is at the experimental upper limit, the shift in the density at which oxygen ignition occurs is substantially smaller.

This transition can affect the critical density at which ^{20}Ne captures begin. The broken lines in Fig. 4.12 shows the critical curves for ^{20}Ne capture obtained by setting the capture rate equal to the fiducial compression rate, corresponding to $\dot{M} = 10^{-6}\,\mathrm{M_\odot\,yr^{-1}}$. With the matrix element at the current experimental upper limit, the onset of captures is shifted to lower density (0.15 dex in $\log_{10}\rho$). At a value a factor of 10^3 below the upper limit, the shift is very approximately halved (depending on the temperature). At a value a factor of 10^6 below the upper limit, the transition ceases to have a substantial effect.

The solid lines in Fig. 4.12 show the evolution of our fiducial model with each of these different choices for the strength of this transition. While the choice substantially affects the onset of ^{20}Ne captures, it has a less significant effect on the density for oxygen ignition. Unlike the other transitions, which reach the critical capture timescale while they are sub-threshold, this transition is super-threshold. Correspondingly, the electron capture rate is less temperature sensitive. Its less rapid increase, coupled with the compression timescale dropping due to the decrease in Y_e, gives time for the core density to increase before the onset of oxygen ignition.

In the calculation with the transition at the upper limit (solid yellow line), the central temperature does not reach the oxygen ignition line. This is because the thermal structure of the remnant is such that ignition occurs mildly off-center. Our future calculations will determine whether this has any effect on the ensuing evolution.

4.6 Discussion

As described by Miyaji et al. (1980), the final outcome of an ONeMg core as it approaches the Chandrasekhar mass, either explosion or collapse, is determined by a competition between the energy release from the outgoing oxygen deflagration and the energy losses due to electron captures on the post-deflagration material, which has burned to nuclear statistical equilibrium (NSE).

As discussed in § 4.3, the small length scale of the deflagration means that we are unable to follow this phase with the MESA calculations presented in this paper. However, in lieu of a full calculation, we present a few order-of-magnitude estimates relevant to the outcome.

At the time of collapse, the total energy of our fiducial white dwarf is $E \approx -6 \times 10^{50}\,\mathrm{erg}$. Oxygen burning to NSE yields approximately $1\,\mathrm{MeV}$ per baryon, meaning the energy release from burning $0.3\,\mathrm{M_\odot}$ of material can unbind the white dwarf. This energy release is required for the deflagration wave to significantly change the structure of the star. Prior to the deflagration wave burning through $\approx 0.3 M_\odot$ of material, the structure of the WD core will remain relatively unchanged unless electron captures cause collapse. If the deflagration moves at some fraction f of the sound speed, the timescale for it to propagate though the central $0.3 M_\odot$ is

$$t_d \approx \int_0^{M_r=0.3M_\odot} \frac{dr}{f c_s} \approx 1\,\mathrm{s}\left(\frac{0.03}{f}\right)\,, \tag{4.24}$$

---

current experimental upper limit.

where we have evaluated the integral using the structure of our MESA model at the end of the calculation.

Nomoto & Kondo (1991) found that the critical deflagration speed that demarcated the boundary between a model that explodes and a model that collapses was $f \approx 0.03$. The work of Timmes & Woosley (1992), which simulated conductively-propagating oxygen deflagrations in detail gives a fitting formula for the laminar deflagration speed of an oxygen flame of

$$v_d = 51.8 \, \text{km s}^{-1} \left(\frac{\rho}{6 \times 10^9 \, \text{g cm}^{-3}} \right)^{1.06} \left(\frac{X_O}{0.6} \right)^{0.688} . \tag{4.25}$$

At $\rho \approx 9 \times 10^9 \, \text{g cm}^{-3}$ and $X_O = 0.5$, this gives $v_d \approx 70 \, \text{km s}^{-1}$, which corresponds to $f = v_d/c_s \approx 0.005$. Based on an analysis of the growth of the Rayleigh-Taylor instability, they conclude that these conductive flames are likely to remain stable. Therefore the laminar flame velocity is representative of the true flame speed in the inner part of the star. In particular, see figure 10 in Timmes & Woosley (1992), noting that $R(M_r = 0.3 M_\odot) \approx 300 \, \text{km}$.

Based on these flame calculations, as well as several KEPLER simulations using these speeds, Timmes & Woosley (1992) concluded that above a core density of $9 \times 10^9 \, \text{g cm}^{-3}$ the white dwarfs should collapse to a neutron star. The lowest central density at which oxygen ignition occurred in our parameter study (§ 4.5) was $\log_{10} \rho_c = 9.93$. That is $\rho_c \approx 8.5 \times 10^9 \, \text{g cm}^{-3}$, which is only marginally below this critical value.

The timescale on which the core is neutronizing due to electron captures on the NSE-composition material can be written as $t_n = (d \ln Y_e/dt)^{-1}$. The methods presented in this paper are not appropriate for calculating weak rates in NSE material. Instead, we take $\dot{Y}_e$ from tables generated by Seitenzahl et al. (2009). Fig. 4.13 shows the neutronization timescale as a function of density and temperature for $Y_e = 0.49$, the approximate central value in our fiducial model at oxygen ignition. Once the deflagration forms, the density of the post-deflagration material is less than the cold, upstream material. The MESA models reach oxygen ignition at $\log_{10} \rho_c \approx 10$, where this density change is small, $\Delta \rho/\rho \approx 0.1$ (Timmes & Woosley 1992). Therefore, the density of the post-deflagration ash will be approximately the same as the density at which oxygen ignites, so Fig. 4.13 indicates that the relevant neutronization timescale is approximately 0.2 s.

This estimate of the neutronization timescale is sufficiently shorter than the timescale on which the deflagration wave unbinds the star (equation 4.24) that it suggests that the end result of oxygen ignition following e-captures on ^{20}Ne will be collapse to a NS rather than a thermonuclear explosion. Future work will clarify this in the context of full-star simulations.

4.7 Conclusions

We have provided an updated analytic and numerical understanding of the evolution of accreting and compressing ONeMg cores up to the initiation of oxygen burning in the core. This study was enabled by new capabilities of the MESA (Paxton et al. 2011, 2013, 2015) stellar evolution code. In particular, we have implemented a highly accurate treatment of
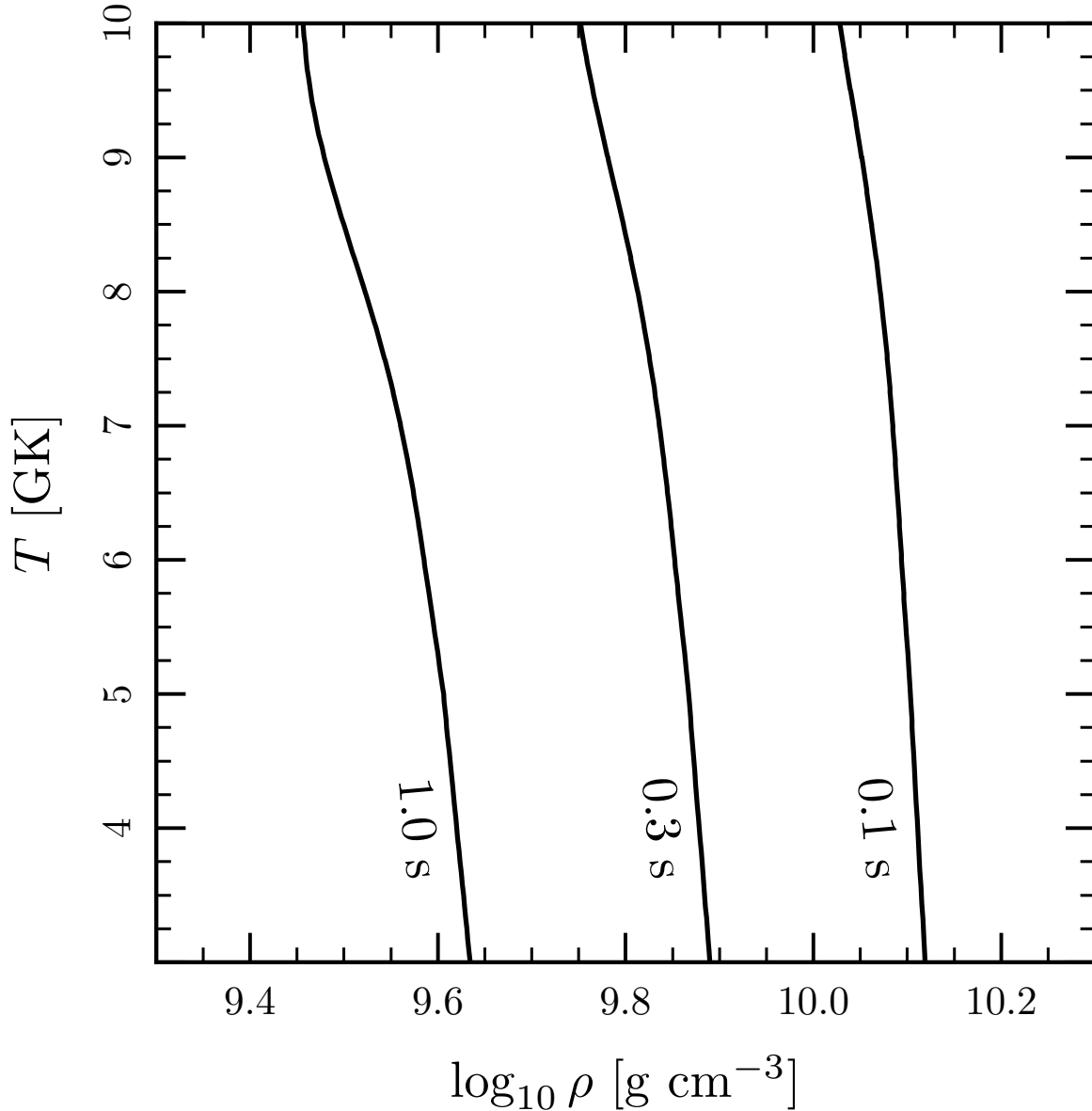
Figure 4.13: The neutronization timescale for $Y_e = 0.49$, which is roughly the central value of Y_e at the end of our fiducial calculation. Contours are labeled by timescale. This uses the NSE electron capture rates from Seitenzahl et al. (2009). Since our compressing ONeMg cores reach oxygen ignition at $\log_{10} \rho_c \approx 10$, the relevant neutronization timescale is approximately 0.2 s. This is less than the timescale for the O deflagration wave to release enough energy to unbind the star (equation 4.24), suggesting that collapse to a NS will ensue.

the key electron capture rates (on $A = 20$ and 24 nuclei) using modern microphysics from Martínez-Pinedo et al. (2014), which is summarized in Appendix 4.A.

We have demonstrated analytically and numerically that neither ^{24}Mg or ^{20}Ne captures release sufficient heat to generate convection in the core. Instead, the core undergoes a thermal runaway triggered by the energy released by ^{20}Ne captures. This centrally concentrated runaway initiates oxygen burning and launches an outgoing oxygen deflagration wave at a time when the central density is at least $8.5 \times 10^9 \, \text{g cm}^{-3}$. Based on order of magnitude estimates and previous work of Timmes & Woosley (1992), we expect objects which ignite oxygen at such high densities will collapse and form a neutron star due to continued electron captures on the NSE ashes produced by oxygen burning.

Given the sensitivity of the final outcome of compressing ONeMg cores to the central density at the time oxygen burning begins (see §4.6), we also performed a parameter study which demonstrated the influence of a number of factors on this density. We investigated the effects of varying the initial ^{24}Mg fraction (§ 4.5.1), the initial central temperature and accretion rate (§ 4.5.2), as well as the potential inclusion of a particular forbidden transition (§ 4.5.3). Figures 4.8 and 4.9 demonstrate that values of $X_{\text{Mg}} \gtrsim 0.07$ cause the core to contract more rapidly after $A = 24$ the captures, which leads to oxygen ignition at higher densities (thus further favoring collapse to form a neutron star). We also demonstrated the importance of the balance between neutrino cooling and compressional heating in setting the central temperature of ONeMg cores during much of their evolution (Paczyński 1971). This implies that the core typically loses memory of its initial central temperature.

The approach of an ONeMg core to the Chandrasekhar mass is relevant to the late stages of evolution for super asymptotic giant branch stars, binary systems with an accreting ONeMg WD, and the remnants of WD-WD mergers. Our calculations here are an important step in producing more realistic progenitor models for these studies.
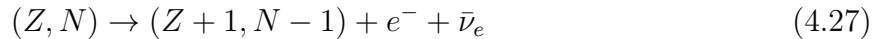
Acknowledgments

4.A Physics of electron-capture and beta-decay

We are interested in the electron-capture reaction

$$(Z, N) + e^- \rightarrow (Z - 1, N + 1) + \nu_e \tag{4.26}$$
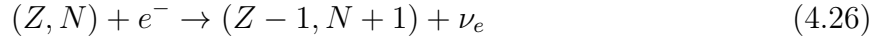
and its reverse reaction, β-decay

$$(Z, N) \rightarrow (Z + 1, N - 1) + e^- + \bar{\nu}_e \tag{4.27}$$

where Z and N are respectively the proton and neutron number of the nucleus. For nuclei in a dense plasma where the electrons are degenerate, the rates of these processes can depend sensitively on the density (though the electron distribution function) and temperature (though the occupation of nuclear energy levels and the electron distribution function). The neutrinos are able to free stream out of the star, and therefore neutrino phase-space is effectively unfilled. For a more thorough discussion of the physics of weak reactions in stellar environments, see e.g. Fuller et al. (1980, 1985).

This section summarizes a simple framework for the rates of these weak processes. More detailed microscopic calculations exist in the literature such as those presented in Oda et al. (1994). However, those particular tables are sufficiently sparse that numerical considerations related to interpolation cause us to elect to use rates calculated in the manner described here, rather than interpolate in tables from more detailed calculations.

The rate of the electron capture or β-decay transition from the i-th state of the parent nucleus to the j-th state of the daughter nucleus can be written as (e.g. Fuller et al. 1980)

$$\lambda_{ij} = \frac{\ln 2}{(ft)_{ij}} I(\mu_e, T, Q_{ij}), \tag{4.28}$$

where (ft) is the comparative half-life and can be either measured experimentally or theoretically calculated from the weak-interaction nuclear matrix elements. I is a phase space factor which depends on the temperature T, electron chemical potential μ_e, and the energy difference Q_{ij} between the (i-th) parent and (j-th) daughter nuclear states.

$$Q_{ij} = (\mu_p - \mu_d) + E_i - E_j \ , \tag{4.29}$$

where μ_p and μ_d are the chemical potentials of the nuclei. For a classical ideal gas, the chemical potential is

$$\mu_I = m_I c^2 + kT \ln \left(\frac{n_I}{n_q} \right) \ , \tag{4.30}$$

where m_I is the rest mass, n_I is the number density, and $n_q = (2\pi m_I kT/h^2)^{3/2}$. Therefore,

$$Q_{ij} = (M_p - M_d) c^2 + kT \ln \left(\frac{n_p}{n_d} \right) + E_i - E_j \tag{4.31}$$

where M_p and M_d are the nuclear rest masses of the parent and daughter nuclei, respectively. Since $|M_p - M_d| c^2 \approx 5\,\text{MeV}$ for the isotopes we consider and we restrict ourselves to temperatures $T < 10^9\,\text{K}$ (so $kT < 100\,\text{keV}$), the term $kT \ln\left(\frac{n_p}{n_d}\right)$ is negligible in comparison and we discard it, leaving

$$Q_{ij} = (M_p - M_d)\,c^2 + E_i - E_j \ . \tag{4.32}$$

Though not generally true, for the set of transitions that we consider, this definition means that $Q_{ij} < 0$ for e-capture and $Q_{ij} > 0$ for β-decay.

We work in the allowed approximation, which neglects all total lepton angular momentum ($L = 0$). This restricts us to the following transitions and corresponding selection rules (e.g. Commins 1973): Fermi transitions, where the total lepton spin is $S = 0$, and therefore the initial and final nuclear spins are equal ($J_i = J_j$), and Gamow-Teller transitions, where $S = 1$, and therefore $J_i = J_j, J_j \pm 1$ (excluding $J_i = J_f = 0$). In both cases, these is no parity change: $\pi_i \pi_f = +1$.

At low temperature, the electron chemical potential is approximately the Fermi energy E_F (the first correction enters at order $(kT/E_F)^2$), and so we use the terms Fermi energy and electron chemical potential interchangeably. In the relativistic limit, the electron chemical potential can be approximated as

$$\mu_e \approx E_F = 5.16 \left(\frac{\rho Y_e}{10^9 \text{g cm}^{-3}}\right)^{1/3} \text{MeV}, \tag{4.33}$$

where $Y_e = \sum_i Z_i X_i / A_i$ is the electron fraction. Z_i, X_i, and A_i are respectively the charge, mass fraction, and atomic mass of the i-th species.

The total rate of the process is the sum of the individual transition rates from the i-th parent state to the j-th daughter state, λ_{ij}, weighted by the occupation probability of the i-th parent state, p_i.

$$\lambda_{\text{total}} = \sum_i p_i \sum_j \lambda_{ij}, \tag{4.34}$$

The i-sum is over all parent states and the j-sum is over all daughter states. We will always assume that the nuclear states are populated with a thermal (Boltzmann) distribution. Some parent nuclei preferentially capture into excited daughter states, but these excited states decay via γ-ray emission with a typical timescale $\sim 10^{-12}$ s. Therefore the level population returns to a thermal distribution on a timescale much shorter than the evolutionary

timescales of interest.[8] The occupation probability is

$$p_i = \frac{2J_i + 1}{P(T)} \exp\left(-\beta E_i\right) \ ,$$

(4.35)

where $P(T)$, the nuclear partition function is $P(T) = \sum_i (2J_i + 1)e^{-\beta E_i}$ and we define $\beta = (kT)^{-1}$.

The remainder of this section considers the rate of a single allowed ($L = 0$) transition in detail, and so for convenience we drop the i,j subscripts. In the case of electron capture, the phase space factor is (e.g., Fuller et al. 1980)

$$I_{\text{ec}} = \frac{1}{(m_e c^2)^5} \int_{-Q}^{\infty} \frac{E_e^2 E_\nu^2}{1 + \exp[\beta(E_e - \mu_e)]} G(Z, E_e) dE_e \ ,$$

(4.36)

along with the energy conservation relationship $E_e + Q = E_\nu$. The quantity G is defined as

$$G(Z, E_e) = \frac{\sqrt{E_e^2 - (m_e c^2)^2}}{E_e} F(Z, E_e)$$

(4.37)

where $F(Z, E_e)$ is the relativistic Coulomb barrier factor (Gove & Martin 1971). We make the approximation that the electrons are relativistic. In this limit,

$$G(Z, E_e) \approx \left(\frac{4\pi E_e R}{hc}\right)^{-\alpha^2 Z^2} \exp\left(\pi\alpha Z\right) \ ,$$

(4.38)

where α is the fine structure constant and R is the size of the nucleus (Fuller et al. 1980). We are considering nuclei with $Z \approx 10$, $A \approx 20$ (and so $R \approx 3\,\text{fm}$), at densities such that $E_e \approx 5\,\text{MeV}$. Therefore, the value of the first term is $\left(\frac{4\pi E_e R}{hc}\right)^{-\alpha^2 Z^2} \approx 0.999$, with an extremely weak E_e and R dependence (since $\alpha^2 Z^2 \approx 0.005$). Therefore we treat $G(Z, E_e)$ as a constant with a value of $\exp(\pi\alpha Z)$.

Changing to dimensionless variables $\epsilon \equiv \frac{E}{m_e c^2}$ and $q \equiv \frac{Q}{m_e c^2}$, the phase space integral becomes

$$I_{\text{ec}} = e^{\pi\alpha Z} \int_{-q}^{\infty} \frac{\epsilon^2(\epsilon + q)^2}{1 + \exp[\beta m_e c^2(\epsilon - \mu_e)]} d\epsilon \quad .$$

(4.39)

We rewrite this integral in simpler form as

$$I_{\text{ec}} = \frac{e^{\pi\alpha Z}}{(\beta m_e c^2)^5} \left[F_4(\eta + \zeta) - 2\zeta F_3(\eta + \zeta) + \zeta^2 F_2(\eta + \zeta) \right] \ ,$$

(4.40)

---

[8]There is one case in which this hierarchy of timescales is not so obvious. The first excited state of ^{24}Na is metastable with a half-life of 2×10^{-2} s (Firestone 2007b) and ground state of ^{24}Mg preferentially captures into this excited state. If the capture rate from this excited state to ^{24}Ne were approximately equal or greater than the rate of decay via γ-ray emission, the relative state populations would be effectively non-thermal. Using the parameters of this transition as listed in Table 4.1, the capture timescale is approximately equal to the half-life at a critical density of $\log_{10} \rho \approx 10.5$ (for $Y_e \approx 0.5$), which is safely outside of the density range that we consider in this work.

where we have defined the quantities $\eta = \beta\mu_e$ and $\zeta = \beta q$ and

$$F_k(y) = \int_0^\infty \frac{x^k}{1 + \exp(x - y)} dx \quad , \tag{4.41}$$

is the complete Fermi integral. Evaluating the rate requires evaluating three complete Fermi integrals, for which efficient numerical routines exist (e.g. Aparicio 1998).

In addition to the e-capture rate, we need the rate of energy loss via neutrinos, which for a single transition can be written as

$$\varepsilon_{\nu,ij} = \frac{m_e c^2 \ln 2}{(ft)_{ij}} J(\mu_e, T, Q_{ij}) , \tag{4.42}$$

where J is phase space factor, defined by an integral similar to equation (4.36), except with an additional power of the neutrino energy:

$$J_{ec} = \frac{1}{(m_e c^2)^6} \int_{-Q}^\infty \frac{E_e^2 E_\nu^3}{1 + \exp[\beta(E_e - \mu_e)]} G(Z, E_e) dE_e . \tag{4.43}$$

In terms of complete Fermi integrals, this is

$$J_{ec} = \frac{e^{\pi\alpha Z}}{(\beta m_e c^2)^6} \left[F_5(\eta + \zeta) - 2\zeta F_4(\eta + \zeta) + \zeta^2 F_3(\eta + \zeta) \right] . \tag{4.44}$$

The total neutrino loss rate can calculated via an occupation-weighted average, analogous to that used to calculated the total rate in equation (4.34).

In the case of β-decay, the phase space factor is

$$I_\beta = \int_{m_e c^2}^Q \frac{E_e^2 E_\nu^2}{1 + \exp[-\beta(E - \mu_e)]} G(Z, E) dE_e , \tag{4.45}$$

and energy conservation $Q = E_e + E_\nu$. Following the same procedure as the electron capture case[9]

$$I_\beta = e^{\pi\alpha Z} \int_1^q \frac{\epsilon^2 (\epsilon - q)^2}{1 + \exp[-\beta m_e c^2 (\epsilon - \mu_e)]} d\epsilon . \tag{4.46}$$

We can convert this integral into a sum of complete Fermi integrals by making use of the mathematical identity

$$\int_0^b \frac{x^k}{1 + \exp(x - y)} = F_k(y) - \sum_{j=0}^k \binom{k}{j} b^{k-j} F_j(y - b) . \tag{4.47}$$

---

[9]It is perhaps less obvious that the assumption that the electrons are relativistic is justified here, given the lower integration limit. But because electron phase space is only empty near or above the Fermi energy (and $\mu_e > 5\,\mathrm{MeV}$ at the densities of interest), the integrand is only significant at the upper portion of the integration range where this approximation is justified.

Defining $\vartheta \equiv \beta m_e c^2$, this yields the following expression:

$$
\begin{aligned}
I_\beta =\ & \frac{e^{\pi\alpha Z}}{(\beta m_e c^2)^5} \left[F_4(\zeta - \eta) - 2\zeta F_3(\zeta - \eta) + \zeta^2 F_2(\zeta - \eta) \right] - \\
& \frac{e^{\pi\alpha Z}}{(\beta m_e c^2)^5} \left[F_4(\vartheta - \eta) - \right. \\
& \qquad F_3(\vartheta - \eta) \times (4\vartheta - 2\zeta) + \\
& \qquad F_2(\vartheta - \eta) \times \left(6\vartheta^2 - 6\vartheta\zeta + \zeta^2 \right) - \\
& \qquad F_1(\vartheta - \eta) \times \left(4\vartheta^3 - 6\vartheta^2\zeta + 2\vartheta\zeta^2 \right) + \\
& \qquad \left. F_0(\vartheta - \eta) \times \left(\vartheta^4 - 2\vartheta^3\zeta + \vartheta^2\zeta^2 \right) \right] \ .
\end{aligned}
\tag{4.48}
$$

Similarly, the factor J_β necessary to calculate the neutrino loss rate is

$$
J_\beta = \int_{m_e c^2}^Q \frac{E_e^2 E_\nu^3}{1 + \exp[-\beta(E - \mu_e)]} G(Z, E) dE_e \ ,
\tag{4.49}
$$

which can be written as

$$
\begin{aligned}
J_\beta =\ & \frac{e^{\pi\alpha Z}}{(\beta m_e c^2)^6} \left[F_5(\zeta - \eta) - 2\zeta F_4(\zeta - \eta) + \zeta^2 F_3(\zeta - \eta) \right] - \\
& \frac{e^{\pi\alpha Z}}{(\beta m_e c^2)^6} \left[F_5(\vartheta - \eta) - \right. \\
& \qquad F_4(\vartheta - \eta) \times (5\vartheta - 3\zeta) + \\
& \qquad F_3(\vartheta - \eta) \times \left(10\vartheta^2 - 12\vartheta\zeta + 3\zeta^2 \right) - \\
& \qquad F_2(\vartheta - \eta) \times \left(10\vartheta^3 - 18\vartheta^2\zeta + 9\vartheta\zeta^2 - \zeta^3 \right) + \\
& \qquad F_1(\vartheta - \eta) \times \left(5\vartheta^4 - 12\vartheta^3\zeta + 9\vartheta^2\zeta^2 - 2\vartheta\zeta^3 \right) - \\
& \qquad \left. F_0(\vartheta - \eta) \times \left(\vartheta^5 - 3\vartheta^4\zeta + 3\vartheta^3\zeta^2 - \vartheta^2\zeta^3 \right) \right] \ .
\end{aligned}
\tag{4.50}
$$

Given the reaction rates and neutrino energy loss rates, we can calculate the net heating rate of the plasma. The energy equation for material in the star is

$$
T \frac{ds}{dt} = -\frac{\partial L}{\partial M} + q_* + q_{\mathrm{ec}} + q_\beta
\tag{4.51}
$$

where q_{ec} and q_β account for the set of weak nuclear reactions we are considering separately and q_* includes all other heating and cooling sources such as thermal neutrino losses and other nuclear reactions. Under the assumption of thermal equilibrium, the energy released by the weak reactions depends only on the total reaction rate, the total neutrino loss rate, and the ion and electron chemical potentials. The energy generation rate (per capture or decay) is

$$
\varepsilon_{\mathrm{ec}} = (-\mu_{I,Z} + \mu_{I,Z-1} + \mu_e)\lambda_{\mathrm{ec}} - \varepsilon_{\nu,\mathrm{ec}}
\tag{4.52}
$$

$$
\varepsilon_\beta = (-\mu_{I,Z-1} + \mu_{I,Z} - \mu_e)\lambda_\beta - \varepsilon_{\nu,\beta}
\tag{4.53}
$$

where $\mu_{I,Z}$, $\mu_{I,Z-1}$ are the chemical potentials of the ions with those charges and μ_e is the chemical potential of the electron. Defining $Q_g \equiv Q_{00} = (M_p - M_d)c^2$, which implicitly making the same assumption used to derive equation (4.32), the specific energy generation rates are

$$q_{\mathrm{ec}} = \frac{n_{\mathrm{ec}}}{\rho} \varepsilon_{\mathrm{ec}} = \frac{n_{\mathrm{ec}}}{\rho} \left[(Q_{\mathrm{g}} + \mu_e)\lambda_{\mathrm{ec}} - \varepsilon_{\nu,\mathrm{ec}} \right] , \tag{4.54}$$

$$q_{\beta} = \frac{n_{\beta}}{\rho} \varepsilon_{\beta} = \frac{n_{\beta}}{\rho} \left[(Q_{\mathrm{g}} - \mu_e)\lambda_{\beta} - \varepsilon_{\nu,\beta} \right] , \tag{4.55}$$

where n_{ec} and n_{β} are the number densities of the species undergoing capture and decay. Therefore, given a list of nuclear levels and the (ft)-values for the transitions between them, we can calculate the rates of and energy generation rates from electron-capture and β-decay.

Using the above approach, it would be possible to generate tables whose points are spaced sufficiently closely, such that interpolation would no longer incur significant errors. But because MESA comes with fast quadrature routines to evaluate equation (4.41), it directly evaluates equations (4.40), (4.44), (4.48), and (4.50) each time one of the weak reaction rates is needed. While this is computationally inefficient, the overall speed of our calculations is sufficiently unaffected that we chose not to optimize this.

4.B Coulomb Corrections

In a dense plasma, the electrostatic interactions of the ions and electrons introduce corrections to the weak rates relative to rates which assume a Fermi gas of electrons and an ideal gas of ions (as do those presented in Appendix 4.A). The leading term in the Coulomb interaction energy for ion-ion interactions (e.g. Shapiro & Teukolsky 1983) is

$$E_{\mathrm{Coulomb}} = -\frac{9}{10} \frac{Z^2 e^2}{a_i} \tag{4.56}$$

where $a_i = \left(\frac{3}{4\pi n_i} \right)^{1/3}$ is the inter-ionic spacing. For $Z \approx 10$, $E_{\mathrm{Coulomb}} \approx -0.2 E_F$ indicating that the interactions are energetically important. The Coulomb interaction energy and the Fermi energy both scale $\propto \rho^{1/3}$ in the relativistic limit, which is the regime of interest since we primarily consider material with $\rho > 10^7 \, \mathrm{g \, cm^{-3}}$.

In this section, we discuss our treatment of these corrections, and compare our approach to previous work. Our treatment is most similar to that discussed in Appendix A of Juodagalvis et al. (2010). Fig. 4.15 illustrates the effects of including these corrections on the evolution of our fiducial model. The change in the evolution is similar to that observed by Gutierrez et al. (1996).

4.B.1 Equation of State

Most straightforwardly, a Coulomb term appears in the ion equation of state. This affects the weak reaction rates, because at a fixed total pressure the electron density is lower. The

MESA equation of state routines, which in the thermodynamic regime of interest are based on the "Helmholtz" equation of state (Timmes & Swesty 2000), include these terms based on the work of Yakovlev & Shalybkov (1989). Fig. 4.14 shows the EOS used by MESA over the relevant portion of density-temperature space for an ONe composition. The solid line shows the temperature density profile of a representative accreting ONe WD model. All of the model is in the part of parameter space covered by the "Helmholtz" EOS (labeled HELM).

4.B.2   Ion Chemical Potential

The energy required to remove an ion of one species and create an ion of another species is given by the difference in the ion chemical potentials. Since electron-capture and beta-decay change the ion charge, the presence of the Coulomb interaction energy changes the energy difference between the parent and daughter nuclear states. The interaction energy is negative, and so decreasing the charge of the nucleus (as electron-capture reactions do) requires additional energy, which will therefore shift the onset of electron captures to higher density.

To calculate this shift, we use the excess (that is, the part in addition to the ideal contribution) ion chemical potential μ_{ex} developed in the following series of papers: Chabrier & Potekhin (1998); Potekhin & Chabrier (2000); Potekhin et al. (2009). We incorporate this effect by shifting the value of Q, as defined in equation (4.29), by an amount $\Delta E = \mu_{ex,p} - \mu_{ex,d}$. This shift,

$$Q' = Q + \Delta E \tag{4.57}$$

then enters the calculation of the phase space factors and the energy generation rates. In Fig. 4.15, the red dotted line labeled "ion chemical potential", shows the effect of including of these corrections.

4.B.3   Screening

The electron density relevant to the reaction rate is not the average electron density, but rather the electron density at the position of the nucleus. Itoh et al. (2002) calculated the value of this screening correction using linear response theory. This correction can be correctly accounted for as a shift in the value of the electron chemical potential that enters the phase space factor.

$$\mu'_e = \mu_e + V_s \tag{4.58}$$

However, this correction does not enter the energy generation rates because it has not changed the energy cost to add or remove an electron from the bulk Fermi sea, which is the net effect of a capture or decay. In Fig. 4.15, the yellow dashed line labeled "electron screening", shows the effect of including these corrections.
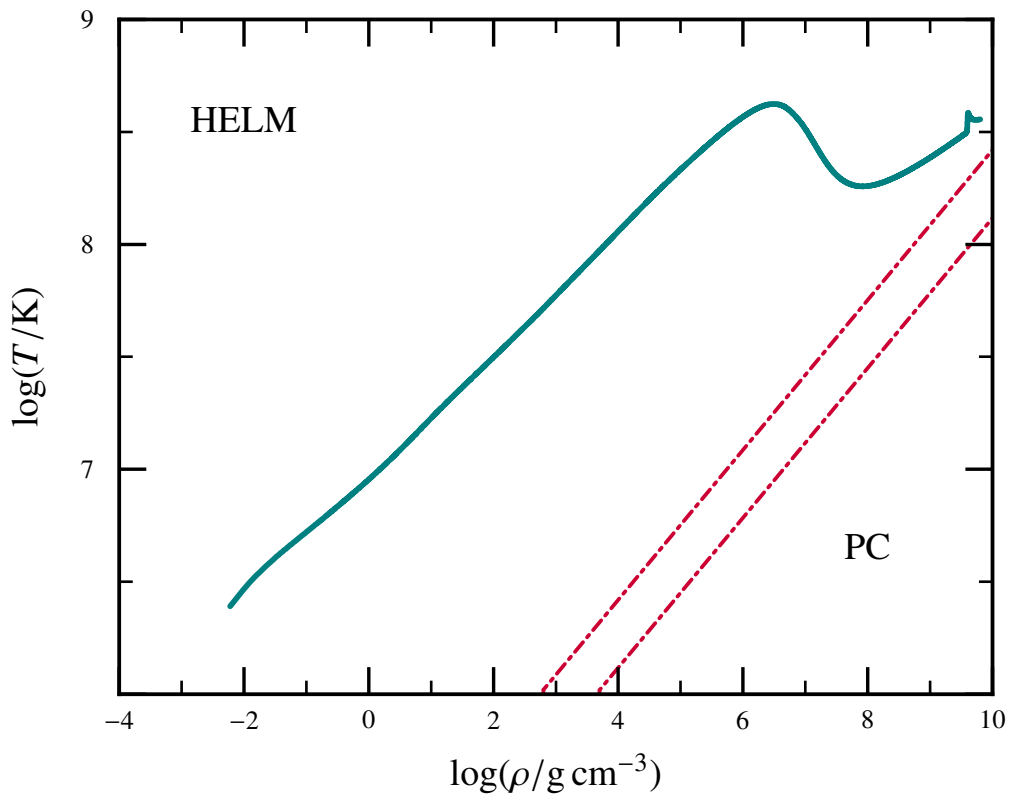
Figure 4.14: The regions in density-temperature space of the MESA equation of state, which is an amalgamation of other EOSes. HELM is the "Helmholtz" EOS (Timmes & Swesty 2000). PC is the EOS from Potekhin & Chabrier (2010). The dot-dashed lines show the blend region between the two. The solid line shows the profile of a representative accreting ONe WD model.
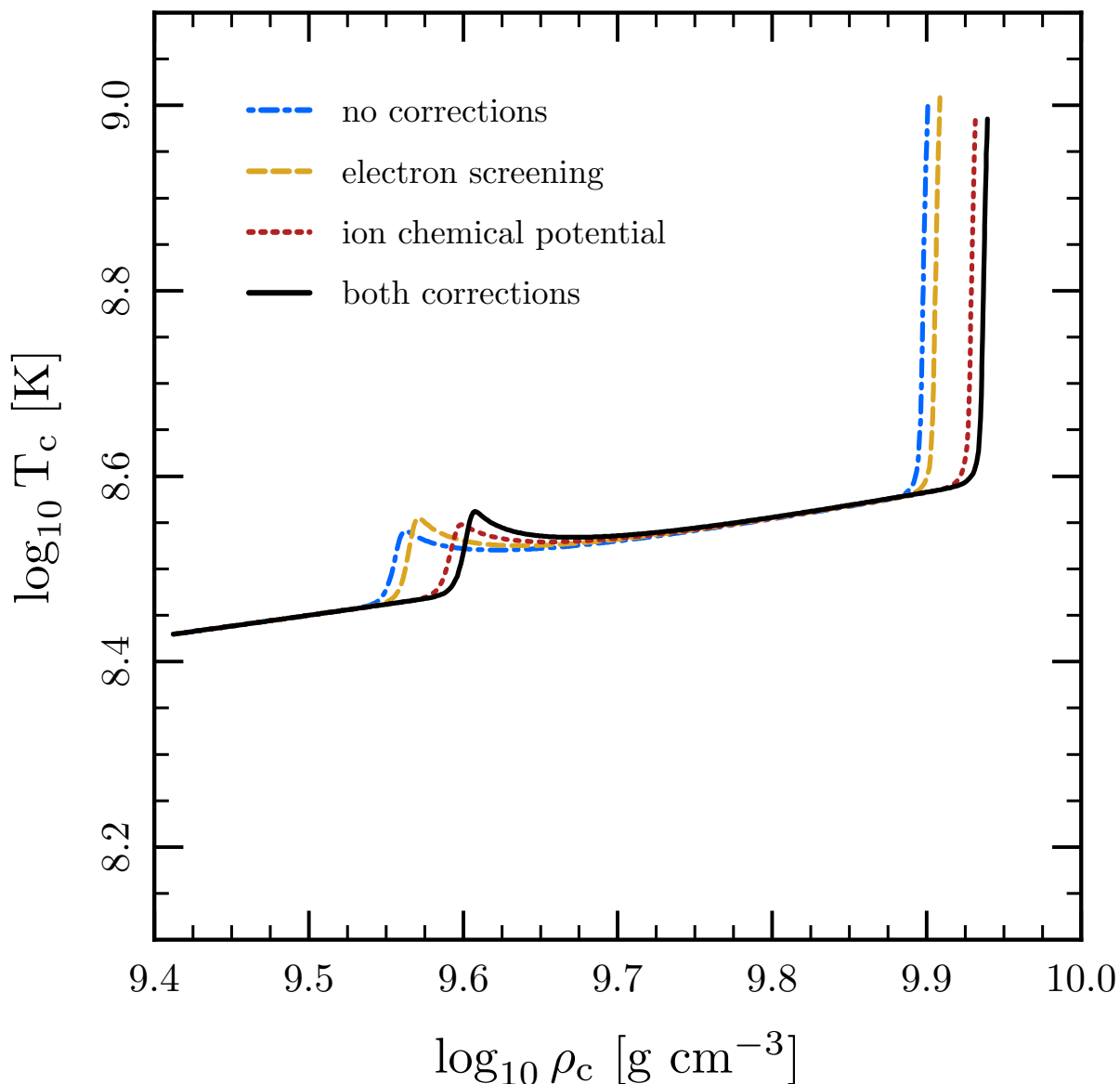
Figure 4.15: Illustration of the effect of Coulomb corrections on the evolution of the central density and temperature of the accreting core. (To better understand this plot the reader may first want to consult Fig. 4.3 and the surrounding discussion.) All calculations include the corrections to the equation of state (§ 4.B.1). The dashed-dotted blue line shows the result with no other corrections. The dashed yellow line shows the effect of the inclusion of the screening corrections (§ 4.B.3). The dotted red line shows the effect of the inclusion of the corrections to the ion chemical potential (§ 4.B.2).The solid black line shows the result with both corrections included, which is the default choice for our calculations. The primary effect of including these corrections is a increase (of about 0.05 dex) in the density at which electron captures occur.

4.B.4   Comparison with Previous Work

The effect discussed in §4.B.2, which is the dominant Coulomb correction, has previously been included in studies of ONeMg cores (e.g. Gutierrez et al. 1996; Takahashi et al. 2013). The approach taken in these studies is to include this effect as a shift in the *electron* chemical potential

$$\mu'_e = \mu_e - \Delta E \tag{4.59}$$

and to use this modified electron chemical potential in the evaluation of the rates. This approach is conceptually incorrect, because μ_e and Q enter the rate expression in different ways, as can be seen in equation (4.36). However, given a table of $\lambda_{ec}(\rho, T)$, one has no ability to shift Q, so the only way to correct the rate is to shift the relation between μ_e and ρ. In the sub-threshold case (see equation 4.6), the most important term is the exponential, which *is* symmetric in Q and μ_e, and so this approach does not lead to a substantial quantitative error in the rate.

When making this correction both Gutierrez et al. (1996) and Takahashi et al. (2013) follow Couch & Loumos (1974) and use the form of the ion free energy from Dewitt et al. (1973). There has been progress in calculating the free energy of electron-ion plasmas in the last few decades. As discussed in § 4.B.2, we use the fitting formula for the free energy from Potekhin et al. (2009). In their work on electron capture rates in NSE material, Juodagalvis et al. (2010) use the formula quoted in Ichimaru (1993). The results of Ichimaru (1993) and Potekhin et al. (2009) agree, while the shift calculated following Dewitt et al. (1973) is approximately 30 per cent larger in magnitude.

The screening correction discussed in § 4.B.3 is not as widely adopted. It is included in Juodagalvis et al. (2010), but not in Gutierrez et al. (1996). The results of Itoh et al. (2002) are within approximately 10 per cent of the results from the Thomas-Fermi approximation

$$V_s \approx Z\sqrt{\frac{4\alpha^3}{\pi}}E_F \ . \tag{4.60}$$

This effect has approximately the magnitude of the difference between older ion chemical potential and the one we adopt discussed in the preceding paragraph, but the opposite sign. Therefore, despite its exclusion, the net difference between our calculations and those of Gutierrez et al. (1996) is small.

4.C   Convergence

In order to demonstrate that our results are robust, we perform a number of tests of the spatial and temporal convergence of our MESA calculations. The parameters of these runs are shown in Table 4.C. We performed runs with each of the spatial and temporal resolutions each separately ten times greater than the fiducial case, as well as a run in which both the spatial and temporal resolutions were three times greater than the fiducial case. Fig. 4.16

shows that the central temperature evolution remains unchanged[10]and we observed that the variation of the result in any quantity of interest was negligible.

---

[10]The small difference at the end of the "Temporal" track is an artifact of a difference in how the stopping condition trigger was tripped.

Run Name	`delta_lgRho_cntr_limit`	`delta_lgRho_cntr_hard_limit`	`varcontrol_target`	`mesh_delta_coeff`
Fiducial	1×10^{-3}	3×10^{-3}	1×10^{-3}	1.0
Temporal	1×10^{-4}	3×10^{-4}	1×10^{-4}	−
Spatial	−	−	−	0.1
Both	3×10^{-4}	1×10^{-3}	3×10^{-4}	0.3

Table 4.2: Parameters for the runs demonstrating the convergence of our results. The column names are the specific MESA controls we used. The controls `delta_lgRho_cntr_limit`, `delta_lgRho_cntr_hard_limit`, `varcontrol_target` control the maximal fractional change in physical variables, which in an implicit code like MESA controls the timestep. The control `mesh_delta_coeff` controls the number of zones used in the calculation. Fig. 4.16 shows that central temperature evolution is essentially identical for these different runs.

In addition, we performed a run with a much larger network (203 isotopes; `mesa_201.net` plus ^{20}O and ^{20}F) and confirmed that our results remained unchanged.

4.D Two-zone WD Models

This section describes the framework we use to understand the evolution of our MESA models after the $A = 24$ captures have occurred. The quantitative estimates shown in Figs. 4.8 and 4.9 were made using the approach described in this Appendix.

After the $A = 24$ electron captures have begun in the center of the WD, the MESA models have two zones: an inner "neutronized" zone in which the captures have occurred and Y_e is lower, and an outer zone whose composition remains unchanged. This property of our MESA models can be seen in Fig. 4.5. The neutronized zone is growing (in a Lagrangian sense) as a function of time.

In § 4.D.1 we write down an idealized model of a white dwarf with this two zone structure. In § 4.D.2 we discuss how we apply these models to understand our MESA calculations.

4.D.1 Details of the Two-Zone Model

Following Cox (1968), we write down a simple model of a zero-temperature white dwarf. We assume spherical symmetry and hydrostatic equilibrium and so solve the Poisson equation in spherical coordinates:

$$\frac{1}{r^2}\frac{d}{dr}\left(\frac{r^2}{\rho}\frac{dP}{dr}\right) = -4\pi G\rho \ . \tag{4.61}$$

We also assume the equation of state of a zero temperature, ideal Fermi gas, which is

$$P = Af(x) \tag{4.62}$$

$$x = \left(\frac{\rho Y_e}{B}\right)^{1/3} \tag{4.63}$$

where

$$f(x) = x\sqrt{x^2 + 1}\left(2x^2 - 3\right) + 3\sinh^{-1}(x) \tag{4.64}$$

$$A = \frac{\pi m_e^4 c^5}{3h^3} \approx 6.0 \times 10^{22}\,\mathrm{dynes\,cm^{-2}}$$

$$B = \frac{8\pi m_e^3 c^3}{3h^3 N_A} \approx 9.7 \times 10^5\,\mathrm{g\,cm^{-3}} \ .$$

Combining this equation of state with equation (4.61) gives

$$\frac{1}{r^2}\frac{d}{dr}\left[r^2\frac{d}{dr}\left(x^2 + 1\right)^{1/2}\right] = -\frac{\pi GB^2}{2AY_e^2}x^3 \tag{4.65}$$
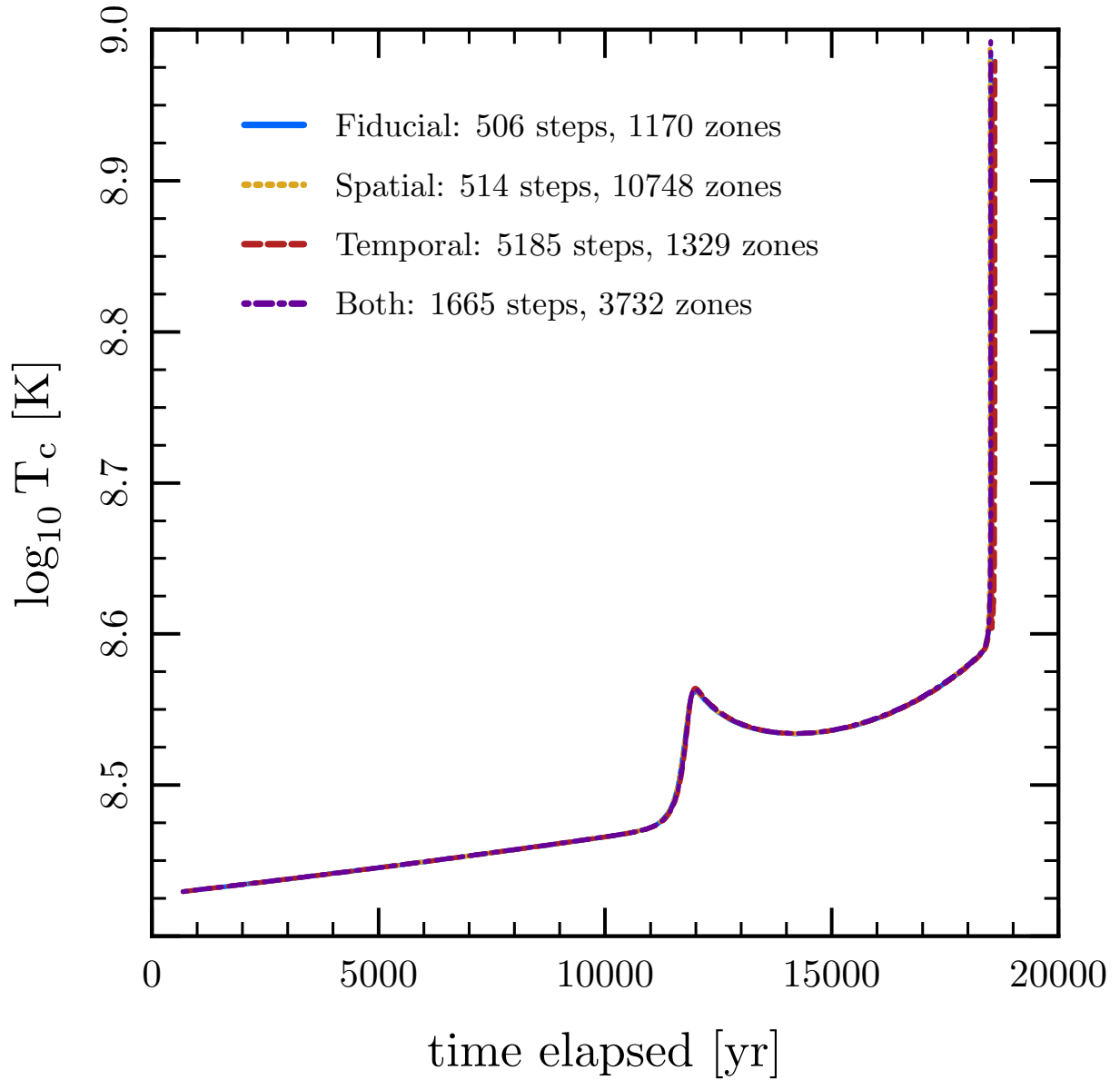
Figure 4.16: The legend shows the number of timesteps and the maximum number of zones used in the calculation of each of the runs shown in Table 4.C. The negligible variation between models indicates our results are converged.

where we have made the assumption that $dY_e/dr = 0$.

In order to non-dimensionalize these equations, define $z^2 = x^2 + 1$ and let z_c be the value of z at center of the model. We also define

$$\alpha \equiv \left(\frac{2A}{\pi G}\right)^{1/2} \frac{1}{Bz_c} \; . \tag{4.66}$$

and transform to the variables

$$r \equiv \alpha\zeta \tag{4.67}$$

$$z \equiv z_c\Phi \; . \tag{4.68}$$

This yields the differential equation

$$\frac{d}{d\zeta}\left(\zeta^2\frac{d\Phi}{d\zeta}\right) = \frac{1}{Y_e^2}\left(\Phi^2 - \frac{1}{z_c^2}\right)^{3/2} \; . \tag{4.69}$$

At the center ($\zeta = 0$), the boundary conditions are

$$\Phi(\zeta = 0) = 1 \tag{4.70}$$

$$\left.\frac{d\Phi}{d\zeta}\right|_{\zeta=0} = 0 \tag{4.71}$$

At the surface ($\zeta = \zeta_s$), $\rho \to 0$ and so $z \to 1$, meaning

$$\Phi(\zeta = \zeta_s) = \frac{1}{z_c} \; . \tag{4.72}$$

Now, we divide the white dwarf into two zones which have different values of Y_e. By assuming a piecewise constant form for Y_e, we can continue to solve equation (4.69) throughout the whole white dwarf. Specifically, we use

$$Y_e = \begin{cases} Y_{e,0} & \text{if } z < z_n \\ Y_{e,n} & \text{if } z > z_n \; . \end{cases} \tag{4.73}$$

The transition between the two zones occurs at ζ_n such that $\Phi(\zeta_n) = z_n/z_c$. The following physical conditions must be satisfied at this interface

$$P_+ = P_- \tag{4.74}$$

$$\left(\frac{1}{\rho}\frac{dP}{dr}\right)_+ = \left(\frac{GM_r}{r^2}\right)_- \; . \tag{4.75}$$

Note that the continuity of P implies the continuity of x, and hence z, even though Y_e is discontinuous. The dimensionless equivalents of these conditions are

$$\Phi(\zeta = \zeta_n^-) = \Phi(\zeta = \zeta_n^+) \tag{4.76}$$

$$\left(Y_e\frac{d\Phi}{d\zeta}\right)_{\zeta=\zeta_n^-} = \left(Y_e\frac{d\Phi}{d\zeta}\right)_{\zeta=\zeta_n^+} \; . \tag{4.77}$$

Constructing a two-zone model is now simple. Specify the three parameters for the equation of state: $Y_{e,0}, Y_{e,n}, z_n$. Select a central density (which sets the value of z_c) and then integrate the ODE observing the boundary and jump conditions. The solution gives the structure of a single two-zone model. A one-parameter family of models can be constructed by varying z_c, which in turn varies the properties (e.g., mass, radius) of the model.

4.D.2 Applications of the Two-Zone Model

Our MESA models are in hydrostatic equilibrium: their evolution is occurring on timescales much longer than the dynamical time. We use the two-zone model to find approximate sequences of hydrostatic models along which the MESA models evolve. This gives us insight into the processes that control the timescale of the evolution.

The piecewise equation of state given in equation (4.73) can be used to represent the $A = 24$ captures: setting $\log_{10} \rho_n = 9.6$, with $Y_{e,0} = 0.5$ and $Y_{e,n} = Y_{e,0} - X_{\mathrm{Mg}}/12$ corresponds to instantaneous neutronization of all available $^{24}\mathrm{Mg}$ at densities above the threshold density.

Fig. 4.17 shows the schematic evolution of models with $X_{\mathrm{Mg}} = 0.05$. The black line is the family of two-zone hydrostatic models. This family of models is generated by varying P_c (the central pressure). Because of the discontinuity in Y_e, the continuous variation in P_c gives a discontinuous variation in ρ_c. (In Fig. 4.17, the density jump is hidden by point 2, but the jumps are apparent in Fig. 4.18.) The grey line shows the family of models without neutronization. For central densities less than ρ_n (e.g., point 1) the two families are equivalent. At point 2, the central density crosses the threshold density and the families diverge. At point 3, the model has a substantial low-Y_e core and has a much higher central density at fixed mass relative to the models without neutronization.

The numbered points in Fig. 4.17 represent a temporal sequence of models. The time evolution is driven by the increase in M set by accretion. For a given value of $\dot{M}$, the timescale for changes in ρ_c is given by equation 4.1, where the value of $d \ln \rho_c / d \ln M$ comes from the sequence of hydrostatic models. In Fig. 4.8, the black dashed line is calculated using the model without neutronization, while the black dotted line is calculated using the two zone model. This latter line does an excellent job of quantitatively describing the more rapid contraction of the MESA model following the $A = 24$ captures.

Fig. 4.18 shows the schematic evolution of models with $X_{\mathrm{Mg}} = 0.15$. The black line is the family of two-zone hydrostatic models. The grey line shows the family of models without neutronization. For central densities less than ρ_n (e.g., point 1) the two families are equivalent. At point 2, neutronization begins to have an effect. At point 3, the model passes the maximum mass possible for the family of models with $\log_{10} \rho_n = 9.60$. Up to this point, as in the case with $X_{\mathrm{Mg}} = 0.05$, the points 1-3 represent a temporal sequence of models whose time evolution is driven by increasing M.

With the equation of state held fixed, point 3 would mark the onset of dynamical instability. However, the characteristic timescale of the electron captures is longer than the dynamical time. Therefore it is not physically possible for ρ_n to remain fixed. Only material at densities where the electron capture timescale is shorter than the evolutionary timescale
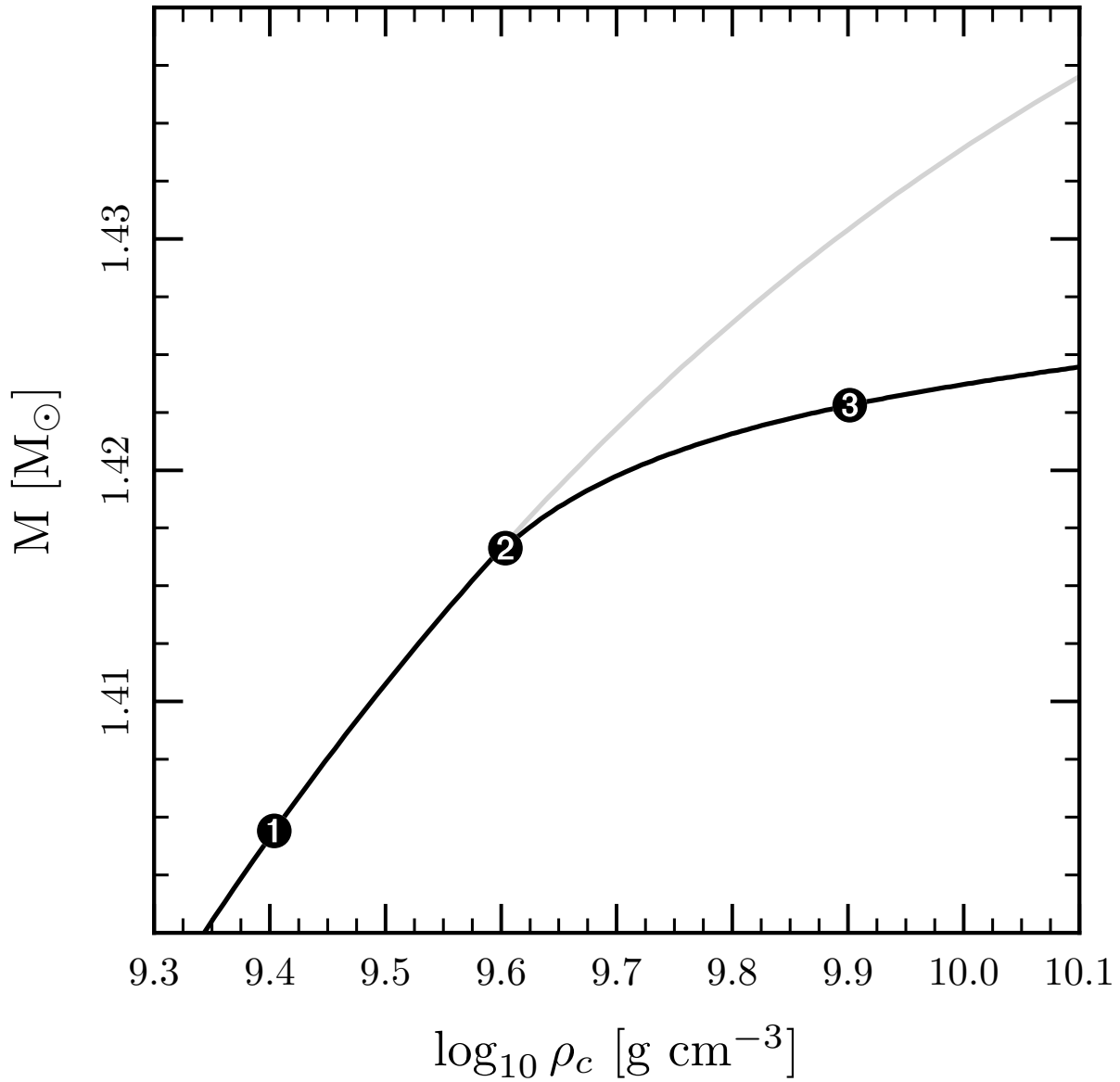
Figure 4.17: The black line shows the sequence of two-zone hydrostatic models with electron captures above $\log_{10} \rho_n = 9.6$ with the change in Y_e corresponding to $X_{\mathrm{Mg}} = 0.05$. The grey line shows a zero-temperature model without neutronization. With neutronization taken into account, the central density increases more rapidly with increasing mass. The numbered points indicate a temporal series of models; specific points are discussed in more detail in the text.

is able to completely neutronize.

For the large X_{Mg} models like that in Fig. 4.18, the evolutionary timescale becomes sufficiently short that there is no longer time for a significant amount of mass to accrete. Therefore, the evolution switches to a sequence of models with constant M, as indicated by the black dashed line and points 4-6 in Fig. 4.18. The fixed value of M is the maximum mass for a model with the initial value of $\log_{10} \rho_n = 9.60$ (i.e., point 3).

The evolution along the temporal sequence of points 3-6 is limited by the electron capture rates. To describe this quantitatively, for a given ρ_c, we find the value of ρ_n that corresponds to the hydrostatic model with a given M. Then we calculate the neutronization timescale (equation 4.23) corresponding to this value of ρ_n. This gives the black dash dotted line shown in Fig. 4.8, which does a good job of reproducing the evolution observed in the MESA model. For simplicity, we used the electron capture rates at fixed temperature ($\log_{10} T = 8.6$) to calculate λ_{ec}.

The qualitatively different evolution experienced by the $X_{\mathrm{Mg}} = 0.05$ and $X_{\mathrm{Mg}} = 0.15$ models is due to the presence of a maximum mass in the families of two-zone models at a central density less than the critical density for $^{20}\mathrm{Ne}$ captures. Calculating the central density at which this maximum occurs for each value of X_{Mg} gives the critical curve shown as a black dashed line in Fig. 4.9.
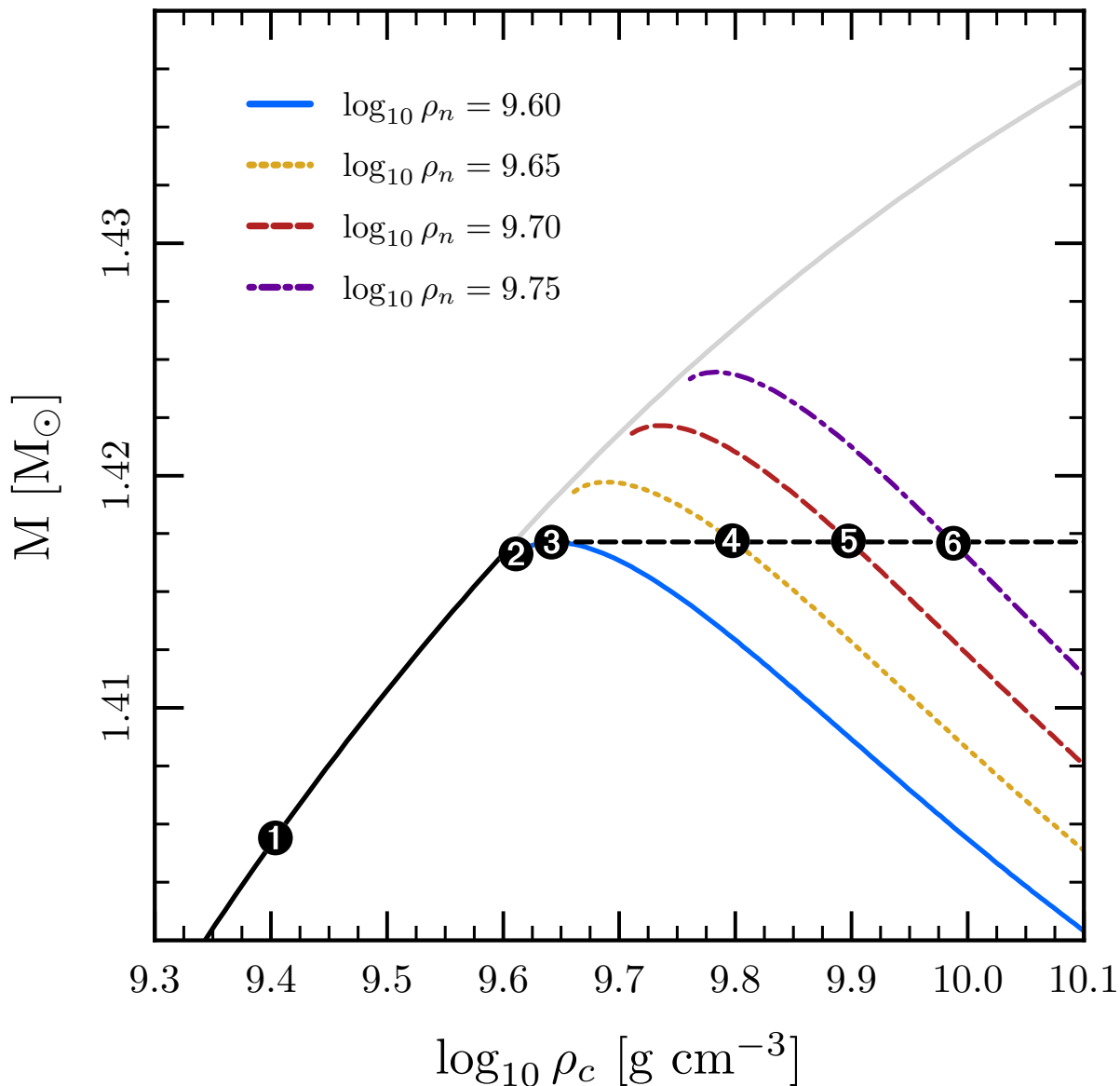
Figure 4.18: The black line shows the sequence of two-zone hydrostatic models corresponding to $X_{Mg} = 0.15$. The grey line shows a zero-temperature model without neutronization. The colored lines show models with neutronization at different densities. The gaps between the colored lines and the grey line are the discontinuities in ρ_c caused by the discontinuity in Y_e; the sequence in continuous in P_c. The numbered points indicate a temporal series of models; specific points are discussed in more detail in the text. The black line changes from solid to dashed when the sequence of models changes from being defined by constant ρ_n to constant M.

Chapter 5

The Importance of Urca-process Cooling in Accreting ONe White Dwarfs

Abstract

We study the evolution of accreting oxygen-neon (ONe) white dwarfs (WDs), with a particular emphasis on the effects of the presence of the carbon-burning products ^{23}Na and ^{25}Mg. These isotopes lead to substantial cooling of the WD via the ^{25}Mg-^{25}Na, ^{23}Na-^{23}Ne, and ^{23}Ne-^{23}F Urca pairs. We derive an analytic formula for the peak Urca-process cooling rate and use it to obtain a simple expression for the temperature to which the Urca process cools the WD. We use the Modules for Experiments in Stellar Astrophysics (MESA) stellar evolution code to evolve a suite of models that confirm these analytic results. We also use our MESA models to demonstrate that while Urca-process cooling substantially modifies the thermal evolution of accreting ONe WDs, it does not significantly shift the density at which oxygen ignites and undergoes a thermonuclear runaway. It thus remains the case that these objects will undergo collapse to a neutron star. The inclusion of the effects of Urca-process cooling is nonetheless an important step in producing more realistic progenitor models for studies of the signature of accretion-induced collapse.

5.1 Introduction

In the Urca process, first discussed by Gamow & Schoenberg (1941), repeated electron-capture and beta-decay reactions give rise to neutrino emission. When this occurs in a stellar interior where the neutrinos are able to free-stream out of the star—such as in a white dwarf (WD)—it becomes an active cooling process. Tsuruta & Cameron (1970) calculated analytic approximations to the energy loss rates from the Urca process and compiled a list of 132 pairs of isotopes that contribute to these energy losses. Paczyński (1973) applied these results in a study of the temperature evolution of degenerate carbon-oxygen (CO) cores, demonstrating that this cooling can shift the density at which pycnonuclear carbon ignition occurs.

In Paczyński (1973) the odd mass number nuclei that participate in the Urca process were assumed to have cosmic abundances. Carbon burning, however, produces significant mass fractions of ^{23}Na and ^{25}Mg; therefore Urca cooling will be significantly more important in stars with oxygen-neon (ONe) compositions, where the material has already been processed by carbon burning (Iben 1978).

Urca cooling has been shown to play an important role in the central temperature evolution of super-asymptotic giant branch stars (Jones et al. 2013). In this context, the dangers of using coarse tabulations of the relevant weak reaction rates has been emphasized by Toki et al. (2013). New tabulations of these rates were calculated by Toki et al. (2013) and then used in the study of Jones et al. (2013). Recently, Paxton et al. (2015) demonstrated the capability of the MESA (Modules for Experiments in Stellar Astrophysics; Paxton et al. 2011, 2013, 2015) code to reproduce these results using weak rates calculated "on-the-fly" from input nuclear data.

In Schwab et al. (2015), hereafter referred to as SQB15, we developed an analytic and numerical understanding of the evolution of ONe WDs towards accretion-induced collapse (AIC) in which we considered only ^{24}Mg, ^{20}Ne, and ^{16}O. In this work, we extend and modify this understanding to include additional isotopes generated during carbon-burning. We demonstrate analytically and numerically that significant temperature changes occur due to Urca-process cooling and we illustrate its effect on the subsequent evolution. Importantly, we find that the density at which oxygen ignition occurs is not significantly altered, and thus the Urca-process cooling phase does not affect the fate of accreting ONe WDs calculated in SQB15.

In Section 5.2 we provide an overview of the microphysics of the Urca process and identify the important isotopes and transitions. In Section 5.3, we make analytic estimates of the importance of Urca cooling in accreting ONe WDs. In Section 5.4, we discuss how we use the MESA stellar evolution code to demonstrate the effects of Urca-process cooling. In Section 5.5, we discuss the results and implications of our MESA calculations. In Section 5.6, we conclude.

5.2 The Urca Process

Take two nuclei $a \equiv (Z, A)$ and $b \equiv (Z - 1, A)$ that are connected by an electron-capture transition

$$(Z, A) + e^- \to (Z - 1, A) + \nu_e \tag{5.1}$$

and beta-decay transition

$$(Z - 1, A) \to (Z, A) + e^- + \bar{\nu}_e \tag{5.2}$$
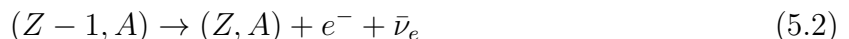
where Z and A are respectively the atomic number and mass number of the nucleus. In all of the electron-capture transitions considered here, there is a threshold energy required for the electron. In a cold, degenerate plasma, electrons with sufficient energy will become available when the Fermi energy $E_{\rm F}$ is equal to the energy difference between the parent and daughter

states Q_0, which includes both the nuclear rest mass and the energy associated with excited states. This corresponds to a threshold density

$$\rho_0 \approx 1.8 \times 10^9 \, \text{g cm}^{-3} \left(\frac{Y_e}{0.5} \right)^{-1} \left(\frac{|Q_0|}{5 \, \text{MeV}} \right)^3 . \tag{5.3}$$

where Y_e is the electron fraction.

5.2.1 Cooling Rate

If the ground state to ground state transition is allowed, then at the threshold density the rates of electron capture and beta decay are comparable. Since each reaction produces a neutrino that free-streams out of the star, this is a cooling process.

Suppose the total number density of the two isotopes in the Urca pair is $n_u = n_a + n_b$. Because the time-scales for electron capture and beta decay are short compared to the evolutionary time-scale of the system, an equilibrium is achieved. The relative abundances are then given by the detailed balance condition $n_a \lambda_{ec} + n_b \lambda_\beta = 0$. Under this assumption, the specific neutrino cooling rate from the Urca process can be written as

$$\epsilon_u = \frac{n_u}{\rho} C = \frac{X_u N_A}{A_u} C \tag{5.4}$$

where X_u is the mass fraction of the Urca pair, A_u is its atomic weight, N_A is Avogadro's number, and

$$C = \frac{\varepsilon_{\nu,ec} \lambda_\beta + \varepsilon_{\nu,\beta} \lambda_{ec}}{\lambda_\beta + \lambda_{ec}} . \tag{5.5}$$

In Appendix 5.A, we write out the full expressions for the rates (λ) and neutrino loss rates (ε_ν) for electron capture and beta decay necessary to evaluate equation (5.5). The key result is that the Urca cooling rate for an allowed ground state to ground state transition is sharply peaked at $E_F = |Q_g|$ and that the maximum value of C is

$$C_{\text{max}} = \frac{7\pi^4 \ln 2}{60} \frac{m_e c^2}{(ft)_\beta + (ft)_{ec}} \left(\frac{k_B T}{m_e c^2} \right)^4 \left(\frac{Q_g}{m_e c^2} \right)^2 \exp(\pi \alpha Z) , \tag{5.6}$$

where (ft) is the comparative half-life and α is the fine structure constant.

5.2.2 Isotopes and Transitions

Table 5.1: A summary of the key weak reactions that occur in accreting ONe WDs. The transition that typically dominates the rate is listed. Electron captures convert the initial isotope to the final isotope. Q_g is the mass difference between the isotopes (in MeV); unlike in the similar tabulation in SQB15 we have already accounted for the electron rest mass. E_i and E_f are the excitation energies of the initial and final states, relative to the ground state (in MeV). J_i^π and J_f^π are the spins and parities of the initial and final states. (ft) is the comparative half-life (in s) for this transition. Q_0 is the threshold energy difference (in MeV). ρ_0 is the approximate density (in $\mathrm{g\,cm^{-3}}$) at which the reaction occurs (as defined in equation 5.3). Effect indicates whether the net effect of the weak reactions is to cool the plasma via Urca-process cooling (odd mass number) or heat the plasma via exothermic electron captures (even mass number).

Initial	Final	Q_g	E_i	J_i^π	E_f	J_f^π	$\log(ft)$	Q_0	$\log\rho_0$	Effect	Notes
^{25}Mg	^{25}Na	-4.346	0.000	$5/2^+$	0.000	$5/2^+$	5.26	-4.346	9.07	Cool	
^{23}Na	^{23}Ne	-4.887	0.000	$3/2^+$	0.000	$5/2^+$	5.27	-4.887	9.22	Cool	
^{24}Mg	^{24}Na	-6.026	0.000	0^+	0.472	1^+	4.82	-6.498	9.60	Heat	[a]
^{24}Na	^{24}Ne	-2.978	0.000	4^+	3.972	4^+	6.21	-6.950	9.69	Heat	[a]
^{25}Na	^{25}Ne	-7.761	0.090	$3/2^+$	0.000	$1/2^+$	4.41	-7.671	9.81	Cool	
^{20}Ne	^{20}F	-7.536	0.000	0^+	1.057	1^+	4.38	-8.593	9.96	Heat	[b]
^{23}Ne	^{23}F	-8.991	0.000	$5/2^+$	0.000	$5/2^+$	5.72	-8.991	10.02	Cool	[c]

[a] for $\log(T/\mathrm{K}) \gtrsim 8.4$, the ^{24}Na will immediately undergo an electron capture to form ^{24}Ne; see Section 5.5.1
[b] the ^{20}F will immediately undergo an electron capture to form ^{20}O
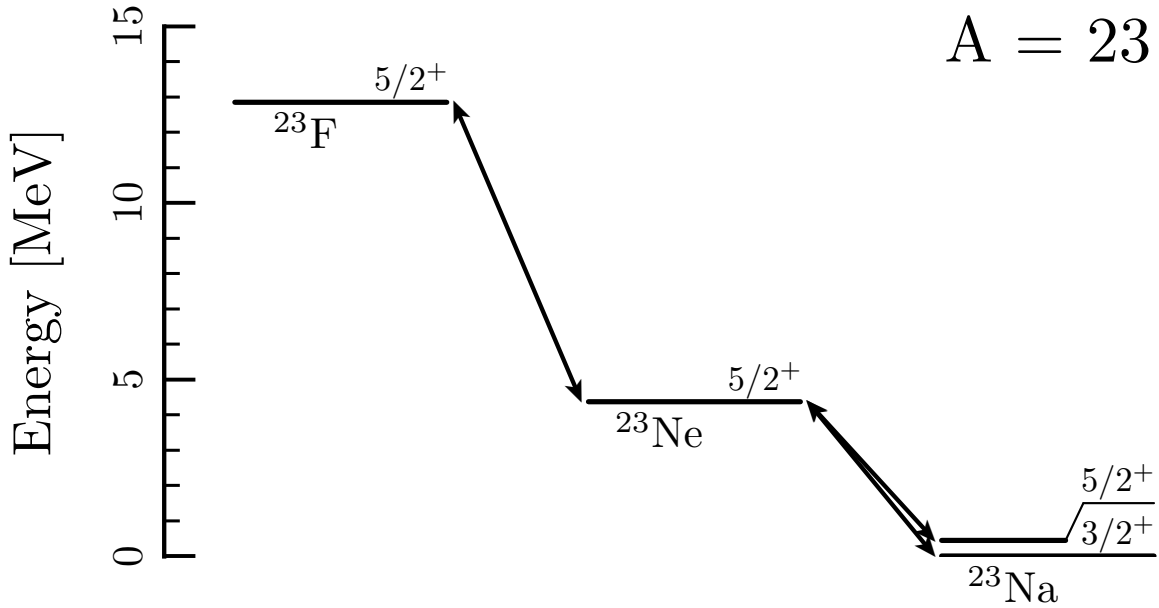[c] the oxygen deflagration begins before our models reach this density

Figure 5.1: Energy level diagram for the $A = 23$ nuclei that we consider. The J^π value is indicated at the right of each level. The most important transitions we consider are indicated with arrows.

Using a nuclear reaction network with 244 species and analytic weak reaction rates, Iben (1978) identified Urca pairs for which the the neutrino loss rates rival or exceed thermal neutrino losses. In material processed by carbon burning, the two most abundant odd mass number isotopes are ^{23}Na and ^{25}Mg and thus the most important Urca pairs are $A = 23$ and 25 (see figure 2 in Iben 1978). Therefore, we restrict our attention to these isotopes, neglecting possible small contributions from $A = 21$ and 29 isotopes.

The nuclear data (energy levels and ft-values) required for this calculation are drawn from the literature (Tilley et al. 1998; Firestone 2007a,b, 2009; Martínez-Pinedo et al. 2014). Table 5.1 summarizes this data. Figures 5.1 and 5.2 show a simplified level structure (excluding excited states $\gtrsim 1\,\mathrm{MeV}$ above the ground state) of the $A = 23$ and $A = 25$ nuclei that we consider.

5.3 Analytic Estimates

The energy equation for material in a spherically symmetric star is

$$T\frac{ds}{dt} = \epsilon - \frac{\partial L}{\partial M} \tag{5.7}$$

where ϵ is the specific energy generation rate, which includes nuclear reactions, neutrino processes, etc. For these estimates, we will consider only the effects of neutrino losses, which we sub-divide into ϵ_ν (thermal neutrino loss rate) and ϵ_u (Urca process neutrino loss rate).

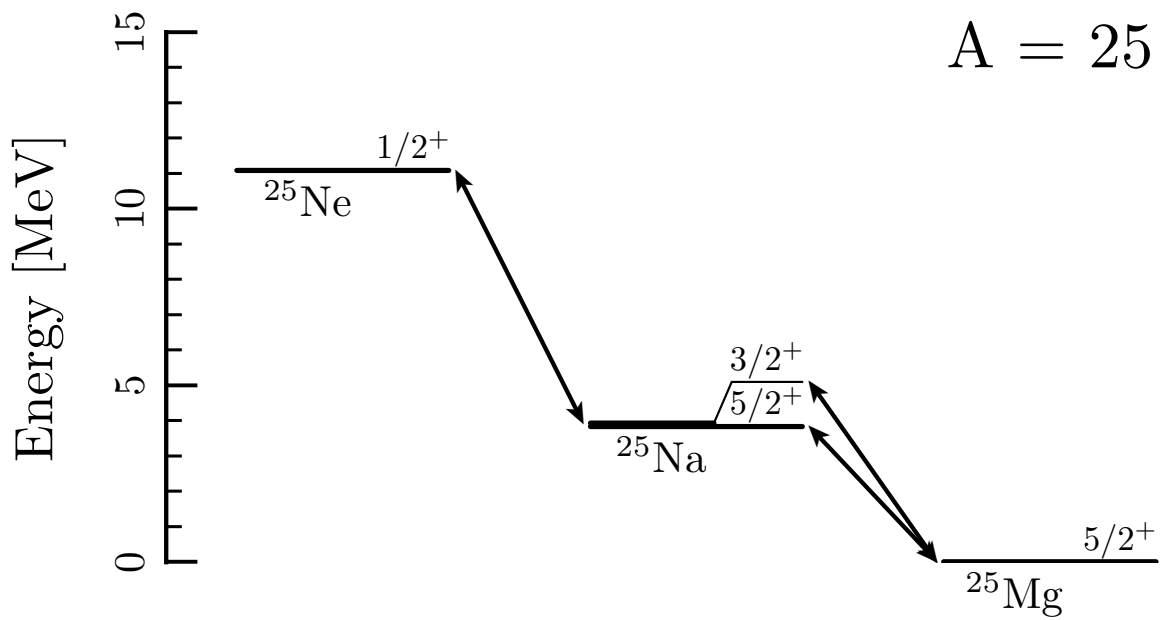*Figure 5.2*: Energy level diagram for the $A = 25$ nuclei that we consider. The J^π value is indicated at the right of each level and is sometimes given an arbitrary offset (indicated via a thin line) in order to enhance legibility. The most important transitions we consider are indicated with arrows. The transition between ^{25}Ne and ^{25}Na is to/from the low-lying first excited state of ^{25}Na.

In the center of these accreting WDs, $\partial L/\partial M$ is negligible, and therefore

$$- (\epsilon_\nu + \epsilon_u) = T_c \, c_v \left[\frac{d \ln T_c}{dt} - (\Gamma_3 - 1) \frac{d \ln \rho_c}{dt} \right] \ , \tag{5.8}$$

where c_v is the specific heat at constant volume and $\Gamma_3 - 1 = (d \ln T / d \ln \rho)_{\mathrm{ad}}$. Depending on which terms dominate, there are three regimes for the evolution of the central temperature:

1. When the left hand side of equation (5.8) is negligible, the central temperature will evolve along an adiabat.

2. When ϵ_ν dominates the left hand side of equation (5.8), the temperature will evolve towards (and then along) the attractor solution discussed by Paczyński (1973), SQB15 and Brooks et al. (2016a), in which thermal neutrino cooling and compressional heating balance. Because of the neutrino losses, this attractor solution is shallower (in ρ-T space) than an adiabat, though it still has positive slope.

3. When ϵ_u dominates the left hand side of equation (5.8), the temperature will decrease. Because the Urca-process cooling is sharply peaked in E_{F}, this will occur at nearly fixed density.

These three regimes are illustrated in Figure 5.3, which shows the evolution of the central density and temperature in one of our MESA models, centered on the density where cooling due to the ^{23}Na-^{23}Ne Urca pair occurs.

It is useful to estimate the magnitude of the temperature decrease caused by the Urca process (regime iii). As we will show, this depends primarily on the mass fraction of the Urca pair and the rate at which the core is being compressed. Paczyński (1973) provides a fitting formula for the temperature change, obtained though careful numerical integration; however this result is unsuitable for our purposes, as it assumes that the value of $d \ln \rho/dt$ is that of a CO core growing via stable He-shell burning, as set by the core mass-luminosity relation.

We assess the Urca-process cooling via a simpler argument. As a result of accretion, the core is being compressed on a time-scale

$$t_\rho = \left(\frac{d \ln \rho_c}{dt} \right)^{-1} = \left(\frac{d \ln \rho_c}{d \ln M} \right)^{-1} \frac{M}{\dot{M}} \ . \tag{5.9}$$

For an ideal, zero-temperature white dwarf, in the range $9 \lesssim \log \rho_c \lesssim 10$ and with $Y_e \approx 0.5$, SQB15 give the approximate result that

$$t_\rho \approx 5 \times 10^4 \, \mathrm{yr} \, \rho_9^{-0.55} \dot{M}_{-6}^{-1} \tag{5.10}$$

where $\rho_9 = \rho/(10^9 \, \mathrm{g \ cm}^{-3})$ and $\dot{M}_{-6} = \dot{M}/(10^{-6} \, \mathrm{M}_\odot \, \mathrm{yr}^{-1})$.

The cooling from an individual Urca pair peaks when $E_{\mathrm{F}} = Q_{\mathrm{g}}$, and is significant for only $\Delta E_{\mathrm{F}} \approx 3 k_{\mathrm{B}} T$ centered around this peak. We can estimate the width of the peak (in
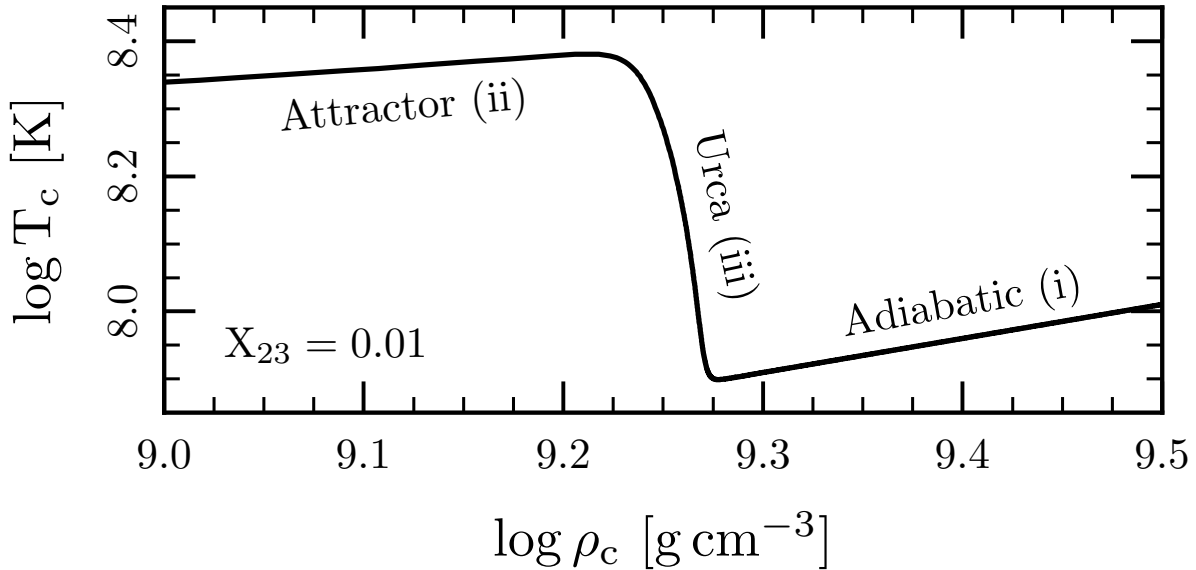
Figure 5.3: The schematic evolution of central density and temperature in a ONe WD accreting at $10^{-6} M_\odot \, \mathrm{yr}^{-1}$. The black line shows the result of evolving a MESA model that has an initial mass fraction of 0.01 ^{23}Na. The three regimes discussed in Section 5.3 are labeled.

density) as $\Delta \ln \rho \approx 3 \Delta E_F / E_F$. Therefore, the time-scale for a parcel to cross the cooling region is

$$t_{\mathrm{cross}} \approx \left(\frac{9 k_B T}{E_F} \right) t_\rho \approx 2 \times 10^{-2} \, T_8 \rho_9^{-1/3} t_\rho \tag{5.11}$$

$$\approx 1 \times 10^3 \, \mathrm{yr} \, T_8 \rho_9^{-0.88} \dot{M}_{-6}^{-1} \ . \tag{5.12}$$

At the density where the Urca cooling peaks, the cooling time-scale t_{cool} is

$$t_{\mathrm{cool}} = \frac{c_v T}{\epsilon_{\mathrm{max}}} = \frac{3 k_B T A_u}{\bar{A} X_u C_{\mathrm{max}}} \tag{5.13}$$

where we have taken ϵ_{max} from the combination of equations (5.4) and (5.6), and we have assumed the specific heat is that given by the Dulong-Petit law ($c_v = 3 k_B / \bar{A}$). Assuming $A_u \approx \bar{A}$,

$$t_{\mathrm{cool}} \approx 4 \times 10^2 \, \mathrm{yr} \, T_8^{-3} \left(\frac{X_u}{0.01} \right)^{-1} \left(\frac{Q_g}{5 \, \mathrm{MeV}} \right)^{-2} \left(\frac{ft}{10^5 \, \mathrm{s}} \right) \ . \tag{5.14}$$

When the core reaches a density where Urca cooling will begin, its initial temperature will have been set by its evolution in regimes (i) or (ii). If $t_{\mathrm{cross}} > t_{\mathrm{cool}}$ initially, since t_{cool} increases more rapidly with decreasing temperature than t_{cross}, the core will evolve towards the condition $t_{\mathrm{cross}} \approx t_{\mathrm{cool}}$. When this condition is reached, the Urca cooling will effectively
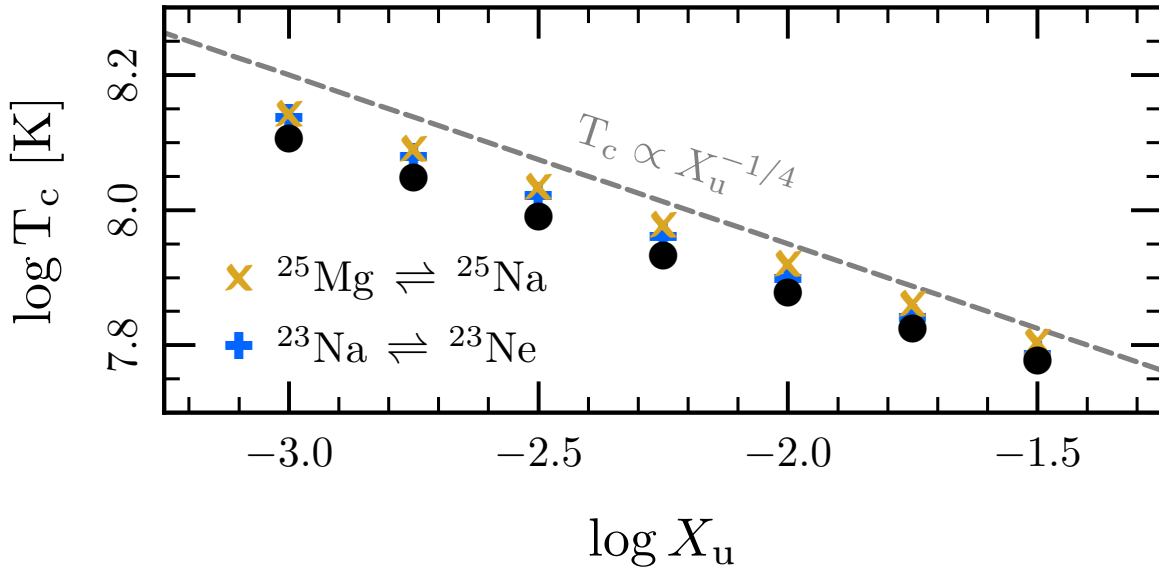
Figure 5.4: The minimum central temperature (T_c) reached after Urca-process cooling as a function of the mass fraction in the Urca pair (X_u). The crosses (Xs) show models with an initial mass fraction X_u of ^{23}Na (^{25}Mg). The solid black circles show models with initial mass fractions X_u of both ^{23}Na and ^{25}Mg. The dashed line shows the analytically expected scaling of equation (5.15).

shut off, since the core will evolve out of the cooling region before significant additional cooling occurs. If $t_{cross} < t_{cool}$ initially—which is never true in the cases we consider—then significant Urca-process cooling will not occur.

Therefore, the relation $t_{cross} \approx t_{cool}$ gives us an estimate for the temperature to which each Urca pair will cool the star. Combining equations (5.11) and (5.13) and taking the fiducial values $Q_g = 5\,\mathrm{MeV}$, $(ft) = 10^5\,\mathrm{s}$, and using a density equal to the threshold density (equation 5.3) for this Q_g, we find that the temperature to which the core cools is

$$T_u \approx 9 \times 10^7\,\mathrm{K}\ \dot{M}_{-6}^{1/4} \left(\frac{X_u}{0.01} \right)^{-1/4} . \tag{5.15}$$

In order to validate this relation we ran a suite of MESA models varying X_u and $\dot{M}$. These numerical results are shown in Figures 5.4 and 5.5 and are in excellent agreement with the analytic scaling given in equation (5.15). We will discuss the implications of this cooling on the subsequent evolution in Section 5.5.

We note that the Urca-process cooling can be significant enough to cause the white dwarf to begin to crystallize. At densities $\rho_9 \approx 1$, the condition for this phase transition ($\Gamma \approx 170$) occurs at $T \approx 5 \times 10^7\,\mathrm{K}$. Therefore, we expect crystallization to begin when $\dot{M}_{-6} X_u^{-1} \lesssim 10$, at which point the Urca cooling will begin extracting the latent heat associated with the phase transition. As shown in Figure 5.5, some of our models reach this regime, but we
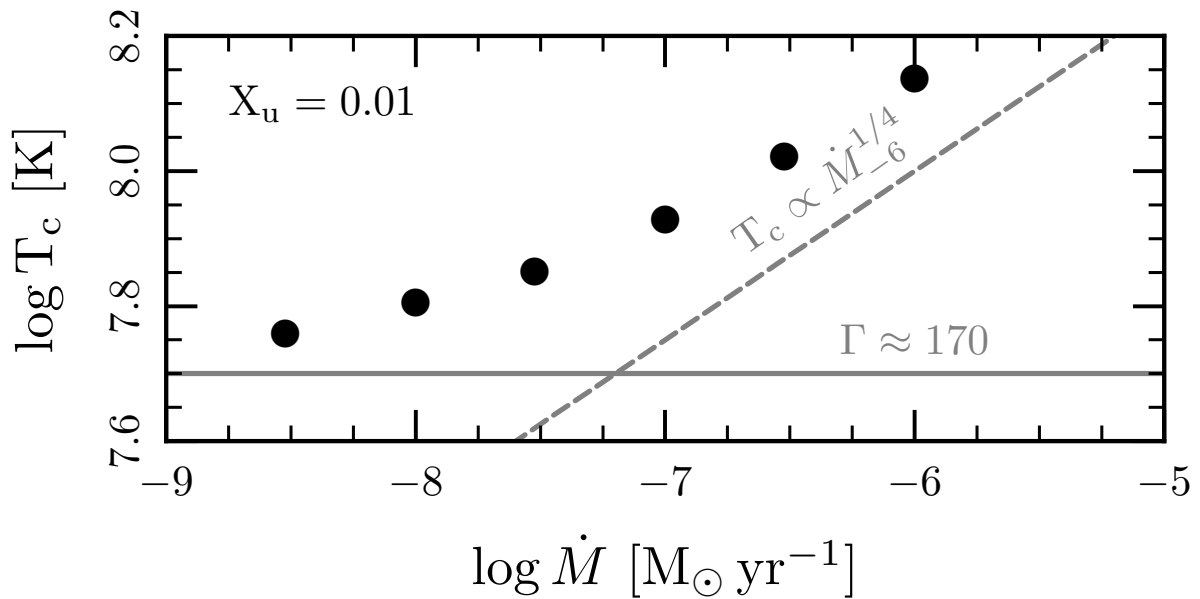
Figure 5.5: The minimum central temperature (T_c) reached after Urca cooling as a function of the accretion rate ($\dot{M}$). All models have $X_u = 0.01$ as ^{23}Na. The solid grey line shows the approximate temperature at which crystallization will begin. If a model began to crystallize, the MESA run was immediately stopped and these points are marked with triangles. The dashed line shows the analytically expected scaling of equation (5.15).

Table 5.2: The set of compositions used in our MESA models. Each composition is referenced in the text by the identifier listed in the top row. Each column lists the mass fractions of the isotopes (listed at left) that were included. Dashes indicate that a particular isotope was not included.

Isotope	SQB15	This Paper	T13	F15
^{16}O	0.500	0.500	0.480	0.490
^{20}Ne	0.450	0.390	0.420	0.400
^{22}Ne	—	—	—	0.018
^{23}Na	—	0.050	0.035	0.060
^{24}Mg	0.050	0.050	0.050	0.030
^{25}Mg	—	0.010	0.015	0.002

choose not to explore this further since we do not expect it to affect the final fate of the accreting WD.

5.4 Details of MESA Calculations

The calculations performed in this paper use a version of MESA based on r7624 (released 2015-06-03). We made a few small modifications to the source code which are described in detail in Appendix 5.B. As required by the MESA manifesto, the inlists necessary to reproduce our calculations will be posted on http://mesastar.org.

5.4.1 Initial Models

We generate our initial models in the same manner as SQB15, except that we stop relaxing the models at lower density ($\log \rho_c \approx 8.6$) so that the Urca processes of interest have not yet occurred.

Our models are initially chemically homogeneous.[1] The models shown as part of the scaling studies in Section 5.3 all have the indicated abundances of ^{23}Na and ^{25}Mg, a mass fraction of 0.5 ^{16}O, with the remainder as ^{20}Ne. In Section 5.5, we show results from four compositions, identified as follows: SQB15, the composition used in SQB15; this paper, the composition used in SQB15 plus ^{23}Na and ^{25}Mg; T13, a composition based on the intermediate-mass star models of Takahashi et al. (2013); and F15, a composition based on the intermediate-mass star models of Farmer et al. (2015). The mass fractions of the isotopes present in each named model are shown in Table 5.2.

5.4.2 Important MESA Options

While our full inlists will be made publicly available, we highlight some of the most important MESA options used in the calculations. This section assumes the reader is familiar

---

[1]The evolution of models with realistic composition profiles will be addressed by Brooks et al. (in prep.).

with specific MESA options. Please consult the instrument papers (Paxton et al. 2011, 2013, 2015) and the MESA website[2] for a full explanation of the meaning of these options.

Most importantly, we use the capability of MESA to calculate weak rates from input nuclear data developed in SQB15 and validated in Paxton et al. (2015). We activate these capabilities using the options:

```
use_special_weak_rates = .true.
ion_coulomb_corrections = 'PCR2009'
electron_coulomb_corrections = 'Itoh2002'
```

Table 5.1 summarizes the weak reactions that we include using this capability. The files containing the input nuclear data will be made available along with our inlists.

During the calculation, material will become cold enough that the MESA equation of state (Paxton et al. 2011, figure 1) will move from using HELM (Timmes & Swesty 2000) to PC (Potekhin & Chabrier 2010). At low temperatures, rapid and significant composition changes will occur as the weak equilibrium shifts. Therefore, it is necessary to ensure that all isotopes are included in the PC calculation[3] by using the options:

```
set_eos_PC_parameters = .true.
mass_fraction_limit_for_PC = 0d0
```

It is essential that we choose a temporal and spatial resolution that will resolve the effects of Urca-process cooling and the exothermic electron captures. We discuss the the details of our approach in Appendix 5.C and demonstrate that it leads to a converged result.

5.5 Discussion of MESA Models

Figure 5.6 compares the evolution of a model with the composition used in SQB15 with a model using a similar composition but including representative mass fractions of ^{23}Na and ^{25}Mg. (The precise compositions are given in Table 5.2.) The evolution of the central temperature is notably different in the two cases. We now discuss the origins and implications of these differences.

In SQB15, the temperature immediately prior to electron captures on ^{24}Mg and ^{20}Ne was was set by a balance between compression and neutrino cooling (the attractor solution). However, the results in Section 5.3 demonstrate that for a wide range of X_u and $\dot{M}$, significant Urca-process cooling will occur. In almost all cases, the WD is cooled to temperatures such

---

[2]http://mesa.sourceforge.net

[3]The MESA default is to only include isotopes with a mass fraction greater than 0.01 in the the PC equation of state calculation. As the chemical composition changes, abundances rise above or fall below this threshold. The sudden inclusion or exclusion of an isotope gives rise to a discontinuity in the equation of state. While the jumps in the computed thermodynamic properties are small, the discontinuous nature of the changes leads to convergence problems in the Newton-Raphson solver as MESA iterates of find the next model.
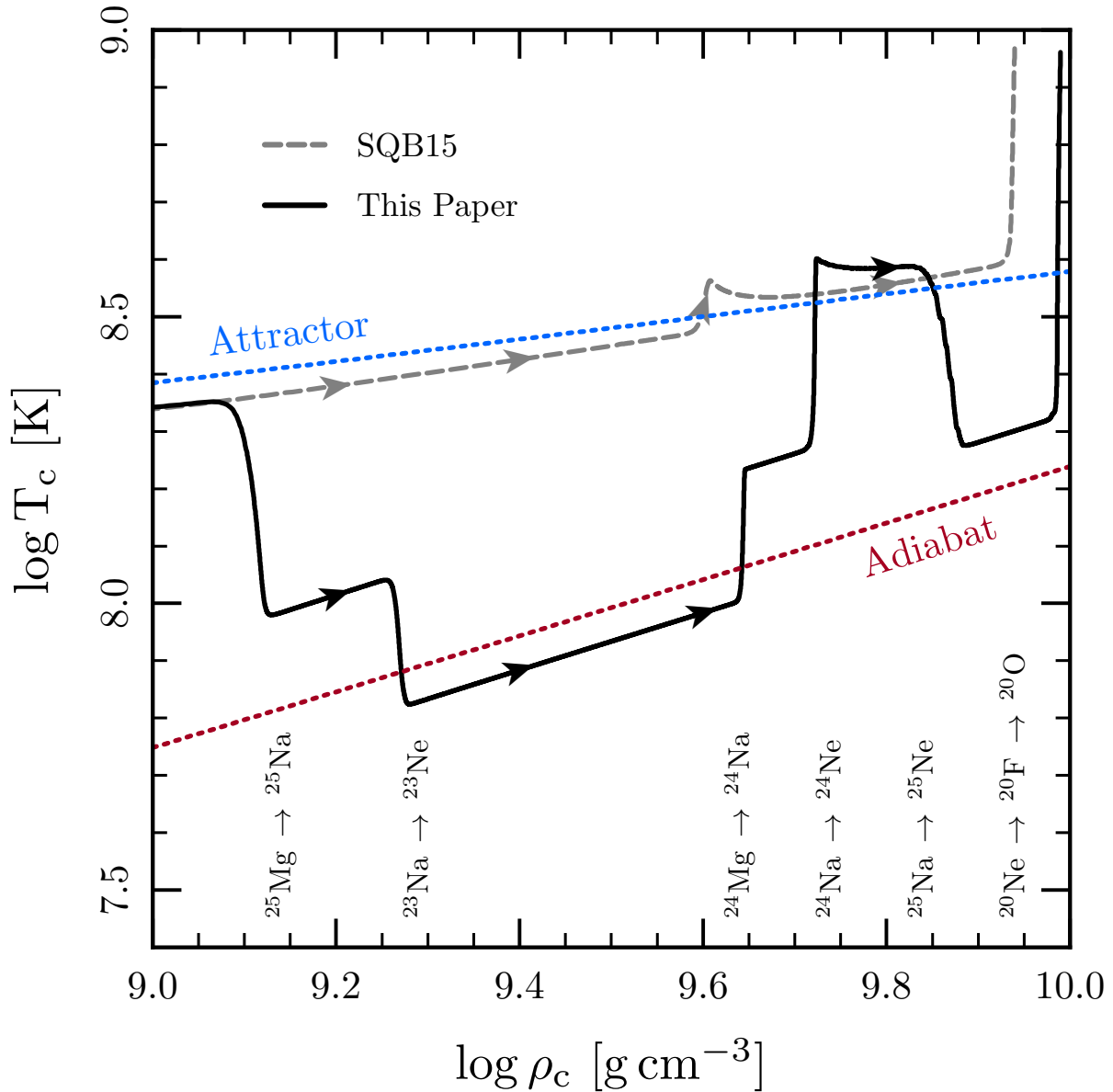
Figure 5.6: Comparison of a model with (This Paper) and without (SQB15) the isotopes ^{23}Na and ^{25}Mg. The precise compositions are given in Table 5.2. The key weak reactions are indicated at the densities at which they occur. The labeled dotted lines show the attractor solution and a sample adiabat. The SQB15 model (grey dashed line) evolves largely along the attractor solution, where neutrino cooling balances compressional heating. The model from this paper (black solid line) exhibits significant Urca-process cooling, and as a result when the electron captures on ^{24}Mg begin $\log(T/\mathrm{K}) < 8.0$. At this temperature, the electron captures on ^{24}Na are delayed until $\log(\rho/\mathrm{g\,cm^{-3}}) \approx 9.7$ (see Section 5.5.1). After the energy release from the $A = 24$ electron captures completes, the model evolves back towards the attractor solution, but around $\log(\rho_c/\mathrm{g\,cm^{-3}}) \approx 9.85$, additional Urca-process cooling associated with ^{25}Na-^{25}Ne occurs. At these lower temperatures, the $A = 20$ electron captures begin at slightly higher densities (≈ 0.05 dex), but this shift is not significant enough to affect the final collapse to a neutron star (see Section 5.5.2).

that energy losses by non-nuclear neutrinos (in these conditions primarily plasma neutrinos, e.g. Itoh et al. 1996) become negligible. Therefore, we enter regime (i), and expect the material to evolve along an adiabat. In these conditions $\Gamma_3 \approx 1.5$ (Chabrier & Potekhin 1998), so $T \propto \rho^{1/2}$.

The difference in threshold density between ^{23}Na (cooling) and ^{24}Mg (heating) is ≈ 0.4 dex, and therefore we expect a temperature increase of 0.2 dex. This relatively small change in temperature means that the star does not evolve back onto the attractor solution before the electron captures on ^{24}Mg begin. The difference in threshold density between ^{25}Na (cooling) and ^{20}Ne (heating) is much smaller, only ≈ 0.1 dex, and therefore the electron captures on ^{20}Ne will begin at a temperature only marginally above the minimum value reached after the cooling due to the ^{25}Na-^{25}Mg Urca pair.

5.5.1 Onset of electron captures on ^{24}Mg and ^{24}Na

When $\log(T/\text{K}) \lesssim 8.4$, the first excited state of ^{24}Na is no longer sufficiently thermally populated for electron captures from this state to the ground state of ^{24}Ne to dominate the rate. Instead, as the density increases, the first transition to become significant is the allowed transition from the ground state of ^{24}Na into the third excited state of ^{24}Ne, which is approximately $4\,\text{MeV}$ above the ^{24}Ne ground state. As a result, after an electron capture on ^{24}Mg produces ^{24}Na, an electron capture on ^{24}Na *does not* immediately occur (as was the case in most models shown in SQB15). Instead, the electron captures on ^{24}Na are delayed until a higher density, at $\log(\rho/\text{g cm}^{-3}) \approx 9.7$.

As discussed in SQB15 the entropy release from these electron captures does not trigger convection because of the stabilizing Y_e-gradient. For a plot of the energy released per capture as a function of density, see figure 12 of Martínez-Pinedo et al. (2014). With a typical ^{24}Mg mass fraction of ≈ 0.05, the heating from ^{24}Mg $\rightarrow$ ^{24}Na is not sufficient to allow for electron captures on the first excited state of ^{24}Na and fails to return the WD to the attractor solution[4].

When the electron captures on ^{24}Na occur while $\log(T/\text{K}) \lesssim 8.4$, each electron capture deposits roughly $4\,\text{MeV}$ of thermal energy. This rapidly heats the plasma, raising the temperature enough that the electron-capture rate becomes dominated by the transition from the first excited state of ^{24}Na. This transition deposits ≈ 10 times less energy per capture. In the models shown, most of the ^{24}Na undergoes electron captures through this less efficient channel.

After both $A = 24$ electron captures have concluded, whether they occurred simultaneously or separately, a similar peak temperature is reached (Figure 5.6). For all the compositions studied (Table 5.2 and Figure 5.7), this peak temperature is mildly above the attractor solution, and so neutrino cooling can quickly return the temperature to the attractor solution.

---

[4]At $\log(\rho/\text{g cm}^{-3}) \approx 9.6$ this corresponds to $\log(T/\text{K}) \approx 8.5$ for the fiducial accretion rate of $10^{-6}\,\text{M}_\odot\,\text{yr}^{-1}$.
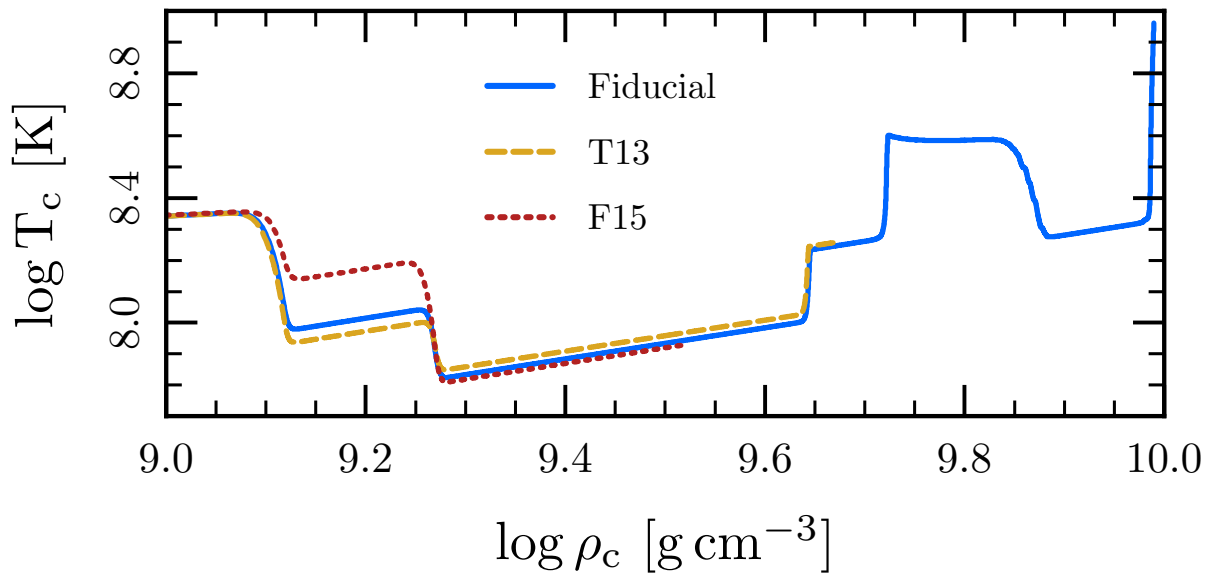
Figure 5.7: Comparison of a model with the fiducial composition (Fiducial) with two compositions based on recent results of the evolution of intermediate mass stars: (T13; Takahashi et al. 2013) and (F15; Farmer et al. 2015). The precise compositions are given in Table 5.2. While Urca-process cooling is sensitive to the detailed abundances, the density at which electron captures on ^{20}Ne trigger the oxygen deflagration is not.

5.5.2 Onset of electron captures on ^{20}Ne and ^{20}F

As discussed in SQB15, the electron captures on ^{20}Ne trigger a thermal runaway that leads to the formation of an outgoing oxygen deflagration wave. The final fate of the star is determined by a competition between the propagation of the oxygen deflagration and electron captures on the material (in nuclear statistical equilibrium; NSE) behind the deflagration front (Nomoto & Kondo 1991). The speed of the deflagration and the electron capture rate on its NSE ash are both functions of density and electron fraction. Timmes & Woosley (1992) found that the deflagration speed scaled $\propto \rho^{1.06}$. At the relevant densities, the neutronization time-scale scales roughly as $\rho^{-0.5}$ (see figure 13 in SQB15 and Seitenzahl et al. 2009).

The temperature effects the density at which the electron captures on ^{20}Ne begin, with lower temperatures corresponding to higher densities (see figure 4 in SQB15). The Urca-process cooling by ^{25}Na-^{25}Ne at $\log(\rho/\mathrm{g\,cm^{-3}}) \approx 9.85$ cools the material sufficiently that it cannot return to the attractor solution, and so effectively sets the temperature at which the electron captures on ^{20}Ne begin. This leads to electron captures on ^{20}Ne that begin at slightly higher density (≈ 0.05 dex) than in SQB15.

Independent of their cooling effects, the electron captures on ^{23}Na, ^{25}Mg, and ^{25}Na have reduced the Y_e of the material. For the fiducial composition, this change is $\Delta Y_e \approx -3 \times 10^{-3}$. A reduction in Y_e increases both of the relevant time-scales. Timmes & Woosley (1992) found that reducing Y_e from 0.50 to 0.48 reduced the deflagration speed by approximately 30 per cent. In the tabulated electron-capture rates on NSE material from Seitenzahl et al. (2009), changing Y_e from 0.50 to 0.48 at $\log(\rho/\mathrm{g\,cm^{-3}}) \approx 9.9$ and $\log(T/\mathrm{K}) \approx 10$ increases the neutronization time-scale by approximately a factor of 2.5. Note that these changes are quoted for a ΔY_e approximately 10 times greater than the difference here.

The exact competition between these two processes is best probed via simulations which can include both the physics of the oxygen deflagration and the NSE electron captures. However, at the level of the analysis in SQB15 the changes due to the increase in density and the decrease in Y_e, which are small and in opposite directions, leave our estimates unaffected. Therefore, the conclusion of SQB15 (which suggests collapse to a NS) remains unchanged.

5.5.3 Other effects of reduced electron fraction

The electron captures on the A=23 and A=25 isotopes reduce Y_e in the material in the WD that has exceeded the threshold density for these reactions. The Chandrasekhar mass scales with Y_e^2, and so at the onset of collapse, models which experience this reduction in Y_e will have lower masses relative to models in which these composition shifts have not been accounted for.

In SQB15, using models with an initial electron fraction of $Y_e = 0.5$, we demonstrated that there was a bifurcation in behavior around an initial ^{24}Mg mass fraction of $X_{\mathrm{Mg}} \approx 0.07$. Below this value, the core continued to evolve to higher densities on a time-scale set by the mass accretion rate; above this value, the core evolved to higher densities on the (much

shorter) electron-capture time-scale.

Because the electron-capture time-scale is short compared to the mass accretion time-scale, models on different sides of this bifurcation will have different masses at the time of the formation of the oxygen deflagration (and hence the collapse to a NS). The mass difference between the two models shown in SQB15 ($X_{\mathrm{Mg}} = 0.05$ and $X_{\mathrm{Mg}} = 0.15$) was 0.007 $M_\odot$. Mass differences of this order-of-magnitude have implications for studies that use the observed mass of low-mass neutron stars (thought to be formed via AIC) to make inferences about the nuclear equation of state (e.g. Podsiadlowski et al. 2005).

The overall reduction in Y_e will not substantially affect the analysis used in SQB15 to determine the critical value of X_{Mg}, as this value is primarily determined by the "instantaneous" change in Y_e associated with the ^{24}Mg electron captures. For the compositions in Table 5.2, the values of X_{Mg} are below this critical value, and thus the mass at the onset of collapse is most closely associated with the central density reaching threshold density for electron captures on ^{20}Ne.

5.6 Conclusions

We have demonstrated the substantial effects of Urca-process cooling on the thermal evolution of accreting ONe WDs. We have provided a simple analytic expression for the peak Urca-process cooling rate (equation 5.6) and used it to derive an approximate expression for the temperature to which the Urca process cools the plasma (equation 5.15). We used a suite of MESA simulations to confirm these simple analytic scalings (Figures 5.4 and 5.5). The magnitude of these effects is inconsistent with earlier work by Gutiérrez et al. (2005), who severely underestimate the amount of Urca-process cooling.

Urca-process cooling by ^{25}Na-^{25}Ne at $\log(\rho/\mathrm{g\,cm^{-3}}) \approx 9.85$ cools the WD and sets the temperature at which the electron captures on ^{20}Ne begin. This temperature is significantly cooler than that realized in SQB15 (and previous calculations) where the temperature was set by a balance between compressional heating and neutrino cooling (Figure 5.6). As a result, the electron captures, and hence the formation of the oxygen deflagration occur at slightly higher density (≈ 0.05 dex). The magnitude of this change is sufficiently small that we do not expect the presence of Urca-process cooling to affect the conclusion that the final outcome of accreting ONe WDs approaching the Chandrasekhar mass is accretion-induced collapse to a neutron star (Nomoto & Kondo 1991).

Ongoing studies (e.g., Brooks et al. in prep.) are simulating the evolution of WDs in binary systems (with non-degenerate companions) where (1) the composition profile of the WD is set self-consistently from stellar evolution calculations and (2) the accretion rate onto the WD is set self-consistently by modeling the orbital evolution of the binary and the shell-burning of the accreted material. The inclusion of the weak reactions discussed in this work and SQB15 in this type of calculation allow for the generation of models with realistic temperature and composition profiles that have been evolved up to the onset of AIC. Such models are the starting point for calculations of the collapse to a NS needed to

better characterize the observational signatures of AIC.

As discussed by Paczyński (1973), Urca-process cooling will also occur in accreting CO WDs, where it leads to an increase in the density at which carbon is ignited. This effect has not been fully explored in the context of Type Ia supernova progenitors.[5] The estimates we provide in Section 5.3 are equally applicable in this case (Martínez-Rodríguez et al. 2016).

Acknowledgements

5.A   Maximum Urca Cooling Rate

The expressions for the rates of electron-capture and beta-decay reactions have been written down previously (e.g. Tsuruta & Cameron 1970; Fuller et al. 1985; Martínez-Pinedo et al. 2014). In this Appendix, for completeness, we give expressions for these rates, specialized to the Urca process, with the goal of extracting a simple expression for the maximum Urca-process cooling rate. We consider only the allowed ground state to ground state transition of an Urca pair. We choose the isotope undergoing electron capture to have charge Z and thus the isotope undergoing beta decay has charge $Z - 1$. We always assume the electrons are relativistic with energy E_e.

The rate of electron capture or beta decay can be written as

$$\lambda = \frac{\ln 2}{(ft)} I(\mu, T, Q), \tag{5.16}$$

where (ft) is the comparative half-life (typically given in units of seconds) and can be either measured experimentally or theoretically calculated from the weak-interaction nuclear matrix elements. I is a phase space factor which depends on the temperature T, electron chemical potential μ, and the energy difference between the parent and daughter states Q. The value

---

[5]The single citation to Paczyński (1973) in a refereed paper published within the last 25 years is a statement that these effects were not included.

of Q includes both the nuclear rest mass and the energy associated with excited states. Similarly, the rate of energy loss via neutrinos is

$$\varepsilon_\nu = \frac{m_e c^2 \ln 2}{(ft)} J(\mu, T, Q) \ , \tag{5.17}$$

where J is a phase space factor that contains an additional power of the neutrino energy.

For convenience, we define $\beta = (k_B T)^{-1}$ and the non-dimensionalized parameters $q = \beta|Q|$, $\theta = \beta m_e c^2$, $\eta = \beta\mu$, $\epsilon = \beta E_e$. The value of I for electron capture can be written as

$$I_{ec} = \theta^{-5} \exp(\pi\alpha Z) \int_q^\infty \frac{\epsilon^2(\epsilon - q)^2}{1 + \exp(\epsilon - \eta)} d\epsilon \ , \tag{5.18}$$

and the value of J for electron capture can be written as

$$J_{ec} = \theta^{-6} \exp(\pi\alpha Z) \int_q^\infty \frac{\epsilon^2(\epsilon - q)^3}{1 + \exp(\epsilon - \eta)} d\epsilon \ , \tag{5.19}$$

where α is the fine structure constant. These integrals can easily be rewritten (using the substitution $x = \epsilon - q$) in terms of the complete Fermi integrals, which are defined as

$$F_k(y) = \int_0^\infty \frac{x^k}{1 + \exp(x - y)} dx \ . \tag{5.20}$$

Doing so gives

$$I_{ec} = \theta^{-5} \exp(\pi\alpha Z) \left[F_4(\delta) + 2q F_3(\delta) + q^2 F_2(\delta) \right] \tag{5.21}$$

and

$$J_{ec} = \theta^{-6} \exp(\pi\alpha Z) \left[F_5(\delta) + 2q F_4(\delta) + q^2 F_3(\delta) \right] \tag{5.22}$$

where we have defined $\delta = \eta - q$.

The value of I for beta decay can be written as

$$I_\beta = \theta^{-5} \exp(\pi\alpha Z) \int_\theta^q \frac{\epsilon^2(\epsilon - q)^2}{1 + \exp[-(\epsilon - \eta)]} d\epsilon \ , \tag{5.23}$$

and the value of J for beta decay can be written as

$$J_\beta = \theta^{-6} \exp(\pi\alpha Z) \int_\theta^q \frac{\epsilon^2(\epsilon - q)^3}{1 + \exp[-(\epsilon - \eta)]} d\epsilon \ . \tag{5.24}$$

These integrals can be rewritten (using the substitution $x = -\epsilon + q$) to be

$$I_\beta = \theta^{-5} \exp(\pi\alpha Z) \int_0^{q-\theta} \frac{(x - q)^2 x^2}{1 + \exp[x - (q - \eta)]} d\epsilon \ , \tag{5.25}$$

and

$$J_\beta = \theta^{-6} \exp(\pi\alpha Z) \int_0^{q-\theta} \frac{(x-q)^2 x^3}{1 + \exp[x - (q-\eta)]} d\epsilon . \tag{5.26}$$

We can now make use of the identity

$$\int_0^b \frac{x^k}{1 + \exp(x-y)} = F_k(y) - \sum_{j=0}^k \binom{k}{j} b^{k-j} F_j(y-b) , \tag{5.27}$$

where we identify $y = q - \eta$ and $b = q - \theta$. The Fermi integrals in the sum (those with argument $y - b$) will be negligible because $\theta - \eta \ll -1$ and $F_k(-z) \propto \exp(-z)$. In other words, we can extend the upper limit to ∞ without incurring substantial error. Doing so gives

$$I_\beta = \theta^{-5} \exp(\pi\alpha Z) \left[F_4(-\delta) - 2q F_3(-\delta) + q^2 F_2(-\delta) \right] \tag{5.28}$$

and

$$J_\beta = \theta^{-6} \exp(\pi\alpha Z) \left[F_5(-\delta) - 2q F_4(-\delta) + q^2 F_3(-\delta) \right] \tag{5.29}$$

where we have again defined $\delta = \eta - q$.

We are interested in the expression

$$C = \frac{\varepsilon_{\nu,\text{ec}}\lambda_\beta + \varepsilon_{\nu,\beta}\lambda_\text{ec}}{\lambda_\beta + \lambda_\text{ec}} = m_e c^2 \ln(2) \left(\frac{I_\text{ec}J_\beta + I_\beta J_\text{ec}}{(ft)_\beta I_\text{ec} + (ft)_\text{ec} I_\beta} \right) \tag{5.30}$$

The limit of interest is $q \gg 1$ and $|\delta| < 1$. Recall that for $y \ll 1$, $F_k(y) \approx -y\Gamma(k+1)$. Therefore, after retaining the dominant terms,

$$C = m_e c^2 \ln(2)\theta^{-6} q^2 \exp(\pi\alpha Z) \left[\frac{F_2(\delta)F_3(-\delta) + F_2(-\delta)F_3(\delta)}{(ft)_\beta F_2(\delta) + (ft)_\text{ec} F_2(-\delta)} \right] . \tag{5.31}$$

Evaluating the term in square braces at $\delta = 0$ gives

$$C = \frac{m_e c^2 \ln 2}{(ft)} \theta^{-6} q^2 \exp(\pi\alpha Z) \left[\frac{7\pi^4}{60} \frac{1}{(ft)_\beta + (ft)_\text{ec}} \right] . \tag{5.32}$$

and the peak value of the Urca cooling rate is thus

$$C_\text{max} = \frac{7\pi^4 \ln 2}{60} \frac{m_e c^2}{(ft)_\beta + (ft)_\text{ec}} \left(\frac{k_B T}{m_e c^2} \right)^4 \left(\frac{Q}{m_e c^2} \right)^2 \exp(\pi\alpha Z) . \tag{5.33}$$

Assuming $(ft)_\beta = (ft)_\text{ec}$, which is true when the ground states have the same spins, we can easily Taylor expand the term in square braces to second order:

$$C \propto \frac{1}{(ft)} \left[\frac{7\pi^4}{120} - \frac{\pi^2\delta^2}{4} \right] . \tag{5.34}$$

The term in square braces is zero when $\delta = \sqrt{7/30}\pi$, implying that the characteristic width of the Urca-process cooling peak is $\approx 3\delta$, that is when $\mu \approx |Q| \pm 1.5 k_B T$.

5.B   Modifications to MESA

The calculations in this paper used a modified version of MESA (based on r7624). We describe each of the changes we made to the source code. Patch files implementing these changes are included along with our inlists.

5.B.1   Number of special isotopes

There is a hard-coded limit on the number of isotopes and reactions that can be treated using the `special_weak_rates` capabilities. We increased these values in order to be able to calculate the necessary reaction rates (which involve 13 isotopes and 16 reactions).

5.B.2   Temperature reconstruction when remeshing

At the beginning of each timestep, MESA dynamically adjusts its mesh in response to the structure and composition profiles of the model. When MESA splits an existing cell, it must assign values of the structure and composition variables to the new cells (for a detailed description of this process, see section 6.5 of Paxton et al. 2011). When in a thermodynamic regime where the electrons are degenerate, the new cells inherit the temperature of the cell that was split, leaving the temperature profile unmodified. Under the conditions encountered in the models in this paper, this approach leads to the formation of spurious convective regions. We modify the post-remesh temperature reconstruction in order to avoid this issue.

The Ledoux criterion for convective instability is

$$\nabla_{\mathrm{ad}} - \nabla_T + B < 0 \tag{5.35}$$

where

$$B = -\frac{1}{\chi_T} \left(\frac{\partial \ln P}{\partial \ln Y_e} \right)_{\rho,T} \frac{d \ln Y_e}{d \ln P} \ . \tag{5.36}$$

When exothermic electron captures occur in our models, unstable thermal gradients (∇_T) develop but these are stabilized by the accompanying electron fraction gradients (B). During electron captures, the magnitude of both these gradients is typically greater than ∇_{ad}. Neglecting ∇_{ad}, as shown in section 3.2 of SQB15, $|B/\nabla_T| \approx \Delta E/E_{\mathrm{F}}$, where ΔE is the energy released per electron capture. Because $\Delta E/E_{\mathrm{F}} < 1$, we have convective stability.

As discussed in Section 5.5.1, the initial electron captures on ^{24}Na occur when $E_{\mathrm{F}} \approx 7\,\mathrm{MeV}$ and release approximately $4\,\mathrm{MeV}$ per capture. While using an unmodified version of MESA r7624, we observed that convective regions began to form during the onset of these electron captures, contrary to the previous stability estimates.

Figure 5.8 shows the temperature profile (top panel) and values of ∇_T (bottom panel) in a MESA model before and after a remesh occurs. The temperature profile remains unchanged and the temperatures in each cell are indicated by black horizontal lines. The vertical lines show the location of the faces. Three cells were split during the remesh and

so three new faces (dashed lines) were added. The black circles in the bottom panel show the corresponding values of ∇_T. Because the newly split cells inherited the temperature of their parent, the temperature gradient at the new faces is zero. Correspondingly, the temperature gradient at existing faces between newly split cells is approximately doubled: the temperature difference across the face has remained the same, but the size of the region surrounding the face has been halved. Thus, when $|\nabla_T| \gtrapprox 0.5|B|$ initially, as is the case during the ^{24}Na electron captures, the remesh causes faces that were previously stable by the Ledoux criterion to become unstable. During the subsequent timestep a convective region spanning the remeshed cells forms.

In order to preserve convective stability, the temperature reconstruction should not substantially alter the profile of ∇_T. To achieve this, we modify MESA so that when cells are split, the same monotonicity-preserving cubic interpolation used to reconstruct other quantities is also applied to the temperature. The grey lines (top panel) and grey circles (bottom panel) in Figure 5.8 demonstrate the result of this reconstruction. The new reconstruction does not maintain a smooth ∇_T profile, but the variations are smaller and no longer lead to the formation of a convective region.

5.C   Convergence

In order for the results of our MESA calculations to be meaningful, we must ensure that the resolution (in both space and time) is sufficient to resolve the processes of interest. Once that condition is achieved, we must also demonstrate that the answer is independent of the resolution. The primary spatial and temporal convergence settings used in our MESA calculations are

```
varcontrol_target = 1e-3
mesh_delta_coeff = 1.0      .
```

Because the peak Urca process cooling is accompanied by a localized composition change, the default controls already do an acceptable job of resolving the cooling.[6] As mentioned in Section 5.4, we use `run_star_extras` to increase our spatial and temporal resolution beyond that provided by these global limits. From Section 5.2, we know that the Urca-process cooling occurs over a range corresponding to change in Fermi energy $\Delta E_F \sim k_B T$. MESA calculates the value of the quantity $\eta = (k_B T/E_F)^{-1}$ in each cell at each timestep. If we ensure the mesh points in our model are selected as to limit variation of $\Delta\eta$ between adjacent cells and ensure that our timestep is such that $\delta\eta$ in a given cell between timesteps is also limited, we will resolve the Urca process.

The scheme by which the spatial resolution in MESA is modified is described in section 6.5 of Paxton et al. (2011). MESA allows the user to specify other "mesh functions" whose cell-to-cell variation will be reduced below the value of `mesh_delta_coeff` during remeshes.

---

[6]The effective timestep limit in a run with these controls is due to the Newton-Raphson solver taking an excessive number of iterations to converge and MESA limiting the timestep in response.
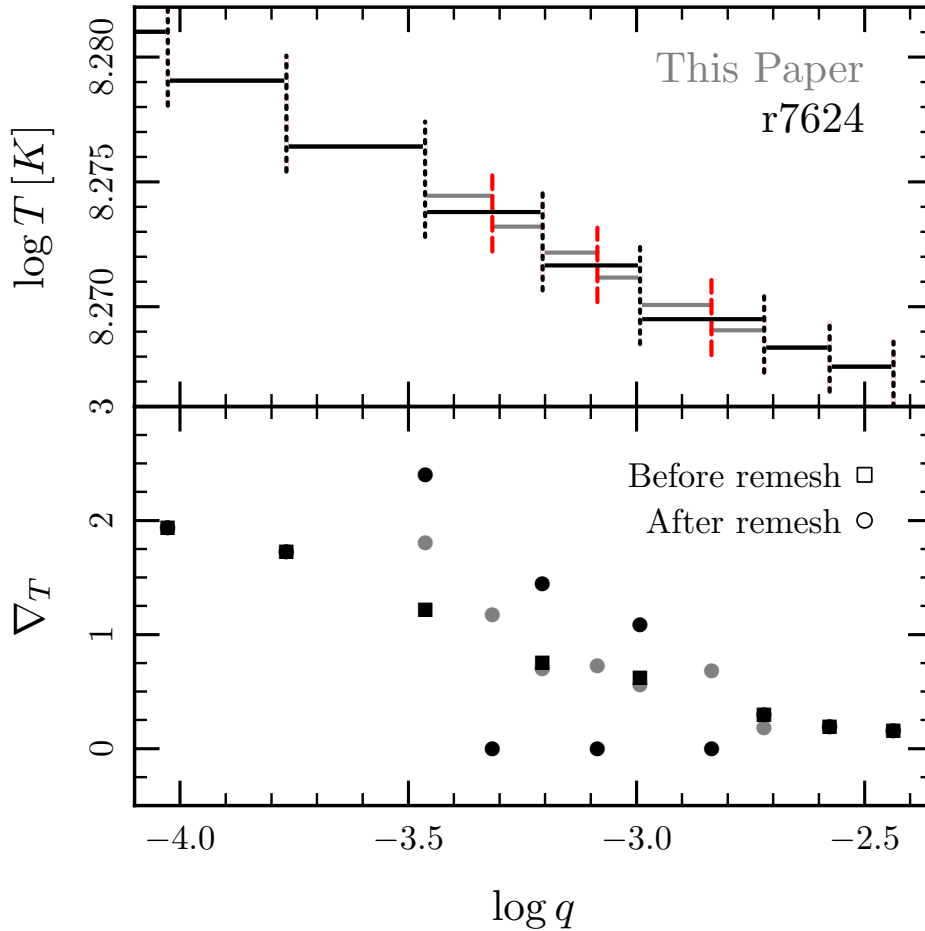
Figure 5.8: The effect of remeshing on the temperature profile (top panel) and value of ∇_T (bottom panel) in a representative MESA model at the onset of electron captures on ^{24}Na. The top panel explicitly shows MESA's finite-volume mesh. The location of the faces in the MESA model are indicated with vertical lines: the dotted lines are the faces present at the end of a timestep and the dashed lines are the faces added during the remesh. The horizontal lines show the temperature in each of the cells. The black lines show the temperature profile before the remesh occurs. In an unmodified version of MESA (r7624), the temperature profile of degenerate material remains unchanged during a remesh, and thus the black lines also show the temperature profile after the remesh. We modify the remesh step to set the temperature of split cells using monotonicity-preserving cubic interpolation. This results in the cell temperatures indicated by the grey lines. The bottom panel shows the values of ∇_T (defined at faces) as determined by the cell temperatures and extents. The black squares show the values of ∇_T before the remesh. Values after the remesh are shown with circles. The black circles show that MESA r7624 increases the value of ∇_T at existing faces between newly split cells. As discussed in the text, this leads to the formation of spurious convection zones. The grey circles show the values of ∇_T produced by the modified version of MESA used in this paper. While the new reconstruction does not maintain a smooth ∇_T profile, the variations are sufficiently small that they do not lead to the formation of a convective region, in agreement with analytic estimates.

Table 5.3: Parameters controlling the spatial and temporal resolution used in the convergence study for $\log(\rho_{\mathrm{c}}/\mathrm{g\,cm^{-3}}) \leq 9.5$. The empty entries for the "Defaults" run indicate that no direct limitation on the variations in η was imposed.

Run Name	$\Delta\eta_{\mathrm{limit}}$ (space)	$\delta\eta_{\mathrm{limit}}$ (time)
Defaults	—	—
Fiducial	3.0	3.0
High	1.0	1.0

Therefore, we define one of the mesh functions to be $f_1 = \eta/\Delta\eta_{\mathrm{limit}}$. Then MESA will limit the change in η between adjacent cells k and $k+1$ at timestep i,

$$\Delta\eta = \left|\eta^i_{k+1} - \eta^i_k\right| \ , \tag{5.37}$$

to be less than $\Delta\eta_{\mathrm{limit}}$. In order to allow high spatial resolutions in the center, we also reduce the maximum central cell size to `max_center_cell_dq = 1d-8`.

We similarly limit the timestep. After the solver has taken the values at timestep i and returned a proposed solution at timestep $i+1$, we calculate the change in η in each cell k and take the maximum,

$$\delta\eta = \max_k \left(\left|\eta^{i+1}_k - \eta^i_k\right|\right) \ . \tag{5.38}$$

If $\delta\eta > \delta\eta_{\mathrm{limit}}$, then the proposed step is rejected and redone with a shorter timestep. This is similar to the way in variations in the structure variables are limited via `varcontrol_target`.

We vary the spatial and temporal parameters and check that our results are unaffected. Table 5.C shows the parameters. Figure 5.9 shows the results of this convergence study for a model composed of ^{16}O, ^{20}Ne, and ^{23}Na (with $X_{\mathrm{Na}} = 0.03$). The results of the fiducial and high resolution cases are indistinguishable in the quantities of interest, demonstrating that our results are converged.
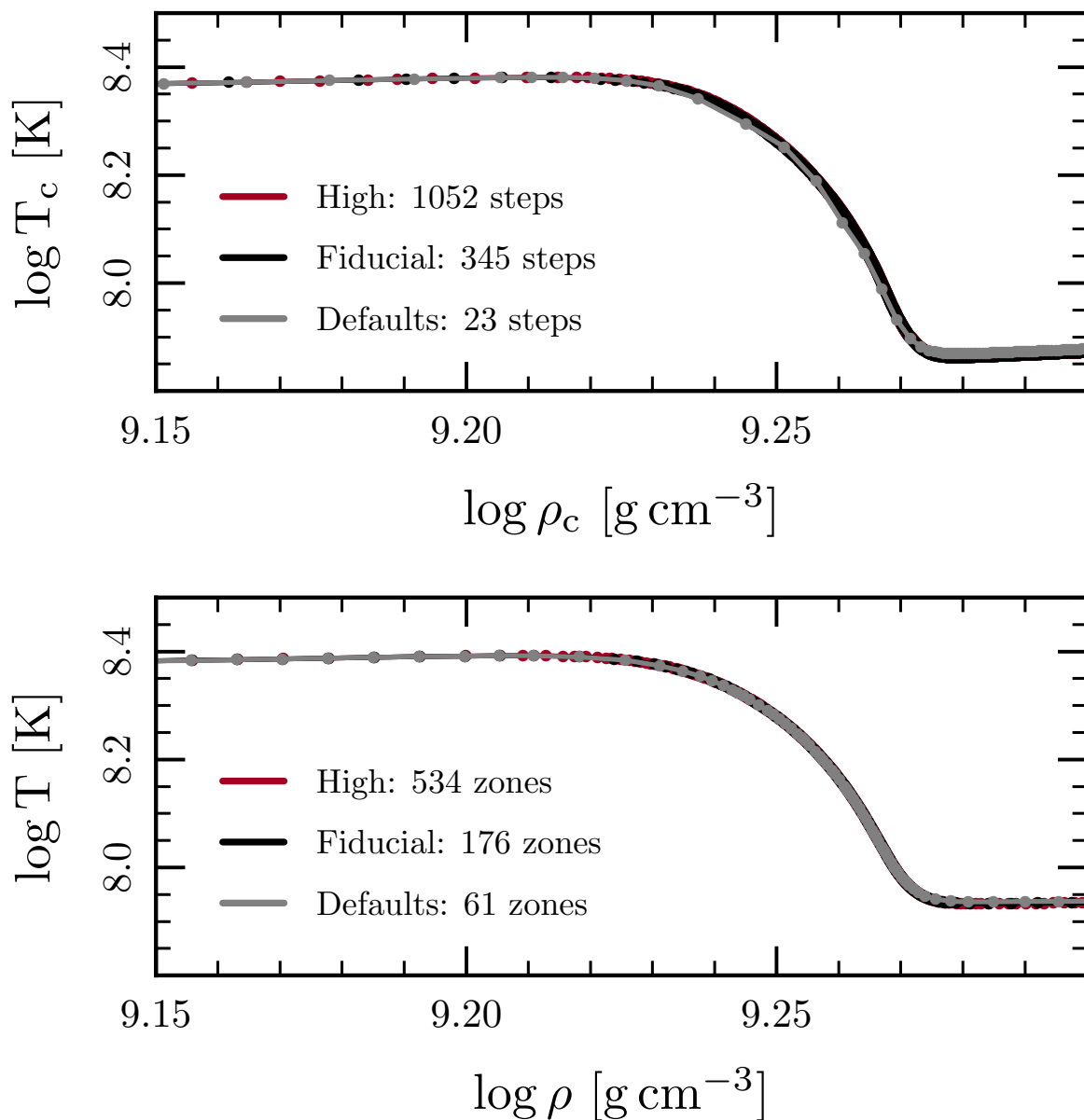
Figure 5.9: The evolution of a model with $X_{\mathrm{Na}} = 0.03$ using the different resolution controls defined in Table 5.C. The top panel shows the evolution of the central density and temperature. Each dot is a timestep. The legend shows the number of timesteps used to go from the (local) maximum temperature to the (local) minimum temperature. The bottom panel shows the density and temperature profile of the model when $\log \rho_{\mathrm{c}} = 9.4$. Each dot is a mesh point. The legend shows the number of mesh points covering the region from the (local) maximum temperature to the (local) minimum temperature.

Bibliography

Aparicio, J. M. 1998, ApJS, 117, 627

Badenes, C., & Maoz, D. 2012, ApJ, 749, L11

Badenes, C., Mullally, F., Thompson, S. E., & Lupton, R. H. 2009, ApJ, 707, 971

Balbus, S. A. 2003, ARA&A, 41, 555

Balbus, S. A., & Hawley, J. F. 1991, ApJ, 376, 214

Benz, W., Cameron, A. G. W., Press, W. H., & Bowers, R. L. 1990, ApJ, 348, 647

Bildsten, L., Shen, K. J., Weinberg, N. N., & Nelemans, G. 2007, ApJ, 662, L95

Blandford, R. D., & Begelman, M. C. 1999, MNRAS, 303, L1

—. 2004, MNRAS, 349, 68

Bloecker, T. 1995, A&A, 297, 727

Bloom, J. S., Kasen, D., Shen, K. J., et al. 2012, ApJ, 744, L17

Brooks, J., Bildsten, L., Schwab, J., & Paxton, B. 2016a, ApJ, 821, 28

—. 2016b, ApJ, To be submitted

Brown, W. R., Gianninas, A., Kilic, M., Kenyon, S. J., & Allende Prieto, C. 2016, ApJ, 818, 155

Brown, W. R., Kilic, M., Allende Prieto, C., Gianninas, A., & Kenyon, S. J. 2013, ApJ, 769, 66

Brown, W. R., Kilic, M., Allende Prieto, C., & Kenyon, S. J. 2010, ApJ, 723, 1072

—. 2012, ApJ, 744, 142

Brown, W. R., Kilic, M., Hermes, J. J., et al. 2011, ApJ, 737, L23

Burkart, J., Quataert, E., Arras, P., & Weinberg, N. N. 2013, MNRAS, 433, 332

Canal, R., Isern, J., & Labay, J. 1992, ApJ, 398, L49

Chabrier, G., & Potekhin, A. Y. 1998, Phys. Rev. E, 58, 4941

Chandrasekhar, S. 1931, ApJ, 74, 81

Clayton, G. C. 1996, PASP, 108, 225

—. 2012, Journal of the American Association of Variable Star Observers (JAAVSO), 40, 539

Clayton, G. C., Geballe, T. R., Herwig, F., Fryer, C., & Asplund, M. 2007, ApJ, 662, 1220

Commins, E. 1973, Weak Interactions (McGraw-Hill)

Corbelli, E. 2003, MNRAS, 342, 199

Couch, R. G., & Loumos, G. L. 1974, ApJ, 194, 385

Cox, J. P. 1968, Principles of stellar structure - Vol.1: Physical principles; Vol.2: Applications

to stars

Cyburt, R. H., Amthor, A. M., Ferguson, R., et al. 2010, ApJS, 189, 240

Dan, M., Rosswog, S., Brüggen, M., & Podsiadlowski, P. 2014, MNRAS, 438, 14

Dan, M., Rosswog, S., Guillochon, J., & Ramirez-Ruiz, E. 2011, ApJ, 737, 89

—. 2012, MNRAS, 422, 2417

Denissenkov, P. A., Herwig, F., Truran, J. W., & Paxton, B. 2013, ApJ, 772, 37

Dewitt, H. E., Graboske, H. C., & Cooper, M. S. 1973, ApJ, 181, 439

Duchêne, G., & Kraus, A. 2013, ARA&A, 51, 269

Dufour, P., Fontaine, G., Liebert, J., Schmidt, G. D., & Behara, N. 2008, ApJ, 683, 978

Dufour, P., Liebert, J., Fontaine, G., & Behara, N. 2007, Nature, 450, 522

Evans, C. R., Iben, Jr., I., & Smarr, L. 1987, ApJ, 323, 129

Farmer, R., Fields, C. E., & Timmes, F. X. 2015, ApJ, 807, 184

Ferguson, J. W., Alexander, D. R., Allard, F., et al. 2005, ApJ, 623, 585

Ferguson, J. W., & Dotter, A. 2008, in IAU Symposium, Vol. 252, IAU Symposium, ed. L. Deng & K. L. Chan, 1

Fields, C. E., Farmer, R., Petermann, I., Iliadis, C., & Timmes, F. X. 2016, ArXiv e-prints, arXiv:1603.06666 [astro-ph.SR]

Firestone, R. B. 2007a, Nuclear Data Sheets, 108, 1

—. 2007b, Nuclear Data Sheets, 108, 2319

—. 2009, Nuclear Data Sheets, 110, 1691

Fuller, G. M., Fowler, W. A., & Newman, M. J. 1980, ApJS, 42, 447

—. 1985, ApJ, 293, 1

Fuller, J., & Lai, D. 2012a, MNRAS, 421, 426

—. 2012b, MNRAS, 421, 426

Gamow, G., & Schoenberg, M. 1941, Physical Review, 59, 539

García-Berro, E., Lorén-Aguilar, P., Aznar-Siguán, G., et al. 2012, ApJ, 749, 25

Geier, S., Heber, U., Kupfer, T., & Napiwotzki, R. 2010, A&A, 515, A37

Geier, S., Napiwotzki, R., Heber, U., & Nelemans, G. 2011, A&A, 528, L16

Gianninas, A., Kilic, M., Brown, W. R., Canton, P., & Kenyon, S. J. 2015, ApJ, 812, 167

Gokhale, V., Peng, X. M., & Frank, J. 2007, ApJ, 655, 1010

Gove, N. B., & Martin, M. J. 1971, Atomic Data and Nuclear Data Tables, 10, 205

Grevesse, N., & Sauval, A. J. 1998, Space Sci. Rev., 85, 161

Guillochon, J., Dan, M., Ramirez-Ruiz, E., & Rosswog, S. 2010, ApJ, 709, L64

Gutiérrez, J., Canal, R., & García-Berro, E. 2005, A&A, 435, 231

Gutierrez, J., Garcia-Berro, E., Iben, Jr., I., et al. 1996, ApJ, 459, 701

Hansen, B. M. S., & Liebert, J. 2003, ARA&A, 41, 465

Hawley, J. F., Gammie, C. F., & Balbus, S. A. 1995, ApJ, 440, 742

Hayes, J. C., Norman, M. L., Fiedler, R. A., et al. 2006, ApJS, 165, 188

Heber, U. 2009, ARA&A, 47, 211

Hillier, J. 2011, CMFGEN: Probing the Universe through Spectroscopy, Astrophysics Source Code Library, ascl:1109.020

Iben, Jr., I. 1978, ApJ, 219, 213

Iben, Jr., I., & Livio, M. 1993, PASP, 105, 1373

Iben, Jr., I., & Tutukov, A. V. 1984a, ApJS, 54, 335

—. 1984b, ApJS, 54, 335

Ichimaru, S. 1993, Reviews of Modern Physics, 65, 255

Iglesias, C. A., & Rogers, F. J. 1993, ApJ, 412, 752

—. 1996, ApJ, 464, 943

Isern, J., Canal, R., & Labay, J. 1991, ApJ, 372, L83

Itoh, N., Hayashi, H., Nishikawa, A., & Kohyama, Y. 1996, ApJS, 102, 411

Itoh, N., Tomizawa, N., Tamamura, M., Wanajo, S., & Nozawa, S. 2002, ApJ, 579, 380

Janka, H.-T., Müller, B., Kitaura, F. S., & Buras, R. 2008, A&A, 485, 199

Jones, S., Hirschi, R., & Nomoto, K. 2014, ApJ, 797, 83

Jones, S., Hirschi, R., Nomoto, K., et al. 2013, ApJ, 772, 150

Juodagalvis, A., Langanke, K., Hix, W. R., Martínez-Pinedo, G., & Sampaio, J. M. 2010, Nuclear Physics A, 848, 454

Karl, C. A., Napiwotzki, R., Nelemans, G., et al. 2003, A&A, 410, 663

Katz, M. P., Zingale, M., Calder, A. C., et al. 2016, ApJ, 819, 94

Kepler, S. O., Kleinman, S. J., Nitta, A., et al. 2007, MNRAS, 375, 1315

Kilic, M., Brown, W. R., Allende Prieto, C., et al. 2011a, ApJ, 727, 3

—. 2012, ApJ, 751, 141

Kilic, M., Brown, W. R., Gianninas, A., et al. 2014, MNRAS, 444, L1

Kilic, M., Brown, W. R., Hermes, J. J., et al. 2011b, MNRAS, 418, L157

Kilic, M., Brown, W. R., Kenyon, S. J., et al. 2011c, MNRAS, 413, L101

Kitaura, F. S., Janka, H.-T., & Hillebrandt, W. 2006, A&A, 450, 345

Kremer, K., Sepinsky, J., & Kalogera, V. 2015, ApJ, 806, 76

Kwok, S. 1993, ARA&A, 31, 63

Langer, N. 1991, A&A, 252, 669

Langer, N., Fricke, K. J., & Sugimoto, D. 1983, A&A, 126, 207

Lecoanet, D., Schwab, J., Quataert, E., et al. 2016, ArXiv e-prints, arXiv:1603.08921 [astro-ph.SR]

Lorén-Aguilar, P., Isern, J., & García-Berro, E. 2009, A&A, 500, 1193

Maoz, D., Badenes, C., & Bickerton, S. J. 2012, ApJ, 751, 143

Marsh, T. R. 1995, MNRAS, 275, L1

Marsh, T. R., Nelemans, G., & Steeghs, D. 2004, MNRAS, 350, 113

Martínez-Pinedo, G., Lam, Y. H., Langanke, K., Zegers, R. G. T., & Sullivan, C. 2014, Phys. Rev. C, 89, 045806

Martínez-Rodríguez, H., Piro, A. L., Schwab, J., & Badenes, C. 2016, ArXiv e-prints, arXiv:1602.00673 [astro-ph.SR]

Miyaji, S., & Nomoto, K. 1987, ApJ, 318, 307

Miyaji, S., Nomoto, K., Yokoi, K., & Sugimoto, D. 1980, PASJ, 32, 303

Moll, R., Raskin, C., Kasen, D., & Woosley, S. E. 2014, ApJ, 785, 105

Monaghan, J. J. 1992, ARA&A, 30, 543

Mullally, F., Badenes, C., Thompson, S. E., & Lupton, R. 2009, ApJ, 707, L51

Napiwotzki, R., Edelmann, H., Heber, U., et al. 2001a, A&A, 378, L17

Napiwotzki, R., Christlieb, N., Drechsel, H., et al. 2001b, Astronomische Nachrichten, 322, 411

Napiwotzki, R., Koester, D., Nelemans, G., et al. 2002, A&A, 386, 957

Narayan, R., & Yi, I. 1994, ApJ, 428, L13

Nelemans, G. 2009, Classical and Quantum Gravity, 26, 094030

Nelemans, G., Yungelson, L. R., & Portegies Zwart, S. F. 2001, A&A, 375, 890

Nelemans, G., Napiwotzki, R., Karl, C., et al. 2005, A&A, 440, 1087

Nomoto, K. 1984, ApJ, 277, 791

Nomoto, K., & Iben, Jr., I. 1985, ApJ, 297, 531

Nomoto, K., & Kondo, Y. 1991, ApJ, 367, L19

Nomoto, K., Thielemann, F.-K., & Yokoi, K. 1984, ApJ, 286, 644

Oda, T., Hino, M., Muto, K., Takahara, M., & Sato, K. 1994, Atomic Data and Nuclear Data Tables, 56, 231

Paczyński, B. 1967, Acta Astron., 17, 287

—. 1971, Acta Astron., 21, 271

—. 1973, Acta Astron., 23, 1

Pakmor, R., Edelmann, P., Röpke, F. K., & Hillebrandt, W. 2012a, MNRAS, 424, 2222

Pakmor, R., Kromer, M., Röpke, F. K., et al. 2010, Nature, 463, 61

Pakmor, R., Kromer, M., Taubenberger, S., et al. 2012b, ApJ, 747, L10

—. 2012c, ApJ, 747, L10

Paxton, B., Bildsten, L., Dotter, A., et al. 2011, ApJS, 192, 3

Paxton, B., Cantiello, M., Arras, P., et al. 2013, ApJS, 208, 4

Paxton, B., Marchant, P., Schwab, J., et al. 2015, ApJS, 220, 15

Piersanti, L., Gagliardi, S., Iben, Jr., I., & Tornambé, A. 2003a, ApJ, 598, 1229

—. 2003b, ApJ, 583, 885

Plewa, T., & Müller, E. 1999, A&A, 342, 179

Podsiadlowski, P., Dewi, J. D. M., Lesaffre, P., et al. 2005, MNRAS, 361, 1243

Potekhin, A. Y., & Chabrier, G. 2000, Phys. Rev. E, 62, 8554

—. 2010, Contributions to Plasma Physics, 50, 82

Potekhin, A. Y., Chabrier, G., & Rogers, F. J. 2009, Phys. Rev. E, 79, 016411

Quirion, P.-O., Fontaine, G., & Brassard, P. 2007, ApJS, 171, 219

Raskin, C., Kasen, D., Moll, R., Schwab, J., & Woosley, S. 2014, ApJ, 788, 75

Raskin, C., Scannapieco, E., Fryer, C., Rockefeller, G., & Timmes, F. X. 2012, ApJ, 746, 62

Raskin, C., Timmes, F. X., Scannapieco, E., Diehl, S., & Fryer, C. 2009, MNRAS, 399, L156

Ritossa, C., García-Berro, E., & Iben, Jr., I. 1999, ApJ, 515, 381

Ruiter, A. J., Belczynski, K., Benacquista, M., Larson, S. L., & Williams, G. 2010, ApJ, 717, 1006

Saio, H., & Jeffery, C. S. 2000, MNRAS, 313, 671

Saio, H., & Nomoto, K. 1985, A&A, 150, L21

—. 1998, ApJ, 500, 388

—. 2004, ApJ, 615, 444

Sato, Y., Nakasato, N., Tanikawa, A., et al. 2015, ApJ, 807, 105

Schaefer, B. E., & Pagnotta, A. 2012, Nature, 481, 164

Schwab, J., Quataert, E., & Bildsten, L. 2015, MNRAS, 453, 1910

Schwab, J., Shen, K. J., Quataert, E., Dan, M., & Rosswog, S. 2012, MNRAS, 427, 190

Seitenzahl, I. R., Townsley, D. M., Peng, F., & Truran, J. W. 2009, Atomic Data and Nuclear Data Tables, 95, 96

Sepinsky, J. F., & Kalogera, V. 2014, ApJ, 785, 157

Shapiro, S. L., & Teukolsky, S. A. 1983, Black holes, white dwarfs, and neutron stars: The physics of compact objects

Shen, K. J. 2015, ApJ, 805, L6

Shen, K. J., Bildsten, L., Kasen, D., & Quataert, E. 2012, ApJ, 748, 35

Spruit, H. C. 2002, A&A, 381, 923

Stone, J. M., Hawley, J. F., Gammie, C. F., & Balbus, S. A. 1996, ApJ, 463, 656

Stone, J. M., & Norman, M. L. 1992, ApJS, 80, 753

Stone, J. M., & Pringle, J. E. 2001, MNRAS, 322, 461

Stone, J. M., Pringle, J. E., & Begelman, M. C. 1999, MNRAS, 310, 1002

Takahara, M., Hino, M., Oda, T., et al. 1989, Nuclear Physics A, 504, 167

Takahashi, K., Yoshida, T., & Umeda, H. 2013, ApJ, 771, 28

Tamm, A., Tempel, E., Tenjes, P., Tihhonova, O., & Tuvikene, T. 2012, A&A, 546, A4

Tange, O. 2011, ;login: The USENIX Magazine, 36, 42

Tauris, T. M., Langer, N., Moriya, T. J., et al. 2013, ApJ, 778, L23

Tauris, T. M., Langer, N., & Podsiadlowski, P. 2015, MNRAS, 451, 2123

Tayler, R. J. 1973, MNRAS, 161, 365

Thompson, T. A., Prieto, J. L., Stanek, K. Z., et al. 2009, ApJ, 705, 1364

Tilley, D. R., Cheves, C. M., Kelley, J. H., Raman, S., & Weller, H. R. 1998, Nuclear Physics A, 636, 249

Timmes, F. X., & Swesty, F. D. 2000, ApJS, 126, 501

Timmes, F. X., & Woosley, S. E. 1992, ApJ, 396, 649

Timmes, F. X., Woosley, S. E., & Taam, R. E. 1994, ApJ, 420, 348

Toki, H., Suzuki, T., Nomoto, K., Jones, S., & Hirschi, R. 2013, Phys. Rev. C, 88, 015806

Tsuruta, S., & Cameron, A. G. W. 1970, Ap&SS, 7, 374

van Kerkwijk, M. H., Chang, P., & Justham, S. 2010a, ApJ, 722, L157

—. 2010b, ApJ, 722, L157

van Loon, J. T., Groenewegen, M. A. T., de Koter, A., et al. 1999, A&A, 351, 559

Waxman, E., & Draine, B. T. 2000, ApJ, 537, 796

Webbink, R. F. 1979, in IAU Colloq. 53: White Dwarfs and Variable Degenerate Stars, ed. H. M. van Horn & V. Weidemann, 426

Webbink, R. F. 1984, ApJ, 277, 355

Wilson, W. J., & Barrett, A. H. 1968, Science, 161, 778

Wongwathanarat, A., Janka, H.-T., & Müller, E. 2013, A&A, 552, A126

Woosley, S. E., & Heger, A. 2015, ApJ, 810, 34

Woosley, S. E., Heger, A., & Weaver, T. A. 2002, Reviews of Modern Physics, 74, 1015

Woosley, S. E., & Kasen, D. 2011, ApJ, 734, 38

Yakovlev, D. G., & Shalybkov, D. A. 1989, Astrophysics and Space Physics Reviews, 7, 311

Yoon, S.-C., Langer, N., & Norman, C. 2006, A&A, 460, 199

Yoon, S.-C., Podsiadlowski, P., & Rosswog, S. 2007, MNRAS, 380, 933

York, D. G., Adelman, J., Anderson, Jr., J. E., et al. 2000, AJ, 120, 1579